Contents

Acknowledgements

I

Introduction

Most of the studies of the transition between a liquid and a glass rely on classical Statistical Mechanics. In many cases neglecting quantum fluctuations is in fact a reasonable assumption, as the de Broglie wavelength is typically much smaller than the inter-particle distance and quantum effects are expected to be irrelevant. However, in the light of several recent experiments and possible interesting applications, it is important to account for an inherent quantum behavior. In this thesis quantum effects are introduced in the framework of a mean-field description of the glassy phase. We consider many-body quantum systems that are accessible to an analytical treatment mainly because of their simplified spatial structure, and we study their most relevant thermodynamical aspects. Moreover we analyze a case of out-of-equilibrium quantum dynamics exploiting ideas and tools originally developed for classical glassy models.

As we mentioned, there are several and quite disparate motivations that encouraged us for this work, which are outlined in Section I.3 of this Introduction. Before though, in Sections I.1 and I.2, we want to touch upon the intriguing features pertaining to the physics of classical glasses, and how these features emerge in a broader range of problems that can actually extend over various domains. Likewise, these many facets coexist also when one studies quantum effects, which are indeed much less understood.

We conclude the Introduction with a summary of the results presented in this thesis, together with the outline of their presentation in Section I.4. In Section I.5 we report the references to the original works where they have been discussed.

I.1   Classical glasses

Glass-forming materials are characterized by their tendency to avoid crystallization during cooling below the melting temperature T_m. Upon approaching the glass transition T_g the relaxation time of glasses increases very fast. The temperature T_g is actually not a true phase transition, but a conventional value below which the system does not flow over any reasonable experimental time scale, due to the dramatic increase of its viscosity. Once quenched below T_g, glasses look like *amorphous solids*, with an infinite viscosity but without any hint for an obvious long-range order. Indeed glasses present an atomic structure close to that of liquids but mechanical properties of solids. In this respect they are like "liquids that can not flow". The understanding of this rigidity is a basic problem of condensed matter, that is susceptible of controversial explanations. In crystals there is a manifest order that emerges abruptly in correspondence of a first-order phase transition. Translational and
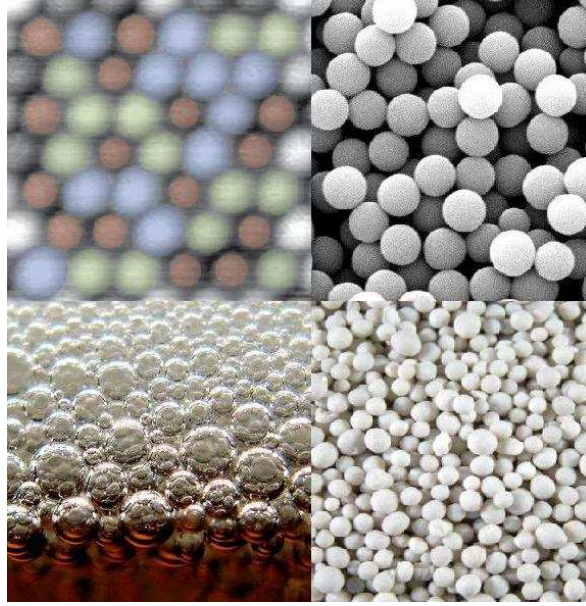
Figure I.1: Different systems, spanning several length scales, develop analogous glassy properties at low temperature or high density. (*Top left*) atomic force spectroscopy image of an alloy, (*top right*) colloidal systems, (*bottom left*) a beer foam, (*bottom right*) granular materials. From [1].

rotational invariances are broken and the particles, on average, are identified with the coordinates of a lattice. The thermodynamics of glasses is instead that of a second-order phase transition, there is no latent heat and the relaxation time increases progressively.

When the relaxation time exceeds the experimental time scale, the system is no longer able to equilibrate and inevitably falls out-of-equilibrium. The peculiar way in which this dynamical regime develops is the hallmark of glassiness. It is important to mention that very different materials show the same glassy behavior, and more specifically analogous dynamics. Glassy physics covers a broad range of time and length scales, such as in atomic, colloidal systems, foams and granular materials (see Fig. I.1). Although the microscopic mechanism responsible for such a slowing down is unknown - and might be different in different cases - the out-of-equilibrium dynamics presents very similar properties like aging, memory effects, hysteresis and the emergence of effective temperatures [2].

I.2 Optimization over complex energy landscapes: many glasses in science

A typical problem that is encountered in almost all branches of science is that of optimizing irregularly shaped cost functions.

In classical combinatorial optimization one considers discrete variables and assigns a cost function to each of their configuration. The cost function is the result of competing local interactions and this frustration inherent to optimization problems is the essential ingredient that preludes to glassy physics. Due to such frustration, the problem of finding the optimal configuration minimizing the cost function turns out to be very hard, typically intractable.

Indeed the cost function displays many local minima separated by extensive barriers. These minima

represent generically metastable states that are ubiquitous in the physics of glasses and are responsible for their slow relaxation, since they trap the system dynamics for long times. For the same reason a local algorithm that performs a dynamical search in phase space, such as (thermal) simulated annealing [3], fails to find the optimal solution of the problem.

The study of the average properties of these models revealed in fact a phenomenology intimately related to that of mean-field glassy systems. The understanding of this analogy has proven particularly fruitful, leading to the development of powerful techniques (replica and cavity method, survey propagation, . . .) able to tackle rough cost functions and finite connectivity graphs. Remarkably, the combination of these approaches allowed one to unveil several features and phase transitions in the configuration space of optimization problems when a control parameter (typically the ratio of the number of constraints in the cost function to the number of variables) is tuned [4, 5, 6].

I.3   Restoring $\hbar$: when quantum fluctuations matter

I.3.1   Quantum annealing for hard problems

The appealing possibility to exploit quantum mechanics to solve hard optimization problems is at the core of the theoretical and experimental research in quantum computation. In the idea of *quantum annealing* [7, 8] resides the suggestion that if the energy barriers are sufficiently "narrow", regardless of their height, quantum fluctuations allow *tunneling* processes to connect local minima, more efficiently than the "jump over" mechanism induced by thermal activation, typical of simulated annealing. This intuition is supported, for instance, by the application of the WKB approximation to the study of a particle in a one dimensional double well potential [9]. From this example one learns that even if the barrier is infinitely high the particle has a finite probability to tunnel through it, and this probability decreases exponentially with the width of the barrier.

In practice, with the quantum annealing, the problem is encoded in a physical system described by a time dependent Hamiltonian that interpolates between a term whose ground state is known (and easy to prepare) at time $t = 0$, and the problem Hamiltonian (the classical cost function) at the end of the process $t = T$, where T is the total duration of the annealing. This interpolating process, i.e. the annealing, takes place at zero temperature and must occur slowly enough, in such a way to maintain the system in the instantaneous ground state of the Hamiltonian. The fact that an infinitely slow annealing maintains the system in its ground state is assured by the adiabatic theorem. Algorithmically though, the interest is in a fast protocol and a reliable criterium to control the speed of the annealing. According to the adiabatic theorem, the probability of a transition to excited states during the annealing is controlled by the minimum spectral gap of the Hamiltonian. Thus, the efficiency of the algorithm is determined by the scaling of the gap with the size of the system and it is limited by the presence of quantum phase transitions or avoided level crossings, at which the gap becomes extremely small. All this highlights that, for a better understanding of these new computational tools, it is necessary to understand the physics of quantum optimization problems. The thermodynamical and spectral properties of these models will be the subject of the first part of this thesis.

I.3.2   Low temperature properties of disordered systems

The presence of frustration and disorder in quantum systems leads to a rich and complex behavior, manifested in unconventional phases and phase transitions, high density of low-energy states and

peculiar dynamical properties [10]. The complexity of these phenomena often lacks a solid theoretical understanding and sometimes also defies a detailed experimental investigation.

Among the motivations that stimulated the first theoretical studies on quantum glasses [11, 12, 13] are some experiments carried out with the dipolar magnet $Li\,Ho_x Y_{1-x} Fe$ [14] that point to the importance of the interplay of glassiness and quantum effects. This compound shows a phase transition from a paramagnetic to a spin-glass ordered phase which is second order at low transverse field whereas it becomes first order at low temperature and larger transverse field, when it is driven by quantum fluctuations. Besides this example there are several observations of quantum glassy phases in electron systems [15] and other structural glasses [16], and, very interestingly, the proposal of a spin-glass phase in the phase diagram of high temperature superconductors [17].

More recently, many experiments on supersolid Helium [18] have raised new excitement in this direction, related to the possibility for (disordered) solid samples of developing off-diagonal long range order [19]. The idea that a solid, crystalline or amorphous, could display a Non-Classical Rotational Inertia (NCRI), interpreted as a superfluid density component, was actually proposed already in the 1970s by Leggett [20] and other authors. The proposal was interesting enough to induce many experimental groups to look for the predicted effect. However only in 2004 the phenomenon of NCRI has been detected experimentally. Lately, the enhancement of the phenomenon with highly disordered samples, obtained by fast quenches that some identified as glasses [21], has been pointed out [22]. Despite these efforts though, a complete explanation of the NCRI mechanism and its relation with disorder is still lacking.

These interesting results naturally draw the attention to the role of quantum fluctuations, and to the possible existence of superfluid phases in amorphous systems, such as glasses or more general frustrated systems. Moreover a new phase of matter, named "superglass", has been proposed in some theoretical works, based on analytical [23, 24] and numerical results [25, 26]. However, a precise characterization of this phase has not been achieved yet and it remains unclear whether it is possible to recover it from the Hamiltonians of classical structural glasses by simply adding a non-commuting term that induces quantum dynamics. The call for a deeper understanding of quantum glasses demanded by the reconstruction of this puzzling picture inspired the second direction of our study. In particular the major question here is whether off-diagonal long range order and glassy behavior can coexist.

I.3.3 Out-of-equilibrium and non-ergodicity

The hallmark of glassy systems is aging and the associated slow, out-of-equilibrium dynamics. Their dynamics is stuck around few amorphous configurations and they can not freely explore the available phase space. Although one-time quantities may look stationary in the long time limit, two-time correlations show remarkable off-equilibrium effects, depending explicitly on both times. This non-equilibrium regime represents the major difficulty that renders their study particularly hard: most of the postulates of statistical mechanics apply in fact only to equilibrium systems. As a result this has stimulated the physics community to develop several tools and ideas for the non-equilibrium. The main questions posed in this context concern the spatial structure of microscopic components, the relaxation time, the possibility to define effective temperatures or, more generally, an effective thermodynamic description [27, 28]. Including quantum fluctuations in this framework, or better, addressing these questions for the quantum dynamics, is definitely an important issue.

Quantum effects further enrich the spectrum of dynamical behavior. We already presented some of the experimental motivations for their investigation. Moreover, the experimental interest is sustained by the overwhelming progress in the field of cold atoms that allows one to explore dynamical aspects

of inherent quantum nature [29]. The level of accuracy and precision achieved in this field allows the realization of perfectly tunable quantum systems, much more controllable than other standard condensed matter materials like electron or magnetic systems. A remarkable example that deals with disorder is the recent realization of Anderson localization with cold atoms.

Localization and thermalization are intertwined because of the lack of ergodicity caused by the transition to localized states which spoils the possibility to approach thermal equilibrium [30]. Understanding ergodicity and thermalization in quantum systems is an open and very broad problem; important distinctions regarding the environment and the interactions are mandatory. Notably, localization in many-body problems [31, 32, 33] is a topic of ongoing research in this direction, where glassy properties are expected, but not necessarily relying on microscopic Hamiltonians as the standard ones for classical glasses. Purely quantum properties may lead to a slow relaxation.

As the study of the quantum dynamics is a very hard problem and many aspects are still poorly understood, in this part of work we consider a simpler situation, avoiding disorder and complex energy landscapes. The non-equilibrium behavior is induced by a sudden change in one of the parameters in the Hamiltonian and the dynamics is unitary, the system being isolated. The third and last problem we focused on in this thesis concerns the study of this dynamical regime and its characterization in terms of the ideas originally proposed for glassy systems out of equilibrium.

I.4 Outline of the presentation and main results

As anticipated in the previous Sections of the Introduction, we organized the thesis into three topics that are the subjects of three Parts:

- **Part A**: Quantum optimization problems

- **Part B**: Quantum glasses

- **Part C**: Out-of-equilibrium quantum dynamics

Clearly they all deal with quantum systems, and they are strongly influenced by important ideas developed in the context of classical statistical mechanics. Motivated by the theoretical ideas and the experimental facts mentioned in the previous Sections, all the works started from the intuition that those "classical" ideas are relevant also for a quantum description. The first Chapter of each Part is devoted to the presentation of the classical context where such ideas naturally apply and have been developed, and to the discussion of the quantum aspects that we aim to understand, i.e. the framework where we have applied them. These introductory Chapters are listed and summarized below.

Introductory and review Chapters

- **Chapter 1** (Part A): Introduces the definitions and some relevant aspects of classical optimization problems. Afterwards, it focuses on quantum computation and specifically on the problem of the quantum annealing. It describes how this applies to optimization problems and discusses the relevant ideas in the literature that motivated our works.

- **Chapter 5** (Part B): Presents the phenomenological aspects of glassy systems (as inferred from experimental evidences and numerical simulations). It introduces the experimental setup in which the non-classical rotational inertia (NCRI) was first observed in solid Helium and

the reason to ask about the role of disorder in the samples. The rest of the Chapter outlines
the theoretical framework on which we base our understanding of "classical" glasses and the
theoretical results reported in the literature that stimulated our investigation.

- **Chapter 8** (Part C): Describes the dynamical aspects of glasses and how they can be recon-
  ciled with a thermodynamical picture through the study of generalized fluctuation-dissipation
  relations (FDRs). In particular it introduces the concept of effective temperature defined from
  FDRs. We discuss the problem and the motivation for the study of the unitary dynamics in
  quantum systems out of equilibrium, in particular when a parameter in the Hamiltonian is
  suddenly changed, a quantum quench. We discuss how a definition of effective temperature
  naturally emerged in this context and the role of the integrals of motion.

- **Chapter 2** (Part A): This Chapter introduces concepts and tools that are recalled also in
  other Parts of the thesis. Moreover it describes how we extend the statistical treatment from a
  classical to a quantum description. It presents the theoretical view that we followed and that
  is able to capture and characterize the average properties of optimization problems as well as
  glassy systems (in a mean-field framework at least). We present these ideas together with the
  cavity method, which is actually a way to derive them precisely. We describe how the cavity
  method has been generalized to quantum systems, what are the natural degrees of freedom and
  the equations that characterize their probability. We present the way in which we sample from
  this probability.

On the basis of these introductory Chapters, the remaining Chapters are devoted to the presentation
of our results.

Chapters presenting novel results

- **Chapter 3** (Part A): In this Chapter we present the study of the quantum version of a simple
  case of optimization problems, the so-called random subcubes model. The classical definition
  of the model was presented in [34] and quantum fluctuations are introduced by the action of a
  transverse field. The classical model displays in a simple manner the most relevant transitions
  which appear in standard optimization problems. In particular it captures the phenomenon of
  "clusterization" of solutions and of the finite entropy which persists at zero temperature. In
  all the studies considered so far in the literature of mean-field glassy models with a transverse
  field this feature was in fact missing and it is supposed to give rise to important effects, due
  to the sensitivity of degenerate states to external fluctuations. Overall, this toy model shows
  that the low-energy spectrum of quantum optimization problems can be very complex, and be
  characterized by different level crossings: internal level crossings in the spin glass phase, or
  the crossing between the spin glass and the quantum paramagnet giving rise to a first-order
  phase transition. Moreover, both entropic and energetic effects are important. Finally we find
  a reentrant condensation transition as a function of the transverse field, meaning that quantum
  fluctuations favor the glassiness of the system. The properties of the model have been derived
  analytically. They combine the probabilistic treatment that was introduced for the classical
  model [34] together with the study of the spectrum of the non-diagonal quantum Hamiltonian.
  Additional results exploit exact diagonalization of finite instances of the system. The results
  presented in this Chapter have been published in [P1].

- **Chapter 4** (Part A): In this Chapter we present the study of the k-XORSAT problem with transverse field on a c-regular random graph. The model is relevant because, contrary to the random subcubes model, it represents a "realistic" optimization problem. The results concern the phase diagram for $k=3$ and $c=3$, $k=4$ and $c=3$ and $k=3$ and $c=4$. The three models are characterized by different classical phase diagrams and at $T = 0$ they are in the SAT or UNSAT phase depending on the ratio c/k. The phase diagrams for the quantum problem, as a function of the temperature and of the transverse field are obtained mainly with the quantum cavity method and quantum Monte Carlo simulations. At low temperature they display a first-order phase transition as a function of the transverse field between a quantum paramagnetic state and the spin-glass phase. Moreover the classical glass transitions extend approximately up to the first-order phase transition with the quantum paramagnet. The first-order phase transition together with the spectral properties of the gap is also studied via exact diagonalization in the case of degenerate and non-degenerate spectrum. Most of the results have been presented in [35]. My contribution concerns the study of the degenerate spectrum, $c = 3$ and $k = 4$, with a numerical exact diagonalization procedure. This, together with the complete description outlined in the Chapter 4 will be presented in [P6].

- **Chapter 6** (Part B): This Chapter presents the generalization of a classical model, the Biroli-Mézard model [36], that is believed to capture the physics of structural glasses, to the quantum case. The model involves a particle system on a lattice, governed by many-body repulsive interactions where quantum fluctuations are introduced through hopping between neighboring sites. The model can be solved on a particular class of lattices through the cavity method, combining an analytical and a numerical treatment which is particularly suited for disordered and frustrated systems.

  The crucial difference compared to other systems showing glassy behavior and already studied in the literature is that classically the model presents a glass transition as a function of the density at zero temperature, where quantum fluctuations are most relevant. Associated with this transition there is a complex organization of the massively degenerate classical ground states which is expected to be very sensitive to quantum perturbations. One of the most interesting results concerning the phase diagram is the emergence of a reentrant behavior of the glass transition as a function of the quantum parameter, meaning that in some regimes quantum fluctuations enhance the glassiness of the system, instead of competing with it. We found the same mechanism in the random subcubes model, presented in Chapter 3, and on the basis of this analogy we devised an explanation which has a general interpretation as an order-by-disorder mechanism, which selects some ground state for entropic reasons. The second point of interest is a phase coexistence between a homogeneous superfluid phase and a glass phase induced by a first order phase transition which could be relevant for some experimental observations. The results of this work have been published in [P2].

- **Chapter 7** (Part B): This Chapter is devoted to the study of a variational bound on the superfluid fraction in a solid proposed by Leggett [20], which is generalized to the case of an amorphous solid. The analysis concerns on the one hand the numerical investigation of the bound, on the other hand the simulation of the imaginary time quantum dynamics of a system of ^{4}He together with a comparison of the classical dynamics of a glassy system, interacting via a Lennard-Jones potential. These estimates suggest that, at least at the level of the upper bound, there is not much difference in terms of superfluid fraction between a glass and a crystal at the

same density, and that possible enhancement of superfluidity due to the disorder of the crystal samples could be attributed to non-equilibrium phenomena. The results have been published in [P3].

- **Chapter 9** (Part C): This Chapter presents the study of the out-of-equilibrium dynamics following a quantum quench in the transverse Ising chain. The aim of the study is to address the issue of thermalization in closed quantum many-body systems from the perspective of the fluctuation-dissipation relations (FDRs). FDRs provide a unique definition of the temperature of equilibrium systems, through a relation between dynamical correlations and responses. The same relation can be used in an out-of-equilibrium dynamics in order to define an *effective temperature* and to study the generality of this quantity. In order to apply this idea we focused our study to the case of critical quenches and we studied two-time correlations and responses for several observables. These observables show different dynamical behavior, in terms of the time decay and of oscillatory factors. The effective temperatures which derive from their study rule out Gibbs thermalization in a strict sense in terms of a unique temperature. However it might be that some quantities that turn out to be particularly well-behaved still have a thermodynamic meaning. Depending on the observable the results are analytical or numerical, according to standard methods for spin chains. Part of these results are discussed in [P4] while some recent developments will be presented in [P7].

I.5   List of publications

Published and submitted works

[P1] L. Foini, G. Semerjian, F. Zamponi
    A solvable model of quantum random optimization problems
    Phys. Rev. Lett. 105, 167204 (2010). `http://arxiv.org/abs/1006.1736`

[P2] L. Foini, G. Semerjian, F. Zamponi
    The quantum Biroli-Mézard model: glass transition and superfluidity in a quantum lattice glass model
    Phys. Rev. B 83, 094513 (2011). `http://arxiv.org/abs/1011.6320`

[P3] G. Biroli, B. Clark, L. Foini, F. Zamponi
    Leggett's bound for amorphous solids
    Phys. Rev. B 83, 094530 (2011). `http://arxiv.org/abs/1011.2863`

[P4] L. Foini, L. F. Cugliandolo, A. Gambassi
    Fluctuation-dissipation relations and critical quenches in the transverse field Ising chain
    Submitted. `http://arxiv.org/abs/1107.5956`

[P5] M. Bailly-Bechet, S. Bradde, A. Braunstein, A. Flaxman, L. Foini, R. Zecchina
    Clustering with shallow trees
    J. Stat. Mech. (2009) P12010. `http://arxiv.org/abs/0910.0767`

Works in preparation

[P6] V. Bapst, L. Foini, F. Krzakala, G. Semerjian, F. Zamponi, in preparation.

[P7] L. F. Cugliandolo, L. Foini, A. Gambassi, in preparation.

The results of the works [P1, P2, P3, P4] are discussed in Chapters 3, 6, 7 and 9 respectively. The work [P5] concerns my MSc thesis and it is not discussed in this manuscript. The works [P6, P7] are in preparation and some of their results are presented in Chapter 4 and 9 respectively.

Part A

Quantum optimization problems

1

Quantum annealing and optimization problems

The aim of this Chapter is to fix the general framework for the discussion of quantum optimization problems and to introduce the original motivation which led to such study, i.e. the possibility to solve the problems by the quantum adiabatic algorithm. We conclude detailing some works present in the literature that are particularly relevant for the quantum annealing and that will be recalled in the next Chapters. In Section 1.1 we recall properties and definitions of classical optimization problems. We distinguish between the focus of computational complexity theory, where they have been first introduced, from a physical point of view. In Section 1.2 we rapidly introduce quantum computation and we focus in more detail on the quantum annealing as a general quantum algorithm to obtain the solution of classical optimization problem. With the quantum annealing algorithm we provide our definition of quantum optimization problems. In Section 1.3 and 1.4 we discuss some aspects, related to the thermodynamics or spectral properties of quantum optimization problems that could have a major effect on the performances of the quantum annealing. The works presented in Section 1.3 are inspired by the analogy between optimization problems and classical glassy systems. The work presented in Section 1.4 is based on a comparison of the spectral properties of quantum optimization problems with those of quantum systems in a disordered environment.

1.1 Classical optimization problems

1.1.1 Definition

A combinatorial optimization problem is usually defined by a set of N elementary degrees of freedom $\{\sigma_i\}_{i=1,\dots,N}$ which take values in a discrete alphabet χ and by a cost $E_J : \chi^N \to \mathbb{R}$ which associates to each configuration $\underline{\sigma} \in \chi^N$ a cost $E_J(\underline{\sigma})$. The subindex J indicates possible "quenched" randomness present in the sign of the interactions. Very often the cost function is the sum of local constraints that involve only a small set of variables, i.e. $E_J(\underline{\sigma}) = \sum_{a=1}^{M} e_a(\{\sigma_i\}_{i\in\partial a}, J)$, where ∂a indicates the "neighborhood" of the interaction a, and $e_a = 0$ if $\{\sigma_i\}_{i\in\partial a}$ satisfies a and $e_a > 0$ otherwise. Note that a strictly related statement of the problem can be given in terms of logical propositions. This leads to the identification of the constraints with logical (Boolean when $|\chi| = 2$) *clauses* and the set of all clauses (the problem) with a *formula*. Any optimization problem can be embedded in a statistical mechanics problem. The idea is to rename the cost function as the energy of the system of N variables

and to define the Boltzmann probability measure over the space of configurations:

$$p_\beta(\underline{\sigma}) = \frac{\exp[-\beta E_J(\underline{\sigma})]}{Z(\beta)} \qquad Z(\beta) = \sum_{\underline{\sigma}} \exp[-\beta E_J(\underline{\sigma})] \qquad (1.1)$$

where β is the inverse temperature and $Z(\beta)$ the partition function of the model. In the limit $\beta \to \infty$ the probability concentrates on the minima of $E_J(\underline{\sigma})$. Given a cost function, the tasks that one may want to solve are:

- *Deciding* if there is a configuration that satisfies all the constraints, i.e. $e_a = 0 \; \forall a = 1, \dots, M$. If it exists the system is said to be SAT, otherwise it is UNSAT. This is the case for example of *constraint satisfaction problems* (CSPs).

- *Counting* the number of configurations of minimal energy.

- *Finding* a configuration with minimal energy.

- *Sampling* configurations according to the probability $p_\beta(\underline{\sigma})$, or other probability measures.

Below we list notable examples of CSPs that will be encountered in the following. For all of them $\chi = \{-1, 1\}$.

- k-XORSAT: $E_J(\underline{\sigma}) = \sum_{a=1}^{M} (1 - J_a \sigma_{i_1^a} \dots \sigma_{i_k^a})$, and J_a are i.i.d. (quenched) random variables taking the values ± 1 with equal probability.

- k-SAT: $E_J(\underline{\sigma}) = \sum_{a=1}^{M} \prod_{i \in \partial a} \frac{1 - J_{a \to i} \sigma_i}{2}$ where $|\partial a| = k$ and the coupling $J_{a \to i}$ as before.

- 1-in-3 SAT (Exact Cover): $E(\underline{\sigma}) = \frac{1}{4} \sum_{a=1}^{M} (\sigma_{i_1^a} + \sigma_{i_2^a} + \sigma_{i_3^a} + 1)^2$.

Given the Hamiltonian, two different approaches consist in studying a single instance of the problem, i.e. a realization of the J's and of the underlying graph (the set of variables involved in each clause), or averaging over the randomness and study its ensemble properties.

1.1.2   Running time and computational complexity

The time needed to solve the problem is a fundamental property of a CSP and crucially characterizes its difficulty according to the computational complexity theory. Classical complexity theory was developed in order to classify how hard a problem it is in the worst possible case. We distinguish here between "easy" and "hard" problems, that are respectively in the P and in the NP class (see [37] for a rigorous treatment). The former are characterized by the existence of an algorithm that can solve them in at most polynomial time steps, i.e. $t \sim w N^k$, with N the size of the system and w and k independent on the specific instance. The latter are those that can be verified in polynomial time. It is widely believed that $P \neq NP$ which means that some problems are intrinsically difficult and they require exponential time to be solved. An important subset of NP is that of NP-complete problems. It is defined by the fact that all NP problems can be mapped in a NP-complete one in polynomial time. Thus, the solution of a single NP-complete problem (in polynomial time) would imply the solution of all problems in NP. According to this classification, in order to understand the efficiency of a classical or quantum algorithm we will be interested in discriminating a polynomial with respect to an exponential running time. k-SAT (for $k \geq 3$) and Exact Cover are NP-complete problems, while k-XORSAT is in P because it is solved in polynomial time by Gaussian elimination. However k-XORSAT remains intractable for most random search algorithms.

1.1.3 Optimization in the typical case

Differently from classical complexity theory, from the perspective of statistical mechanics of disordered systems it is natural to study the "average case", considering the properties of an ensemble of instances. Moreover, as always in physics one is interested in the thermodynamic limit of large instances where N and M (the number of constraints) both diverge with a fixed ratio $\alpha = M/N$. Natural ensembles for the underlying graph characterizing *random CSPs* are:

- *Random regular graphs*: each constraint involves k distinct variables (as in k-SAT or k-XORSAT), and each variable appears in exactly c different clauses. It holds the relation $c = kM/N = \alpha$ and the graphs have the same uniform probability.

- *Erdös-Rényi random graphs*: for each of the M constraints a k-uplet of distinct variable indices $(i_a^1, i_a^2, \ldots, i_a^k)$ is chosen uniformly at random among the $\binom{N}{k}$ possible ones. To compare with regular graphs one considers the average connectivity $c = k\alpha$.

In this thesis the definition of Bethe lattice will be equivalent to that of random regular graph. This convention is not universally established and in the literature the Bethe lattice may refer to different mathematical objects. In the limit of zero temperature the statistical analysis is restricted to the "ground states" of the energy and the density of constraints α works as a control parameter over the probability of finding zero energy configurations. It is believed in fact that, in the thermodynamical limit, random CSPs display a sharp threshold value α_s (SAT/UNSAT transition) above which the probability of finding a satisfying assignment goes from one to zero abruptly. This sharp phenomenon is reminiscent of a phase transition to the eye of a physicist. Thoughtful studies of the properties of the solutions of random CSPs close to the satisfiability threshold revealed in fact complex phase diagrams in the space of configurations as a function of α which resemble that of mean field glassy system [4, 5, 6, 38, 39]. In Chapter 2 we will explain in more detail the phase diagram, also at finite temperature. For the moment let us argue that, in the limit of large system size, in the SAT phase for increasing α, the structure of the set of solutions of the problem gets fragmented in a large number $\mathcal{N}$ of "disconnected" components (pure states or clusters) that corresponds to the minima of the energy landscape over the space of configurations. In addition to the lowest global minima there exist also other local minima, with positive energy, that are as well separated from the rest of the configurational space. At $\beta \to \infty$, we say that two clusters (two minima) are separated if their ground states are at extensive (in N) Hamming distance. In turn, this is associated to extensive energy barriers among the pure states. Clearly, the understanding of this complex phenomenon strongly relies on the investigation of the *configurational entropy* $\Sigma = \log \mathcal{N}/N$ which represents the fundamental object of study for random CSPs and in general for mean-field glassy systems.

Let us conclude with some remarks about random CSPs [40]. We hope that this may give an intuition about different perspectives under which CSPs have been addressed.

- *Rigorous results.* Despite the intense research, the existence of a *satisfiability threshold* for the random k-SAT problem remains a widely accepted conjecture. The major achievement in this direction was brought by the work of Friedgut [41] that rigorously proves the existence of a non-uniform sharp threshold. In the limit $k \to \infty$ it was shown [42] that the upper and lower bound for α_s (that always exist) become tight. The *clustering phenomenon* is as well a crucial property that lacks of a general rigorous understanding. However in the case of random XORSAT instances [43, 44, 45, 46], as well as for k-SAT, for k sufficiently large [39, 47], its existence has been demonstrated rigorously.
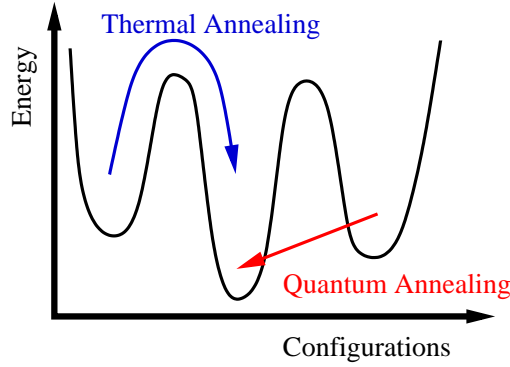
Figure 1.1: Schematic picture of the thermal and quantum annealing processes.

- *"Physics-based" algorithms.* Since in the next Section we will explain the algorithm based on thermal annealing (because of its relevance for quantum annealing) here we aim to mention other algorithms that are used for solving SAT formulas. The *walk-SAT algorithm* [48] is a stochastic process in the space of configurations characterized by small steps moving when one or a few variables are modied. Contrarily to simulated annealing it does not respect the detailed balance condition, namely it does not fulfill an "equilibration" protocol with respect to the assigned Gibbs distribution. Another class is that of *decimation based algorithms*, as the one proposed by Davis, Putnam, Loveland and Logemann (DPLL) [49, 50]. Given an initial formula, whose satisability has to be decided, DPLL proceeds by assigning sequentially the value of some of the variables. The formula can be then simplied under such a partial assignment. In this way, within an "optimized" exponential time, the algorithm responds to the question. The last class is that of *message passing algorithms.* The basic objects are messages on the directed edges of the graph representation of the problem. These messages are iteratively updated and they finally provide the marginal probabilities of the variables in the uniform measure over optimal congurations (or in the Gibbs distribution over all the configurations). These marginals can be finally used to efficiently construct a tentative solution. Belief Propagation (BP) is one of the simplest and paradigmatic algorithm of this category. The key to the success of the physics approach in this direction is in the development of smart algorithms for finding solutions in the "hard" clustered region and it relies in the understanding of the rugged energy landscapes. This intuition in fact brought, most notably, to Survey Propagation (SP) [51, 4] which is an extension of BP able to tackle the clustering phenomenon (BP and SP will be recalled in Chapter 2, see [52] for a detailed presentation).

- *Practical importance.* The study of the typical case is also interesting for practical purposes, as for instance in error correcting codes. Low Density Parity Check codes (LDPCs) represent the best error correcting codes and they are produced applying message-passing algorithms over random generated formulas [53].

1.1.4 Thermal annealing

It turns out that close to the satisfiability threshold finding the solutions to the problem becomes particularly hard and the algorithms suffer of a dramatical slowing down. Quite generally this phenomenon is attributed to the presence of many minima in the energy landscape and to the organization of the solutions in phase space. Simulated (thermal) annealing [3] is one of most famous algorithms

designed to tackle complex energy landscapes. Despite the fact that it only partially accomplished this task as it actually fails when too many clusters dominate the partition function (see Chapter 2 for a more rigorous statement), it represented a true breakthrough in the domain and it is still exploited in many applications. The prescription of simulated annealing is that of initialize the algorithm with a random, high temperature, configuration. Then, lower the temperature, eventually down to zero, in discrete steps according to an assigned protocol, and at each step, perform a given number of local movements in phase space - Monte Carlo steps - in order to equilibrate at that temperature and use the last generated configuration to initialize the search at the new temperature. Technically this is the implementation of a *time dependent Markov chain*. The idea behind this algorithm is that thermally activated processes allow to overcome the energy barriers and at the latest stages the zero temperature limit converges towards the solution. However this is a simplified picture and the algorithm often fails to find a solution. This happens when the dynamics falls out-of-equilibrium. This is because the probability to overcome the barriers is exponentially small in the size of the system and the pure states of the Gibbs measure trap the dynamics infinitely long. Clearly, in an arbitrarily large time a well defined Markov chain is assured to converge to the equilibrium configuration. However we implicitly assumed that the number of Monte Carlo steps can not grow indefinitely with the size of the system, as an efficient algorithm should perform in a polynomial running time and this is not enough to overcome extensively large barriers.

1.2 Quantum adiabatic computing

1.2.1 Quantum computation

As for classical computation, the aim of quantum computation is that of designing efficient methods to solve problems. The problem may be the same, so that the input and the output could be expressed in terms of classical degrees of freedom, i.e. $\{\sigma_i\}_{i=1,...,N}$. However the algorithm used to solve the problem is very different and exploits quantum mechanics. For this reason the basic degrees of freedom lie in a Hilbert space $\mathcal{H}$, which is generally spanned by the vector basis $\{|\underline{\sigma}\rangle : \underline{\sigma} \in \chi^N\}$. It is natural to believe that the possibility to act simultaneously on the "entire" Hilbert space $\mathcal{H}$, namely on linear superposition of the vector basis, rather than on the discrete bit-strings could lead to much more powerful algorithms. Indeed this was emphasized most notably by the factoring algorithm designed by Peter Shor [54] and by the Grover's algorithm [55] for searching an unsorted database. Since much before[1] in fact, the captivating idea to exploit quantum mechanics to overtake classical computations has encouraged several theoretical and experimental groups in the search for quantum computers and efficient quantum algorithms.

The suggestion of the *Quantum Adiabatic Algorithm* (QAA) [8, 7] represented a promising idea to implement quantum computation and solve hard optimization problems, alternative to the standard circuit based model of quantum computation. The essence of the adiabatic quantum computation relies in the encoding of the problem in a suitable physical system. In this way, at the end of a well-defined procedure, the ground state of the system is supposed to provide the desired solution with arbitrarily high probability.

---

[1]The idea of a *universal quantum simulator* was already proposed by R. Feynmann in 1982. See [56] for more details.

1.2.2   Quantum optimization problems

Let us introduce the quantum counterpart of optimization problems that will be necessary for discussing QAA. The quantum version can be easily defined as follow. Consider the Hilbert space spanned by vectors $\{|\underline{\sigma}\rangle : \underline{\sigma} \in \chi^N\}$ and the operator $\hat{H}_P$ that is diagonal on this basis such that $\hat{H}_P = \sum_{\underline{\sigma}} E(\underline{\sigma})|\underline{\sigma}\rangle\langle\underline{\sigma}|$. Occasionally we will refer to $E(\underline{\sigma})$ as the "classical energy". The ground states of $\hat{H}_P$ then encodes the "satisfying assignments", i.e. the solutions of the problem. In order to exploit quantum fluctuations one has to introduce a second operator $\hat{H}_Q$ acting on the same Hilbert space and non-commuting with $\hat{H}_P$. For the purposes of quantum adiabatic computing $\hat{H}_Q$ has to be simple enough that its ground state is easy to find. Usually $\hat{H}_Q$ is taken to be the sum of operators acting on the i-th variable only.

We will consider $\{\sigma_i\}$ to be Ising spins, i.e. $\chi = \{-1, 1\}$, and their quantum counterpart, often called qubits, are the eigenstates $|\sigma_i\rangle$ of the z-component of Pauli matrices $\hat{\sigma}_i^z$. For concreteness and unless otherwise specified we will take $\hat{H}_Q = \sum_i \hat{\sigma}_i^x$, even if different possibilities can be studied. Then the total Hamiltonian is given by

$$\hat{H}(\Gamma) = \hat{H}_P + \Gamma \hat{H}_Q \ , \tag{1.2}$$

where Γ is a parameter which tunes the strength of quantum fluctuations. We note that the Hamiltonian $\hat{H}(s) = s\hat{H}_P + (1-s)\hat{H}_Q$ is just a rescaling of (1.2) with $\Gamma = (1-s)/s$. This is the convention used more often in the literature of QAA and we will also use it contextually.

1.2.3   Quantum adiabatic algorithm

The quantum adiabatic algorithm is specified by the state of the system which is prepared in the ground state of $\hat{H}_Q$ and it is then let evolve through the Shrödinger equation according to a time dependent Hamiltonian of the form of (1.2):

$$\hat{H}(t) = s(t)\hat{H}_P + (1 - s(t))\hat{H}_Q \ . \tag{1.3}$$

In (1.3) $s(t)$ is an interpolating function such that $s(0) = 0$ and $s(T) = 1$, T being the total time of the annealing, and it is usually taken linear i.e. $s(t) = t/T$. We will denote $|\psi(t)\rangle$ the state of the system at time t and $|GS(t)\rangle$ the ground state of the Hamiltonian at time t.

The algorithm relies on the adiabatic theorem [57] which ensures that for a sufficiently slow annealing, i.e. when $T \to \infty$, the system remains in the instantaneous ground state of $\hat{H}(t)$, i.e. $|\psi(t)\rangle = |GS(t)\rangle \, \forall t$. At the end of the annealing then, the state of the system will encode the solution of the problem $|GS(T)\rangle$. Of course one is not interested in an infinitely slow algorithm and instead aims to control how the total time of the annealing T has to scale with the size of the system in order to have a reliable outcome. A criterium for this requirement can be found by a closer look at the adiabatic theorem. Let us define $\Delta_{min} = \min_{s=t/T \in [0,1]}(E_1(s) - E_0(s))$ the minimum gap of the interpolating Hamiltonian that governs the annealing. Then the condition

$$T \gg \mathcal{O}(\Delta_{min}^{-2}) \ , \tag{1.4}$$

ensures that the probability of finding the system in the ground state of $\hat{H}(T) = \hat{H}_P$, i.e. $|\langle GS(T) | \psi(T) \rangle|^2$, can be made arbitrarily close to 1. Thus, the time of the protocol is governed by the minimum gap and by its scaling with N.

A useful simplification is that of considering a two level system, made by the ground state and the first excited state in correspondence of an *avoided level crossing*. In absence of special symmetries in $\hat{H}(t)$ and when the size of the system is finite (even if very large), true level crossings are not expected since
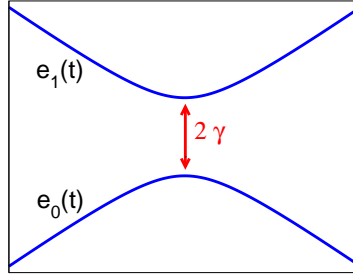
Figure 1.2: Schematic representation of the eigenvalues of (1.5) as a function of time t. Note the avoided level crossing in correspondence of the minimum spectral gap.

even tiny off-diagonal elements prevent them from intersecting. The following "reduced" Hamiltonian describes two levels that at a certain moment t^* during the evolution get extremely close:

$$\hat{H}_{\text{red}}(t) = \begin{pmatrix} \epsilon(t - t^*) & \gamma \\ \gamma & -\epsilon(t - t^*) \end{pmatrix} . \tag{1.5}$$

Then the instantaneous gap is $\Delta(t) = 2\sqrt{\gamma^2 + \epsilon^2(t - t^*)^2}$, and also when the two diagonal ("unperturbed") elements are equal, in $t = t^*$, no matter how small γ the states will never cross and $\Delta_{min} = 2\gamma$. From this simple problem one can also heuristically understand (1.4). In fact from the Landau-Zener formula [58] one can exactly compute the probability of a *diabatic* transition to an excited state in a two-level system described by a Hamiltonian of the form (1.5). This is $P = e^{-2\pi\gamma^2/(\hbar\epsilon)}$, and since $\epsilon \propto \frac{1}{T}$ is the rate with which the two levels approach, it means that for an adiabatic process $T \gg \gamma^{-2} \simeq \Delta_{min}^{-2}$.

It is clear then that the bottleneck of QAA will be represented by phase transitions or avoided level crossings, where the gap is expected to close approaching the thermodynamical limit. On the basis of complexity theory we are then particularly interested in discriminating between Hamiltonians whose minimum gap vanishes polynomially and those for which Δ_{min} is expected to be exponentially small in N.

Initially the proposal of QAA appeared quite promising since the analytical study of simple Hamiltonians [8] and numerical results for more difficult Hamiltonians for small system sizes suggested a minimum gap that closes polynomially in N. However later works revealed that exponentially small gaps are expected in the annealing of quantum optimization problems, either due to first order phase transitions [59, 35, 60, 61] or to avoided level crossing in the "glassy phase" [62, 63]. Interestingly enough this was associated to a kind of Anderson localization phenomenon in phase space [62]. All these studies raised severe questions about the performances of the QAA and in the rest of the Chapter we will review some of these results. In response to these criticisms some works [64, 65, 66] focused on the possibility of finding safe paths in the adiabatic annealing, that avoid the intersection with exponentially small gaps. However it might be quite difficult to sample efficiently those paths. It is in fact very likely that such paths that are constructed randomly, will correspond to rare large deviations from the average behavior.

An important observation is that most of the works up to now focused on the efficiency of the algorithm in *solving* the problems. The performances of QAA in finding approximated solutions remain instead widely unexplored [67, 68]. Already in [69], it was shown some evidence that QAA could outperform classical simulated annealing within the same exponential scaling of the running time. Moreover its inherent robustness against external noise makes it very interesting from the point of view of the

experimental realizations of quantum computation.

Before entering in the discussion of the problematics related to the efficiency of QAA let us note that we assumed that $\hat{H}$ interpolates linearly in time between $\hat{H}_Q$ and $\hat{H}_P$. One can instead consider smarter algorithms that interpolate at variable rate, going slower in proximity of an avoided level crossing and speeding up away from that [70, 71]. It was shown that this can improve the efficiency of the algorithm but it can not change an exponential scaling into a polynomial one.

1.3   First-order phase transitions

From the discussion of the previous Section it is clear that quantum phase transitions represent a serious obstacle for the efficiency of QAA. In this respect second-order phase transitions seem less dangerous since they are often accompanied with a gap that closes polynomially with N [72]. However this is not a general rule and most notably the presence of disorder can modify this scaling [73]. Instead, in the case of first-order phase transitions several analytical and numerical results support the evidence of exponentially small gaps at the critical point [11, 59, 35, 60, 61]. We note that the presence of first-order phase transitions was found also in fully connected quantum glassy systems through techniques that combine replica and Suzuki-Trotter methods [12, 13, 74]. The classical thermodynamics of fully connected glassy systems, as well as of diluted optimization problems, is well described by the so-called "Random First Order Transition" (RFOT) theory (see Chapter 2 for a discussion on diluted optimization models and Chapter 5 for more details on RFOT in the context of glassy systems). Then, one can expect that first-order phase transitions are quite universal phenomena for systems belonging to this classical universality class, when transverse field-like terms are added to the quantum Hamiltonian.

Contrarily to simulated annealing where the search is more influenced by the height of the energy barriers, heuristically one expects QAA to perform the best in presence of barriers that regardless of their height are not too wide (see Fig. 1.1). However this is not the case of discontinuous transitions, where the two competing low energy states are far away in phase space.

The authors of [11, 59] considered the quantum version of the Random Energy Model (REM), described by the Hamiltonian

$$\hat{H}(\Gamma) = \sum_{\underline{\sigma}} E(\{\underline{\sigma}\})|\underline{\sigma}\rangle\langle\underline{\sigma}| - \Gamma \sum_i \hat{\sigma}_i^x \tag{1.6}$$

where $E(\{\underline{\sigma}\})$ are independent random variables extracted from a Gaussian probability density with zero average and variance $N/2$. Despite its simplicity the REM is known to capture several aspects of the physics of mean-field glassy systems [75]. In fact it is the limit of a class of fully-connected systems with quenched disorder and p-spin interactions, $\hat{H}_P = \sum_{i_1 < \cdots < i_p} J_{i_1 \ldots i_p} \hat{\sigma}_{i_1} \ldots \hat{\sigma}_{i_p}$, when p goes to infinity, representing the paradigm of the glass transition in RFOT. We summarize here some of the results on this model [59] that will be useful to understand more complicated situations and will be recalled in Chapter 3.

- *Extreme cases*

    Let us first discuss the two limiting cases of the annealing, (i) $\Gamma = 0$ and (ii) $\Gamma = \infty$. (i) When $\Gamma = 0$ the model has a phase transition as a function of the temperature [75]. Call $\mathcal{N}(E)$ the average number of energy levels in the interval $[E, E + dE]$. Then $\mathcal{N}(E) = 2^N P(E) = 2^N e^{-E^2/N} = e^{N(\log 2 - (E/N)^2)} = e^{N s_a(E/N)}$ with $s_a(e) = \log 2 - e^2$ the "annealed" entropy density. Therefore there is a critical value $e^* = \pm\sqrt{\log 2}$ such that for $|e| < |e^*|$ the density of levels

is exponentially large and its fluctuations are very small, so the "quenched" entropy coincides with the annealed value $s(e) = s_a(e)$. Instead if $|e| > |e^*|$, $s_a(e) < 0$ and the typical density of states is exponentially small. There are no configurations at energy Ne and the quenched entropy is $s(e) = 0$. The thermodynamic transition between the two regimes happens at the critical temperature $T_c^{-1} = \frac{ds(e)}{de}|_{e=e^*} = 2\log 2$ and it is interpreted as a *glass transition*. In the high temperature phase $T > T_c$ the free energy density is $f(T) = -\frac{1}{4T} - T\log 2$ and an exponential number of states contribute to the partition function. For $T < T_c$ the thermodynamical potentials are constant $f(T) = -\sqrt{\log 2}$ and $e(T) = -e^*$, and only a finite (not exponential) number of states dominate the partition function, $s(T) = 0$. This phenomenon is often referred as the *condensation* of the Gibbs measure on rare configurations.

(ii) When $\Gamma = \infty$ the system is made of N independent spins in a transverse field. So the free energy is $f(T) = -T\log 2 - T\log(\cosh(\Gamma/T))$ and the entropy density $s(e)$ is the log of a binomial distribution in $[-\Gamma, \Gamma]$.

- *Perturbation theory*

  In order to connect the two extreme cases one can apply perturbation theory. Starting from $\hat{H}_P$ and considering perturbation in Γ through $\hat{H}_Q$ on *extensive* low-energy states, one finds for the energy density $e_i^P(\Gamma)$ of the i-th level:

$$e_i^P(\Gamma) = e_i^P + \frac{\Gamma^2}{Ne_i^P} + O\left(\frac{1}{N^2}\right) , \tag{1.7}$$

  where e_i^P is the intensive energy of the unperturbed REM. In the opposite limit, calling e_i^Q the unperturbed (intensive) energy of the i-th low-energy state of $\hat{H}_Q$, the perturbative expansion which starts from large values of Γ reads:

$$e_i^Q(\Gamma) = e_i^Q - \frac{1}{2N\Gamma} + O\left(\frac{1}{N^2}\right). \tag{1.8}$$

  The result is that nothing happens at the leading order in N to the spectrum of the two phases, and energy, entropy and free energy density are not modified. The partition function then can be written $Z(\Gamma, \beta) = \min[\text{Tr}e^{-\beta\hat{H}_P}, \text{Tr}e^{-\beta\hat{H}_Q}]$. This leads to a first-order phase transition separating the regimes where $f_P(T, \Gamma) \lessgtr f_Q(T, \Gamma)$. The derivation of this transition can be also obtained using the replica method [11]. The spectrum and the phase diagram of the model in the plane (Γ, T) are shown in Fig. 1.3.

- *Gap*

  A good approximation of the minimum gap is given considering a two level problem similarly to (1.5) where the space is that spanned by the ground states of $\hat{H}_P$ and $\hat{H}_Q$, respectively $\left|E_0^P\right\rangle$ and $\left|E_0^Q\right\rangle$. The diagonal matrix elements are the (un)-perturbed energies (1.7-1.8). The off-diagonal elements are proportional to the overlap $\Gamma\langle E_0^P|E_0^Q\rangle = \Gamma 2^{-N/2}$. This implies that $\Delta_{min} \propto 2^{-N/2}$ and the accuracy of this scaling is shown in the inset of Fig. 1.3. In [59] they also presented a more sophisticated "instantonic" calculation [9], applicable to fully-connected models, that allows to get accurate predictions for Δ_{min}.

The phase diagram of the quantum REM shares strong analogies with the results obtained in other quantum glassy models [12, 13, 74, 35], consistently with the fact that the REM is a good approximation for more complex systems. In all these problems the classical glass transition occurs as a
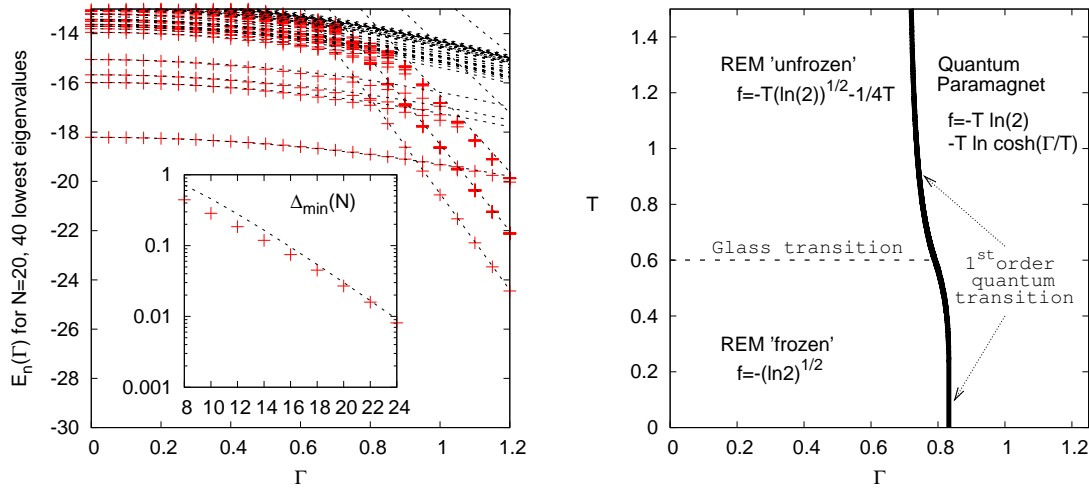
Figure 1.3: *Left panel*: Spectrum of the REM in a transverse field Γ as a function of Γ. Red dots represent the results from exact diagonalization of a system with $N = 20$, dotted lines are the analytical values. The inset shows the scaling of the minimal gap as a function of the size N. *Right panel*: Phase diagram as a function of temperature and transverse field. Figures taken from [59].

function of the temperature. At $T = 0$ the system is in the glass phase and the classical ground state is not (extensively) degenerate. Whereas in many other optimization problems, like k-SAT, the glass transition arises at $T = 0$ as a function of another parameter that generally controls the density of constraints. In these cases there is a zero temperature non-vanishing entropy and the transition is an entropic phenomenon. In Chapter 3 we will generalize the results obtained for the REM in order to take into account entropic contributions and in Chapter 4 we will compare the result of REM with that of k-XORSAT on a random regular graph, i.e. a "realistic" optimization problem.

Finally we mention that a related phenomenology has been found in the study of Exact Cover with a transverse field. The problem has been addressed by different groups [8, 61, 62] already from the earliest works. Initially, in the original work by Farhi et al. [8], based on numerical studies of small system sizes, it was suggested that QAA could find satisfying assignments with finite probability in polynomial time. However later, it was shown by Young et al. [61], performing Quantum Monte Carlo in the case where $\hat{H}_P$ has unique satisfying assignment (USA), that an increasing (with N) number of instances of $\hat{H}_P$ displays discontinuous transitions and an exponentially small gap.

1.4   Small gaps and Anderson localization

In their work, Altshuler et al. [62] raised other objections to the efficiency of QAA, pointing out that the breakdown of the algorithm may be induced by the appearance of avoided level crossings in the spectrum during the adiabatic evolution. The statement was strongly appealing for the physicists community since they claimed that the phenomenon is related to a manifestation of Anderson localization on the N-dimensional "hypercube". We note that the avoided level crossings that are discussed here do not necessarily induce singularities in the thermodynamical quantities, especially at finite temperature, such as first order phase transitions. In the literature they have been also referred to as "perturbative crossings" [66, 76].

In [62] the Exact Cover problem in a transverse field was considered. Their analysis started by taking

two configurations $\underline{\sigma}_1$ and $\underline{\sigma}_2$ that are solutions of $M-1$ clauses. These configurations represent degenerate eigenvectors for $\Gamma = 0$. However, as soon as $\Gamma > 0$ the two ground state energies must split. Let us call $|E_1(\Gamma)\rangle$ and $|E_2(\Gamma)\rangle$ the two eigenvectors and $E_1(\Gamma)$ and $E_2(\Gamma)$ the corresponding energies. Suppose that there exist a Γ^* such that $E_2(\Gamma^*) - E_1(\Gamma^*) > 4$. If one adds an M-th clause, it still holds that $E_2(\Gamma^*) > E_1(\Gamma^*)$, because a clause introduces at most a penalty $\Delta E_{max} = 4$. However there is a finite probability that the clause will be satisfied by $\underline{\sigma}_2$ but not by $\underline{\sigma}_1$, so that $E_1(0) > E_2(0)$. Since in the Hamiltonian there are no particular symmetries, $E_1(\Gamma)$ and $E_2(\Gamma)$ do not cross and the introduction of the additional clause induces an avoided level crossing. The absence of level crossings in presence of non-vanishing off-diagonal matrix elements descends from the Wigner-von Neumann non-crossing rule and in the literature of Anderson localization it is sometimes referred to as *level repulsion*. The non-crossing rule emerges also from the analysis of the eigenvalues of (1.5). The Hamiltonian (1.5) is the prototype of two levels that, as a function of t, come close at $t = t^*$ but that can never touch as soon as $\gamma \neq 0$. The analogy with Anderson localization is more transparent if one thinks to $\hat{H}_Q = \sum_i \hat{\sigma}_i^x$ as to the hopping of a particle on a N-dimensional hypercube so that the total Hamiltonian reads:

$$\hat{H} = \sum_{\underline{\sigma}} E(\underline{\sigma})|\underline{\sigma}\rangle\langle\underline{\sigma}| - \Gamma \sum_{\underline{\sigma},\underline{\sigma}':d(\underline{\sigma},\underline{\sigma}')=1} |\underline{\sigma}'\rangle\langle\underline{\sigma}| \ , \tag{1.9}$$

where $d(\underline{\sigma}, \underline{\sigma}')$ represents the Hamming distance of two classical configurations, so that $\underline{\sigma}$ and $\underline{\sigma}'$ differ for one spin only in $\hat{H}_Q$. Then $\hat{H}_P$ provides the disordered environment that induces localization on one of the vertices. In his seminal paper [30] Anderson considered a particle moving on a L^d lattice, where d is the space dimension and L the length of the lattice, subject to a random disordered potential. This is a good starting point for the comprehension of transport properties in metals and the metal-insulator transition. In this setting then, the Anderson model describes an electron hopping in a disordered environment and the Hamiltonian reads

$$\hat{H}_{AM} = -t \sum_{\langle i,j \rangle} \hat{c}_i^\dagger \hat{c}_j + \hat{c}_j^\dagger \hat{c}_i + \sum_{i=1}^{N} \epsilon_i \hat{c}_i^\dagger \hat{c}_i \ , \tag{1.10}$$

where the first sum runs over the edges of the lattice, the second sum runs over all N sites, $\hat{c}_i$ is the fermionic creation operator and ϵ_i are i.i.d. variables, taken from a given distribution. Neglecting the statistics of the particle, which is however not crucial for the discussion, and comparing the Hamiltonians (1.9) and (1.10) one can interpret (1.9) as an Anderson model for a particle that hops in a 2^N space, instead of the conventional L^d. Moreover since close to the satisfiability threshold, the diagonal energy is supposed to be very rugged on the hypercube this may induce localization-like phenomena. However, contrary to (1.10) where the onsite potential is the realization of i.i.d. random variables, in (1.9) it is generated by the interaction of the spins and thus it is correlated from site to site. The estimation of the gap follows from the computation of the effective off-diagonal element of (1.5). In [62] it was argued that since close to the satisfiability threshold classical solutions are separated by an extensive (in N) Hamming distance in phase space, a perturbative calculation via (1.9) will connect them just at order $\sim \Gamma^N$ in perturbation theory, creating an exponentially small gap. The perturbative calculation starts with the classical Hamiltonian $\hat{H}_P$, in which all the eigenstates are localized at the vertices of the hypercube and then with Γ creates exponentially small tunneling probability. This was put in relation with the exponential suppression in real space of the localized wave function of a particle hopping in disordered environment [30]. In [62] it was argued that the occurrence of the avoided level crossing Γ_c should tend to the end of the annealing as $\Gamma_c = \mathcal{O}(N^{-1/8})$. Such scaling was never found in the numerical experiments, but it was attributed to the small exponent, visible only for large N.

The work of Altshuler at el. [62] takes in consideration only two solutions of the problem, while even close to the satisfiability threshold the number of solutions is exponentially large, and so we expect that the detailed spectrum should be much more complex. However the phenomenon presented in [62] appears to us a very reasonable prediction of what could happen representing a serious bottleneck for QAA.

In Chapter 2 we will study the appearance of avoided level crossings due to entropic reasons through a simple model which takes into account the degeneracy of solutions.

2

Glassy systems and the cavity method

In this Chapter we present a detailed picture of the phase diagram of classical random CSPs in terms of the solutions of the cavity method equations. This discussion allows us to explain some concepts introduced in the previous Chapter that are fundamental for the understanding of the properties of random CSPs and more general mean-field glassy systems. Moreover at the same time we will introduce some relevant ideas behind the cavity method at the classical level, and then, we will extend them to the study of quantum models. This turns out to be important for the discussions in Chapter 4 and 6 that strongly rely on the results of the cavity method. Section 2.1 is devoted to the study of the self-consistent equations of the classical cavity method as well as to their numerical resolution. Section 2.2 presents the method for quantum Ising spins and outlines the strategy for the numerical solution.

2.1 Phase diagram of CSPs and the (classical) cavity method

In the following we review the main ideas of the cavity method in an informal way, giving reference to the original papers for a more comprehensive discussion. Our aim is to use the cavity method to describe the different phases that contradistinguish the phase diagram of glassy systems. The cavity method is a powerful technique to access properties of frustrated systems on tree-like graphs in the thermodynamic limit. It is very general since it applies to problems described by local Hamiltonians, whose Gibbs measure reads

$$p_\beta(\underline{\sigma}) = \frac{\exp[-\beta E_J(\underline{\sigma})]}{Z(\beta)} \qquad Z(\beta) = \sum_{\underline{\sigma}} \exp[-\beta E_J(\underline{\sigma})] = \sum_{\underline{\sigma}} \prod_{a=1}^{M} e^{-\beta e_a(\underline{\sigma}_{\partial a})} \prod_{i=1}^{N} e^{-\beta h_i \sigma_i} \ . \qquad (2.1)$$

It allows to compute marginal probabilities or the free energy density:

$$\eta_i(\sigma_i) = \sum_{\underline{\sigma} \backslash \sigma_i} p_\beta(\underline{\sigma}) \qquad f(\beta) = -\frac{1}{N\beta} \log Z(\beta), \qquad (2.2)$$

as well as other thermodynamic quantities, providing the exact solution when the underlying graph is tree-like and otherwise it corresponds to a sophisticated mean field approximation of the problem (2.1). In Eq. (2.1) we indicated with i the "spin variables" of the graph, the degrees of freedom
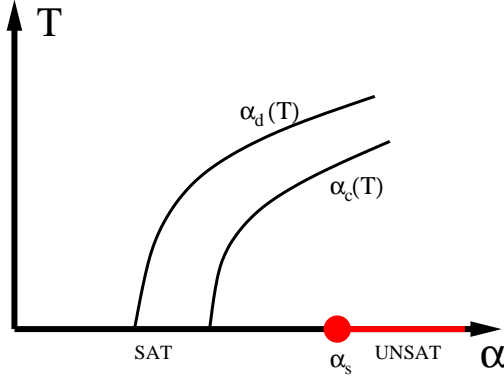
Figure 2.1: Schematic phase diagram for a generic CSP in the plane (α, T). $\alpha_d(T)$ and $\alpha_c(T)$ represent respectively the dynamical and the condensation transition. $\alpha_s(T = 0)$ corresponds to the SAT/UNSAT transition.

σ, and with a the "interactions variables" defined by the Hamiltonian (this notation is necessary in case of $(p > 2)$-body interactions). We also indicated with ∂a the "neighborhood" of a, i.e. the spin variables involved in the constraint a. In Eq. (2.2) and in the following we also use the symbol $\underline{\sigma}\backslash\sigma_i$ to consider the sum over all the variables in the l.h.s. of $\backslash$ but those in the r.h.s.. The method in its Replica Symmetric (RS) formulation is equivalent to the Bethe-Peierls approximation and this will be our starting point. The Replica Symmetry Breaking (RSB) approach is necessary to study the glass phase. Within this scheme one has access to the configurational entropy (or complexity) Σ, that, as argued in Section 1.1.3, is a fundamental quantity characterizing the structure of the phase space of the problem. The dynamical and the condensation transitions, as reported in Fig. 2.1 with α_d and α_c, are defined in terms of the complexity and they are universal features shared by most of random CSPs (those described by a 1-step RSB solution of the cavity equation). We will explain the nature of these transitions in terms of the properties of the solution of the RSB equations. For a thorough treatment of the properties of CSPs and of the cavity method we refer to [52].

2.1.1 Replica symmetric ansatz

Take for simplicity a model of Ising spins with pairwise interactions $E_J(\underline{\sigma}) = -\sum_{\langle ij \rangle} J_{ij}\sigma_i\sigma_j$ on a generic given graph. Imagine to remove from the graph the i-th spin and all the c links connected to it. This process will create c "cavity" variables $\{\sigma_j\}_{j \in \partial i}$ and let $\eta^{(i)}(\{\sigma_j\}_{j \in \partial i})$ denote their joint marginal probability when i is absent. The Bethe Peierls approximation consists in the factorization of this probability:

$$\eta^{(i)}(\{\sigma_j\}_{j\in\partial i}) = \prod_{j\in\partial i} \eta_{j\to i}(\sigma_j) \equiv \prod_{j\in\partial i} \frac{e^{\beta h_{j\to i}\sigma_j}}{2\cosh(\beta h_{j\to i})} \ . \tag{2.3}$$

In Eq. (2.3) we introduced $h_{j\to i}$ to parametrize the cavity probabilities (or *messages*) as Boltzmann weight of independent spins subject to a cavity field $h_{j\to i}$. Clearly within this approximation the marginal probability $\eta_i(\sigma_i)$ of the spin i-th in the whole graph is

$$\eta_i(\sigma_i) = \frac{1}{z_i} \sum_{\{\sigma_j\}_{j\in\partial i}} \prod_{j\in\partial i} e^{\beta[h_{j\to i}\sigma_j + J_{ij}\sigma_i\sigma_j]} \equiv \frac{e^{\beta h_{\text{eff}}^i\sigma_i}}{2\cosh(\beta h_{\text{eff}}^i)} \ , \tag{2.4}$$
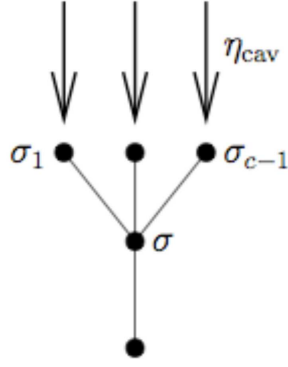
Figure 2.2: A schematic representation of a cavity iteration.

where z_i is a normalization constant and

$$h^i_{\text{eff}} = \sum_{j \in \partial i} \text{artanh}\Big[\tanh[\beta J_{ij}] \tanh[\beta h_{j \to i}] \Big] / \beta \; . \tag{2.5}$$

Then, while $\eta_i(\sigma_i)$, or h^i_{eff}, encode physical quantities the fundamental objects of to be computed are the cavity fields $\eta_{j \to i}(\sigma_j)$ or $h_{j \to i}$. Note that the validity of Eq. (2.3) takes to a great simplification because it allows to encode a probability over 2^c configurations in only c numbers. Most importantly it ensures a way to efficiently compute them by iteration. In fact the merging of $c - 1$ cavities with the addition of the missing links will create a new cavity variable σ_i whose cavity field satisfies:

$$\eta_{i \to k}(\sigma_i) = \frac{1}{z_{i \to k}} \sum_{\{\sigma_j\}_{j \in \partial i \setminus k}} \prod_{j \in \partial i \setminus k} e^{\beta[h_{j \to i}\sigma_j + J_{ij}\sigma_i\sigma_j]} \equiv \frac{e^{\beta h_{i \to k}\sigma_i}}{2\cosh(\beta h_{i \to k})} \equiv \bar{\eta}(\{\eta_{j \to i}\}_{j \in \partial i \setminus k}) \; , \tag{2.6}$$

where $\partial i \setminus k$ denotes the neighborhood of i but k and $\langle ik \rangle$ is the c-th missing edge. Introducing a set of messages $\{\eta_{j \to i}\}$ for each oriented edge $\{j \to i\}$ and the corresponding set of self-consistent equations like (2.6), the equations are iterated to converge (hopefully) to their fixed point. These are the basic ingredients of the Belief Propagation (BP) algorithm [77].

Knowing $\{\eta_{j \to i}\}$ one can recover the free-energy density of the problem $f(\beta)$ from the so-called *Bethe free energy*:

$$f(\beta) = f^{RS}(\{\eta_{j \to i}\}) \tag{2.7}$$

which is a well known function of the messages. Similarly one can also compute the free energy shift which is induced by the addition of a cavity site, i.e. using the notation of Eq. (2.6) $f_{i \to k} = -\log[z_{i \to k}]/\beta = \bar{f}(\{\eta_{j \to i}\}_{j \in \partial i \setminus k})$.

However for arbitrary graphs a fixed point of Eq. (2.6) not necessarily exists or correctly represents the true marginals and this is related to the validity of the Bethe Peierls approximation, Eq. (2.3). On tree graphs Eq. (2.3) is clearly satisfied because removing an edge breaks the system into two disconnected components. Random regular graphs are also tree-like objects because they have long loops of typical length $\mathcal{O}(\log N)$ which ensures that if correlations decay fast enough locally one is not able to distinguish the graph from a tree and Eq. (2.3) is correct. Moreover on the one hand random graphs circumvent the problematic treatment of the boundary in trees which is extensive in the number of variables. On the other hand their loops frustrate the system and forbid the formation of periodic patterns (think to antiferromagnetic solutions).

The cavity method [78] in its Replica Symmetric (RS) formulation consists in focusing on the fixed point of Eq. (2.6) in the thermodynamic limit of a random tree-like graph (actually over an ensemble of graphs). The thermodynamic limit allows to loose the precise reference to an edge and if the local environment of each spin is the same (same connectivity and same couplings $J = J_{ij}$) one gets a unique self-consistent equation with the substitution in the l.h.s. and r.h.s of Eq. (2.6) of all the messages with the same $\eta = \eta^{RS}$ which is equivalent to:

$$h = \frac{c-1}{\beta} \operatorname{artanh}\Big[\tanh[\beta J] \tanh[\beta h] \Big] \, . \tag{2.8}$$

Once that h has been determined h_{eff} can be computed from Eq. (2.5) with the same simplification. From the linearization of Eq. (2.8) it follows that the critical temperature for the ferromagnetic transition is determined by $(c - 1)\tanh(\beta_c J) = 1$. Note that for $c = 2$ (Ising chain) it correctly predicts $\beta_c = \infty$. This should convince that despite that Eq. (2.3) is a mean-field assumption, already at the RS level the method is more refined than a naive mean-field approach that assumes the variables around σ_i uncorrelated also in presence of σ_i.

There are cases however in which one has to allow η to fluctuate from site to site and wants to compute its probability distribution. In this case one has to distinguish between two kinds of fluctuations. On the one hand fluctuations may be induced by an external disordered environment that do not create competition among the variables, as the fluctuating connectivity of an Erdös-Rényi graph or an on-site random potential as h_i in Eq. (2.1). On the other hand the presence of competing interactions (which may also be attributed to quenched disorder in the Hamiltonian) may lead to the growth of a local amorphous order induced by frustration. While in the former case Eq. (2.3) holds and one can resort to a more complicated formulation of the RS equation (2.8), the latter needs a new "paradigm". This is indeed the object of the 1-RSB cavity method.

2.1.2 Replica symmetry breaking

As we mentioned loops can frustrate the system and it may be that the Bethe Peierls approximation does not hold also on tree-like graphs. One can recognize the breakdown of the assumption in Eq. (2.3) by finding unphysical RS solutions (for instance leading to negative entropies) or by inspecting their stability. This is caused by long-range correlations that signal a transition to a highly correlated (glassy) region. It is indeed what happens in CSPs with many constraints. The glass phase is signaled by the appearance of multiple solutions of the Belief Propagation equations, Eq. (2.6), and for large systems size they are interpreted as pure states of the Gibbs measure. Inside the pure states correlations decay and thus their probability measure satisfies Eq. (2.3). This means that each pure state α is associated to a (non-homogeneous) solution $\{\eta^\alpha_{j \to i}\}$ of the RS equations (2.6) and that its free-energy is given by the Bethe free energy (2.7) $f_\alpha = f^{RS}(\{\eta^\alpha_{j \to i}\})$. The cavity method at the one-step Replica Symmetry Breaking (1RSB) level corresponds then, to a statistical treatment of these pure states.

The 1RSB approach assumes that the number of these states with free energy density f is exponential in N, $\mathcal{N}(f) \sim e^{N\Sigma(f)}$, where $\Sigma(f)$ is the complexity (see discussion in Section 1.1.3). On the tree a pure state can be identified by a particular choice of the boundary conditions, exactly as in the standard (ferromagnetic) phase transitions determined by a spontaneous symmetry-breaking. If we associate to each pure state α a probability measure $p^\alpha_\beta(\underline{\sigma})$, this implies the decomposition of the Gibbs measure:

$$p_\beta(\underline{\sigma}) = \frac{1}{Z(\beta)} \sum_\alpha e^{-\beta N f_\alpha} \, p^\alpha_\beta(\underline{\sigma}) \, , \tag{2.9}$$

which can be interpreted as a Gibbs distribution over the states. Under these assumptions we consider the partition function of the form:

$$Z(m;\beta) = \sum_\alpha e^{-\beta N m f_\alpha} \simeq \int_{f_{\min}}^{f_{\max}} df e^{N(\Sigma(f)-\beta m f)} \simeq e^{-N\beta \min_{f\in[f_{\min},f_{\max}]}(mf-\frac{1}{\beta}\Sigma(f))} = e^{-N\beta m \phi(m;\beta)} ,$$
(2.10)

where the sum is over all the pure states, and the interval $[f_{\min}, f_{\max}]$ corresponds to the domain where $\Sigma(f) \geq 0$. We call f^* the value where the saddle point is taken. In Eq. (2.10) we introduced the parameter m, which is known in the literature as the Parisi parameter and plays the role of a Lagrange parameter conjugated to f (as an effective temperature). The "replicated free energy" $\phi(m)$ and Σ are Legendre transforms one of the other [79],

$$m\,\phi(m) = \min_{f\in[f_{\min},f_{\max}]}\{mf - T\Sigma(f)\} ,$$
(2.11)

and from the properties of the Legendre transform one has

$$\partial_f\Sigma(f) = m\beta , \qquad \Sigma = \beta\,m^2\partial_m\phi(m) , \qquad f = \partial_m[m\,\phi(m)] .$$
(2.12)

The usual partition function, which appears in Eq. (2.9), is recovered from Eq. (2.10) by setting $m = 1$. However it can happen that for $m = 1$, $\Sigma(f^*) < 0$, which makes no sense. Then, one has to look at $\Sigma(m)$, as a function of m, and find the value m^* such that $\Sigma(m^*) = 0$. In these cases the dominant contribution to the partition function corresponds to the pure states with free-energy $f = f_{\min}$. The study in terms of m, then, amounts to put a physical bound to the possible values of f^* in the saddle point in order to ensure $\Sigma(f^*) \geq 0$. Negative values of Σ are interpreted as the occurrence of exponentially rare states (a mechanism similar to the REM in Section 1.3), and the parameter m allows a correct sampling.

The computation of $\phi(m)$ is performed through a statistical study of the solutions of (2.6) among the various pure states. The scope is to determine the probability distribution $\mathcal{P}_{j\to i}(\eta_{j\to i})$ of the local cavity marginals $\eta_{j\to i}$ given the probability of the states (2.9). This is done in the 1-RSB approach by writing self-consistent equations for $\mathcal{P}_{j\to i}$ similarly to what has done before for $\eta_{j\to i}$. The cavity fields $\{\eta_{j\to i}^\alpha\}$ take the place of the $c-1$ cavity variables and the states α correspond to the configurations. One can think to $\mathcal{P}_{j\to i}$ as probabilities (messages) that live on the oriented edges of a finite graph. These probabilities are the basic objects of the celebrated Survey Propagation (SP) [51, 4] which generalizes BP to tackle with the phenomenon of proliferation of clusters of solutions.

With the 1RSB cavity method one access the properties of an infinite tree-like graph. Thus the explicit spatial references are dropped and one gets a self-consistent equation for the probability distribution $\mathcal{P}(\eta)$ which describes the bulk of the "tree". Assuming that $\mathcal{P}$ does not fluctuate (this is the analogue of taking a single h in Eq. (2.8)) the equation takes the form

$$\mathcal{P}(\eta) = \frac{1}{\mathcal{Z}}\int\prod_{i=1}^{c-1}\mathrm{d}\eta_i\mathcal{P}(\eta_i)\,\delta\Big(\eta - \bar{\eta}(\{\eta_i\}_{i=1,\ldots,c-1})\Big)\,z_{\mathrm{iter}}^m(\{\eta_i\}_{i=1,\ldots,c-1}) ,$$
(2.13)

with $z_{\mathrm{iter}} = e^{-\beta\bar{f}(\eta_1,\ldots,\eta_{c-1})}$ and $\bar{f}(\eta_1,\ldots,\eta_{c-1})$ defined shortly after Eq. (2.7). In terms of the solution of this equation, the free energy $\phi(m)$ can be computed according to the formula:

$$\phi = \Delta\phi_{\mathrm{site}} - \frac{c}{2}\Delta\phi_{\mathrm{link}}$$
(2.14)

with

$$\Delta\phi_{\text{site}} = -\frac{1}{\beta m} \ln \int \prod_{i=1}^{c} d\eta_i \mathcal{P}(\eta_i) \, z_{\text{site}}^m(\eta_1, ..., \eta_c) \tag{2.15}$$

$$\Delta\phi_{\text{link}} = -\frac{1}{\beta m} \ln \int d\eta_1 d\eta_2 \, \mathcal{P}(\eta_1)\mathcal{P}(\eta_2) \, z_{\text{link}}^m(\eta_1, \eta_2) \,, \tag{2.16}$$

where z_{site} and z_{link} are well-defined function of the cavity fields.

Let us sketch the possible solutions of Eq. (2.13) defining the phase diagram in Fig. 2.1.

- The RS solution: $\mathcal{P}(\eta) = \delta(\eta - \eta^{RS})$. Plugging these quantities in Eq. (2.13) clearly returns the simpler RS equation for η^{RS}. This solution holds for $T(\alpha) > T_d(\alpha)$ and implies that in Eq. (2.9) the sum is made by a single pure state with free energy $f(\beta) = f^{RS}(\eta^{RS})$. All sites are statistically equivalent because the Gibbs distribution coincides with a unique measure defined over a homogeneous connected component in configuration space.

- The d-1RSB solution: $\mathcal{P}(\eta)$ is not trivial and $\Sigma(f^*) > 0$ with $m = 1$. Then, exponentially many states dominate the partition function. This corresponds to the intermediate phase, $T_d(\alpha) > T(\alpha) > T_c(\alpha)$ and $T_d(\alpha)$ signals the point where the solution suddenly appears for the first time with a jump of $\Sigma(f^*)$ from zero to a finite value. In this region $\Sigma(f^*)$ manifests its thermodynamical significance as it accounts for the entropic contribution from the exponentially degenerate pure states. It turns out that the average value $\langle\eta\rangle$ over the probability $\mathcal{P}(\eta)$ satisfies the RS equation. In fact, despite the jump of $\Sigma(f^*)$ at $T_d(\alpha)$, the (free) energy as well as other thermodynamical quantities are analytical at this point. $T_d(\alpha)$ is instead referred as a dynamical transition because it corresponds to the point where a local algorithm which performs a stochastic dynamical search (as thermal annealing) fails to the reach the equilibrium value [80]. In fact the existence of many pure states separated by extensive barriers makes the probability of departure from metastable local minima exponentially small in N.

- The c-1RSB solution: $\mathcal{P}(\eta)$ is not trivial and $\Sigma(f^*) = 0$ with $m < 1$. It coincides with the region $T(\alpha) < T_c(\alpha)$ and $T_c(\alpha)$ is the point where $\Sigma(f^*)$ vanishes for the first time with a non trivial solution at $m = 1$. The complexity vanishes continuously at the transition and it remains zero afterwards with an appropriate tuning of m, i.e. $\Sigma(m^*) = 0$. The measure condensates in a sub-exponential number of states and along $T_s(\alpha)$ the free energy has a discontinuity of the second order. $T_c(\alpha)$ marks a thermodynamic transition. As we will discuss in Chapter 5 it is the analogue of a glass transition for mean-field glassy systems. Note that $(m^*\beta)^{-1}$ can be interpreted as an effective temperature (see Chapter 8) for the glass phase.

- The $T = 0$ solution: The limit of zero temperature can be taken explicitly in the equations and it is particularly important for the CSPs [81, 6]. It allows in fact the investigation of the SAT phase at zero temperature in terms of the entropy s of the pure states. α_d and α_c have the same interpretation as for finite T. α_s represents the SAT/UNSAT transition, which occurs at $T = 0$ only and it is recovered in the limit $m = 0$. α_s corresponds to the point where the probability of finding a solution drops from one to zero.

In Section 3.2 we will see the emergence of this phase diagram in the simple case of a toy model. Remarkably the simplicity of its Hamiltonian allows to get an intuition of these transitions without resorting to the cavity method.

2.1.3 Population dynamics

We present here the idea for the numerical resolution of Eq. (2.13). This will turn out to be particularly useful for discussing the quantum case. Let us note that h, the field that parametrizes η, is a real number and a self-consitent equation for the distribution $\mathcal{P}(\eta)$, as (2.13), is not easy to solve. However a numerical method that goes under the name Population Dynamics proved to be very successful in this task. It is based on the representation of the probability distribution $\mathcal{P}(\eta)$ as a weighted sample. Starting with an initial representation (*population*) of $\mathcal{P}(\eta)$ in the form:

$$\mathcal{P}(\eta) = \sum_{i=1}^{\mathcal{N}_\eta} w_i \, \delta(\eta - \eta_i) \quad \text{such that} \quad \sum_{i=1}^{\mathcal{N}_\eta} w_i = 1 \; , \tag{2.17}$$

it amounts to the generation of a sampled representation of the l.h.s. of Eq. (2.13), assuming the knowledge of the r.h.s. In this scheme Eq. (2.13) amounts to repeat $\mathcal{N}_\eta$ times the following steps:

1. sample $c - 1$ elements $\{\eta_{i_1}, \ldots, \eta_{i_{c-1}}\}$ from $\mathcal{P}(\eta)$, independently with the probabilities w_i;

2. compute a new field $\eta = \bar{\eta}(\eta_{i_1}, \ldots, \eta_{i_{c-1}})$;

3. add to the new population the element η with weight $\propto e^{-\beta m \bar{f}(\eta_{i_1}, \ldots, \eta_{i_{c-1}})}$.

after which a new representation is available and it is substituted to the older one. The fixed point of Eq. (2.13) is found by iterating this procedure many times. Once convergence is reached all thermodynamic observables can be computed by sampling from the distribution.

The numerical accuracy of the population dynamics obviously depends on the number $\mathcal{N}_\eta$ of representatives of the distribution $\mathcal{P}(\eta)$. However, a large value of $\mathcal{N}_\eta$ is not sufficient to ensure a good precision of this discretized representation: if only a few weights w_i dominate the sum in (2.17) the effective size of the population is the number of such dominant elements. To be more quantitative one can define the inverse participation ratio:

$$\text{IPR} = \frac{1}{\mathcal{N}_\eta} \left(\sum_{i=1}^{\mathcal{N}_\eta} w_i^2 \right)^{-1} \; , \tag{2.18}$$

where w_i are the normalized weights of the sampled population defined in (2.17). Its value is easily evaluated in the two limits of a perfectly balanced population and of a single dominant weight:

$$\text{IPR} = \begin{cases} \mathcal{O}(1) & \text{if } w_i \sim \mathcal{O}(1/\mathcal{N}_\eta) \\ \mathcal{O}(1/\mathcal{N}_\eta) & \text{if } w_i \sim \delta_{i,i^*} \end{cases} \; , \tag{2.19}$$

and one can define an effective population size as $\mathcal{N}_{\text{eff}} = \mathcal{N}_\eta \times \text{IPR}$. The inverse population ratio should thus be maintained as close as possible to one to achieve a good numerical precision.

2.2 Quantum cavity method

In the following we present the quantum cavity treatment of the ferromagnetic model:

$$\hat{H}(\Gamma) = - \sum_{\langle ij \rangle} \hat{\sigma}_i^z \hat{\sigma}_j^z - \Gamma \sum_i \hat{\sigma}_i^x \; , \tag{2.20}$$

where $\langle ij \rangle$ are the edges of a tree-like graph. The object of the study, as before, is the computation of the partition function $Z(\beta, \Gamma) = \text{Tr} e^{-\beta \hat{H}(\Gamma)}$. We will present the method in the RS version which
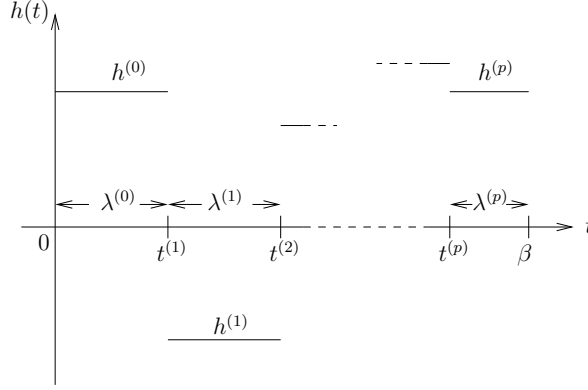
Figure 2.3: A cavity field $h(t) = \sum_{i=1}^{k} \sigma_i(t)$. The $\{t^{(j)}\}$ indicate the discontinuities at which jumps have occurred, while $\{\lambda^{(j)}\}$ are the intervals when $h(t)$ remains constants. A trajectory $\sigma(t)$ is analogous, but it can take values only in $\{-1, 1\}$. Figure from [82].

encodes the essential novelty. We will comment on that and on the 1-RSB version at the end of the section. For a detailed treatment of the quantum cavity method for spin systems and bosonic particles we refer to [82, 83, 84].

2.2.1   Path integral and cavity equations

The method is based on a path integral formulation of Z:

$$Z = \int_{\underline{\sigma}(0)=\underline{\sigma}(\beta)} \prod_{i=1}^{N} D\boldsymbol{\sigma}_i \, v_i(\boldsymbol{\sigma}_i) \, e^{\sum_{\langle ij \rangle} \int_0^\beta \mathrm{d}t \, \sigma_i(t)\sigma_j(t)} \ , \tag{2.21}$$

whose mathematical derivation is rigorously stated. In (2.21) bold symbols represent spin trajectories in "imaginary" time and in particular $\boldsymbol{\sigma}_i$ is a piecewise constant function $\sigma_i(t) : [0, \beta] \to \chi = \{-1, 1\}$ (see Fig. 2.3). The integration measure $D\boldsymbol{\sigma}_i$ stems for:

$$\int D\boldsymbol{\sigma}_i \equiv \sum_{n=0}^{\infty} \sum_{\sigma_i^0,\dots,\sigma_i^n} \int_0^\beta \mathrm{d}t_1 \int_{t_1}^\beta \mathrm{d}t_2 \dots \int_{t_{n-1}}^\beta \mathrm{d}t_n \quad \text{and} \quad v(\boldsymbol{\sigma}_i) = (\Gamma)^n \prod_{j=1}^{n} \delta_{\sigma_i^{j-1},-\sigma_i^j} \ , \tag{2.22}$$

where $\sigma_i^j = \sigma_i(t_j^+)$ and the $\{t_j\}$ are the times at which the spin-flips occur. Each time t_j is unambiguously associated to a spin σ_i. In order to emphasize the similarity with the classical partition function (2.1) we use the notation $\sum_{\boldsymbol{\sigma}_i}$ for $\int D\boldsymbol{\sigma}_i$ and we write Z for generic interactions ε_a:

$$Z = \sum_{\underline{\sigma}} \prod_{a=1}^{M} w_a(\underline{\boldsymbol{\sigma}}_{\partial a}) \prod_{i=1}^{N} v_i(\boldsymbol{\sigma}_i) \ , \qquad w_a(\underline{\boldsymbol{\sigma}}_{\partial a}) = e^{-\int_0^\beta \mathrm{d}t \, \varepsilon_a(\underline{\boldsymbol{\sigma}}_{\partial a}(t))} \ . \tag{2.23}$$

The quantum computation is reduced to a classical one, the cost to be paid being the replacement of the discrete Ising variable σ_i with a function (trajectory) $\boldsymbol{\sigma}_i$ as basic degrees of freedom. However the "spatial" structure of the interactions encoded in the factor graph is the same in the classical and in the quantum case. In particular as soon as the classical energy part of the quantum Hamiltonian falls into the category of models that can be studied by the cavity method (i.e. sparse random graphs), then this is true also for the quantum problem. The Bethe-Peierls approximation in this case will concern the marginal cavity probabilities of the trajectories. For random regular graphs, under the

Bethe-Peierls assumption, the equation for the cavity marginal $\eta(\boldsymbol{\sigma})$ is exactly the same as that of the classical model with the partition function Z but with $\boldsymbol{\sigma}$ changed in σ:

$$\eta(\boldsymbol{\sigma}) = \frac{1}{\mathcal{Z}} \, v(\boldsymbol{\sigma}) \Big[\sum_{\boldsymbol{\sigma}'} \eta(\boldsymbol{\sigma}') \, e^{\boldsymbol{\sigma}' \cdot \boldsymbol{\sigma}} \Big]^k , \tag{2.24}$$

where $k = c - 1$ and $\boldsymbol{\sigma}' \cdot \boldsymbol{\sigma} = \int_0^\beta \mathrm{d}t \, \sigma'(t)\sigma(t)$. Despite we introduced trajectories as continuous time functions, a *discrete* set of numbers (over a continuous domain $[0, \beta]$) encodes all the information. Algorithmically this is a crucial observation. The trajectory $\boldsymbol{\sigma}$ is indeed parametrized by the initial condition $\sigma^0 \in \{-1, 1\}$ and the set of times $t_1, \ldots, t_n$ specifying its n discontinuities. Note that as far as β is finite n is finite as well. We define the effective fields $\boldsymbol{h}$ as the sum of k of trajectories:

$$\boldsymbol{h} = \boldsymbol{h}(\boldsymbol{\sigma}_1, \ldots, \boldsymbol{\sigma}_k) = \sum_{i=1}^k \boldsymbol{\sigma}_i . \tag{2.25}$$

The definition of $\boldsymbol{h}$ is transparent in terms of the relation $h(t) = \sum_{i=1}^k \sigma_i(t) \; \forall t$. Clearly, as for $\boldsymbol{\sigma}$, a clever representation of $\boldsymbol{h}$ relies only on a discrete set. Algorithmically Eq. (2.25) amounts to return the initial condition $h^0 = \sum_{i=1}^k \sigma_i^0$ of $\boldsymbol{h}$ and the set $(t_1, h^1), \ldots, (t_{N_k}, h^{N_k})$ characterizing its jumps. The set $\{(t_i, h^i)\}$ is the (time ordered) list of the $N_k = \sum_{j=1}^k n_j$ discontinuities t_i in $\{\boldsymbol{\sigma}_j\}$ and $h^i = h(t_i^+)$. This is just to emphasize that $\boldsymbol{h}$ is a generalization of $\boldsymbol{\sigma}$ for $|\chi| > 2$, actually $|\chi| = k + 1$. The fixed point of Eq. (2.24) is found thanks to the fundamental observation that Eq. (2.24) can be recast in the form:

$$\eta(\boldsymbol{\sigma}) = \frac{1}{\mathcal{Z}} \sum_{\boldsymbol{\sigma}_1, \ldots, \boldsymbol{\sigma}_k} \eta(\boldsymbol{\sigma}_1) \ldots \eta(\boldsymbol{\sigma}_k) \, p(\boldsymbol{\sigma}|\boldsymbol{h}) \, z(\boldsymbol{h}) , \tag{2.26}$$

with $\boldsymbol{h} = \sum_{i=1}^k \boldsymbol{\sigma}_i$. In Eq. (2.26) we introduced the probability law $p(\boldsymbol{\sigma}|\boldsymbol{h})$ on the trajectories $\boldsymbol{\sigma}$ by

$$p(\boldsymbol{\sigma}|\boldsymbol{h}) = \frac{1}{z(\boldsymbol{h})} \, v(\boldsymbol{\sigma}) \, e^{\boldsymbol{h} \cdot \boldsymbol{\sigma}} , \qquad z(\boldsymbol{h}) = \sum_{\boldsymbol{\sigma}} v(\boldsymbol{\sigma}) \, e^{\boldsymbol{h} \cdot \boldsymbol{\sigma}} , \tag{2.27}$$

$z(\boldsymbol{h})$ ensuring the normalization of $p(\boldsymbol{\sigma}|\boldsymbol{h})$. Assuming that one is able to sample from $p(\boldsymbol{\sigma}|\boldsymbol{h})$ and to compute the associated normalization $z(\boldsymbol{h})$, the knowledge of $\eta(\boldsymbol{\sigma})$ and of the thermodynamical quantities follows.

2.2.2 Path generation

The resolution of Eq. (2.26) is brought back to a population dynamics algorithm. It amounts in fact to the generation of a sampled representation of its l.h.s., assuming the knowledge of the r.h.s., in particular the ability to draw the trajectories from the probability laws $\eta(\boldsymbol{\sigma})$. Suppose that one has an estimation of the r.h.s. $\eta(\boldsymbol{\sigma})$ given by a representative weighted sample of elements $\{\boldsymbol{\sigma}_i\}$:

$$\eta(\boldsymbol{\sigma}) = \sum_{i=1}^{\mathcal{N}_{\text{traj}}} w_i \, \delta(\boldsymbol{\sigma} - \boldsymbol{\sigma}_i) , \tag{2.28}$$

such that the weights w_i add up to one. To construct the representation of the l.h.s., i.e. a set of sampled trajectories $\{\boldsymbol{\sigma}_i'\}$ and their corresponding weights $\{w_i'\}$, one has to repeat $\mathcal{N}_{\text{traj}}$ times independently, for $j \in [1, \mathcal{N}_{\text{traj}}]$, the following steps:

- draw the $\boldsymbol{\sigma}_1, \ldots, \boldsymbol{\sigma}_k$ from the distribution $\eta(\boldsymbol{\sigma})$, according to the weights w_i.

- compute the field $\boldsymbol{h} = \sum_{i=1}^k \boldsymbol{\sigma}_i$ according to Eq. (2.25).

- extract a trajectory $\boldsymbol{\sigma}'_j$ from the law $p(\boldsymbol{\sigma}|\boldsymbol{h})$ and set its (not normalized) weight equal to $w'_j = z(\boldsymbol{h})$.

Once these steps have been performed $\mathcal{N}_{\mathrm{traj}}$ times, renormalize the weights,

$$w'_j \leftarrow \frac{w'_j}{w'_1 + \cdots + w'_{\mathcal{N}_{\mathrm{traj}}}} \ . \tag{2.29}$$

After that this procedure has been iterated a new representation of the population is available and it can be plugged in the r.h.s. of Eq. (2.26) in order to converge to the fixed point. A moment of thought reveals that this is indeed the correct algorithmic translation of Eq. (2.26). We are thus left with the problem of generating a path according to the law $p(\boldsymbol{\sigma}|\boldsymbol{h})$ defined in Eq. (2.27) and of computing the normalizing factor $z(\boldsymbol{h})$. As all trajectories $\boldsymbol{\sigma}_i$ are piecewise-constant, the same holds for the field $\boldsymbol{h}$ (see Fig. 2.3). Let us call p the number of discontinuities on $[0, \beta]$ of $\boldsymbol{h}$, that occur at times $0 \le t_1 \le \cdots \le t_p \le \beta$, and denote $h^0, h^1, \ldots, h^p$ the values of $h^i = h(t_i^+)$. We also denote $\lambda^0 = t_1$, $\lambda^1 = t_2 - t_1$, $\ldots$, $\lambda^p = \beta - t_p$ the duration of these intervals. Consider now the following single-spin Hamiltonian:

$$\left\langle \sigma|\widetilde{H}(\Gamma, h)|\sigma' \right\rangle = -h\sigma\, \delta_{\sigma,\sigma'} - \Gamma\, \delta_{\sigma,-\sigma'} \ , \tag{2.30}$$

defined on the 2-dimensional Hilbert space spanned by $\{|\sigma\rangle \, |\sigma \in \{-1, 1\}\}$. We shall write $\widetilde{W}(\Gamma, h, \lambda) = e^{-\lambda\widetilde{H}(\Gamma, h)}$ its associated propagator on an interval of imaginary time of length λ, and $W(\Gamma, h, \lambda)_{\sigma, \sigma'} = \left\langle \sigma|\widetilde{W}(\Gamma, h, \lambda)|\sigma' \right\rangle$ the matrix elements of the propagator. It is then possible to prove that the sought-for normalizing factor $z(\boldsymbol{h})$ reads

$$z(\boldsymbol{h}) = \mathrm{Tr}\left[\prod_{i=0}^{p} \widetilde{W}(\Gamma, h^i, \lambda^i) \right] \ . \tag{2.31}$$

This is a computationally affordable expression: it requires diagonalizing p matrices of dimension 2×2, exponentiating them and multiplying them together. Finally the process of generation of $\boldsymbol{\sigma}$ with the law $p(\boldsymbol{\sigma}|\boldsymbol{h})$ can be implemented as follows:

- draw the values $\sigma^0, \ldots, \sigma^p$ that $\boldsymbol{\sigma}$ assumes at times $0, t_1, \ldots, t_p$.

- on each of the $p+1$ intervals $[t_i, t_{i+1}]$, draw a trajectory representative of the evolution $\widetilde{W}(\Gamma, h^i, \lambda^i)$ in a constant field h^i, with boundary conditions $\sigma(t_i) = \sigma^i$, $\sigma(t_{i+1}) = \sigma^{i+1}$ (we set $t_0 = 0$ and $\sigma^{p+1} = \sigma^0$).

More precisely, the first step consists in extracting these $p + 1$ values from the joint law

$$p(\sigma^0, \ldots, \sigma^p) = \frac{1}{z(\boldsymbol{h})} W(\Gamma, h^0, \lambda^0)_{\sigma^0, \sigma^1} W(\Gamma, h^1, \lambda^1)_{\sigma^1, \sigma^2} \ldots W(\Gamma, h^p, \lambda^p)_{\sigma^p, \sigma^0} \ . \tag{2.32}$$

This can be easily done by first drawing σ^0 from its marginal probability, then σ^1 conditioned on the value of σ^0, and so on until σ^p has been extracted. The procedure to follow for the second step is more apparent once an integral equation on $\widetilde{W}$ is written:

$$W(\Gamma, h, \lambda)_{\sigma, \sigma'} = e^{\lambda h\sigma}\delta_{\sigma, \sigma'} + \Gamma \int_0^\lambda \mathrm{d}t\, e^{th\sigma}\, W(\Gamma, h, \lambda - t)_{-\sigma, \sigma'} \ . \tag{2.33}$$

In terms of the path-integral representation of $\widetilde{W}$, the two terms in this equation represent respectively the contribution of a constant path (possible only if the boundary conditions are the same at time $t = 0$ and $t = \lambda$) and of a path whose first discontinuity occurs at time t, where $\sigma(t)$ jumps from σ to $-\sigma$. In consequence, the procedure to draw a path from $\sigma(t = 0) = \sigma$ to $\sigma(t = \lambda) = \sigma'$ in presence of a constant field $\vec{h}$ reads

- if $\sigma = \sigma'$, with probability $e^{\lambda h \sigma}/W(\Gamma, h, \lambda)_{\sigma,\sigma}$, exit with the constant path $\sigma(t) = \sigma \ \forall t \in [0, \lambda]$.

- otherwise

  - draw a random time $u \in [0, \lambda]$ with the cumulative distribution $G(u) = \mathbb{P}[t \leq u]$

  $$G(u) = \frac{\int_0^u \mathrm{d}t \, e^{th\sigma} \, W(\Gamma, h, \lambda - t)_{-\sigma,\sigma'}}{\int_0^\lambda \mathrm{d}t \, e^{th\sigma} \, W(\Gamma, h, \lambda - t)_{-\sigma,\sigma'}} \tag{2.34}$$

  - set $\sigma(t) = \sigma$ for $t \in [0, u]$, and call recursively the same procedure to generate the path on $[u, \lambda]$, with boundary conditions $\sigma(u) = -\sigma$, $\sigma(\lambda) = \sigma'$.

2.2.3 Discussion

The analysis of the ferromagnetic model presented above can be generalized to treat the addition of a transverse field term to all "classical" Hamiltonians that are accessible through the standard cavity method (many body interactions, $\sigma \in \{1, \ldots, q\}$, quenched disorder, ...). In Chapter 4 we will resort to a similar generalization to study the k-XORSAT problem on a random regular graph. Remarkably, one can extend the study to the partition function of a bosonic system, whose natural degrees of freedom are occupation numbers $\nu \in \{0, 1, \ldots, n_{\max}\}$ and the non-diagonal part of the Hamiltonian represents the hopping of particles between neighboring sites. In Chapter 6 we will study with this technique a model of interacting particles on the Bethe lattice. The results obtained by cavity method are exact for models defined on tree-like structures, as random optimization problems, but they can also be interpreted as a sophisticated mean-field (Bethe-Peierls) approximation for Euclidean lattices. The novelty of the quantum cavity method with respect to the classical one shows up already at the RS level: the basic degrees of freedom become imaginary-time trajectories. Then, the quantum 1-RSB treatment generalizes the quantum RS ansatz in same way as for the classical case, i.e. the 1-RSB equations are formally identical.

Note that other approximate formulations of the quantum cavity method have been proposed in [85, 86, 87]. They rely on the description of the system in terms of single-site actions or Hamiltonians whose coupling parameters are determined by self-consistent equations imposed on the expectation values of the observables in the cavity graph. The cavity equations in this case involve the effective fields that define the local Hamiltonian. These techniques have the advantage to overcome high computational costs and for disordered, non-frustrated, systems they proved to display accurate results [85, 86, 87]. A rigorous understanding of this method and of its generality is definitely important because the cavity method in this formulation represents a very efficient tool to study complex quantum systems. The 1RSB approach relies on some assumptions, most importantly the decomposition of the Gibbs measure into exponentially many pure states. These postulates are used to derive quantitative predictions (as the SAT/UNSAT transition for instance). Although there is not a completely rigorous understanding of these assumptions in some cases the predictions have been confirmed by rigorous results and in any case they have never been contradicted. In order to ponder the amount of results and of complementary checks it should be clear that the method deals with a "phase" that is unaccessible to many other techniques. In the quantum case the assumptions are the same. Of course, since the method is much more recent the validity of such assumptions also on a heuristic level is much less understood. In Chapter 4 we will see that the results obtained with quantum Monte Carlo are in agreement with the 1RSB quantum cavity method for the k-XORSAT problem. Encouraged by the success in the classical case, the quest for a deeper understanding of the quantum 1RSB phase is definitely an important and open problem. From a theoretical point of view it concerns the fundamental

understanding of quantum Gibbs states. This has to do with quite general concepts related to the dynamics and the thermodynamics of quantum systems. Moreover it is important for the design of efficient algorithms to investigate the properties of "hard" quantum mean-field models.

3

Random Subcubes Model

In this Chapter we analyze a toy model of CSPs, that despite its simplicity catches most of the qualitative behavior of more complicated problems. The classical model is in the spirit of the REM, discussed in Section 1.3, but with the intention of reproducing the phenomenon of the *clusterization* and the entropy of solutions. The study is useful to get analytical results to answer some questions that have been addressed in the literature previously but are difficult to treat in concrete systems, due to the complexity of the Hamiltonians. In particular the degeneracy of the ground states and the entropy of the solutions which is a crucial property of many classical problems is generally omitted in many works discussing QAA because standard methods can not handle it easily. Within this model it is instead a fundamental ingredient. This study serves as an illustration, in a very simple setting, of some phenomena that arise with the account of quantum fluctuations and that will be partially discussed also in the next Chapter treating a more "realistic" optimization problem.

In Section 3.1 we introduce the definition of the model. The model distinguishes configurations in a set of low energy clusters and in the remaining set of high energy configurations, V being their energy. In Section 3.2 we discuss the properties of the classical model and we recover the phase diagram of more "standard" optimization problems. All our analysis of the quantum problem is restricted to the limit of large enough α when the clusters are well disjoints. In Section 3.3 we study the spectrum of the clusters at finite N in the limit $V \to \infty$. In this limit the Hamiltonian is block diagonal, each block corresponding to one cluster. The spectrum is characterized by true level crossings between states belonging to different clusters. The level crossings are due to the interplay of the classical energy and the entropy of the clusters. Quantum fluctuations, indeed, favor more entropic clusters. In Section 3.4 we consider the case of finite V (still at finite N). A finite V reintroduces a lot of additional states that have to be taken into account. They allow to connect the clusters by single spin flips, therefore the Hamiltonian is no longer block diagonal. We treat this situation by perturbation theory and variational arguments to show that a finite V induces only minor modifications with respect to the infinite V case. In Section 3.5 we show the results of the low energy spectrum obtained by exact diagonalization for finite system sizes, finding avoided level crossings. In Section 3.6 and 3.7 we consider the system in the thermodynamic limit and at finite V. In Section 3.6 we focus on the ground state, i.e. we study the system at $T = 0$. We find a first order phase transition that separates a "quantum paramagnetic" phase, at large Γ, from a "spin glass" phase, at smaller Γ. In the spin glass phase the ground state continuously changes from one cluster to the other as a function of Γ. In Section 3.7 we consider, instead, the case $T > 0$ and in particular we discuss the glass transition. We find that quantum fluctuations promote the glass transition. Finally, in Section 3.8 we summarize

and we comment the results.

3.1   The model

The quantum version of the Random Subcubes model [34] is defined as follows. We take the Hilbert space $\mathcal{H}$ of N spins 1/2 (qubits), in the basis of the Pauli matrices σ_i^z, $|\underline{\sigma}\rangle = |\sigma_1, \cdots, \sigma_N\rangle$. A *cluster* A is a subset (subcube) of the Hilbert space

$$A = \{ |\underline{\sigma}\rangle \,|\, \forall i \, \sigma_i \in \pi_i^A \} \,, \tag{3.1}$$

where π_i^A are independent random sets defined as follows:

$$\pi_i^A = \left\{ \begin{array}{cc} -1 & \text{with probability } \dfrac{p}{2} \\ 1 & \text{with probability } \dfrac{p}{2} \\ \{1, -1\} & \text{with probability } 1-p \end{array} \right\} \begin{array}{c} \sigma_i \text{ is FROZEN in cluster } A \\[2ex] \sigma_i \text{ is FREE in cluster } A \end{array} \,. \tag{3.2}$$

Thus, with probability p the variable i is "frozen" in A and with probability $1-p$ it is "free". With this definition the number of states, i.e. classical configurations, in a cluster A is a random variable equal to $2^{Ns(A)}$, where $Ns(A)$ is the number of free variables and we call $s(A)$ the *internal entropy* of a cluster. We next define a set $\mathcal{S}$ as the union of $2^{N(1-\alpha)}$ random clusters:

$$\mathcal{S} = \bigcup_{i=1}^{2^{N(1-\alpha)}} A_i \tag{3.3}$$

and the total entropy of the set reads:

$$s_{tot} = \frac{1}{N} \log_2 |\mathcal{S}| \,. \tag{3.4}$$

The parameter α here is analogous to the density of constraints in CSPs. The probability p that a variable is frozen instead plays the role of the clause size k in k-SAT or the number of colors q in the q-coloring problem.

For each cluster A we assign a Hamiltonian $\hat{H}_A = Ne_0(A) \sum_{\underline{\sigma} \in A} |\underline{\sigma}\rangle\langle\underline{\sigma}|$ with $e_0(A) \geq 0$ and a "penalty" Hamiltonian $\hat{H}_V = NV \sum_{\underline{\sigma} \notin \mathcal{S}} |\underline{\sigma}\rangle\langle\underline{\sigma}|$ which describes the classical energy of states not belonging to $\mathcal{S}$. The problem Hamiltonian $\hat{H}_P = \hat{H}_V + \sum_A \hat{H}_A$ is then diagonal in the basis $|\underline{\sigma}\rangle$. With this definition we wish to interpret the states in $\mathcal{S}$ as "local minima" of $\hat{H}_P$ and the others as "excited states". A sharp distinction between them can be obtained by sending the positive constant V to infinity; for finite V, we will always assume that $V \gg \max_A e_0(A)$. As a non-commuting quantum term we choose $\Gamma \hat{H}_Q = -\Gamma \sum_{i=1}^N \hat{\sigma}_i^x$, i.e. a transverse field acting on the spins. Note that taking instead an $\hat{H}_Q$ proportional to $\sum_{\underline{\sigma},\underline{\sigma}'} |\underline{\sigma}\rangle\langle\underline{\sigma}'|$ would lead to the simpler multi-solution Grover problem investigated in [70].

3.2   Analysis of the classical Hamiltonian

In this Section we briefly recall the structure of the set $\mathcal{S}$, shown in Fig. 3.1, which has been derived in [34]. Here we focus on the cluster structure of the classical problem ($\Gamma = 0$) neglecting the energy of the clusters. This analysis leads to a characterization of the structure of $\mathcal{S}$ when α is varied in terms of the entropy of the dominating clusters. We will see that one recovers the transitions α_d, α_c
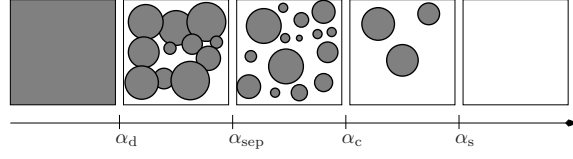
Figure 3.1: Pictorial representation of the different phase transitions in the set of solutions of the Random Subcubes model [34].

and α_s (for $T = 0$) outlined in Section 1.1.3. In [34] it has been shown that similar results apply to the description of the energy landscape where a joint distribution of entropy and energy defines the thermodynamical properties of $\mathcal{S}$ at $T > 0$. In order to unveil the structure of the space of the solutions we will extensively make use of two well-known results of probability theory called the *union bound* and *Chebychev inequality*. In fact, in complete generality the properties of $\mathcal{S}$ can be traced back to probability statements concerning 2^{Nb} events E_i each with probability $\mathcal{P}(E_i) = 2^{-Na}$, for some a and b. Under these conditions the *union bound* states:

$$\mathcal{P}\Big(\bigcup_{i=1}^{2^{Nb}} E_i \Big) \leq \sum_{i=1}^{2^{Nb}} \mathcal{P}(E_i) = 2^{N(b-a)} \ , \tag{3.5}$$

which implies that when $a > b$ the probability $\mathcal{P}(\cup_i E_i)$ is exponentially suppressed in the size of the system N. Before considering the opposite case $a < b$ first we note that when the events are i.i.d. for the number of true events $\mathcal{N}$ holds $\langle \mathcal{N} \rangle = 2^{N(b-a)}$ and $\langle \mathcal{N}^2 \rangle = 2^{N(b-a)}(1-2^{-Na})$. Then for arbitrary small ϵ one can apply *Chebychev inequality*:

$$\mathcal{P}\Big(\frac{|\mathcal{N} - \langle \mathcal{N} \rangle |}{\langle \mathcal{N} \rangle} > \epsilon \Big) \leq \frac{\langle \mathcal{N}^2 \rangle}{\langle \mathcal{N} \rangle^2 \, \epsilon^2} \leq \frac{1}{2^{N(b-a)}\epsilon^2} \tag{3.6}$$

which ensures that when $a < b$, $\mathcal{N}$ is *self-averaging* in the large N limit, i.e. the average is exponentially large and concentration around the average $\mathcal{N} \sim \langle \mathcal{N} \rangle$ is found. Applying these arguments one identifies the following structure in the space of solutions when α is varied.

- For $\alpha \leq \alpha_d = \log_2(2 - p)$, each state $|\underline{\sigma}\rangle$ belongs to an exponential number of clusters and the space $\mathcal{S}$ coincides with $\mathcal{H}$.

  Proof: The probability that a configuration $|\underline{\sigma}\rangle$ belongs to a cluster A is $\mathcal{P}(|\underline{\sigma}\rangle \in A) = (1 - \frac{p}{2})^N$ and

  $$\mathcal{P}(|\underline{\sigma}\rangle \notin \mathcal{S}) = \Big[1 - \Big(1 - \frac{p}{2} \Big)^N \Big]^{2^{N(1-\alpha)}} \ . \tag{3.7}$$

  Then from the union bound if $\alpha < \alpha_d = \log_2(2 - p)$:

  $$\mathcal{P}(\mathcal{S} \neq \mathcal{H}) = \mathcal{P}(\cup_{|\underline{\sigma}\rangle} |\underline{\sigma}\rangle \notin \mathcal{S}) \leq 2^N e^{-2^{N[\log_2(2-p)-\alpha]}} \to 0 \ , \tag{3.8}$$

  which implies that all states are in $\mathcal{S}$ and $s_{tot} = 1$.

- For $\alpha > \alpha_d$ picking at random a configuration with probability 1 when $N \to \infty$ this will not belong to $\mathcal{S}$. Thus $\mathcal{S} \neq \mathcal{H}$. The number of clusters $\mathcal{N}(s)$ of entropy s is given by

  $$\Sigma(s) = N^{-1} \log_2 \mathcal{N}(s) = 1 - \alpha - D(s||1 - p) \ , \tag{3.9}$$

  where $D(x||y) = x \log_2(x/y) + (1 - x) \log_2[(1 - x)/(1 - y)]$ for $s \in [s_{\min}, s_{\max}]$ and it is zero otherwise. The function $\Sigma(s)$ is the configurational entropy, or *complexity*, discussed in Chapter 2.

Proof: Recalling (3.7) one sees that when $\alpha > \alpha_{\mathrm{d}}$ $\mathcal{P}(|\underline{\sigma}\rangle \notin \mathcal{S}) \to 1$. Thus $\mathcal{S} \neq \mathcal{H}$ and $s_{tot} < 1$. In order to compute $\Sigma(s)$ then one notes that

$$\mathcal{P}(s(A) = s) = \binom{N}{Ns} p^{N(1-s)} (1-p)^{Ns} \tag{3.10}$$

and the number of clusters $\mathcal{N}(s)$ of entropy s follows a binomial distribution with parameter $\mathcal{P}(s)$ and $2^{N(1-\alpha)}$ terms. Applying the union bound or Chebychev inequality to the random variable $\mathcal{N}(s)$ then one obtains

$$\lim_{N\to\infty} \frac{1}{N} \log_2 \mathcal{N}(s) = \begin{cases} \lim_{N\to\infty} \frac{1}{N} \log_2 \left(2^{N(1-\alpha)}\mathcal{P}(s) \right) = \Sigma(s) & \text{if } \Sigma(s) \geq 0 \\ -\infty & \text{otherwise} \end{cases} . \tag{3.11}$$

The expression for $\Sigma(s)$ that one obtains is the one given in (3.9) and it is restricted to the interval $s \in [s_{\min}, s_{\max}]$ for which $\Sigma(s) \geq 0$. From the physical point of view what characterizes α_{d} is that for α above this value there is "ergodicity breaking" in the sense that a local random walk over solutions starting in one cluster takes an exponentially long time to reach another cluster [34].

- For $\alpha > \alpha_{\mathrm{sep}} = 1 + \log_2(1 - p^2/2)/2$, the clusters are well separated, in the sense that with probability 1 for $N \to \infty$ the Hamming distance (number of opposed spins) between any two clusters is of order N.

Proof: We note that $\mathcal{P}(A \cap A' \neq \emptyset) = (1 - \frac{p^2}{2})^N$. Then we can apply the union bound over all possible intersections in the set $\mathcal{S}$

$$\mathcal{P}(\cup_{ij}(A_i \cap A_j \neq \emptyset)) \leq \frac{1}{2} 2^{N(1-\alpha)} (2^{N(1-\alpha)} - 1)(1 - \frac{p^2}{2})^N \to 0 \tag{3.12}$$

for $\alpha > \alpha_{\mathrm{sep}}$. This means that with probability 1 when $N \to \infty$ the clusters are disjoint, i.e. their Hamming distance is strictly positive. The probability to find clusters at distance x is finite only when $x = \mathcal{O}(N)$.

- For $\alpha_{\mathrm{d}} < \alpha < \alpha_{\mathrm{c}} = p/(2-p) + \log_2(2-p)$ most of the solutions belong to one of the exponentially many clusters of size s^*, with $\Sigma(s^*) > 0$ and $s^* \in (s_{\min}, s_{\max})$. On the contrary when $\alpha > \alpha_{\mathrm{c}}$, $s^* = s_{\max}$ and most of the solutions belong to the largest clusters whose number is subexponential in N since $\Sigma(s_{\max}) = 0$.

Proof: One can compute the total number of states in $\mathcal{S}$ by observing that

$$|\mathcal{S}| = 2^{Ns_{\mathrm{tot}}} = \sum_A 2^{Ns(A)} \sim \int_{s_{\min}}^{s_{\max}} \mathrm{d}s \, 2^{N[\Sigma(s)+s]} , \tag{3.13}$$

therefore $s_{\mathrm{tot}} = \max_{s\in[s_{\min},s_{\max}]}[\Sigma(s)+s]$. Studying the function $\Sigma(s)+s$ it turns out that up to α_{c} its maximum value, dominating the saddle point in the integral, is taken inside the allowed interval and thus $\Sigma(s^*) > 0$. When $\alpha > \alpha_{\mathrm{c}}$ instead the maximum is achieved at the boundary of the interval, implying $\mathcal{N}(s^*) = \mathcal{O}(1)$.

- Finally, for $\alpha > \alpha_s = 1$ there are no more solutions.

Proof: This follows trivially from the definition of the number of clusters, equal to $2^{N(1-\alpha)}$. Then for $\alpha > 1$ there are no more clusters and the set $\mathcal{S}$ is empty. In the language of CSP α_s corresponds to the SAT/UNSAT transition.
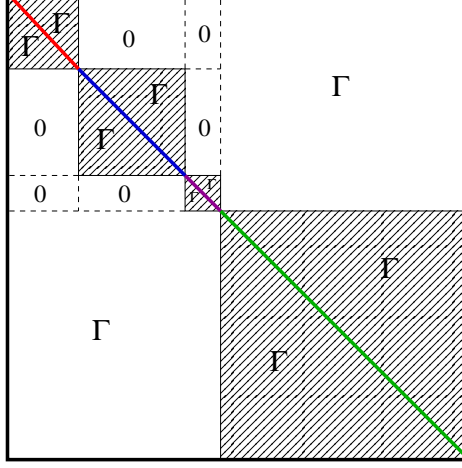
Figure 3.2: Schematic Hamiltonian matrix representing a finite size realization of the system with 3 clusters (red, blue and purple components). The biggest green sector represents states which do not belong to $\mathcal{S}$. The Hamiltonian has zero matrix elements between states belonging to different clusters since for $\alpha > \alpha_{sep}$ their Hamming distance is bigger than one. The size n_A of each cluster block is fixed by its entropy $n_A = 2^{Ns(A)}$ while the size of green component is much larger $n_V \sim 2^N$. We indicated with Γ the sectors of the Hamiltonian where there are non-zero off-diagonal matrix elements. Γ connects classical configurations at Hamming distance 1.

3.3 Spectrum of the cluster Hamiltonian

We will now study the spectrum of the quantum Hamiltonian $\hat{H} = \hat{H}_P + \Gamma \hat{H}_Q$ as a function of Γ, and from now on we focus on the region $\alpha > \alpha_{\text{sep}}$ where clusters are well separated, which is the most interesting for our purposes. The computation of the spectrum for $\alpha < \alpha_{\text{sep}}$ is more complicated, since in this region the clusters have overlaps and the arguments below do not apply straightforwardly (although they might be generalized for $\alpha > \alpha_{\text{d}}$ where the overlaps are exponentially small [34]). A schematic example of the Hamiltonian describing a finite system with three clusters in the regime where the clusters are well-separated is shown in Fig.3.2.

We consider first the ("hard") $V \to \infty$ limit where $\hat{H}_P$ is infinite for the states that do not belong to $\mathcal{S}$: then we can project out these states from the Hilbert space and look to the restriction of $\hat{H} = \sum_A \hat{H}_A + \Gamma \hat{H}_Q$ on $\mathcal{S}$, which contains $2^{Ns_{\text{tot}}}$ states. Since the matrix $\hat{H}_Q$ only connects configurations at unit Hamming distance, and different clusters have distance of order N, the Hamiltonian $\hat{H}$ has no matrix elements connecting different clusters. Therefore we can diagonalize $\hat{H}$ separately in each cluster. The restriction of $\hat{H}$ to a given cluster A with $Ns(A)$ free spins is equal to $\hat{H}_A$ plus the Hamiltonian of $Ns(A)$ uncoupled spins in a transverse field, its spectrum is hence made of levels

$$E_k(A) = Ne_0(A) + (2k - Ns(A))\Gamma , \quad k = 0, \cdots, Ns(A) , \tag{3.14}$$

each $\binom{Ns(A)}{k}$ times degenerate. In particular the lowest level has energy per spin $e_{GS}(A) = e_0(A) - \Gamma s(A)$, therefore the energy of clusters with larger entropy decreases faster with Γ. In this regime then one expects level crossings between states belonging to different clusters. In the situation where bigger clusters at $\Gamma = 0$ have larger classical energy, which is the case for more concrete CSP, the level crossings concern the ground state and at $T = 0$ each crossing corresponds to a global rearrangement of the system. A simple example of a spectrum in the $V = \infty$ limit regime for a finite system made
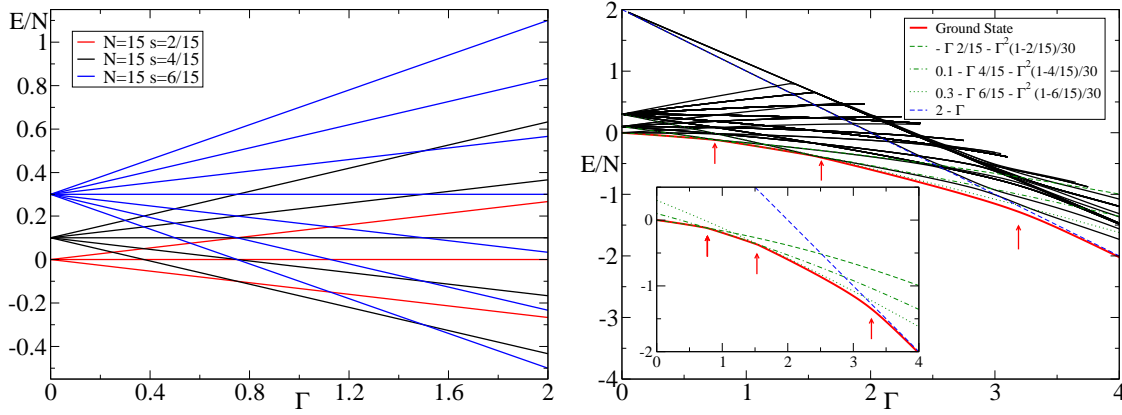
Figure 3.3: Low energy spectrum for a system with $N = 15$ and 3 clusters at Hamming distance larger than 1 such that $\{(s(A_i), e(A_i))_{i=1,2,3}\} = \{(2/15, 0); (4/15, 0.1); (6/15, 0.3)\}$. *Left panel:* Spectrum in the $V = \infty$ case. To each cluster A_i corresponds the spectrum of $Ns(A_i)$ free spins in a magnetic field. *Right panel:* Partial spectrum for finite $V = 2$ obtained by Exact Diagonalization. Red arrows indicate the points where level crossings appear. At small Γ the low energy spectrum is in good agreement with that at $V = \infty$. For larger values of Γ instead the degeneracy of the states is partially lifted and an avoided crossing between the ground state and the lowest energy state belonging to the V-band signals the presence of a first order phase transition in the $N \to \infty$ limit between states coming from the classical low energy spectrum (set $\mathcal{S}$) and the remaining states.

by 3 clusters is shown in the left panel of Fig.3.3. Note that also at finite size, as long as one takes the clusters well-separated, due to the $V \to \infty$ limit, there are no corrections in the size of the system, the crossings are not avoided and the degeneracy of the states is not removed, due to the complete independence of the Hamiltonian sectors describing each cluster.

3.4   Quantum paramagnetic state

Next, we consider a "soft" version of the model in which V is finite (still with $V \gg \max_A e_0(A)$). Therefore now H is defined on the full Hilbert space $\mathcal{H}$. In this case, in addition to the $2^{Ns_{tot}}$ energy levels discussed above (that we shall refer to as the $\mathcal{S}$-band), there exists another set of $2^N - 2^{Ns_{tot}} \sim 2^N$ levels (the V-band), whose energy is expected to be of order V at small Γ.

For the states in the $\mathcal{S}$-band we use perturbation theory in Γ. As soon as the transverse field is switched on a first order correction in Γ to the states in the $\mathcal{S}$-band is present. This correction comes from the partial lifting of the degeneracy within the cluster and it is given by the spectrum $E_k(A)$ in (3.14). A second order correction instead is induced by the presence of the V-band at finite V. In order to compute it one can apply perturbation theory assuming as unperturbed basis that which diagonalizes the perturbation $\hat{H}_Q$ inside each clusters. In particular we are interested in the correction to the lowest energy level $e_{GS}(A)$ in the clusters whose state $|GS(A)\rangle$ is given by all free spin polarized in the direction of the field. Then the correction is

$$\Delta E_A^{\Gamma^2} = \sum_{|\psi\rangle \notin A} \frac{|\langle \psi | \hat{H}_Q | GS(A) \rangle|^2}{E_\psi - E_{GS(A)}} = \frac{\Gamma^2 (1 - s) N}{NV - Ne(A)} \tag{3.15}$$

and at any finite order n the correction to the energy per spin is $\mathcal{O}((\Gamma^2/(NV))^n)$, so it vanishes in

the thermodynamic limit. This mechanism is similar to the REM due to the fact that states at the boundary of the clusters have $\Delta E \sim N$.

To study the lowest energy level in the V-band $e_{GS(V)}$ it is convenient to rewrite the Hamiltonian in the following way:

$$\hat{H} = \underbrace{NV\hat{\mathbb{1}} - \Gamma \sum_i \hat{\sigma}_i^x}_{\hat{H}_{QP}} - \underbrace{N \sum_A (V - e(A))|A\rangle\langle A|}_{\hat{H}_{\mathcal{S}}} = \hat{H}_{QP} - \hat{H}_{\mathcal{S}} , \qquad (3.16)$$

where $|A\rangle\langle A| = \sum_{\underline{\sigma} \in A} |\underline{\sigma}\rangle\langle\underline{\sigma}|$ indicates the projector over the cluster A. $\hat{H}_{QP}$ acts on the entire Hilbert space while $\hat{H}_{\mathcal{S}}$ only on the subspace spanned by the clusters. This form aims to interpret $\hat{H}_{\mathcal{S}}$ as a "perturbation" over $\hat{H}_{QP}$ which describes a system of N free spins in a transverse field with a shift in the energy NV equal for all. However the "perturbation" is not in the strength of the energy, which may be large, but in the number of states that are involved. Note, in fact, that $\text{Rank}(\hat{H}_{\mathcal{S}}) \ll \text{Rank}(\hat{H}_{QP})$, being $\text{Rank}(\hat{H}_{\mathcal{S}}) = \mathcal{R} = 2^{Ns_{\text{tot}}}$ and $\text{Rank}(\hat{H}_{QP}) = 2^N$. This, together with the fact that the perturbation matrix is positive defined (it shifts some states all in the same direction) allows to apply the results of small rank perturbation analysis [88] in order to study $e_{GS(V)}$. From these results we can safely say that

$$E_{QP}^{k-\mathcal{R}} \leq E_H^k \leq E_{QP}^k \qquad \text{for } k = 1, \dots, 2^N , \qquad (3.17)$$

where E_{QP}^k and E_H^k are respectively the k-th eigenvalues of $\hat{H}_{QP}$ and $\hat{H}$, and we assume $E_{QP}^k = -\infty$ when $k \leq 0$. In particular when Γ is small since $e_{GS(V)}$ is larger than all the energies in the $\mathcal{S}$-band this implies that

$$V - \Gamma \leq e_{GS(V)} . \qquad (3.18)$$

The results from small rank perturbation (3.17) also shows that the spectrum of the V-band is close to the one of N free spins in transverse field with classical energy NV:

$$E_V^k = NV + (2k - N)\Gamma , \quad k = 0, \cdots, N ,$$

with degeneracy close but not equal to $\binom{N}{k}$. We expect that the unperturbed ground state of $\hat{H}_{QP}$, that we call *Quantum Paramagnetic state* ($|QP\rangle$), well describes the lowest energy level of the V-band $e_{GS(V)}$ and remains unaffected by the presence of the states in $\mathcal{S}$ for all Γ except from the region where it crosses the spectrum of $\mathcal{S}$. The reason for this comes from the intuition that in absence of $\hat{H}_{\mathcal{S}}$ the spectrum of H_{QP} is highly degenerate, especially in the middle of the band. Then, also comforted by the results of exact diagonalization, we expect that the states that recombine the most in order to create the S-band when $\hat{H}_{\mathcal{S}}$ is applied, are those belonging to the more degenerate part of the spectrum. On the contrary, $|QP\rangle$ is made of all spins aligned along Γ without degeneracy and thus it is weakly perturbed by $\hat{H}_{\mathcal{S}}$. A rigorous study of this energy level is not feasible thus we proceed with some arguments which we still believe describe its behavior. The state $|QP\rangle$ has exponentially small overlap with any state in the $\mathcal{S}$-band $\langle\psi(A)|QP\rangle \sim \mathcal{O}(2^{-Ns(A)/2})$ and thus it gives an expectation value of $\hat{H}$ equal to $\langle QP|\hat{H}|QP\rangle = N(V - \Gamma) + \mathcal{O}(2^{-\gamma N})$ for some γ. It means that if we interpret this as a variational upper bound on the true ground state of the V-band we get:

$$e_{GS(V)} \leq V - \Gamma . \qquad (3.19)$$

Combining (3.18) and (3.19) we obtain

$$e_{GS(V)} = V - \Gamma + \mathcal{O}(2^{-\gamma N}) , \qquad (3.20)$$

and the corresponding eigenvector remains up to exponentially small corrections the same $|QP\rangle$, which is uniformly extended in the basis $|\underline{\sigma}\rangle$.
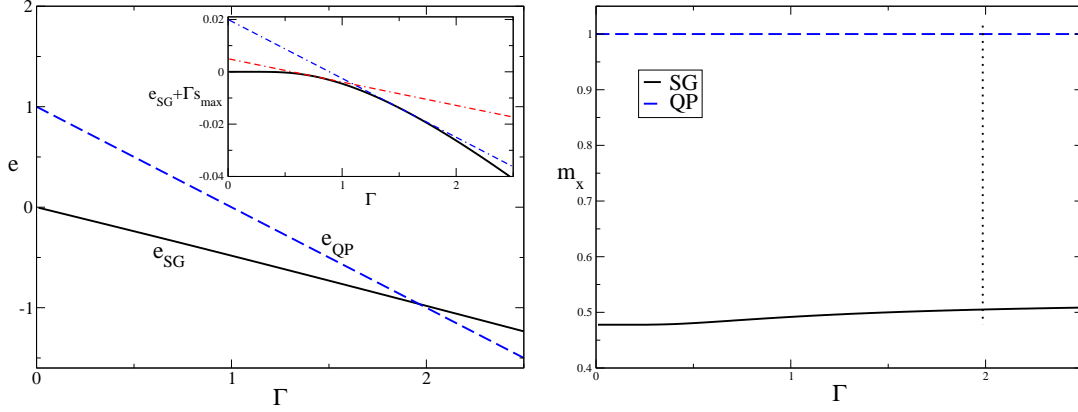
Figure 3.4: *Left panel*: Low energy spectrum of the model for $\alpha_{\mathrm{sep}} < \alpha < \alpha_{\mathrm{s}}$. As an example we choose (following [34]) $p = 0.7$, $\alpha = 0.85$, and $\Sigma(e_0) = (1 - \alpha)[2 + e_0/e_{\mathrm{m}} - (e_0/e_{\mathrm{m}}) \ln(e_0/e_{\mathrm{m}})]/3$ for $e_0 \in [0, e_{\mathrm{m}}]$ with $e_{\mathrm{m}} = 0.1$. *Main panel*: Energy of the SG (cluster) ground state [Eq. (3.21), full line] and of the QP state $e_{\mathrm{QP}} = V - \Gamma$ for $V = 1$ (dashed line). A first order transition between the two states happens at $\Gamma \sim 2$. *Inset*: Level crossings in the SG state. For better readability we plot $e_{\mathrm{SG}} + \Gamma s_{\max}(0)$ [Eq. (3.21), full line] and show the energy $e_0 - \Gamma[s_{\max}(e_0) - s_{\max}(0)]$ of two different clusters with $e_0 = 0.05, 0.2$ (dot-dashed lines). *Right panel*: Transverse magnetization m_x as a function of the transverse field Γ for the same parameters. For large enough Γ the first order phase transition between the "spin-glass" phase to the "quantum paramagnetic" phase is manifested by a jump in the transverse magnetization, shown with a vertical dotted line. The value of m_x associated to the SG ground state is shown with a solid black line, while that of the QP ground state is shown with a dashed blue line. Note that the latter is bigger because it corresponds to a more entropic phase.

3.5   Exact diagonalization results

We checked these predictions for the spectrum by means of exact diagonalizations for a system made of $N = 15$ spins. The results are shown in Fig.3.3, in the right panel. There we have plotted the spectrum of a system made by three clusters characterized by classical energy and entropy $\{(s(A_i), e(A_i))_{i=1,2,3}\} = \{(2/15, 0); (4/15, 0.1); (6/15, 0.3)\}$ and $V = 2$. The plot shows that for small Γ the states in the V-band do not affect those in the set $\mathcal{S}$, whose spectrum is in good agreement with that at $V = \infty$, in the left panel. At larger Γ avoided level crossings first appear between the ground states of different clusters and finally an avoided crossing with the ground state of the V-band whose slope in Γ is steep due to the big entropy which characterizes the sector. We have also plotted in green the analytical result that we obtain up to second order in perturbation theory for the lowest energy level of each cluster and in blue the energy of the quantum paramagnetic state. We see that the true ground state, crossing after crossing, well interpolates between all these curves. Since the clusters have Hamming distance proportional to N, we expect all these crossings to be avoided at finite N producing exponentially small gaps [60, 62, 64].

3.6   Level crossings in the thermodynamic limit

We discuss now the zero temperature phase diagram of the model for $\alpha > \alpha_{\mathrm{sep}}$ and $N \to \infty$. To get a meaningful thermodynamic limit, the number of clusters of energy e_0 is set to $2^{N\Sigma(e_0)}$, where
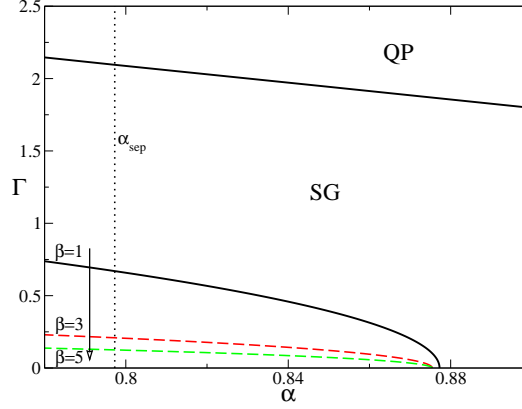
Figure 3.5: Phase diagram of the model for $p = 0.7$, $\Sigma(e_0)$ as in Fig. 3.4, and $\beta = 1$ (full lines). The vertical line corresponds to $\alpha_{\text{sep}} = 0.797$ for this value of p. The higher Γ line is the first order transition between SG and QP. Above the lower Γ line $\alpha_c(\Gamma, \beta = 1)$ the system is in the condensed phase. The condensation transition lines $\alpha_c(\Gamma, \beta)$ are also reported (dashed lines) for different values of β, showing that the non-condensed phase disappears for $\beta \to \infty$. The complexity of the zero-energy clusters is $\Sigma(e_0 = 0) = 2(1 - \alpha)/3$, hence one has $\alpha_c(\Gamma = 0, \beta = \infty) = \frac{2p-1}{2-p} + \frac{3}{2} \log_2(2 - p) = 0.875$.

$\Sigma(e_0)$ is an arbitrary increasing function of $e_0 \in [0, e_{\text{m}}]$ (as in most random optimization problems). We assume that $\Sigma(e_{\text{m}}) = 1 - \alpha$ so the total number of clusters in $\mathcal{S}$ is still $2^{N(1-\alpha)}$. Since the frozen variables are chosen independently for each cluster, the complexity of clusters of energy e_0 and entropy s is $\Sigma(e_0, s) = \Sigma(e_0) - D(s || 1 - p)$. It vanishes for a given value $s_{\text{max}}(e_0)$ which is also an increasing function of e_0. The $\mathcal{S}$-band, or spin glass (SG), ground state energy is

$$
\begin{aligned}
e_{\text{SG}} &= \min_{e_0 \in [0, e_{\text{m}}]} \left[\min_{s \in [s_{\text{min}}(e_0), s_{\text{max}}(e_0)]} (e_0 - \Gamma s) \right] \\
&= \min_{e_0 \in [0, e_{\text{m}}]} \left[e_0 - \Gamma s_{\text{max}}(e_0) \right] .
\end{aligned}
\tag{3.21}
$$

The minimum is in $e_0 = 0$ as long as $\Gamma < \Gamma_{\text{lc}} = 1/(s'_{\text{max}}(0))$. Above this value, the minimum is in a different e_0 for each value of Γ: in this region the ground state changes abruptly from one cluster to another upon changing Γ by an infinitesimal amount [89, 90].

Note that in some relevant cases the slope of $\Sigma(e_0)$ in $e_0 = 0$ is infinite, therefore $\Gamma_{\text{lc}} = 0$ and level crossings happen at all Γ. The energy e_{QP} crosses the spin-glass ground state given by Eq. (3.21), giving rise to a first-order phase transition between the spin-glass and the quantum paramagnet [59, 11, 12, 74, 13, 35] at a critical $\Gamma \propto V$. As a consequence, the transverse magnetization $m_x = de/d\Gamma$ has a jump at the transition [35] (see the right panel of Fig. 3.4). Note that $m_x = s$, thus the transverse magnetization is determined by the entropy of the ground state, and the entropy of the V-component is much larger than those of the clusters. Moreover m_x can also be associated to the inverse participation ratio $\mathcal{I}$, since $I = \sum_{\underline{\sigma}} |\psi(\underline{\sigma})|^4 = 2^{-Ns}$ and $\mathcal{I} = -\frac{1}{N} \log_2 I = s = m_x$. A similar result for the inverse participation ratio was found for a typical excited state in a mean-field model with a random field [91].

3.7   Finite temperature: the condensation transition

The previous analysis shows that in the region $\alpha_{\mathrm{sep}} < \alpha < \alpha_{\mathrm{c}}$ the perturbation $\Gamma \hat{H}_Q$ has a dramatic effect. At $\Gamma = 0$, most of the states in $\mathcal{S}$ belong to one of exponentially many small clusters, while at any $\Gamma > 0$ the few largest clusters of entropy $s_{\max}$ have the smallest energy. This is related to the fact that the presence of a transverse field introduces a correction to the energy that favors the more entropic clusters. A more complete picture is obtained by studying the model at finite temperature. It is convenient to separate the contribution of the two phases of the partition function, $Z = \mathrm{Tr}\, e^{-\beta \hat{H}} = Z_{\mathrm{SG}} + Z_{\mathrm{QP}}$, with $c = 2 \cosh(\beta \Gamma)$:

$$Z_{\mathrm{QP}} \sim \sum_k e^{-\beta E_k^V} = e^{-\beta N V} c^N \ ,$$

$$Z_{\mathrm{SG}} \sim \sum_{A,k} e^{-\beta E_k(A)} = \int \mathrm{d}e_0 \mathrm{d}s\, 2^{N\Sigma(e_0,s)} e^{-\beta N e_0} c^{Ns} \ .$$

The free energy is $f = -(T/N) \ln Z = \min\{f_{\mathrm{SG}}, f_{\mathrm{QP}}\}$, analogously to what was found in [59] for the REM (discussed in Chapter 1), with $f_{\mathrm{QP}} = V - T \ln c$ and

$$f_{\mathrm{SG}} = -T \max_{\substack{e \in [0, e_{\mathrm{m}}] \\ s \in [s_{\min}(e), s_{\max}(e)]}} [\Sigma(e_0, s) \ln 2 - \beta e_0 + s \ln c] \ . \tag{3.22}$$

The first-order transition happens when the free energies f_{SG} and f_{QP} cross, while the condensation transition happens when the maximum in Eq. (3.22) is attained in $s_{\max}$ for the first time. In Fig. 3.5 we plot the lines $\alpha_c(\Gamma)$ for several temperatures. We observe that in the limit $\beta \to \infty$, the lines $\alpha_c(\Gamma)$ shrink to the horizontal axis and the system is in the condensed phase for any $\Gamma > 0$. The first-order transition to the QP phase happens for larger values of Γ at fixed temperature, and it is reported in the plot for $\beta = 1$.

3.8   Discussion

In this Chapter we introduced a simple toy model of a quantum optimization problem, based on the random subcubes model of [34]. In the classical case $\Gamma = 0$, the model captures the essential structure of the space of solution of random optimization problems, and displays several phase transitions that are present also in more realistic problems such as k-SAT, at least at large k. We explored the consequences of this complex structure on the spectrum of the quantum Hamiltonian at $\Gamma > 0$, and we showed that: (i) Quantum fluctuations lower the energy of a cluster proportionally to its size. (ii) As clusters have an energy distribution, level crossing between different clusters are induced as a function of Γ in the spin glass phase, due to a competition between energetic and entropic effects. These crossings happen in a continuous range of Γ, giving rise to a complex spin glass phase characterized by a continuously changing ground state and an exponentially small gap. (iii) At large $\Gamma \sim V$ the spin glass phase undergoes a first order transition towards a quantum paramagnetic phase [11, 12, 74, 13, 59, 35], corresponding to the complete delocalization of the ground state in the computational basis $|\underline{\sigma}\rangle$. (iv) At finite temperature, there is a line of condensation transitions $\alpha_{\mathrm{c}}(\Gamma)$ that shrinks to $\Gamma = 0$ at low temperatures: indeed, at zero temperature the condensation transition becomes abrupt. While at $\Gamma = 0$ the space of solutions is dominated by an exponential number of clusters of intermediate size, for any $\Gamma > 0$ the biggest clusters contain the ground states.

Overall, this toy model shows that the low energy spectrum of quantum optimization problems can be very complex, and characterized by different level crossings: internal level crossings in the spin

glass phase, or the crossing between the spin glass and the quantum paramagnet giving rise to a first order phase transition. Moreover, both entropic and energetic effects are important. We expect that this complex structure of the low-energy spectrum of the quantum Hamiltonian will have deep consequences on the behavior of quantum algorithms: for instance, the quantum adiabatic algorithm proposed in [8] should run into difficulties because of the exponentially small gaps that are expected at the crossings.

4

Locked models: XORSAT on a regular graph

In this Chapter, we examine the k-XORSAT problem on a c-random regular graph. In the classical case the model is representative of a class of problems known as "locked models" [92]. The main property of these models is that clusters of solutions don't have internal entropy: they are isolated points in configuration space [92]. Therefore we do not expect the entropic effects that were discussed for the RSM in Chapter 3, at least at the level of the ground states of different clusters. This simplifies the numerical analysis of the models. We will show that a first order phase transition is found in these models, as well as in the REM or RSM. We will present the phase diagram derived with the quantum cavity method and quantum Monte Carlo. XORSAT is in fact the simplest yet not-trivial model to study with the cavity method, allowing us to illustrate the usefulness of the method. We will finally study the scaling of the gap with N at the transition in different situations. According to the value of α the typical classical ground state may or may not be degenerate and this has to be accounted in the analysis of the gap. In Section 4.1 we introduce the model. In Sections 4.2, 4.3 and 4.4 we present the phase diagrams for a particular study of the $c < k$, $c = k$ and $c > k$ case, respectively. These cases are in fact distinct in the classical limit for their properties at $T = 0$. In Section 4.5 we summarize the results. We also compare different energy landscapes of CSPs and the impact of quantum perturbations on them.

4.1   Definition of the model

We focus on the k-XORSAT problem, defined on a random c-regular graph, which has been studied in details in the classical case in [93, 94]. As we did before, we add a quantum transverse field to the classical Hamiltonian. In quantum spin language, the model is defined by the following Hamiltonian:

$$\hat{H} = \hat{H}_P + \hat{H}_Q = \sum_{a=1}^{M}(1 - J_a \hat{\sigma}_{i_1^a}^z \ldots \hat{\sigma}_{i_k^a}^z) - \Gamma \sum_{i=1}^{N} \hat{\sigma}_i^x \ . \tag{4.1}$$

Here, $J_a = \pm 1$ with equal probability. The k spins $i_1^a, i_2^a, \cdots, i_k^a$ involved in clauses $a = 1, \cdots, M = Nc/k$ are chosen uniformly at random among all possible choices such that each spin enters *exactly* in c clauses. This defines a regular random graph structure where variables have connectivity c and interactions have connectivity k.

We recall that as usual, in the classical limit $\Gamma = 0$, a given instance of the problem (defined by the choice of the random graph and of the couplings J_a) is called *satisfiable* (SAT) if there is a ground state of zero energy, UNSAT otherwise. It has been shown in [93, 94] that when $\Gamma = 0$, the entropy of the solutions equals $s = \log 2 \, (1 - c/k)$; when this entropy is positive ($c \leq k$) the model is in the SAT phase, when it is negative it is in the UNSAT phase. In particular, for $c < k$ the model is SAT with a probability going to 1 as $N \to \infty$ and the typical number of solutions is exponential in N; it is typically UNSAT for $c > k$; while in the marginal case $c = k$ the model is SAT with finite probability, and when it is SAT the number of solutions is typically finite.

We will be particularly interested in instances of $\hat{H}_P$ having a Unique Satisfying Assignment (USA), i.e., a single classical ground state, which were the focus of most of the previous studies of quantum optimization problems [8] since in this case the spectral gap can be easily defined, as we will discuss in the following. Based on the above discussion, it is clear that these instances are exponentially rare if $c \neq k$, while they have a finite probability for $c = k$. For $c = k = 3$ it was found in [35] numerically that for $N \to \infty$, the fraction of SAT and USA instances are $f_{\text{SAT}} = 0.609 \pm 0.003$ and $f_{\text{USA}} = 0.2850 \pm 0.0022$, as determined by using a Davis-Putnam-Logemann-Loveland–like algorithm [95] to count the number of solutions of 40000 instances of different sizes and extrapolating the result to $N \to \infty$.

Many of the results that we present in this Chapter on the quantum model (4.1) were reported in [35], where the existence of a first order transition was shown. We present the results in much more detail in the rest of this section, together with some previously unpublished results. It is worth to mention that in the limit $k = c \to \infty$ (taken after $N \to \infty$), it is possible to show that the model approaches a particular quantum REM where the distribution of the classical energies is a binomial. This model was recently analyzed in [96], and the existence of a first order transition was shown rigorously, supporting the results obtained with the cavity method at finite k and c. In the rest of this Chapter we discuss the results of the quantum cavity method, for the RS and the 1-RSB ansatz. We compare the quantum cavity method with the results of the quantum Monte Carlo (QMC) algorithm described in [35] across the transition. Moreover, we investigate the behavior of the spectral gap, determined by means of Exact Diagonalization (ED) and new results about the degenerate case will be presented.

4.2   Exponentially degenerate ground state: $c < k$

As a representative of the case $c < k$, we consider here $k = 4 > c = 3$. The classical ground state is exponentially degenerate with entropy $\log(2)\,(1 - c/k) = \log(2)/4$. As we mentioned, it can be shown via the cavity and replica methods [93, 94, 92] or using rigorous methods [44, 43] that the ground states are arranged in *isolated clusters*. Therefore, the internal entropy of each cluster is zero, the complexity of clusters is $\Sigma = \log(2)/4$, and typically the clusters (solutions) have Hamming distance of order N, therefore they are very far away in configuration space. The classical equilibrium complexity as a function of temperature is plotted in the inset of Fig. 4.2. The model is SAT with probability one and the typical number of ground states is $\exp(N\Sigma) = 2^{N/4}$.

We start by examining the phase diagram of the quantum model at finite Γ, as obtained from the cavity method, which is reported in Fig. 4.1. The RS computation predicts, at low enough temperature $T \lesssim 0.3$, a first-order transition between two different paramagnetic ($m_z = \langle \hat{\sigma}_i^z \rangle = 0$) phases: the *Classical Paramagnet* (CP) characterized by a small value of transverse magnetization $m_x = \langle \hat{\sigma}_i^x \rangle$, and the *Quantum Paramagnet* (QP) that has a larger value of m_x. The first order transition is signaled by a jump of m_x and a crossing of the free energies of the two phases, that can be clearly seen in
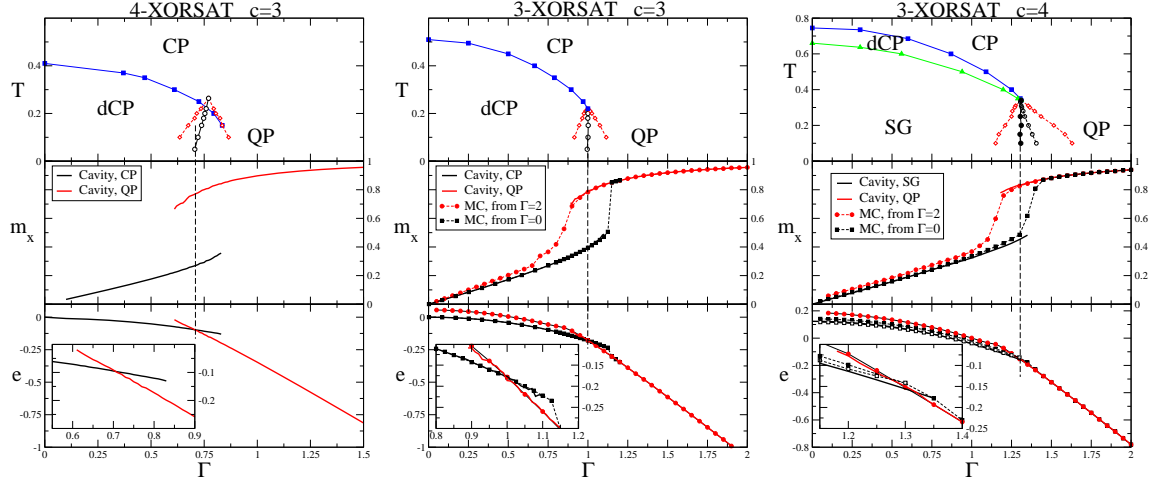
Figure 4.1: Phase diagram of the k-XORSAT model Eq. (4.1) on a c-regular random graph. The top panel represents the (T, Γ) phase diagram, displaying four possible phases: Classical Paramagnet (CP), dynamical Classical Paramagnet (dCP), Quantum Paramagnet (QP), and Spin Glass (SG). Open symbols are results of the RS calculation: first-order transition line (open circles) separating the CP and QP, with the corresponding spinodals (open diamonds). Full symbols are the result of the 1RSB calculation: clustering transition (full squares) separating the CP and dCP, Kauzmann transition (full triangles) separating dCP and SG, first-order transition separating the SG and QP (full circles). The middle panel reports the transverse magnetization as a function of Γ, and the bottom panel reports the free energy density from the cavity method or the energy density from Quantum Monte Carlo (QMC) as a function of Γ, both at fixed temperature $T = 0.05$. In these panels, full lines are the result of the cavity computation (RS or 1RSB depending on the figure) while symbols are QMC results.

(*Left*) $k = 4$ and $c = 3$. In this case there is no SG phase. The CP phase becomes a dCP at low enough temperature, while a first-order transition separates the CP (or dCP) and QP phases on increasing Γ. The transverse magnetization jumps at the first-order transition.

(*Center*) $k = c = 3$. Also in this case there is no SG phase. QMC data are reported, for a sample with $N = 2049$: red diamonds are obtained starting from the QP ($\Gamma = 2$) and decreasing Γ, while black squares are obtained starting from a classical ground state (found using Gaussian elimination) and increasing Γ.

(*Right*) $k = 3$ and $c = 4$. In this case a SG phase is present and delimited by the full triangles. A first order transition between the SG and QP phases is found. QMC data are reported for $N = 120$ and averaged over 20 samples (full symbols) and extrapolated in $1/N$ to the $N \to \infty$ limit (open symbols). Black curve, starting from the classical ground state found using an exact MAXSAT solver [97]. Red curve, starting from the QP.
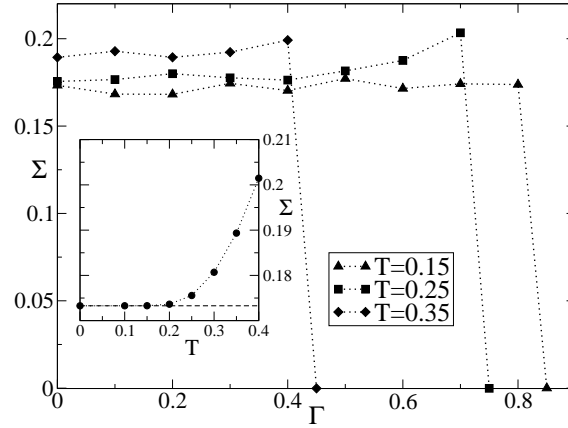
Figure 4.2: Complexity of the 4-XORSAT model at $c = 3$. (*Main panel*) Equilibrium complexity as a function of Γ at fixed T. The complexity remains finite up to the spinodal of the CP phase, where it jumps abruptly to zero. (*Inset*) Equilibrium complexity of the classical model ($\Gamma = 0$) as a function of temperature. The dashed line marks the $T = 0$ value, $\log(2)/4$.

Fig. 4.1. As in any first order transition for a mean field model, the two phases can be continued in the region where they are metastable until a well defined spinodal point. The transition line and the corresponding spinodals are shown in the (Γ, T) phase diagram in Fig. 4.1; the transition is found at a slightly temperature-dependent $\Gamma_c(T) \approx 3/4 = c/k$. We also report in Fig. 4.1 the cavity method predictions for m_x and the free energy density $f = -T \log(Z)/N$ at very low temperature $T = 0.05$.

Next, we discuss the outcome of the 1RSB computation. Following the classical case, discussed in a simpler situation in Chapter 2, the key quantity that is computed in this approach is the equilibrium complexity $\Sigma(\Gamma, T)$, which is reported in Fig. 4.2 as a function of T and Γ. Below the classical dynamical transition $T_d(\Gamma = 0) \sim 0.41$, the complexity is positive in the classical case (see the inset of Fig. 4.2). Increasing Γ, we found that $\Sigma(\Gamma, T)$ remains independent of Γ, until the first order transition is met, the system jumps to the QP phase, and the complexity vanishes abruptly. The fact that Σ is independent of Γ can be argued based on the discussion of the random subcubes model (Chapter 3). If the clusters don't have any internal entropy, and if their relative Hamming distance is of order N, different solutions are not mixed at any finite order of perturbation theory in Γ. Therefore, each classical ground state is continuously transformed in a quantum eigenstate. Moreover, since the local environment around each ground state is the same for $N \to \infty$, at any finite order of perturbation theory the quantum energy is the same for all ground states, and the degeneracy is not lifted. The number of ground states remains constant and equal to its classical value, $2^{N/4}$, so the complexity is constant as a function of Γ. Indeed, performing exact diagonalization (see the left panel of Fig. 4.3) one sees that there are no level crossings between low-energy states that classically have different intensive energies, as in the quantum random energy model [59].

The main outcome is then that the equilibrium complexity is positive or zero everywhere. The implications of this result are twofold: first of all, it confirms that the RS computation of the thermodynamic observables is in this case correct in the whole phase diagram (Γ, T). Therefore, the only thermodynamic singularity is on the first order RS transition line. Secondly, the complexity is strictly positive for low enough values of T and Γ, implying that the CP phase is actually a "dynamical CP" where an exponential number of states coexist. As seen in Chapter 2, the point where the complexity becomes

positive is called *dynamical transition temperature* $T_d(\Gamma)$, and is reported in Fig. 4.1. We also recall that equilibrium thermodynamic properties are unaffected as one crosses the transition between CP and dCP.
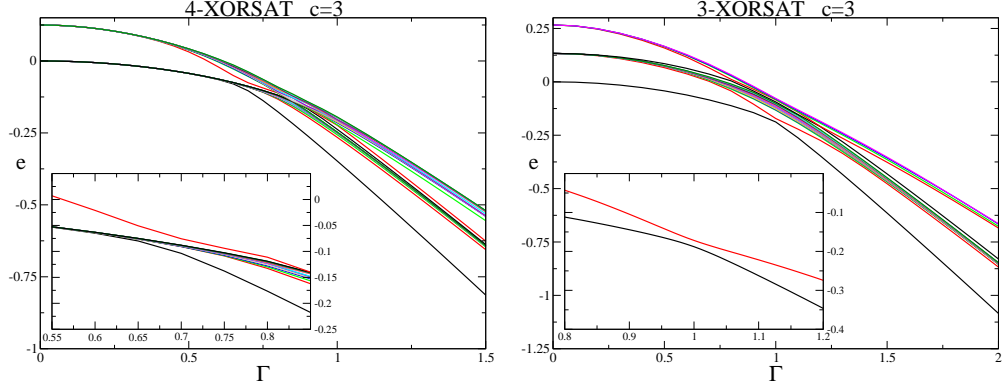
Figure 4.3: Lowest energy levels of k-XORSAT on a c-regular random graph, from exact diagonalization. In the inset the region close to the phase transition is magnified. *Left panel:* Typical instance of the 4-XORSAT model at $c = 3$, with $N = 16$. The classical ground state degeneracy is $2^4 = 16$. *Right panel:* USA instance of 3-XORSAT at $c = 3$, with $N = 15$.

In Fig. 4.3 we show Exact Diagonalization results for this case. The lowest part of the spectrum of a typical instance with $N = 16$ is plotted as a function of Γ. The instance we show has a ground state degeneracy $\mathcal{N} = 2^{N/4} = 16$ at $\Gamma = 0$, which is the most probable value. Increasing Γ, we see that the lowest 16 levels remain extremely close in energy (the difference is expected to be exponentially small), up to a value of $\Gamma \approx 0.75$, the location of the first order transition in the thermodynamic limit. At this value of Γ we observe that the 17th state (the first classical excited state) goes down in energy and approaches the bunch of ground states. The figure suggests the presence of an avoided crossing between this state and the set of ground states. These data confirm the cavity prediction: the ground state remains exponentially degenerate at any finite $\Gamma < \Gamma_c$, while at Γ_c a first order transition happens, caused by a level crossing between these degenerate SG states and the QP.

The determination of the gap is complicated by the fact that for a given instance the ground state has degeneracy $\mathcal{N}$, the average of $N^{-1} \log \mathcal{N}$ over instances being equal to the zero-temperature complexity $\log(2)/4$. Therefore, the interesting gap to determine the performances of quantum adiabatic algorithms is the minimal gap (as a function of Γ) between the lowest energy state and the $(\mathcal{N}+1)$-th excited state: transitions to any lower energy state are not dangerous since these states will continuously transform into one of the classically degenerate ground states (although a more detailed discussion of the transition dynamics in presence of almost degenerate levels might be in order here, we leave this for future work). Since $\mathcal{N}$ increases exponentially fast in N (it concentrates quickly around the value $2^{N/4}$), one has to compute an exponentially large number of levels, which slows down considerably the exact diagonalization code and in practice limits us to $N \leq 20$. In Fig. 4.4 we report data for the minimum gap as defined above. Despite the strong size limitations, the scaling of the gap appears to be exponential in N, as expected at a first order transition. We observed that fluctuations in $\mathcal{N}$ induce large fluctuations of the gap: indeed, restricting the average to instances having exactly $2^{N/4}$ classical ground states reduces a lot the fluctuations, and the curve is much closer to an exponential, at the same time the difference at large N being extremely small (we don't show the corresponding data). We will discuss further the behavior of the gap at the transition in the simpler

case $c = k$, which we analyze next.
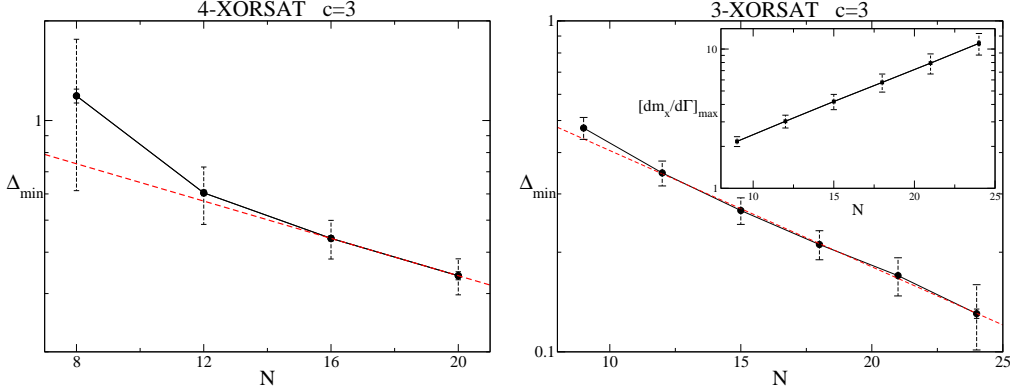
Figure 4.4: Exact diagonalization data for the minimum gap for k-XORSAT on c-regular random graphs. *Left panel:* Data for $k = 4$ and $c = 3$ on random instances. In this case the classical ground state has and instance-dependent degeneracy $\mathcal{N}$, so the relevant gap is the one between the ground state and the $(\mathcal{N} + 1)$-th state, see Fig. 4.3. Full circles represent the average over instances (100 for $N = 8, 12$ and 60 for $N = 16, 20$) of the minimal gap $\Delta_{\min}$ as a function of N. Full bars represent statistical errors on the average, while dashed bars represent the standard deviation over the instances of a single realization of the random variable $\Delta_{\min}$. Fluctuations are extremely large at small N, the main contribution being due to the fluctuations of $\mathcal{N}$. Data are limited to $N \leq 20$ due to the need to compute $\mathcal{N} + 1$ states for each instance. The dashed line is the function $\Delta_{\min}(N) = 1.244 \exp(-0.065N)$ that appears to describe the large N behavior *Right panel:* Data for $c = k = 3$ on USA instances. Here we can reach larger sizes, and moreover fluctuations are reduced. (Main panel) Average of the minimal gap $\Delta_{\min}$ as a function of N. Dashed line is a fit to $\Delta_{\min}(N) = 0.911 \exp(-0.081N)$. Inset: average of $[dm_x/d\Gamma]_{\max}$. In both cases, error bars are of the order of the symbol size except when explicitly shown ($N = 24$). Dashed bars represent the standard deviation of a single realization of the random variables $\Delta_{\min}$ and $[dm_x/d\Gamma]_{\max}$.

4.3   Finitely degenerate ground state: $c = k = 3$

We now turn to the case $c = k$, where the complexity at $T = 0$ vanishes and the number of ground states is finite with finite probability. We choose as the simplest example $c = k = 3$. The phase diagram, reported in Fig. 4.1, is qualitatively identical to the one we obtained for $c < k$, the only difference being that the equilibrium complexity now vanishes for $T = 0$ and any $\Gamma > 0$, so the number of ground states is finite for any Γ. Another quantitative difference is that the first order transition line looks exactly vertical and equal to $\Gamma_c = c/k = 1$, suggesting the existence of a hidden duality relating the model at large and small Γ, which was indeed proven in [98]. Finally, we note that in this case the spinodal lines seems to merge with the dynamical transition line exactly at the point where the first order transition disappears; however, we believe that this is just a visual effect, since we don't find any reason why this should be the case.

There is a definite advantage in this case, namely that a finite fraction $f_{\text{USA}} = 0.2850 \pm 0.0022$ of instances have a single ground state, as discussed above, making the numerical determination of the minimum gap much easier (while in the previous case, as in [8], USA instances are exponentially rare, therefore impossible to be constructed at large N). We have therefore investigated the consequences

of the transition at Γ_c for the spectral gap by investigating with exact diagonalization tools the dependence on Γ of the low-energy part of the spectrum of H for small sizes. We restrict to USA instances in order to unambiguously define the gap $\Delta(\Gamma)$ between the ground state of H and its first excited state at all values of Γ. The spectrum of a typical USA instance of $N = 15$ spins is reported in Fig. 4.3. We observe, as expected, that the gap $\Delta(\Gamma)$ has a minimum $\Delta_{\min}$ close to the phase transition at Γ_c (recall that $\Gamma_c \approx 1$ for $c = 3$ at $N \to \infty$). Around the same Γ_c, m_x changes abruptly, hence its derivative has a large maximum $[dm_x/d\Gamma]_{\max}$. In Fig. 4.4 we show the behavior of the average $\Delta_{\min}$ and $[dm_x/d\Gamma]_{\max}$ as a function of N. The data are clearly consistent with an exponential scaling of the gap, which is expected in presence of a first-order transition (see [59] for a discussion on how to compute the prefactor in the exponential in fully-connected models), and an exponential divergence of $[dm_x/d\Gamma]_{\max}$. The probability distribution over instances of $\Delta_{\min}$ and $[dm_x/d\Gamma]_{\max}$ has a unique peak close to their average, and its variance is also reported in Fig. 4.4 (dashed bars). This shows that all instances undergo a first order transition of the same kind in the thermodynamic limit.

Another very instructive example of the relevance of the first order transition is found by comparing the cavity results with Quantum Monte Carlo (QMC), see Fig. 4.1. As we already stressed several times, in the case $c = k = 3$, instances have a finite probability of being SAT, and otherwise have an energy of order $1/N$ (see [93, 94]): moreover, a ground state of SAT instances can be found in polynomial time using the Gauss elimination algorithm. This curcial observation allows to find a classical ground state of SAT instances for very large sizes ($N = 2049$). In [35] the results of QMC simulations have been reported. Starting from the classical ground state at $\Gamma = 0$ and slowly increasing Γ, the system follows the evolution of the classical ground states upon introduction of quantum fluctuations. In particular the QMC data follow closely the cavity result up to Γ_c, see Fig. 4.1. Then, as expected for a first-order transition, there exists some hysteresis around Γ_c and until the system finally jumps to the QP phase. Next, it was considered a more interesting QMC run starting from large $\Gamma = 2$ in the QP phase and slowly decreasing Γ. In this case, QMC data follow the cavity ones down to the transition Γ_c, but then the energy remains *extensively higher* than the ground-state energy for any $\Gamma < \Gamma_c$. This is obviously due to the difficulty in following adiabatically the ground state across an exponentially small gap, and is then an important indication of the difficulty of finding the ground state, even in presence of quantum fluctuations. This result is also an important proof of the usefulness of the cavity method: in fact, if it weren't for the Gaussian elimination that allowed to find the classical ground state and run the QMC starting from it, one would never be able to compute the quantum ground state using QMC. In some models (of which we give an example just below), finding the classical ground states is extremely difficult for any classical algorithm. The cavity method allows at least to compute the ground state energy, even when Monte Carlo methods fail to find solutions of the problem.

4.4 UNSAT case: $c > k$

Finally, we discuss the UNSAT case $c > k$, taking as an example $c = 4$ and $k = 3$. The results for the phase diagram are displayed in Fig. 4.1. In this case the model has a richer phenomenology, very similar to the one of fully-connected mean-field models [11, 12, 74, 13]. At the RS level, the phenomenology is unchanged and a first order is found between the CP and QP phases, as usual. However, in this case the equilibrium complexity in the dCP phase becomes negative below a temperature $T_c(\Gamma)$, the condensation transition discussed in Chapter 2, signaling that the RS solution becomes incorrect. The dCP phase then undergoes a thermodynamically second-order phase transition at $T_c(\Gamma)$ to a true *glass* (SG) phase, with a sub-exponential number of pure states. Therefore, at low enough temperature the

first-order thermodynamic transition happens directly between the 1RSB Spin Glass and the Quantum Paramagnet. For this reason, the RS computation gives a wrong result for the first-order transition line, see top panel of Fig. 4.1. The correct result is obtained by finding the crossing between the QP free energy and the SG free energy, and the latter has to be computed by optimizing over m the 1RSB free energy and is in general higher than the CP free energy as obtained from the RS calculation. Still, also in this case we conclude on the existence of a first-order quantum phase transition at $\Gamma = \Gamma_c$ and zero temperature, separating the SG from the QP. The transition extends in a line $\Gamma_c(T) \approx c/k = 4/3$ at low enough temperature, and is almost independent of T (at variance with the RS result).

Quantum Monte Carlo simulation was finally implemented using the same protocol as in the $c = k$ case [35]. However, in this case the problem is typically UNSAT [93, 94]: the classical ground states have a finite energy per spin, they are typically finite, and finding them is extremely hard (actually, NP-hard). Therefore, in this case one is severely limited in the search of the classical ground state, and we can only find it for quite small sizes ($N \leq 120$). Still, repeating the QMC procedure of increasing Γ starting from the classical ground state, it was computed the ground state energy at finite Γ. A good extrapolation in $1/N$ to the thermodynamic limit is possible, and the result agrees well with the cavity method result, see Fig. 4.1. As in the previous case, the QMC run starting at large Γ and reducing Γ fails to find the ground state at small Γ.

4.5   Discussion

In this Chapter, we discussed the phase diagram of a typical locked problem: the k-XORSAT model on a c-regular random graph. As in the REM, discussed in Section 1.3, low energy states are far apart in phase space (point-like ground states) but the Hamiltonian is a sum of local constraints, so that a spin-flip changes the total energy of order $\Delta E = \mathcal{O}(1)$. The full phase diagram of the quantum model as a function of T and Γ has been detailed. The main features that emerge are:

1. There is a first-order quantum phase transition at $T = 0$ between the low temperature classical phase (which can be either a classical paramagnetic or a spin-glass phase) and a quantum paramagnetic phase, at a critical value of $\Gamma = \Gamma_c$.

2. The transition is due to a crossing between the low-Γ classical-like ground states, and the high-Γ quantum paramagnetic state. It is of very different nature from the level crossing at infinitesimal Γ between different spin-glass ground states discussed in [60, 62, 64].

3. The first-order transition is observed for almost all instances, even for very small N. In general, finite size effects are extremely small in this model, and they are mainly due to the fluctuations in the number of classical ground states.

4. The first order transition is generically associated to an exponentially vanishing gap of H [59], hence, in this model, the quantum adiabatic algorithm requires a run time scaling exponentially with system size to find the ground state.

The main missing ingredient in locked models with respect to the general picture outlined in Chapter 3 is the internal entropy of the clusters of solutions. Since in these models clusters are isolated configurations, and they are very far away from each other, their degeneracy is not lifted by quantum fluctuations. Hence, level crossings at small Γ are absents in these models, at least at the level of the ground state, and in the thermodynamic limit the ground states remain exactly degenerate on increasing Γ up to the first order phase transition.

4.5.1 Energy landscapes and quantum perturbations

In this Section we aim to compare different scenarios that are drawn from the study of the quantum random energy model, discussed in Section 1.3, the random subcube model in Chapter 3, k-XORSAT, discussed in this Chapter, and k-SAT, whose study has not been addressed, yet. We start the discussion from the classical energy landscape of the models, as we believe that it is particularly important for understanding the effect of quantum fluctuations. In Fig. 4.5 we sketch pictorially the energy per spin as a function of the configuration for different models. Points close on the x-axis represent configurations close in phase space in terms of their Hamming distance. Points far apart are thought to be connected by a large number of spin flips. The picture highlights the main features that distinguish the models:

a. The entropy (or the number of configurations) associated to each local minima. Local minima may be exponentially degenerate (the entropy is positive) or not (the entropy is zero).

b. The energy associated to a spin flip of the low energy configurations. The variation in the intensive energy can be either $\mathcal{O}(1)$ or $\mathcal{O}(1/N)$.

It also shows some very general aspects of mean field-like glassy systems, which are shared by all the models considered here:

c. The energy landscape is dominated by many local minima

d. The distance between low energy configurations belonging to different minima is $\mathcal{O}(N)$

e. The height of the energy barriers separating two different minima in terms of the intensive energies is $\mathcal{O}(1)$

Let us explain in some more detail these properties considering separately each model.

1. *Random Energy Model*

   The schematic picture of the classical energy landscape of the REM is depicted in the upper left panel of Fig. 4.5. In the case of REM almost all configurations have zero energy per spin. Typical fluctuations of the total energy are of order $\sqrt{N}$ and they all concentrate close to the line $e = 0$ in the large N limit. Large deviations associated to $e \sim \mathcal{O}(1)$ are exponentially rare but thermodynamically relevant in the low-temperature phase. In Fig. (4.5) they are represented by the departure of few points from the zero-energy trend. (In the picture we omitted large deviations of positive energies because these are completely irrelevant).

   Note that a configuration with $e \sim \mathcal{O}(1)$ is immediately followed by a "typical" configuration, with $e \sim \mathcal{O}(1/\sqrt{N}) \to 0$ meaning that a single spin flip from a low energy configuration will typically cause an extensive change in the total energy. This is a property that derives from the unstructured nature of model, it is shared with the RSM and does not survive in Hamiltonians with local interactions. Adding a transverse field has no effect on the classical spectrum of the spin-glass. In fact, as it was shown in Section 1.3, the perturbative expansion of the low-energy states of the REM reads:

$$e_i^P(\Gamma) = e_i^P + \frac{\Gamma^2}{N e_i^P} + O\Big(\frac{1}{N^2}\Big) , \qquad (4.2)$$

   and there is a second order correction in Γ which is subleading in N and so it cancels in the thermodynamical limit.
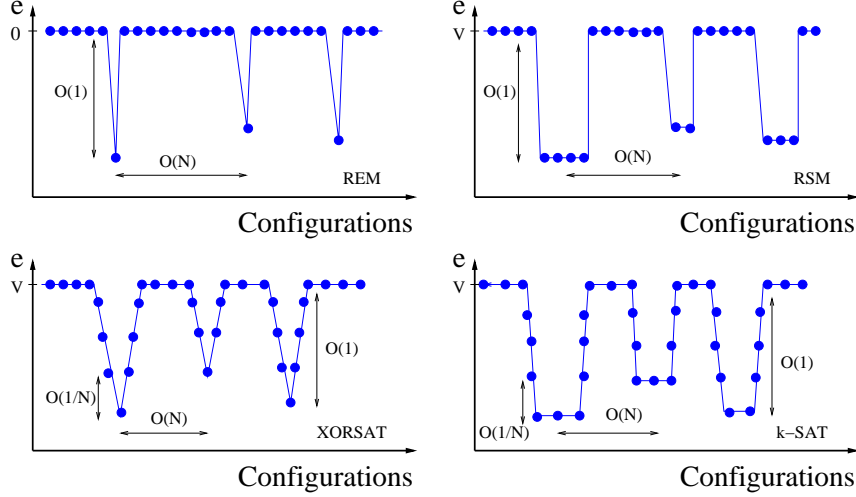
Figure 4.5: Pictorial energy landscape of the Random Energy Model (upper left panel), Random Subcubes Model (upper right panel), XORSAT on a random regular graph (lower left panel) and k-SAT (lower right panel). The figures aim to represent the energy per spin as a function of the configurations. Close points on the x-axis refer to configurations that have a small Hamming distance. Furthest points are thought to be far away in configuration space.

2. *Random Subcube Model*

In the case of the Random Subcubes Model the situation is quite different with respect to the REM. The classical landscape of the model is shown in the upper right panel of Fig. 4.5. Most of configurations belong to the V-level, out of the set $\mathcal{S}$. Several configurations live on the same local minima (cluster). These minima are extensively degenerate which means that each of them has its own entropy. In this respect REM and RSM differ concerning point (a). The entropy allows to make local movements remaining to the bottom energy. Then flipping a spin in a cluster may produce a configuration which either belongs to the cluster itself or to the V sector. This is associated respectively with a change in the total energy $\Delta E = 0$ or $\Delta E \sim \mathcal{O}(N)$. Considering the latter case, RSM and REM have the same behavior regarding point (b). According to what we discussed a transverse field inducing quantum fluctuations will have a strong impact on top of such landscape, degenerate states being particularly sensitive to fluctuations. When a transverse field acts on the classical Hamiltonian of the RSM the corrections to the intensive ground state energy e_i^P of each cluster i are the following:

$$e_i^P(\Gamma) = e_i^P - \Gamma s_i^P + \frac{\Gamma^2(1 - s_i^P)}{N(V - e_i^P)} + O\Big(\frac{1}{N^2}\Big) \,, \tag{4.3}$$

where we changed a little the notation with respect to Chapter 3 to make it here more similar to that used for the REM. The first order correction in Γ is due to the lifting of the degeneracy of the clusters. This contribution remains in the thermodynamical limit. The second order correction in Γ is subleading, as for the REM, and it vanishes at large sizes. In fact due to the form of $\hat{H}_Q$ at the second order in perturbation theory (removing first the degeneracy inter-cluster for RSM) only the configurations distant one spin-flip and that do not belong to the same cluster contribute. However, exactly as in the REM, these have typically an extensive energy difference from the minima and this causes the scaling with N of the correction.

Conversely, states in clusters far apart will be connected at higher order in perturbation theory, $\sim \Gamma^{N\mathcal{O}(1)}$, because they are distant $\mathcal{O}(N)$ spin flips, as explained in point (d). This will then induce only exponentially small corrections.

3. *k-XORSAT on a regular graph*

   In the lower left panel of Fig. (4.5) we represented a schematic view of the landscape of the k-XORSAT problem on a random c-regular graph and $c \geq k$.

   As in the REM each local minimum has a unique ground state, as a point-like cluster, and consequently it has zero entropy. According to property (a) REM and XORSAT behave the same. However due to the structure of the Hamiltonian of XORSAT the barriers can be climbed through local movements, allowing intermediate energies. More precisely since the Hamiltonian is a sum of local terms a single spin flip of a low-energy configuration always leads to a change $\Delta E \sim \mathcal{O}(1)$ in the total energy. Thus, REM and XORSAT are different with respect to point (b). This makes a substantial difference when a transverse field is acting. In fact due to the presence of low excited states surrounding the local minima perturbative calculations give to the unperturbed energies e_i^P second (and higher) order contributions of the form

   $$e_i^P(\Gamma) = e_i^P + \Gamma^2 \mathcal{O}(1) \ldots, \tag{4.4}$$

   with corrections at the leading order in N which persist in the thermodynamical limit, differently from REM.

4. *Random k-SAT*

   In k-SAT (or q-COL), even close to the satisfiability threshold, it is possible to flip some spins within a satisfying configurations, and end up with a solution of the problem, so that the lowest energy minima are degenerate as in RSM. However, since the Hamiltonian is the sum of local constraints, as in XORSAT, spin flips give corrections $\Delta E \sim \mathcal{O}(1)$ to the total energy. Thus random k-SAT shares the same behavior regarding property (a) with RSM, while it is similar to XORSAT for what concerns point (b). Recalling the situation of RSM and XORSAT, and the consequence of point (a) and (b) with respect to the application of a transverse field, we are led to conclude that perturbation theory over the lowest excited states with energy e_i^P will have leading contributions in N at all orders in Γ^n and in particular it will start from the first order in Γ because of entropic effects:

   $$e_i^P(\Gamma) = e_i^P + \underbrace{\Gamma \mathcal{O}(1)}_{\text{Entropic effects}} + \underbrace{\Gamma^2 \mathcal{O}(1)}_{\text{Energetic effects}} \ldots. \tag{4.5}$$

Despite the fact that the scaling with N of the corrections to the low energy states of k-SAT might not change dramatically the physics displayed by the RSM, it definitely makes the spectrum more complex in particular by enhancing finite size effects. Indeed, it turns out to be quite difficult to study numerically problems with a finite entropy at $T = 0$, as k-SAT. The difficulties rely mostly on the fact that one has to consider large system sizes in order to achieve a satisfactory scaling limit in which both the entropy of solutions and quantum corrections (or the spectral gap) scale properly with N. Note that the quantum cavity method can be used to study k-SAT and similar problems, however the computational cost is quite heavy, in terms of time and memory resources. For this reason the study requires a careful analysis that we aim to pursue in the future.

Part B

Quantum glasses

5

Facets of glassiness

This Chapter outlines the relevant phenomenology of glassy systems emerged by experimental or numerical studies. It discusses also the "anomalous" behavior observed in solid Helium at low temperatures and the reasons for the proposal of a superglass phase. Then, it introduces one the classical theoretical framework in which these phenomena have been explained and important results presented in the literature that deal with quantum (super)-glass phases. In Section 5.1 we discuss the experimental results, regarding glasses or solid Helium at low temperatures. In Section 5.2 we review the theoretical studies and the ideas of the literature.

5.1 Some phenomenology of glassy systems

5.1.1 Beyond the melting transition

A large number of different liquids form a glass when they are cooled fast enough in order to avoid crystallization [99]. The metastable phase that the system explores at temperatures below the avoided melting transition T_m, is called "supercooled liquid". In this regime the characteristic time scales of the system increase dramatically until becoming experimentally unaccessible at the glass transition T_g. Very remarkably the typical time τ over which density fluctuations relax, varies of 14 order of magnitude (from $\sim 10^{-12}$s at T_m to $\sim 10^2$s at T_g) in a small range of temperature $(T_m - T_g \sim T_m/3)$. The variation of $\tau(T)$ is associated with an increase of the viscosity $\eta(T)$. At T_g the liquid does not flow anymore and for all practical purposes it can be considered as an amorphous solid, a *glass*. However T_g depends on the protocol, in particular on the cooling rate: indeed the definition of solidity relies on a reference time scale [100]. Thus, the temperature T_g is conventionally defined as the point where the viscosity reaches the value $\eta(T_g) = 10^{13}$ Poise.

5.1.2 Relaxation time and fragility

As we said in the supercooled phase the change in the relaxation time is very large and it is very sharp as a function of the temperature. However the detailed dependence of $\tau(T)$ with respect to temperature is quite different from glass to glass and the concept of *fragility* was introduced in order to discriminate between different behaviors. Supercooled liquids divide in strong and fragile glass-formers and the easiest way to visualize the difference is to look at the so-called Angell plot [99]. The Angell plot reports the logarithm of $\tau(T)$ against T_g/T and the left panel of Fig.5.2 is an example. Liquids which fall on the straight dotted line in 5.2 are strong-glass formers and their τ follows an
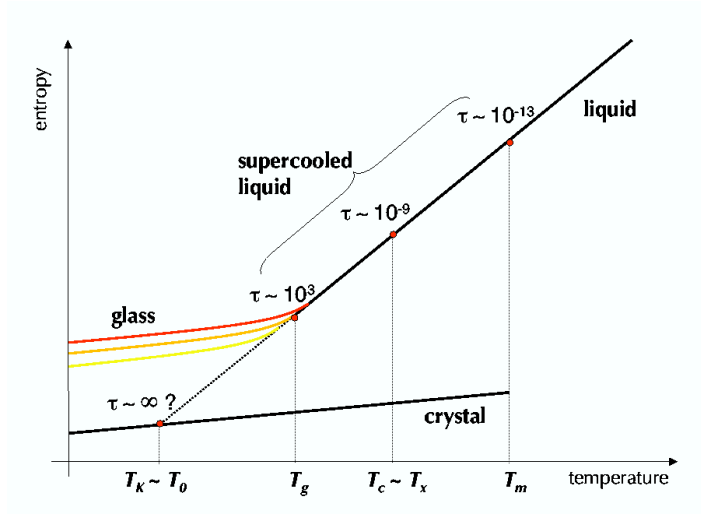
Figure 5.1: Schematic representation of the entropy as a function of the temperature for a glass-forming liquid. For the sake of simplicity we introduce only the most relevant temperatures for our discussion. T_m is the melting point. T_c corresponds to the dynamical transition in mean-field models (what is called T_d in the manuscript). T_g represents the conventional experimental glass transition. T_K indicates the ideal thermodynamic glass transition (the condensation transition T_c in the previous Chapters). Picture from [101].

Arrhenius law:

$$\tau(T) = \tau_0 \exp\left(\frac{E}{k_B T}\right) . \tag{5.1}$$

Eq. (5.1) is the expected behavior for a relaxation dynamics which follows an activated behavior driven by an energy barrier E, and where the barrier does not depend on temperature. Archetypes of this behavior are window glasses (SiO_2). Fragile liquids, instead, are those plotted in Fig. 5.2 and they can not be fitted by a straight line on the Angell plot. The correct fitting law in this case in not evident and it reflects some assumptions on the glass transition. A good fit is provided by the Vogel-Fulcher-Tamman law (VFT):

$$\tau(T) = \tau_0 \exp\left(\frac{E}{k_B(T - T_0)}\right) \tag{5.2}$$

which predicts a divergence of the relaxation time at finite temperature T_0. Other good fittings with a divergence at $T = 0$ have been also proposed. Despite the fitting form it is clear that, contrary to (5.1), the barrier E depends on the temperature and it becomes steeper and steeper close to T_g. This suggests the emergence of a cooperative phenomenon close to T_g and T_0 is interpreted as a temperature at which a structural arrest takes place. The comprehension of this phenomenon is the subject of a vast literature and remains still unresolved [2].

5.1.3 Thermodynamics

The slowdown of the dynamics of liquids close to T_g is characterized by a first time scale in which particles relax in their local environment, determined by one of the many minima ("cage") of the energy landscape in which they are trapped. Then a second slow relaxation from one minima to the other occurs. In this picture one divides the entropy of the liquid in a vibrational contribution, which
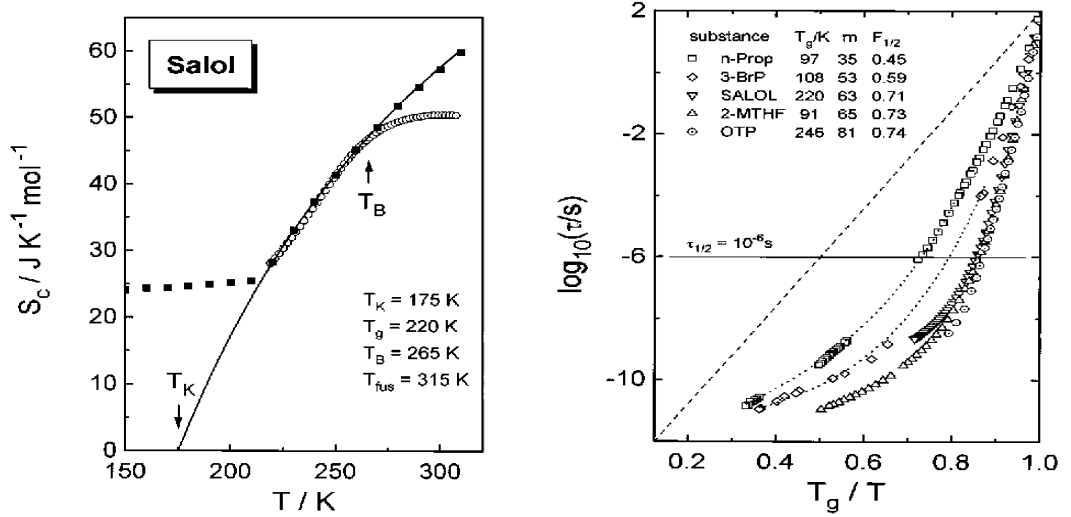
Figure 5.2: *Left panel*: Excess entropy $S_c(T)$ as a function of the temperature. The black dots are obtained by calorimetric measurements of the entropy, while the open dots derive from the measurements of the relaxation time, inverting the relation (5.6). At $T = T_g$ the system freezes in one of the amorphous states, with an extensive configurational entropy with respect to the crystal. The extrapolation $S_c(T_K) = 0$, obtained by the fit with Eq. (5.5) (solid line) defines the Kauzmann temperature T_K. *Right panel*: Relaxation time $\log \tau$ for Salol and other materials as a function of the temperature. The dashed line indicates the Arrhenius behavior. T_g is conventionally taken as the temperature below which the system is unable to establish equilibrium within a time scale set by the experimental conditions $\tau_g \sim 10^2 s$. From [102].

is associated to the free volume intra-cage and a "configurational" entropy which counts the number $\mathcal{N}_m$ of possible metastable states:

$$S_{liq}(T) = S_{vib}(T) + S_c(T) = S_{vib}(T) + \log \mathcal{N}_m \ . \tag{5.3}$$

In the approximation in which the vibrational contribution of the liquid and of the crystal are taken equal S_c also quantifies the excess of entropy of the glass with respect to the crystal:

$$S_c(T) = S_{liq}(T) - S_{vib}(T) \sim S_{liq}(T) - S_{cryst}(T) \ . \tag{5.4}$$

The measurements for determination of S_c (see Fig. 5.2, left panel) reveal a finite contribution per particle, suggesting an exponential number of metastable states. Below T_g, however, the glass remains stuck in some amorphous configuration and one cannot follow entirely the curve describing the dependence of S_c with the temperature (see Fig. 5.2, left panel). Along the equilibrium phase $S_c(T)$ is well described by the function

$$S_c(T) = S_0\Big(1 - \frac{T_K}{T}\Big) \tag{5.5}$$

and the extrapolation of such curve predicts that S_c vanishes linearly at some finite temperature T_K (the Kauzmann temperature), so that $S_c(T_K) = 0$. Remarkably, for a large number of liquids it turns out that, within a tiny error, $T_K \simeq T_0$, where T_0 is the temperature where VFT predicts the divergence of the relaxation time. The relation between T_K and T_0 let people argue that the divergence of τ is

related to the vanishing of S_c and from this follows the proposal of Adam and Gibbs:

$$\tau(T) = \tau_0 \exp\left(\frac{E}{TS_c(T)}\right) , \tag{5.6}$$

where E is a system dependent energy scale. Eq. (5.6) has been successfully tested with many liquids and Fig. 5.2 is an example. However since S_c is supposed to count the number of states, it is odd that it could become negative below T_K, as Kauzmann first noticed. This suggests that the specific heat $T\, dS_c/dT$ jumps at $T = T_K$ and a (continuous) phase transition takes place.

5.1.4 Static and dynamic correlations

One of the most challenging and open problems in the study of glasses is the identification of a diverging static correlation length. This represents an important issue if one assumes the existence of a critical point at $T = T_K$. However one cannot rely on standard observables which are suited for detecting a crystalline order. Consider for example the structure factor

$$S(\mathbf{q}) = \langle \rho_{\mathbf{q}} \rho_{-\mathbf{q}} \rangle , \tag{5.7}$$

where $\rho_{\mathbf{q}} = 1/\sqrt{N} \sum_{j=1}^{N} e^{i\mathbf{q}\mathbf{r}_j}$ is the Fourier transform of the density, N is the number of particles and $\{\mathbf{r}_j\}$ their position. The structure factor of a glass does not show remarkable differences from that of a liquid. The structure of a glass, then, looks like that of a liquid. This is in contrast to what happens for crystals, where $S(\mathbf{q})$ displays Bragg peaks revealing that a well-defined order is established. So, if an emerging length scale develops approaching T_g, it should be much more subtle.

An encouraging theoretical result in favor of the existence of such length was the rigorous proof that the existence of a diverging time scale, must be accompanied by a diverging length scale [103]. Unfortunately one is not able to follow the equilibrium behavior of the liquid at small temperatures and verify the presence of such divergence of τ at finite temperature. This is instead deduced from a fitted extrapolation and it leaves room for debate as we discussed. Conversely the slow dynamics of glass-forming liquids is interpreted as the real fingerprint of glassy system.

The dynamical correlation function, known as coherent scattering function

$$F(\mathbf{q}, t) = \langle \rho_{\mathbf{q}}(t) \rho_{-\mathbf{q}}(0) \rangle , \tag{5.8}$$

where now $\rho_{\mathbf{q}}(t) = 1/\sqrt{N} \sum_{j=1}^{N} e^{i\mathbf{q}\mathbf{r}_j(t)}$ and the average is over the dynamical histories, measures how quickly correlations decay in time. Approaching T_g, the coherent scattering function, as well as other dynamical correlations, changes qualitatively and develops a plateau at intermediate times which signals a *two-step relaxation*, see Fig. 5.3.

The time scale on which the system approaches the plateau does not depend on the temperature, while the length of the plateau increases as the temperature is lowered. It is this second time scale which is associated with the sharply increasing relaxation time τ. This two-step relaxation is consistent with the picture that we gave above of the movement of particles constrained in a cage for some time and a successive collective rearrangement toward a more favorable minimum.

Another important remark is that the emergence of the plateau is quite gradual in temperature, however its height is immediately different from zero as soon as it appears. In this respect the "transition" is discontinuous. The height of the plateau is often called the non-ergodicity factor. Remarkably, the quantity (which coincides with the non-ergodicity factor within the glass phase)

$$f(\mathbf{q}) = \lim_{t\to\infty} \lim_{N\to\infty} F(\mathbf{q}, t) , \tag{5.9}$$

defines a dynamical order parameter for the glass transition, which is zero for liquids and different from zero in the limit of a diverging relaxation time.
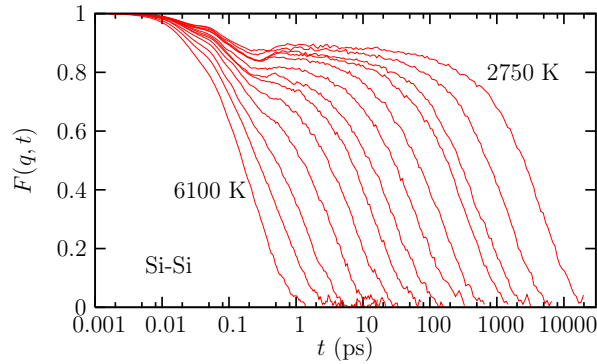
Figure 5.3: Coherent scattering function of atoms of Si at $q = 1.7$ Å^{-1} at different temperatures, obtained with molecular dynamics. From [1].

5.1.5 Quantum effects: glassy behaviour in disordered supersolids

In one of the first pioneering works on supersolidity in 1970, Leggett [20] suggested the idea that the property of non classical rotational inertia, inherent of superfluid liquid Helium, could manifest also in crystalline systems for large enough quantum fluctuations.

Since then, the possibility that a solid state, i.e. a system with broken translational and rotational invariance and with periodic structure in the case of a crystalline phase, could display off-diagonal long range order and thus macroscopic quantum coherence revealed to be attractive enough to induce many groups to look for it. This phase of matter was named "supersolid". However the first experimental evidence of this phenomenon came only more than thirty years later, in 2004, when Kim and Chan [104, 18, 19] found striking anomalies in the so-called torsional oscillator experiments with solid ^{4}He (see Fig. 5.4). In their experiment Kim and Chan considered an oscillating cell suspended through a torsional rod and containing solid Helium in an annular channel. At resonance the period τ of the oscillations is related to the inertia I of the sample through the relation $\tau = 2\pi\sqrt{I/K}$, where K is an elastic constant determined essentially by the rigidity of the rod. The period of the oscillations can be measured with high accuracy and it is seen to decrease with the temperature. This phenomenon is interpreted as the decrease of the inertia of the rotating system caused by the appearance of a superfluid component which decouples from the motion of the cell. Due to the existence of a critical velocity in the hydrodynamics of superfluids the shift in the period is maximum for small driving velocities, cfr. Fig. 5.4. The relative change in the inertia is called "non-classical rotational inertia fraction" (NCRIF) and it is identified with the superfluid fraction:

$$\text{NCRIF } = \frac{\rho_s}{\rho} = \frac{I(T) - I(T_0)}{I(T_0)} \, , \tag{5.10}$$

where ρ_s is the superfluid density, ρ is the density of the system, $I(T_0)$ and $I(T)$ are the inertia of the sample above and below the critical temperature T_0. Fig. 5.4 (right panel) reports the measurements of NCRIF in the Kim and Chan's experiment as a function of the temperature.

After Kim and Chan's experiments many other groups carried out analogous studies, confirming the presence of several anomalies, not only in the rotational properties, but also in the elastic behavior or in the specific heat [19] of solid ^{4}He samples. Despite the huge efforts from both the theoretical and the experimental sides, however, the interpretation of these results is still debated, although the ensemble of the results seems to support the idea that such anomalies are the manifestation of a supersolid
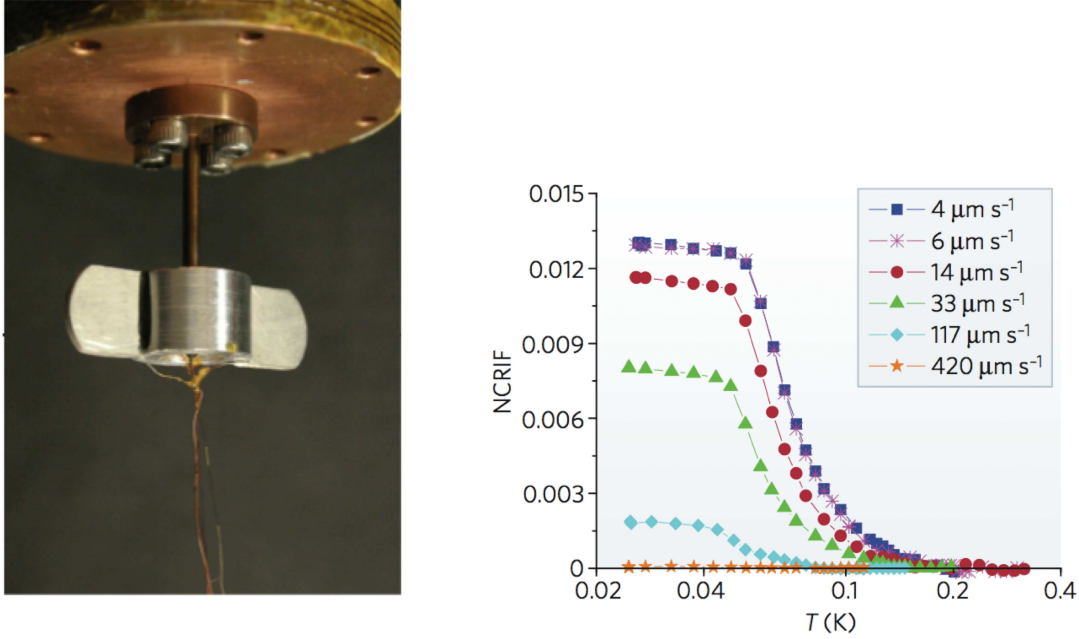
Figure 5.4: *Left panel*: Torsional oscillator used by Kim and Chan [18, 104]. Picture from [19]. *Right panel*: Measurements of the non classical rotational inertia fraction (NCRIF) done by Kim and Chan as a function of the temperature, for different velocities of the oscillating cell. Picture from [105].

state of matter. One of the most prominent question which is raised by the experiments is the role of impurities in the superfluid behavior of solid samples and whether disorder can help it or not. Even if many theorists agree on the necessity of defects to induce such phenomenon the consensus is not universal and the possibility of supersolidity as an intrinsic property of perfect crystals is still under verification [105].

The numerous experiments performed after the discovery by Kim and Chan pointed out some discrepancies among the measurement of the superfluid fraction of solid ^{4}He with different protocols and samples. Important studies about the effect of disorder where carried out by Rittner and Reppy [22, 106], who investigated the effect of the cooling rate. They first annealed the samples of solid ^{4}He for 14 hours. Annealing is a well-known method to improve the quality of the sample and in this way they obtained that the magnitude of the NCRIF decreased below the noise level of their experiments. Afterwards they considered rapidly cooled systems systems. They found that when the sample was quickly quenched so that the solid was rich of defects, the percentage of NCRIF was remarkably larger. The series of experiments by Rittner and Reppy highlighted the relevance of the disorder due to the sample preparation in the final value of NCRIF.

Later, in [21] it was argued that the relaxation time of the resonant frequency and of the dissipation as a function of temperature, during the cooling procedure increases very fast. It was also shown that the response has a history dependence and displays aging effects. This slow dynamics and the out-of-equilibrium effects, together with the anomalous rotational inertia, were interpreted as the presence of a *superglass* phase, different from the crystalline structure of ^{4}He solid usually discussed. Although
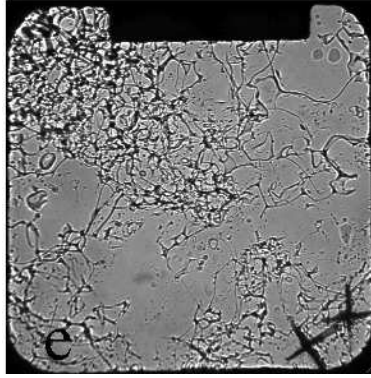
Figure 5.5: Snapshot of a ^{4}He crystal sample with many defects. From [19].

the interpretation of the experiments is very difficult and debated, these results motivate a deeper theoretical investigation of this superglass phase. This is one of the main motivations that drive our study on quantum glasses and the superglass phase.

5.2 Theoretical framework

As we already discussed in Chapter 2, our approach to glasses is based on mean-field theory. This leads to a scenario called RFOT theory that is described below. Note, however, that other approaches have been also proposed [1].

5.2.1 Mean-field approach

Before discussing the theoretical studies of quantum glasses and the superglass phase, let us first introduce the theoretical framework on which we base our understanding of a "classical" glass. The features outlined in the previous Section call for a classical theory of the glass phase able to encode (i) the dynamical slowdown measured experimentally, (ii) the two-step relaxational dynamics and (iii) a large number of amorphous states, the analogue of S_c. Random First Order Transition theory (RFOT) is a mean field approach which starts from these observations and leads to a coherent picture of the glass phase. RFOT theory [107] is the result of several years of studies and the merging of the results obtained independently and consistently within three theories (Adam Gibbs Theory [108], Mode Coupling Theory [109] and Spin Glass Theory [110]).

A number of thorough studies brought to a complete picture of fragile glasses [111, 112, 113], consistently accounting for points (i) (ii) and (iii). These works focus on interacting potentials defined in real space and apply mean-field-like approximations to compute the thermodynamics in a 3-dimensional geometry. One of the major difficulties in the study of amorphous systems is that it is not easy to handle the site-to-site fluctuations of densities which exist already at the mean field level. One cannot express the free energy as a function of a single (order) parameter, but instead it is necessary to take into account the entire density field. Connected to this problematic there are also some subtleties in the computation of the order parameter which, following Edwards and Anderson, is defined as:

$$q_{EA} = \frac{1}{V} \int_V d\mathbf{r} \ \langle \delta\rho(\mathbf{r}) \rangle^2 \tag{5.11}$$

where $\delta\rho(\mathbf{r}) = \rho(\mathbf{r}) - \rho$ is the fluctuation of density. The average in Eq. (5.11) is over one of the
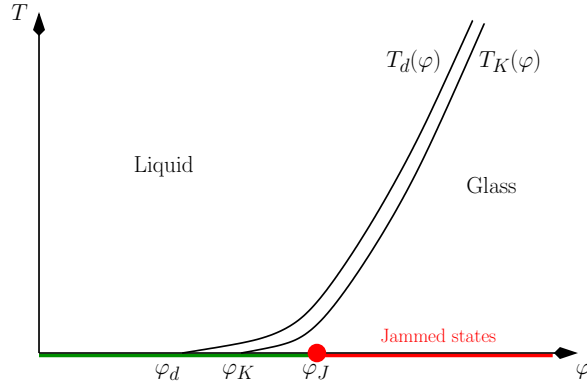
Figure 5.6: Phase diagram of soft spheres in the plane (φ, T). The two black lines indicate the dynamical and the Kauzmann transition, $T_d(\varphi)$ and $T_K(\varphi)$. At $T = 0$, φ_J indicates the jamming transition. Figure from [113].

equilibrium amorphous states and the result, in the limit of large volume, is not expected to depend on the choice of such state.

In Section 6.1 we will recover some of these results but in the simplification of a *lattice* model. The model is a generalization of [36] which proved to be a good lattice model for structural glasses. In [36] a model of interacting particles is defined through a repulsive potential which prevents particles from having more than ℓ neighbors, where ℓ is a parameter. This amounts to enforce a hard constraint, assigning an infinite energy to "unsatisfying configurations". In Section 6.1 we will consider instead of the infinite barrier a finite repulsive soft potential. This is the analogue on the lattice of the work [113] which focuses in the continuum on particles interacting with a harmonic soft potential and which extends at finite temperature and high densities the results obtained for hard-sphere models [111, 112]. The phase diagram is shown in Fig. 5.6.

In the absence of thermal fluctuations (so in the case of hard spheres) the only control parameter is the density $\rho = N/V$, where N is the number of particles and V the volume. Equivalently in the continuum one can use the packing fraction $\varphi = \pi \sigma^3 \rho / 6$, σ being the particle diameter. Dealing with soft-potentials one has two parameters at disposal to tune in order to drive the system into the glass phase. Natural choices are the density ρ and temperature T.

As we already discussed in Chapter 2, a fundamental quantity in mean field models is the configurational entropy or complexity which counts the number of metastable states. It is the analogue of S_c, discussed in Section 5.1, and it is customary to indicate it $\Sigma(\rho, T)$. There are three main points which distinguish the phase diagram of mean-field glasses and in which Σ plays an important role.

- The *dynamical transition* (also known as *clustering transition*) signals the appearance of an exponential number of glassy states. It occurs in correspondence of a given density ρ_d (or temperature T_d), beyond which the dynamics is arrested while the thermodynamic quantities are analytic. This point is identified with the dynamical transition predicted by Mode-Coupling Theory. Remarkably the dynamics of systems approaching ρ_d has a two-step relaxation.

- A *Kauzmann* transition is the "true" thermodynamical glass transition, where the compressibility or the specific heat have a jump. The transition is second order from the thermodynamic point of view. Beyond ρ_K the system is frozen in a sub-exponential number of amorphous states.

- For a system of hard spheres the (random) close packing point defines the highest possible

density that can be reached in the limit of infinite pressure. Higher densities are not allowed. In the case of soft potentials it coincides with the *jamming transition* ρ_J at $T = 0$ where the energy increases continuously from zero. For $\rho > \rho_J$ the particles are not able to arrange in the volume without overlapping and consequently the ground state has a positive energy [113].

In the interval $\rho \in [\rho_d, \rho_K]$ the complexity is positive. For $\rho < \rho_d$ it jumps to zero in a discontinuous way, while at ρ_K is vanishes continuously remaining zero for $\rho > \rho_K$.

Interestingly, all these transitions, as well as the configurational entropy $\Sigma(\rho, T)$, are the same outlined in Chapter 2 and thus have an analogue in the study of constraint satisfaction problems. The density of particles plays the role of the density of constrains and the complexity takes the same meaning. Then, the dynamical transition α_d, the condensation transition α_c and the SAT/UNSAT transition α_s of CSPs are the counterparts of ρ_d, ρ_K and ρ_J, as they describe the same physical phenomena. This picture, on the analogy between CSPs and glasses, is the further result which followed the initial observations on the similarities between spin-glasses and supercooled liquids obtained by RFOT theory.

5.2.2 Quantum glassy systems: first-order phase transitions

The extension of RFOT theory to quantum systems has been initiated by studying different quantum versions of fully connected p-spin glasses [11, 12, 74, 13]. Quantization of the models was carried out by introducing a transverse field [11, 12] or by considering the spherical spins as the coordinate of a particle moving in a N dimensional space and then by introducing the momentum with appropriate commutation relations [74, 13]. The models were studied via imaginary time path integral and replica method, or by a TAP approach extended to the quantum case. In all the cases considered in [12, 74, 13], where classically the model undergoes a RFOT transition, it was found that the system displays a second to first-order phase transition at low temperature T as a function of the quantum parameter Γ. Along the first-order phase transition the linear susceptibility has a jump and there is latent heat. These studies highlight the strict connection between the thermodynamical properties of CSPs introduced in Chapter 1 and structural glasses. Indeed the phase diagrams found in [12, 74, 13] and in the quantum REM or in XORSAT on a regular random graph are very similar (see Figs. 1.3 and 4.1). The strong similarities shared by the p-spin model and k-XORSAT can be understood because the latter is the dilute version (finite connectivity) of the fully connected p-spin model. However, the picture provided by these studies is not complete, since all the models are in the glass phase at low enough T in absence of the quantum term; in other words, none of these models display, in the classical limit $\Gamma = 0$, a glass transition at low temperature as a function of another control parameter (e.g. the density). The possibility of studying the glass transition at low T as a function of ρ adds an important ingredient to the discussion, which is entropy. In fact, the models studied in [11, 12, 74, 13, 59, 114, 35] have a non-extensively degenerate ground state, hence their entropy at $T = 0$ vanishes. Conversely, lattice glass models might have a finite entropy even at $T = 0$ (think for instance to hard spheres [112]) and in this case the glass transition is completely driven by entropy. In Chapter 3 we presented a preliminary attempt to take into account the role of entropy in this class of problems with a toy model. We showed that due to the interplay of classical entropy and quantum fluctuations, the latter may induce the formation of a glass: from a liquid phase at $\Gamma = 0$ the system can fall in a glassy situation as soon as $\Gamma > 0$.

A crucial aspect concerning the properties of classical glassy systems is their slow dynamics. From the perspective of quantum systems this issue has been first addressed in [115], thanks to a Schwinger-Keldish formalism which enables the study of the real time dynamics. We will comment more on this

in Section 8.2, however for the moment let us anticipate that in [115] it was shown that a quantum p-spin model displays the same slow dynamics and the two-step relaxation as the classical counterpart. Thus, quantum fluctuations, at least for some region in phase diagram, do not destroy glassiness. Interestingly enough, very recently [116] a thoughtful study on quantum particles interacting via a Lennard-Jones potential suggested that quantum fluctuations could promote the glass transition, analogously to what we found in the random subcube model. Differently from the p-spin interaction this model retains entropic effects also at low temperature. In order to study this problem it was developed a suitable scheme to extend the results of mode coupling theory to quantum systems. The glass transition was then identified dynamically, as the point where the relaxation time diverges. A similar phenomenon where quantum fluctuations favor the formation of the glass phase has been shown very recently in an analytical study based on the replica method on quantum particles with Lennard-Jones interactions [117]. Within this scheme the complexity is accessible and it turns out that the Kauzmann transition at fixed density occurs at higher temperature in the quantum case with respect to the classical model. However in both works [116] and [117] the techniques used did not allow to include exchange effects, so that the interplay with the superfluid phase could not be investigated.

5.2.3   Superglass phases

A very interesting point that remains open is the possibility that a glass could display superfluidity. The studies presented in the previous Section either do not take into account the exchange of particles or they consider a quantum term which is not responsible for superfluidity (like a transverse field). Moreover the low temperature transition between the glass phase and the quantum paramagnetic phase is of first order. This led to argue that the "quantum" and the "glass" regime are well distinguished and do not interplay cooperatively. On the contrary, the simultaneous presence of amorphous order together with off-diagonal long range order would lead to a particular supersolid phase called "superglass". From the experimental side the understanding of this issue is of prominent importance, being one of the proposals for the explanations of some experiences with disordered samples of ^{4}He. As discussed in Section 5.1 the experimental results obtained by Ritner and Reppy [22, 106] raised the question on the role of impurities in the superfluid behavior of solid ^{4}He samples and whether disorder could help it or not. The natural and still open question is why freezing in an amorphous density profile should enhance superfluidity compared to the crystalline case, which instead is thought to show zero or very small condensate fractions [118, 119].

The existence of a superglass phase has by now only been shown numerically [25] or analytically in [23]. The model considered in [23] consists of bosonic particles interacting via a short-range potential in three dimensions. The approach is based on a mapping between quantum Hamiltonians and (classical) Fokker-Planck operators which allows to fully characterize the ground state wavefunction and to obtain time-dependent correlations from the analysis of the stochastic dynamics of a classical equilibrium system. In this way they found a model with a glassy order and a small but strictly non-zero superfluid density fraction. In [25] a system of ^{4}He was simulated by imaginary time Path Integral Monte Carlo method (PIMC) for two representative densities, $\rho = 0.0292$ Å^{-3} and $\rho = 0.0359$ Å^{-3}. They initialized the simulation with two different initial conditions, one corresponding to a *hcp* crystal and one highly disordered which was afterwards quenched down in temperature. It turned out that the one-body density matrix $n(\mathbf{r}', \mathbf{r}) = \langle \psi^\dagger(\mathbf{r}')\psi(\mathbf{r}) \rangle$ decays exponentially with the distance $|\mathbf{r}' - \mathbf{r}|$ for the crystalline configuration (see Fig. 5.7), while it remains finite for the amorphous state, which they called "superglass". In Chapter 7 we will comment more on these results.
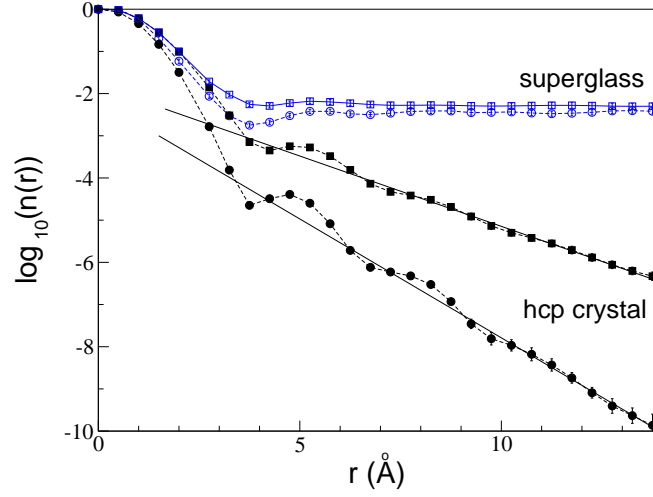
Figure 5.7: Single particle density matrix $n(r)$ for the glass (open symbols) and the crystal (filled symbols) at the same densities and temperature. $n(r)$ is the spherical average of $n(\mathbf{r}', \mathbf{r}) = \langle \psi^\dagger(\mathbf{r}' + \mathbf{r})\psi(\mathbf{r}') \rangle$ where $\psi(\mathbf{r})$ is the annihilation operator. The glass exhibits off-diagonal long range order. Picture from [25].

Clearly it is very hard to to study the quantum glass phase. The phase is in fact metastable with respect to the crystalline order, and this can represent a problem also for a classical study. However the analysis of the dynamics is much more complex in the quantum case. In a classical system, for instance, one can quite easily simulate the physical dynamics of the system by solving Newton's equations of motion [120]. In contrast, the real-time dynamics of quantum systems is very often not accessible numerically, because of the sign problem for instance, and calculating properties involving glassy quantum system is problematic.

We conclude by mentioning that other examples of superglass phases have been found in systems displaying a standard second order spin-glass transition [110, 24, 26]. However, the physics of RFOT is quite different from that of a second order spin-glass transition, therefore the extension of these results to the RFOT scenario is not straightforward.

6

Quantum glasses on the Bethe lattice

In this Chapter we study a bosonic quantum version of a lattice model (the Biroli-Mézard lattice glass model [36]) whose classical counterpart captures the physics of structural glasses. The aim is to examine the effect of quantum fluctuations in the system. In particular we are interested in the interplay between quantum effects and the amorphous order developed in the glass phase, and with the large degeneracy of states that in the classical limit leads to a finite entropy at $T = 0$. We compute the phase diagram of the system to find the liquid-glass transition line, and we investigate if a superglass phase is present. We do this by means of the quantum cavity method, whose treatment for the particular problem is reported in Appendix A. We find a complex phase diagram at low temperature, characterized by two phenomena: (i) A re-entrance of the glass transition line towards lower density on increasing quantum fluctuations, driven by entropy; (ii) A first-order phase transition between superfluid and glass at zero temperature. Our results suggest that a true superglass phase is not present in the model, but we find a phase coexistence between superfluid and glass, which might have interesting phenomenological consequences.

The Chapter is divided as follows. In Section 6.1 we introduce the classical model. We discuss the RS and the 1RSB solutions and the phase diagram that emerges. In Section 6.2 we generalize the model as a quantum many-body system. Then we present the main results for the quantum system, discussing in different subsections the order parameters of the different phases, some details of the cavity computations and the main results on the phase diagram of the model. Finally we investigate the quantum dynamics of the model in imaginary-time: we show that approaching the glass phase the quantum dynamics becomes slower and slower and the density correlations do not relax. Finally, in Section 6.3 we summarize our results.

6.1 The classical model

The classical model considered in the following is a generalization of a lattice glass model proposed in [36, 121] and widely used as a prototype for the description of particle systems undergoing a glass transition. Its degrees of freedom are occupation numbers $n_i = \{0, 1\}$ of the sites $i = 1, \ldots, N$ of a graph, a particle being present on site i if and only if $n_i = 1$. If a site i is occupied it feels a repulsive interaction with the particles on the neighboring sites of the graph, the set of which shall be denoted

∂i. More precisely, each particle can have at most ℓ neighbors without any energy cost and it is subject to an interaction $V > 0$ for every neighboring particle in excess. The Hamiltonian describing this interaction is the following:

$$H = V \sum_i n_i \, q_i \, \theta(q_i) - \mu \sum_i n_i \ , \tag{6.1}$$

where $q_i = \sum_{j \in \partial i} n_j - \ell$ is the number of neighbors "in excess". Here and in the following $\theta(x) = 0$ if $x < 0$ and $\theta(x) = 1$ if $x \geq 0$. We included in H the chemical potential μ conjugated to the total particle number. The original model of [36, 121] corresponds to the case $V \to \infty$; configurations where one particle has more than ℓ neighboring sites occupied are then strictly forbidden. This finite V version will be more convenient for the quantum generalization described later on.

The model above can be defined on any finite graph. Its finite dimensional version has been studied numerically by Monte Carlo simulations in [36, 122, 123], demonstrating that it exhibits the phenomenology of glassy systems. Note that there is no quenched disorder in the Hamiltonian; as in real liquids the disorder and frustration that yield an amorphous glassy order are in fact self-generated by the different possible arrangements of particles. In order to obtain analytical results we will study the model on the Bethe lattice through the cavity method, similarly to [36, 121].

For completeness let us give here the definition and the relations between thermodynamic observables, i.e. the partition sum at temperature $T = 1/\beta$, $Z(\beta, \mu) = \sum_{\{n\}} e^{-\beta H(\{n\})} = e^{-\beta N f(\mu, \beta)}$, the Gibbs-Boltzmann distribution $\mu(\{n\}) = e^{-\beta H(\{n\})}/Z(\beta, \mu)$, the free energy per particle $f(\mu, \beta) = e - \mu \rho - Ts$, where $e = V \partial_V f$, $s = -\partial_T f$, $\rho = -\partial_\mu f$ are respectively the average energy and entropy per particle, and the density.

6.1.1   The liquid phase: RS solution

We now proceed to discuss the cavity method at the replica symmetric (RS) level, extending the derivation of [121] to the soft (finite V) model. The derivation of the RS cavity equations (see Chapter 2) can start by considering the solution of the model on a finite tree (a slightly different method will be used in Appendix A). As represented pictorially in Fig. 6.1, trees admit naturally a recursive description. Consider the sites $1, \ldots, k$ in absence of their common neighbor 0 (they become so-called "cavity sites"). Because of the tree structure the Gibbs-Boltzmann probability distribution factorizes over the k-subtrees rooted at $1, \ldots, k$. Each "cavity site" i can be found in three different states: *empty* if $n_i = 0$, *saturated* if $n_i = 1$ and if the number of occupied neighbors *above* it (which is k at most) is $\geq \ell$ and *unsaturated* if $n_i = 1$ and if the number of neighboring particles above is $< \ell$. We shall denote $\{\psi_i^e, \psi_i^u, \psi_i^s\}$ the respective probabilities of these three states with respect to the Gibbs-Boltzmann measure. Thanks to the factorization properties of trees one can obtain recursion relations between these cavity probabilities [78, 121]:

$$
\begin{aligned}
\psi_0^e &= \frac{1}{z_{\text{iter}}} \\
\psi_0^u &= \frac{e^{\beta \mu}}{z_{\text{iter}}} \left(\prod_{i=1}^k \psi_i^e \right) \sum_{j=0}^{\ell-1} \sum_{1 \leq i_1 < \cdots < i_j \leq k} \prod_{p=1}^j \frac{\psi_{i_p}^u + \psi_{i_p}^s \, e^{-\beta V}}{\psi_{i_p}^e} \\
\psi_0^s &= \frac{e^{\beta \mu}}{z_{\text{iter}}} \left(\prod_{i=1}^k \psi_i^e \right) \sum_{j=\ell}^k e^{(\ell-j)\beta V} \sum_{1 \leq i_1 < \cdots < i_j \leq k} \prod_{p=1}^j \frac{\psi_{i_p}^u + \psi_{i_p}^s \, e^{-\beta V}}{\psi_{i_p}^e}
\end{aligned}
\tag{6.2}
$$

where z_{iter} is a normalization constant ensuring $\psi_0^e + \psi_0^u + \psi_0^s = 1$. Note that the $j = 0$ term in the sum in the second line of the above equation (which is the only one for $\ell = 1$) should be interpreted
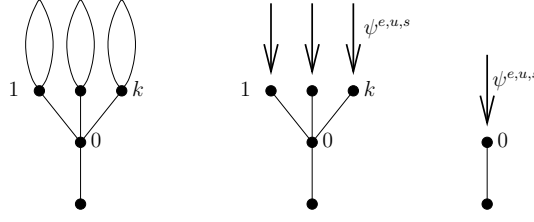
Figure 6.1: Illustration of a cavity iteration for the classical system. The sites $1, \cdots, k$ are described, in absence of site 0, by cavity fields $\psi_l^{e,u,s}$, $l = 1, \cdots, k$. Integrating out these sites leads to the expression of $\psi_0^{e,u,s}$ in Eq. (6.2).

formally as giving a contribution equal to 1. Deep inside a very large regular tree, for an homogeneous liquid phase, the cavity probabilities converge to the fixed-point solution of Eq. (6.2),

$$\psi^e = \frac{1}{z_{\text{iter}}}$$

$$\psi^u = \frac{e^{\beta\mu}}{z_{\text{iter}}} \sum_{i=0}^{\ell-1} \binom{k}{i} (\psi^e)^{k-i} (\psi^u + \psi^s e^{-\beta V})^i$$

$$\psi^s = \frac{e^{\beta\mu}}{z_{\text{iter}}} \sum_{i=\ell}^{k} \binom{k}{i} (\psi^e)^{k-i} (\psi^u + \psi^s e^{-\beta V})^i e^{(\ell-i)\beta V} \ .$$

(6.3)

The solution of Eq. (6.3) can be easily found numerically for any choice of the parameters β, μ, V. The recursive equations written above were strictly valid for trees. The local tree-like character of random graphs allows however, under the correlation decay hypothesis of the RS cavity method, to apply these results to the thermodynamic limit of Bethe lattices. One finds in particular for the free energy density [78, 121]:

$$f = \Delta f_{\text{site}} - \frac{c}{2} \Delta f_{\text{link}} = -\frac{1}{\beta} \log z_{\text{site}} + \frac{c}{2\beta} \log z_{\text{link}}$$

(6.4)

with

$$z_{\text{link}} = (\psi^e)^2 + 2\psi^e\psi^u + (\psi^u)^2 + 2\psi^e\psi^s + 2\psi^s\psi^u e^{-\beta V} + (\psi^s)^2 e^{-2\beta V} \ ,$$

$$z_{\text{site}} = 1 + e^{\beta\mu} \left[\sum_{i=0}^{\ell-1} \binom{k+1}{i} (\psi^e)^{k+1-i} (\psi^u + \psi^s e^{-\beta V})^i + \sum_{i=\ell}^{k+1} \binom{k+1}{i} (\psi^e)^{k+1-i} (\psi^u + \psi^s e^{-\beta V})^i e^{(\ell-i)\beta V} \right] \ .$$

(6.5)

Equations (6.4) and (6.5) express the Bethe free energy, that we introduced in Chapter 2 with the generic equation (2.7), for this particular model. All thermodynamic observables can then be obtained from Eq. (6.4) by derivation with respect to the parameters β, μ, V. Actually only their explicit dependence has to be derived, the order parameter equations (6.3) being stationary point conditions of f with respect to $\psi^{e,u,s}$.

The replica symmetric solution provides the natural description for the homogeneous, liquid (or paramagnetic) phase where all correlations are short ranged. However, the correctness of the RS ansatz breaks down when one approaches the glass phase, where the system develops amorphous density profiles and long range correlations. In this model this happens at low enough temperature, when the competition between the chemical potential μ and the interaction energy V is the strongest. One

evidence for the inconsistency of the RS assumption is the fact that the associated entropy becomes negative in this region of parameters, which is impossible for a discrete model. Another criterion for the incorrectness of the RS ansatz is the divergence of the so-called "spin-glass" susceptibility, defined as $\chi_{\mathrm{SG}}(\beta, \mu) = N^{-1} \sum_{i,j} \langle n_i n_j \rangle_c^2$. For all parameters we investigated we found no divergence of the susceptibility. This means that the resolution of the *entropy crisis* requires a phase transition which has to be discontinuous since it is not associated to a diverging susceptibility. This scenario is typical for models displaying *1 step replica symmetry breaking* (1RSB) [121].

6.1.2   The glass phase: 1RSB solution

As we discussed in Chapter 2 in the 1RSB description one partitions the Gibbs measure characterizing the model in many pure states, identified by an index α, each of them having free-energy f_α and assumes that these states are exponentially numerous $\mathcal{N}(f) \sim e^{N\Sigma(f)}$.

We call $\eta = \{\psi^e, \psi^u, \psi^s\}$ the set of the (normalized) fields that appear in Eq. (6.2) and $\mathcal{P}(\eta)$ their joint probability distribution. Eq. (6.2) defines a map $\eta_0 = \bar{\eta}(\eta_1, \cdots, \eta_k)$ that allows to construct a new field from a set of k fields. Using this map, the 1RSB equation reads:

$$\mathcal{P}(\eta) = \frac{1}{\mathcal{Z}} \int \prod_{i=1}^{k} d\eta_i \, \mathcal{P}(\eta_i) \, \delta(\eta - \bar{\eta}(\eta_1, ..., \eta_k)) \, z_{\mathrm{iter}}(\eta_1, ..., \eta_k)^m \, , \qquad (6.6)$$

where $\mathcal{Z}$ is the normalization constant and $z_{\mathrm{iter}} = \exp(-\beta \Delta f_{\mathrm{iter}})$, similarly to what we discussed in Chapter 2. Moreover the quantities defined by the equations (2.15) and (2.16), that enter in the definition of $\phi(m)$, Eq. (2.14), for this model are given by:

$$z_{\mathrm{site}}(\eta_1 \cdots \eta_{k+1}) = 1 + e^{\beta\mu} \left(\prod_{i=1}^{k+1} \psi_i^e \right) \left(\sum_{j=0}^{\ell-1} \sum_{1 \leq i_1 < \cdots < i_j \leq k+1} \prod_{p=1}^{j} \frac{\psi_{i_p}^u + \psi_{i_p}^s \, e^{-\beta V}}{\psi_{i_p}^e} \right.$$
$$\left. + \sum_{j=\ell}^{k+1} e^{(\ell-j)\beta V} \sum_{1 \leq i_1 < \cdots < i_j \leq k+1} \prod_{p=1}^{j} \frac{\psi_{i_p}^u + \psi_{i_p}^s \, e^{-\beta V}}{\psi_{i_p}^e} \right) ,$$
$$z_{\mathrm{link}}(\eta_1, \eta_2) = \psi_1^e \psi_2^e + \psi_1^e \psi_2^u + \psi_1^u \psi_2^e + \psi_1^u \psi_2^u + \psi_1^e \psi_2^s + \psi_1^s \psi_2^e + \psi_1^u \psi_2^s e^{-\beta V} + \psi_1^s \psi_2^u e^{-\beta V} + \psi_1^s \psi_2^s e^{-2\beta V} \, .$$
$$(6.7)$$

Depending on the value of the external parameters β, μ, V and m the three situations already outlined several times can occur: (i) the RS solution $\mathcal{P}(\eta) = \delta(\eta - \eta^{RS})$, (ii) the d-1RSB solution with $\mathcal{P}(\eta)$ non trivial, $m = 1$ and $\Sigma > 0$, (iii) the c-1RSB solution with $\mathcal{P}(\eta)$ not trivial, $m < 1$ and $\Sigma = 0$.

The RSB equations (6.6) can be solved through the population dynamics method [78], as explained in Section 2.1.3. As we discussed, in order to get an accurate solution of the 1RSB equations by the iteration of the population dynamics algorithm, the inverse participation ratio (IPR) should be maintained as close as possible to one. We observed that the implementation of the population dynamics method with the definition of the fields given in Eqs. (6.2) leads to very small values of the IPR (this can be traced back to the presence of the factor $e^{\beta\mu}$ which takes very high values for the relevant values of the parameter). It turns out that a redefinition of the fields allows to bypass this problem. We found much larger values of the IPR using:

$$\phi_i^e = \frac{1}{z'_{\mathrm{iter}}} \psi_i^e \qquad \phi_i^u = \frac{e^{-\beta\mu r_u}}{z'_{\mathrm{iter}}} \psi_i^u \qquad \phi_i^s = \frac{e^{-\beta\mu r_s}}{z'_{\mathrm{iter}}} \psi_i^s \, , \qquad (6.8)$$

where r_u and r_s are two a priori arbitrary parameters (a good choice for the case $c = 3$, $\ell = 1$ was $r_u = 1/5$ and $r_s = 2/5$). In terms of the transformed fields, the local self consistent equations (given

here only for $\ell = 1$ for simplicity) become:

$$\phi_0^e = \frac{1}{z_{\text{iter}}'} \prod_{i=1}^{k} \left(\phi_i^e + \phi_i^u e^{\beta\mu r_u} + \phi_i^s e^{\beta\mu r_s} \right)$$

$$\phi_0^u = \frac{e^{\beta\mu(1-r_u)}}{z_{\text{iter}}'} \prod_{i=1}^{k} \phi_i^e$$

$$\phi_0^s = \frac{e^{\beta\mu(1-r_s)}}{z_{\text{iter}}'} \prod_{i=1}^{k} \phi_i^e \sum_{j=1}^{k} e^{(1-j)\beta V} \sum_{1 \le i_1 < \cdots < i_j \le k} \prod_{p=1}^{j} \frac{\phi_{i_p}^u e^{\beta\mu r_u} + \phi_{i_p}^s e^{-\beta V + \beta\mu r_s}}{\phi_{i_p}^e}$$

$$= \frac{e^{\beta\mu(1-r_s)}}{z_{\text{iter}}'} e^{\beta V} \left(\prod_{i=1}^{k} \left(\phi_i^e + e^{-\beta V}(\phi_i^u e^{\beta\mu r_u} + \phi_i^s e^{-\beta V + \beta\mu r_s}) \right) - \prod_{i=1}^{k} \phi_i^e \right) .$$

(6.9)

Of course analogous transformations take place in the expression of z_{site} and z_{link} given in Eq. (6.7). This change of parameters was particularly important in the quantum case discussed below where the population sizes are much more limited by computational costs.

6.1.3 Thermodynamics of the classical model

In Fig. 6.2 we report the phase diagram for the classical model with $c = 3$ and $\ell = 1$, as a function of density and of temperature (in units of V). The two lines denote the dynamic and Kauzmann transitions, below which the system is found in the glass phase. Increasing the density from a low value, for a fixed low enough temperature, the system encounters first the dynamic transition and then the Kauzmann transition towards the condensed glass phase. However if one keeps increasing the density the system returns to a liquid phase; this is because if the chemical potential is large enough ($\mu \gg V$), almost all sites will be occupied leaving only a small fraction of "holes". The system of holes has a short range interaction similar to the original one (i.e. for particles) and is therefore liquid when the density of holes is small enough, while it becomes glassy when the density of holes is large enough. The "hole glass" transition which is approached from higher density is therefore due to the fact that we introduced a finite repulsion V which can be overcome by a large enough μ, and it is qualitatively equivalent to the transition which takes place at lower densities. A very similar phase diagram has been found in the study of a realistic model for colloidal systems [124], which confirms the validity of the Biroli-Mézard model to describe the physics of structural glasses.

The thermodynamics of the system inside the glass phase has to be computed exploiting the 1RSB formalism. Fig. 6.3 shows in blue the density as a function of the chemical potential at $\beta = 8$ and $\beta = 30$, both in the liquid and in the glass phase. The red dashed line represents the RS solution within the glass region, which clearly differs from the true 1RSB solution. For the same two temperatures the behavior of the parameter m^* as a function of the density is shown in Fig. 6.3. It differs from one only inside the condensed glass phase, after the Kauzmann transition. It decreases fast going deeper into the glass phase, down to a value proportional to the temperature. Note that the model presents a glass transition also at zero temperature, as a function of the density, with $\rho_d = 0.5708$ and $\rho_K = 0.5725$ on the "particle" side [121, 125]. This is of particular interest in view of the extension of the model to the quantum case.

In the limit of zero temperature the parameter m^* approaches zero at a finite density $\rho_J = 0.57574$ [121, 125]. Below this value of density, the average energy is zero, while above this value it becomes non-zero (the system is so dense that it is unable to satisfy the constraint that each particle has less or equal than ℓ neighbors). This point corresponds to the "random close packing" or "J-point" in the
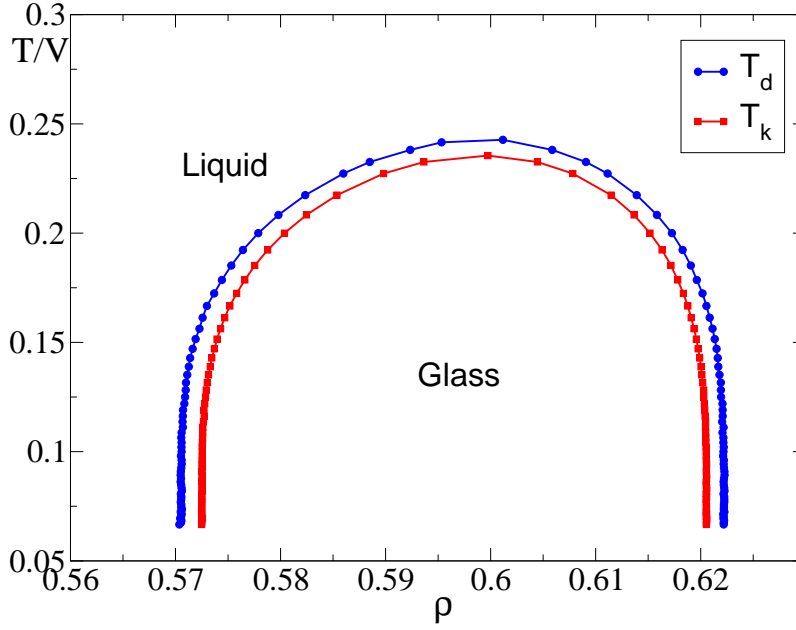
Figure 6.2: Classical phase diagram in the (ρ, T) plane for $c = 3$ and $\ell = 1$. The dynamical (T_d) and Kauzmann (T_K) temperatures are plotted as a function of the density. See Ref. [124] for a study of a realistic model that displays a similar phase diagram.
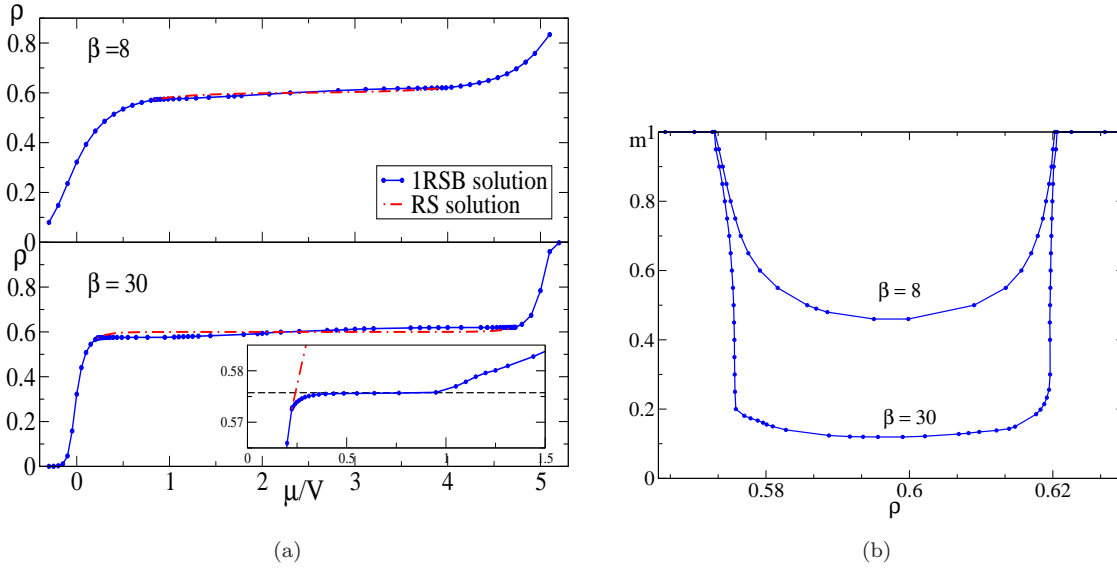
Figure 6.3: *Left panel*: Average density as a function of the chemical potential, at $\beta = 8$ (upper panel) and $\beta = 30$ (lower panel). The inset shows a zoom of the $\beta = 30$ data around the Kauzmann transition. *Right panel*: Behavior of the parameter m^* as a function of the density at $\beta = 8$ and $\beta = 30$.

literature on hard spheres in the continuum, that we introduced in Section 5.2 (see e.g. [112] for a review and a list of relevant references). This is seen in more detail in the inset of Fig. 6.3 which reports data for $\beta = 30$ that are very close to the zero temperature limit: above the glass transition ρ_K, the density in the 1RSB solution increases slower than in the RS solution and reaches a plateau at the value $\rho_J = 0.57574$ for $\mu < V = 1$. Only when $\mu > V = 1$ the constraints are violated at zero temperature and the density can increase above ρ_J. The latter is marked by the horizontal dashed line in the figure.

One can recognize that the glass transition of the original model proposed in [36, 121] is recovered here as the zero temperature limit of the glass transition, and it is here reached in the "SAT" (namely zero energy) phase. It corresponds indeed, to the limit $\beta V \to \infty$ for a suitable and finite value of $\beta\mu$. On the other hand, in that context, the presence of a "hole" glass transition is excluded a priori by the definition of the model, which does not allow configurations violating the energy constraint.

6.2 The quantum model

The quantum version of the model is obtained by adding to its classical potential energy a kinetic term allowing hoppings of particles between neighboring sites. Since the classical energy forbids configurations with more than one particle per site, we are in fact dealing with interacting hard-core bosons. The Hamiltonian is now an operator acting on the Hilbert space spanned by the 2^N classical configurations of the occupation numbers. The potential energy is diagonal in this basis. Denoting J the intensity of the quantum tunneling between neighboring sites one obtains the following Hamiltonian:

$$\hat{H} = -J \sum_{\langle i,j \rangle} (\hat{a}_i^\dagger \hat{a}_j + \hat{a}_j^\dagger \hat{a}_i) + V \sum_i \hat{n}_i \, \hat{q}_i \, \theta(\hat{q}_i) - \mu \sum_i \hat{n}_i \ , \qquad (6.10)$$

where the first sum runs over the pairs of adjacent sites, $\hat{a}_i^\dagger$ and $\hat{a}_i$ are standard hard-core bosonic creation and annihilation operators on site i, $\hat{n}_i = \hat{a}_i^\dagger \hat{a}_i$ and $\hat{q}_i = \sum_{j \in \partial i} \hat{n}_j - \ell$. A thermodynamic study of the model then amounts to the computation of the quantum partition function $Z = \text{Tr}\left[e^{-\beta\hat{H}}\right]$ and of the average value of the observables $\hat{O}$ defined as $\langle \hat{O} \rangle = \text{Tr}\left[e^{-\beta\hat{H}}\hat{O}\right]/Z$.

As in the classical case we consider the model on the Bethe lattice and we solve it through the quantum cavity method that was outlined in Chapter 2. The particular equations for this model are instead reported in the Appendix A. We remark, that differently from the discussion of Section 2.2 that deals with quantum spins in a transverse field, here, the case of hopping particles needs a more sophisticated treatment, explained in Appendix A.

The system investigated here presents a rich phase diagram, which emerges from the classical case discussed in Section 6.1 when the additional effect of the hopping is taken into account. In the following we first discuss the finite temperature phase diagram, which is directly accessible to our method, and then we argue on how it extrapolates to the zero temperature limit.

Note that the hopping amplitude J/V controls the strength of quantum fluctuations. As we showed in the previous sections, for the classical problem where $J = 0$, the thermodynamic glass phase is delimited by the curve $T_K(\rho)$ of Fig. 6.2 (while the dynamical glass is delimited by $T_d(\rho)$) in the temperature-density plane, similarly to what happens for more realistic models of structural glasses [124]. One can then imagine to approach the glass phase from higher or lower densities. As we discussed in section 6.1.3, the two transitions are qualitatively equivalent and in the following we will focus on the region of the phase diagram corresponding to small densities. From a physical point of view, this side of the glass transition is the most interesting one, since it corresponds to a packing

problem, which we have relaxed through the soft constraint V. From now on we will focus on the model defined by $c = 3$ and $\ell = 1$. As before we will measure energies in units of V throughout this section, leaving it implicit in the text (but not in the figures).

6.2.1   Order parameters: definitions

Edwards-Anderson parameter

As we already discussed for the classical case, a fingerprint of the glass transition is the appearance of a local inhomogeneous density profile, signaling the breaking of translation invariance. If one considers the Gibbs measure over imaginary-time paths which is constructed by the Suzuki-Trotter decomposition, the transition that separates the liquid phase from the glass is of the same kind of the one described in Section 6.1.2 for the classical system.

As in Section 6.1.2, we can label the different glass states by an index α; each state has free energy f_α and we can perform the same construction as in Section 6.1.2 to compute the complexity for the Gibbs measure on imaginary-time paths. We denote by $\langle \hat{O} \rangle_\alpha$ the average of an observable $\hat{O}$ in the restriction of the Gibbs measure to a given glass state. Inside each glass state one has $\langle \hat{n}_i \rangle_\alpha \neq \frac{1}{N}\sum_i \langle \hat{n}_i \rangle = \rho$, while the average density is the same for each state, $\rho = \frac{1}{N}\sum_i \langle \hat{n}_i \rangle_\alpha$. These density fluctuations are conveniently characterized by the Edwards-Anderson order parameter [110]:

$$q_{EA} = \overline{\frac{1}{N}\sum_i \sum_\alpha W_\alpha [\langle \hat{n}_i \rangle_\alpha - \rho]^2} \,, \tag{6.11}$$

where we take the average over the states according to their weights $W_\alpha \propto \exp(-\beta N f_\alpha)$, and the over bar indicates the average over random graphs. The order parameter q_{EA} jumps to a finite value at the dynamical transition, where the glassy states appear for the first time [126]. This non-zero value of q_{EA} corresponds physically to the long time limit of the density-density correlation function [126], as we will discuss later on. As we already said, the jump of the order parameter is a peculiarity of the glass transition which still remains second order from the point of view of the singularity of the free energy.

Condensate density

In presence of a finite hopping strength, the system might display Bose-Einstein condensation (BEC). This is manifested by a finite expectation value of the bosonic operator $\overline{\langle \hat{a} \rangle} \neq 0$ in the grand-canonical ensemble. However, since the number of particles is conserved by the Hamiltonian and by the cavity equation, in absence of symmetry breaking terms the expectation value $\overline{\langle \hat{a} \rangle}$ is always zero. More precisely, one possibility to define the order parameter of the BEC transition amounts to add a small perturbation to the Hamiltonian that breaks that symmetry $\hat{H}_h = \hat{H} - h\sum_i (\hat{a}_i + \hat{a}_i^\dagger)$ and then send it to zero after the thermodynamic limit is taken

$$\overline{\langle \hat{a} \rangle} = \lim_{h \to 0} \lim_{N \to \infty} \overline{\langle \hat{a} \rangle}_h \,, \tag{6.12}$$

where $\langle \bullet \rangle_h$ denotes the thermodynamic average in presence of the perturbation. Note that this procedure does not present any particular difficulty for the cavity method, that gives direct access to the thermodynamic limit. However, an equivalent and more practical way to allow the symmetry breaking, that we used here, is to initialize the population dynamics algorithm with a fraction of "asymmetric trajectories", i.e. trajectories such that the number of hoppings from a given site i to a given neighbor j is not equal to the hoppings from j to i. In absence of BEC, these trajectories

disappear under the cavity iterations, while in the BEC phase the symmetry breaking is preserved, thus allowing for a non zero value of $\overline{\langle \hat{a} \rangle}$. Indeed in the BEC phase, there are long range exchanges, and "incoming" and "outgoing" currents from a site to a given neighbor do not balance: even if they balance on average, they do not on each individual trajectory of the population. The mathematical reasons for this have been detailed in [83] and we have reported it in Appendix A.

The order parameter $\overline{\langle \hat{a} \rangle}$ defined above also signals the presence of off-diagonal long range order in the system [127]. In a uniform phase such as the liquid phase, one can define the condensate density as [127]:

$$\rho_c = \lim_{|i-j| \to \infty} \overline{\langle \hat{a}_i^\dagger \hat{a}_j \rangle} = \overline{|\langle \hat{a} \rangle|^2} \; . \tag{6.13}$$

If the latter is finite, there is off-diagonal long range order; ρ_c represents the number of bosons that are condensed in the ground state divided by the volume. In a non-uniform phase, one has:

$$\rho_c^\alpha = \frac{1}{N} \sum_i |\langle \hat{a}_i \rangle_\alpha|^2 \tag{6.14}$$

for each glass state, and one can define the average over states and graphs:

$$\rho_c = \overline{\sum_\alpha W_\alpha \rho_c^\alpha} \; . \tag{6.15}$$

6.2.2 Order parameters: results

In the following we give the results and some details of our implementation of the procedure used to solve the cavity equations and to investigate the properties of the different phases. In [128] we reported the details of our computations and the parameters used. Let us note that the RSB calculations turned out to be particularly demanding. As far as possible given our computational resources, the results have been checked to be robust with respect to these parameters by increasing the population sizes in some representative points.

RS calculations: the superfluid-normal liquid transition

In Fig. 6.4 we show the behavior of the order parameter of the superfluid phase, ρ_c/ρ (black circles), as a function of increasing μ (corresponding to increasing density). We observe two different behaviors depending on the hopping strength:

- At high temperature or small hopping (small βJ), we observe that ρ_c/ρ vanishes continuously at some μ_c corresponding to the superfluid transition (upper panel in Fig. 6.4), which is then a second order transition. The density is also continuous at the transition. Close to μ_c, we observe a power-law behavior $\overline{\langle \hat{a} \rangle} \sim |\mu - \mu_c|^{1/2}$, with an exponent $1/2$ typical of the mean field nature of the underlying lattice; correspondingly, the condensate fraction vanishes linearly.

- At low temperature or large hopping (large βJ) we observe that ρ_c/ρ jumps to zero at some value μ_c, indicating that the transition is first order (middle panel in Fig. 6.4). In this case, we observe a small hysteresis when we perform increasing or decreasing μ scans (see the middle panel of Fig. 6.4). As a consequence of the first order phase transition in the μ variables, the density, which is defined as $\rho = -\partial f(\mu)/\partial \mu$, has a jump at μ_c, which implies the existence of a region of phase coexistence for $\rho \in [\rho_-, \rho_+]$ in the canonical ensemble. The determination of μ_c and of ρ_-, ρ_+ can be done in two equivalent ways: either by looking at the grand-canonical free energy as a function of μ (which is directly accessible within the cavity method) and determining
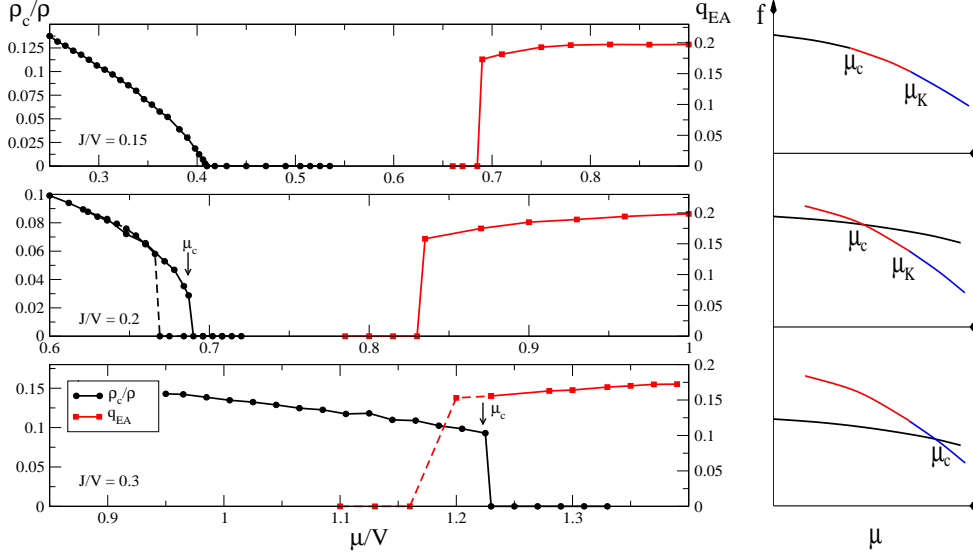
Figure 6.4: *Left panel*: Order parameters of the superfluid (ρ_c/ρ, black circles, left scale, RS cavity method) and glass (q_{EA}, red squares, right scale, 1RSB cavity method) phases for $c = 3$ and $\ell = 1$, for three representative values of the hopping J at the same temperature $\beta V = 15$, as functions of the chemical potential μ. The first order transitions are accompanied by hysteresis; full lines corresponds to following the solution upon increasing μ, dashed lines correspond to decreasing μ. Arrows mark the first order transition points μ_c as determined by the Maxwell construction. See text for a more detailed description. *Right panel*: Sketches of the free energy as a function of μ for the corresponding left panels: from left to right, black lines represent the superfluid, red lines the normal liquid, blue lines the glass; μ_c and μ_K indicate the phase transitions (we do not report data because the jump in the derivative of f at the first order transition is very small and would be invisible in the figure).

the point at which the free energies of the two phases cross, or Legendre transforming the free energy as a canonical function of ρ and then performing the Maxwell construction over it. Since the jump in density is extremely small at the transition, $\rho_+ - \rho_- \ll (\rho_+ + \rho_-)/2$, we found that the Maxwell construction is numerically more precise than looking directly at the slope of the free energy $-\partial f(\mu)/\partial\mu$, which is dominated by the average density.

1RSB calculations: the glass transition

The 1RSB calculation turned out to be very involved. Fig. 6.4 shows the behavior of the order parameter of the glass phase, q_{EA} (red squares), obtained through the 1RSB cavity method, as a function of the chemical potential. In general, we found that μ_K and μ_d are always extremely close to each other, as in the classical case. A precise determination of μ_K can be done by looking at the point where the complexity at $m = 1$ vanishes. On the contrary, the determination of μ_d is much more difficult since it corresponds to the point where the non-trivial 1RSB solution disappears and $q_{EA} = 0$; this is a kind of "spinodal point" and its precise location is very sensible to details of the computation such as population size, initialization, number of iterations, etc. Although we managed to get reliable data for μ_d, in the following we focus only on μ_K, keeping in mind that the two are very close and follow similar trends. Finally, it is worth to note at this point that we did not find any superfluid non-trivial 1RSB solution: we comment on this in more details in the following.

Summary

To summarize, we observed generically three different behaviors upon varying μ, that are summarized in the three panels of Fig. 6.4 (we set $\beta = 15$ in the figure):

1. The upper panel, at small hopping ($J = 0.15$), represents a second-order superfluid-normal liquid phase transition, followed by a liquid-glass transition at higher μ. The system is superfluid until ρ_c vanishes at μ_c, then it is a normal liquid in an interval of μ, until the parameter q_{EA} jumps from zero to a finite value signaling the dynamic glass transition μ_d. Upon further increasing μ, the complexity vanishes at μ_K and the system enters the glass phase, where $m^* < 1$ (note that μ_d and μ_K are indistinguishable on the scale of the figure). Both the transitions are second order in the sense of Ehrenfest classification: the first derivative of the free energy is always continuous and the second derivative is discontinuous at both transition points.

2. The middle panel ($J = 0.2$) shows a first order transition between the superfluid and a normal fluid, followed again by a liquid-glass transition. Here the condensate fraction ρ_c/ρ jumps suddenly to zero at μ_c. In this regime the free energy of the superfluid intersects that of the normal liquid at μ_c with a discontinuity in the first derivative. As in the previous case, the glass transition happens here at a higher value of μ where q_{EA} jumps to a finite value and the free energy of the glass grows smoothly from that of the liquid with continuous first derivative. The figure also shows the hysteresis which is a consequence of the first order transition, when we follow the evolution of the order parameter ρ_c coming from the superfluid phase or from the normal phase.

3. The lower panel, corresponding to a larger hopping $J = 0.3$, shows a direct first order phase transition between the superfluid and the glass phases. Indeed, in this case the free energy of the superfluid crosses directly the free energy of the glass at μ_c. At the transition the condensate fraction jumps to zero while q_{EA} jumps to a non-zero value. Also in this case we observe a phenomenon of hysteresis, and the exact first order transition point has to be determined by the crossing of the RS free energy of the superfluid phase and the 1RSB free energy of the glass phase.

In the next section, we investigate the evolution of these phase boundaries by varying hopping, temperature and chemical potential.

6.2.3   Phase diagram of the quantum model

The quantum cavity method (at least in its present formulation) allows only to access the finite temperature properties of the system. We therefore start the discussion of the phase diagram from finite temperature, and then we discuss how to extrapolate the results to the $T = 0$ limit.

Finite temperature phase diagram

The phase diagram, at finite temperature in the (μ, J) plane is shown in Fig. 6.5.
For any fixed (and low enough) temperature, there is a curve $\mu_c(J)$, or $J_c(\mu)$, which separates a superfluid phase from a normal phase. A tricritical point divides this transition line into two parts. On one side, at small chemical potential, the transition is second order. Beyond the tricritical point instead, the transition becomes first order. This happens at bigger values of μ, close to the glass transition. We chose different colors to represent the phase diagram at different temperatures. Solid
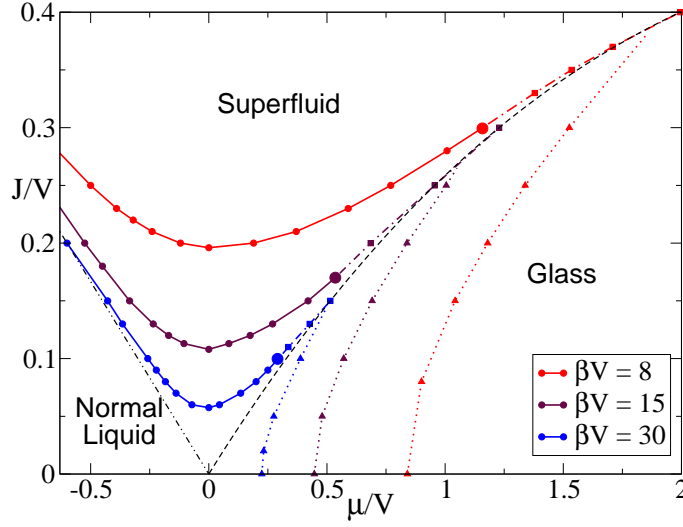
Figure 6.5: Phase diagram for the quantum model in the $(\mu/V, J/V)$ plane, for $c = 3$ and $\ell = 1$, for three different temperatures $\beta V = 8, 15$ and 30. The lines divide the phase diagram into three main regions where the system is found in a glass, superfluid or (normal) liquid phase. Solid lines and circles indicate the second order superfluid transition. The large dots mark the tricritical point where the superfluid line changes from second to first order. Dash-dotted lines and squares represent the first order transition between the superfluid phase and the normal (glass or liquid) phase. Dotted lines and triangles indicate the Kauzmann glass transition $J_K(\mu)$. The dot-dot-dashed black line indicates the normal liquid-superfluid transition for hard core bosons at zero temperature. Since below this line $\rho = 0$ at $T = 0$, the interaction is not relevant around it, so this line is the $T = 0$ limit of the normal liquid-superlfuid transition also for the model investigated here. The dashed black line serves as a guide to the eye: it has been obtained by interpolating the large μ superfluid lines at different temperatures (see text for details).

lines and circles indicate second-order superfluid transitions while their continuations, dash-dotted lines and squares, represent first-order transition between a superfluid phase and a normal liquid or glass phase. The liquid-glass Kauzmann transition, $\mu_K(J)$ or $J_K(\mu)$, is reported using a dotted line and triangles. It hits the horizontal axis, at $J = 0$, in correspondence of the classical glass transition; on the other side, it crosses the first-order superfluid-normal phase transition. The dynamic transition line is very close to the Kauzmann transition so we don't report it for clarity.

We now describe the phase diagram as a function of the density. Since the cavity method works necessarily in the grand-canonical ensemble, we are forced to measure the density at fixed μ. Therefore, the density has some fluctuations due to numerical noise. Unfortunately, for this model the interesting part of the phase diagram is contained in a very small interval of density, and for this reason the noise is important and prevents us to obtain transition lines as clean as in the (J, μ) phase diagram of Fig. 6.5. For this reason, in Fig. 6.6 we report a schematic (J, ρ) phase diagram together with the actual data. We keep the same code of colors and lines as in Fig. 6.5.

The main difference between the (J, μ) and (J, ρ) phase diagrams is that in the latter case, as already discussed, we observe a phase coexistence between the superfluid phase and a normal (liquid or glass) phase. The region of superfluid-glass phase coexistence is particularly interesting since it represents a region which manifests both amorphous order and off-diagonal long range order, even if they are phase
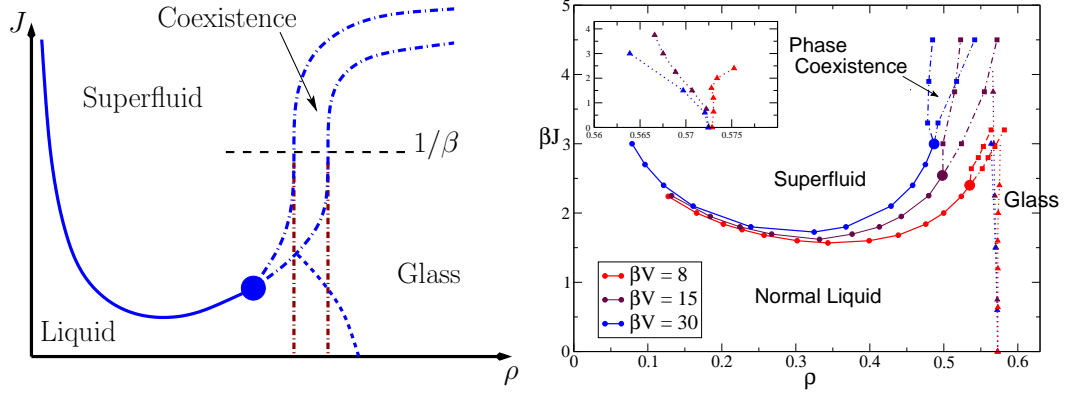
Figure 6.6: *Left panel*: Schematic $(J/V, \rho)$ phase diagram of the model. The full line represents the second order superfluid transition $J_c(\rho)$, separated by a tricritical point (large dot) from a first order superfluid transition accompanied by phase coexistence (dot-dashed lines). The dotted line represents the Kauzmann transition $J_K(\rho)$. In the limit $T \to 0$, the transition lines have distinct behaviors: the first order transition line has $J \gg T$, and it has a finite limit for $T \to 0$. On the contrary, the other lines have $J \propto T$ and they shrink to the $J = 0$ axis for $T \to 0$. Therefore, at $T = 0$ and for $J > 0$, the low-ρ part of the phase diagram contains the superfluid phase while the large-ρ part contains the glass. The red lines indicate the behavior of the superfluid-glass transition at $T = 0$. *Right panel*: Data for the $(\beta J, \rho)$ phase diagram, for $c = 3$ and $\ell = 1$, and for three different temperatures $\beta V = 8, 15$ and 30. The three regions, glass, superfluid and normal liquid phase, are here reported. The transition lines are plotted using the same styles as in Fig. 6.5. As a consequence of the first order phase transition a region of phase coexistence – delimited by dash-dotted lines – is present. The inset shows the re-entrant behavior of the glass transition line, at low enough temperature. We plot βJ on the vertical axis in order to show that the transition lines are proportional to T in the limit $T \to 0$.

separated. Besides the superfluid transition in Fig. 6.6 we reported the glass (Kauzmann) transition (dotted line) which is also expanded in the inset. From the inset it is clear that the glass transition as a function of the "quantum parameter" βJ, has re-entrant behavior. In fact, looking at the $\beta = 30$ or $\beta = 15$ curves, one can note that the system reaches the glass phase at lower densities when we switch on quantum fluctuations. This phenomenon, which at first sight can appear very surprising, has been recently found in a related work, focusing on the description of the quantum glass transition from the point of view of a microscopic theory of the system dynamics [116]. Moreover it has also been found analytically in the random subcubes model, in Section 3.7. In that context the introduction of the transverse field has in fact the effect of promoting the clusters with largest entropy and this induces a rapid condensation phenomenon. Finally, in a similar way it has been shown recently in an analytical study based on the replica method on quantum particles with Lennard-Jones interactions [117] that, at fixed density, the quantum model undergoes the Kauzmann transition at higher temperatures than the classical one. In general, one can imagine that, beyond the details which pertain to this model, this re-entrant behavior might have a more general interpretation, in terms of an order-by-disorder mechanism which is induced by quantum fluctuations and in which a particular order is selected for entropic reasons, as we will argue in the following.

Zero temperature limit

We now give some hand-waving arguments on the behavior of the transition lines for $T \to 0$. Although we don't expect our arguments to be completely convincing, the following is the only consistent scenario we were able to elaborate that is in agreement with the observed behavior of the lines at low temperatures.

The evolution of the phase transition lines in the (μ, J) plane of Fig. 6.5, suggests that in the limit $T \to 0$ both the second order superfluid transition line and the Kauzmann transition line shrink to the origin of the axis. Note that we are not interested in the region $\mu < 0$ since in this region, at $T = 0$, the system has a small density and it behaves very similarly to weakly interacting hard core bosons. Note also that in the classical case $J = 0$, we know that μ_K is proportional to T at low temperature, which is consistent with the shrinking of the line $\mu_K(J)$ to the origin. Therefore, for $T \to 0$ the glass phase "invades" the lower part of the phase diagram in Fig. 6.5, while the superfluid phase "invades" the upper part, and the first order superfluid-glass transition line at $\mu > 0$ extends down to the origin ($J = 0$ and $\mu = 0$).

Unfortunately, our 1RSB code becomes very slow and unstable for too large βJ, preventing us from drawing the superfluid-glass line for $J \gg T$. Still, we observe that the lines at higher temperature seem to be close to the continuation of the lines at lower temperature. This indicates that, as expected, for large enough J and μ, the system has reached its zero temperature limit. At the same time, this allows us to "extrapolate" the first order superfluid-glass transition line at $T = 0$ by taking, at each T, the largest values of J that we can access, and interpolating these values. The result is shown as a black dashed line in Fig. 6.5, and we believe that the extrapolation is a very reliable representation of the $T = 0$ line. Therefore, at strictly zero temperature ($T = 0$) and positive hopping ($J > 0$), the phase diagram contains only a superfluid and a glass phase separated by a first order transition. On the other hand, at strictly zero hopping $J = 0$ and zero temperature, one recovers the classical model of [36], which displays a RFOT between a liquid and a glass (however, one has to rescale μ by the temperature in the classical limit, therefore the transition happens at $\mu = 0$ in Fig. 6.5). Hence, at $T = 0$, the limit of vanishing hopping is extremely singular, the behavior of the quantum model at any $J > 0$ being completely different from that of the classical model at $J = 0$.

It is interesting to understand in more details how this singularity develops in the limit $T \to 0$. Indeed, at large β, the normal liquid phase exists only in a region $0 \leq \mu \lesssim 1/\beta$ and $0 \leq J \lesssim 1/\beta$, see Fig. 6.5. Since both J and μ go to zero with temperature, in this part of the phase diagram V is much larger than any other energy scale and one can consider it as infinite. Then, only the three energy scales J, μ, T remain and the phase diagram must be a function of βJ and $\beta \mu$ only. In the limit $\beta \to \infty$, also this energy scale disappears, and we conclude that at $T = 0$, $J_c(\mu) \propto \mu$, i.e. the superfluid-glass transition line must be linear at small J and μ.

When we eliminate the chemical potential and look to the plane (ρ, J), the scenario described above leads to a phase diagram characterized by two distinct regimes, as shown schematically in the left panel of Fig. 6.6:

- If J remains finite while $T \to 0$ (i.e. if $\beta J \gg 1$), the normal liquid phase disappears. Only the superfluid and glass phase survive, and they are separated by a phase coexistence region, determined by the Maxwell construction, and delimited by lines that reach a finite limit when $T \to 0$. We expect that when $J/V \gtrsim 1$ the system is superfluid at all densities while when $J/V \lesssim 1$ the glass phase appears at large enough densities: therefore the coexistence line must have the shape reported in the schematic plot (left panel) of Fig. 6.6. Although our 1RSB code is unable to access the region $J \sim V \gg T$, we could check that these lines have the expected

behavior at least within the RS approximation, which should be a good approximation at least for not too small temperatures (we don't report these data to avoid confusion in the figures).

- On the contrary, in the interval $J \lesssim 1/\beta$ the system is still sensitive to finite temperature effects, but as we argued above, we expect these effects to depend only on the quantity βJ at fixed ρ, since no other energy scale is relevant here ($J \sim T \ll V$, therefore V is infinite and disappears from the problem). In this regime a normal liquid phase, a second order superfluid transition $J_c(\rho)$ and a glass transition $J_K(\rho)$ still survive, but both critical values of J vanish proportionally to the temperature in the limit $T \to 0$, therefore confining the liquid phase to a smaller and smaller region of the phase diagram which at $T = 0$ reduces to the classical region $J = 0$ alone.

- The phase coexistence boundaries start from the tricritical point, located at $J \propto T$ for $T \to 0$, and they extend into the large J region of the phase diagram where they have a finite limit for $T \to 0$. The only possibility to match the two regimes is that the lines become vertical in the (ρ, J) plane in the region $\beta J \sim 1$; this should be evident from the schematic plot in the left panel of Fig. 6.6. In this way we define the two values of density that delimit the coexistence region at $T = 0$ and small $J > 0$.

Looking at the data at finite temperature in right panel of Fig. 6.6 one sees that the superfluid transition far from the glass satisfies well the scaling with βJ for $\rho \lesssim 0.3$, where the transition remains second order for all values of β. However Fig. 6.6 shows that around densities of the order $\rho \simeq 0.3$ the transition lines do not scale very well. To observe the scaling with βJ one has to go to lower temperatures which are not easily accessed with our method. Still, the phase coexistence lines become almost vertical at large βJ around $\rho \sim 0.5$ which is an estimate of the coexistence density for $T = 0$ and $J \gtrsim 0$, according to the argument above. The glass transition line is strongly re-entrant at the lowest temperature (we recall that for the classical model $\rho_K \simeq 0.5725$), which is consistent with this estimate. This means that in presence of quantum fluctuations a glass can be formed at zero temperature for densities as low as $\rho = 0.5$, where the corresponding classical system is in the liquid phase and quite far from the glass.

The re-entrance of the glass transition line

The re-entrance of the glass transition shown in the inset of Fig. 6.6 is rather unexpected a priori. It shows that if we consider the classical model at a density slightly below the Kauzmann transition, then it is possible to make it condense into a glass phase just by switching on quantum fluctuations, for low enough temperatures. This means that the quantum dynamics induced by the hopping between neighboring sites has a profound effect on the thermodynamical properties of the systems. In fact, the kinetic exchange selects as equilibrium states some states which are no more exponentially numerous, inducing the vanishing of the complexity function. As we mention, we can interpret it with a mechanism similar to that displayed by the random subcubes model, in terms of the entropy of the states (see Section 3.7). Since the re-entrance happens close to the classical glass transition, we can for this discussion consider $V \gg \mu, J, T$, i.e. $V = \infty$ going back to the original hard sphere model of Biroli and Mézard [36]. At low enough temperatures, since $V = \infty$, only zero energy configurations contribute to the measure. Beyond the dynamical transition ρ_d, the states (or "clusters") in which the Gibbs measure splits, are generically characterized by a distribution of internal entropies, encoded in the complexity $\Sigma(s)$, whose generic form for a classical system is that shown in Fig. 6.7. Assuming that when quantum fluctuations are introduced, if J is sufficiently small, the distribution $\Sigma(s)$ is not
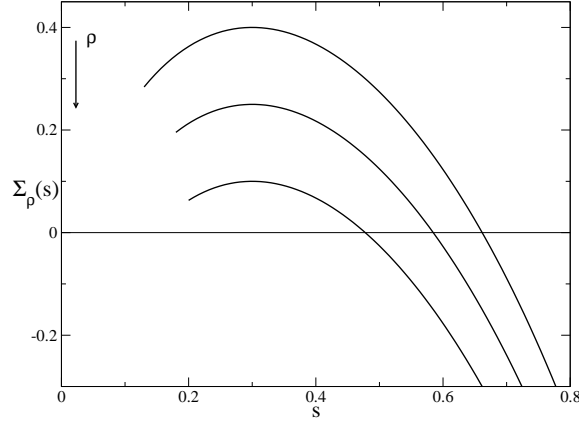
Figure 6.7: A schematic plot of the typical behavior of the complexity as a function of the internal entropy of the states for various densities ρ increasing from top to bottom.

strongly modified, then, the major effect of quantum fluctuations in this regime is rather to induce, for each cluster, a kinetic energy gain proportional to its entropy. This gain comes from the fact that higher entropy clusters are larger, therefore in those clusters particles can delocalize more, allowing to lower the kinetic energy. Conversely, in small entropy clusters, particles are tightly packed and cannot delocalize to lower their kinetic energy. In other words, the entropy of each cluster measures the number of "neighboring" configurations belonging to the state, namely configurations which can be reached one from the other through single particle movements. The shift of the quantum energy, proportional to J times the classical entropy, has an effect on the selection of the equilibrium states: it will favor states with bigger entropy because their energy is lowered more. Since these states are less numerous, increasing the hopping J, one expects that the complexity will be lowered, and a condensation transition will be eventually induced at large enough J. Based on the analogy on the random subcubes, moreover, all these arguments are not modified when besides the entropy, each state is also characterized by a classical energy (i.e. for finite V). A distribution of energies of the states must be included, but this does not change the result, just implying a more complicated temperature dependence.

6.2.4   Imaginary time quantum dynamics

From a classical point of view the dynamics of glassy systems has received a lot of attention and their slow dynamic behavior has been the subject of a vast part of the literature (see e.g. [120, 129]). Since dynamics and thermodynamics are inevitably intertwined in quantum mechanics, the study of time dependent equilibrium correlations is particularly interesting to understand to what extent the phenomenology of glassy quantum systems resembles that of their classical counterpart. In this Section we analyze the local Green function and the local density-density correlation in imaginary time.

Green function and time scales

The Green function is defined, for $-\beta/2 \leq \tau \leq \beta/2$, by

$$G^i(\tau) = \theta(\tau)G^i_>(\tau) + \theta(-\tau)G^i_<(\tau) = \left\langle T\hat{a}_i(\tau)\hat{a}_i^\dagger(0) \right\rangle, \tag{6.16}$$
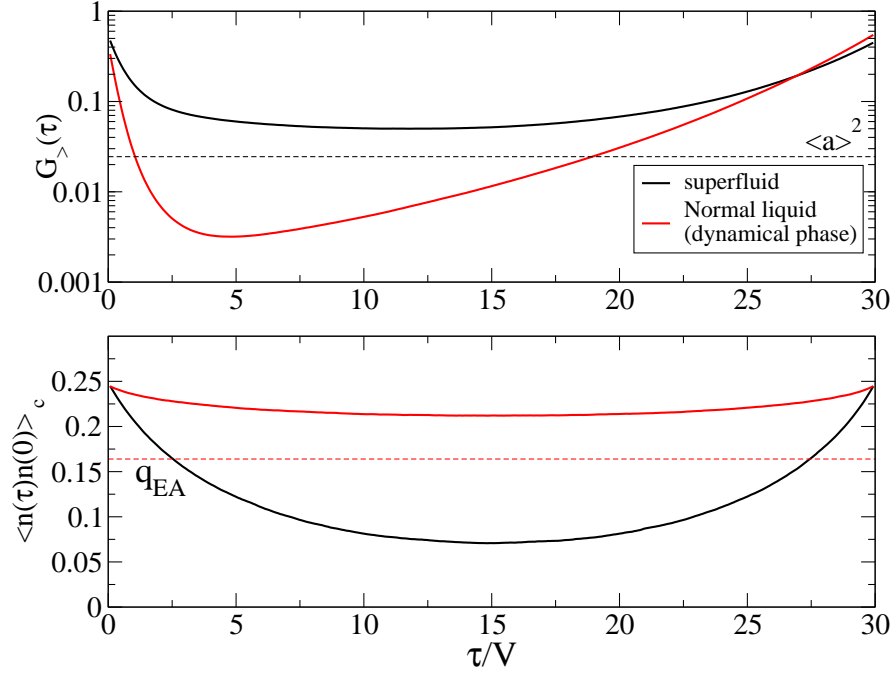
Figure 6.8: Time-dependent correlation functions obtained with the RS cavity method. *Upper panel*: Imaginary time advanced Green function $G_>(\tau)$, for $c = 3$ and $\ell = 1$, at $\beta V = 30$ and $J/V = 0.1$, in the superfluid phase at $\mu/V = 0.275$ and in the liquid phase just before the Kauzmann transition, at $\mu/V = 0.388$. The dotted line indicates the square of the expectation value of the bosonic operator $\langle \hat{a} \rangle^2$ corresponding to the superfluid phase. Note that the Green function $G(\tau)$ is obtained by the periodic image of period β of this function for $\tau \in [-\beta/2, \beta/2]$. *Bottom panel*: Time dependent density-density correlation for the two same regimes. The dotted line indicates the value of the q_{EA} for the normal liquid (obtained with the 1RSB cavity method).

with the advanced and retarded Green functions

$$
\begin{aligned}
G_>^i(\tau) &= \left\langle \hat{a}_i(\tau)\hat{a}_i^\dagger(0) \right\rangle = \frac{1}{Z}\text{Tr}\left[e^{-(\beta-\tau)\hat{H}}\hat{a}_i e^{-\tau\hat{H}}\hat{a}_i^\dagger\right] = \frac{1}{Z}\sum_{a,b} e^{-(\beta-\tau)E_a - \tau E_b}|\langle\psi_b|\hat{a}_i^\dagger|\psi_a\rangle|^2 \\
G_<^i(\tau) &= \left\langle \hat{a}_i^\dagger(0)\hat{a}_i(\tau) \right\rangle = \frac{1}{Z}\text{Tr}\left[e^{-(\beta+\tau)H}\hat{a}_i^\dagger e^{\tau\hat{H}}a_i\right] = \frac{1}{Z}\sum_{a,b} e^{-(\beta+\tau)E_a + \tau E_b}|\langle\psi_b|\hat{a}_i|\psi_a\rangle|^2 \ ,
\end{aligned}
\tag{6.17}
$$

where the many-body eigenvalues and eigenstates satisfy $\hat{H}|\psi_a\rangle = E_a|\psi_a\rangle$. The way to compute time-dependent correlation functions such as the above within the cavity formalism has been detailed in [83] and we reported in Appendix A.

The plot in Fig. 6.8 shows the advanced Green function $G_>(\tau)$ in the superfluid phase and in the normal liquid phase, just before the Kauzmann glass transition and slightly above the dynamical transition. The Green function follows three main regimes. First, for $\tau \to 0^+$ one finds a fast decay of the correlations. The energy scale which fixes the particle decay is the interaction potential. This is the dominant contribution to the average energy of the state $a_i^\dagger|\psi_a\rangle$ just after the insertion of one particle on a low energy state $|\psi_a\rangle$. On the other hand the contributions from the chemical potential and the kinetic energy are negligible with respect to V. Then for $\tau \to 0^+$ the process brings the system to highly excited states first. On the contrary, on the side of holes, when $\tau \to \beta^-$, the interaction V

doesn't play any role. Removing a particle cannot lead to a cost in terms of V, and for short time the dominant energy excitation is measured by a loss of chemical potential and the proper time scale is fixed by μ. Finally, in between the two exponential relaxations, the Green function present a third regime in which the decay is slower. Here in the region where the system is not superfluid we expect an exponential decay, with a small exponent, of the order of the hopping.

Density correlation and ergodicity breaking

The second time-dependent correlation which is interesting from the point of view of glassy dynamics is the density-density correlation, defined in imaginary time as follows:

$$\langle \hat{n}_i(\tau)\hat{n}_i(0)\rangle = \frac{1}{Z}\mathrm{Tr}\big[e^{-(\beta-\tau)\hat{H}}\hat{n}_i e^{-\tau\hat{H}}\hat{n}_i\big] \ . \tag{6.18}$$

In the limit of large time and small temperatures this quantity (in particular its connected component) decays to the overlap parameter q_{EA} defined in (6.11). In fact, rewriting Eq.(6.18) we obtain

$$\begin{aligned} \langle \hat{n}_i(\tau)\hat{n}_i(0)\rangle &= \frac{1}{Z}\sum_{a,b} e^{-\beta E_a - \tau(E_b - E_a)}|\langle\psi_a|\hat{n}_i|\psi_b\rangle|^2 \\ &= \frac{1}{Z}\sum_{a} e^{-\beta E_a}|\langle\psi_a|\hat{n}_i|\psi_a\rangle|^2 + \frac{1}{Z}\sum_{a\neq b} e^{-\beta E_a - \tau(E_b - E_a)}|\langle\psi_a|\hat{n}_i|\psi_b\rangle|^2 \ . \end{aligned} \tag{6.19}$$

The second term in (6.19) goes to zero when $\beta J \gg \tau J \gg 1$ (assuming that $J \lesssim V, \mu$ since this is the interesting regime for the purpose of this discussion), therefore in this limit

$$\langle \hat{n}_i(\tau)\hat{n}_i(0)\rangle \to \frac{1}{Z}\sum_{a} e^{-\beta E_a}|\langle\psi_a|\hat{n}_i|\psi_a\rangle|^2 \ . \tag{6.20}$$

The same result is obtained for real time correlations in the large time limit, for any β, if one assumes that terms in the sum with $a \neq b$ vanish due to fast oscillations. In the following we focus on imaginary time correlations in the regime $\beta J \gg \tau J \gg 1$, but the same arguments can be repeated for real time correlations at any β and large times. Moreover, in the following we implicitly assume that the thermodynamic limit $N \to \infty$ is taken before any other limit.

Let us discuss first what happens in the liquid phase. Here, we expect that the connected correlation functions vanish in the large time limit (since the liquid phase is assumed to be *ergodic*). Therefore we expect that the large time limit of $\langle \hat{n}_i(\tau)\hat{n}_i(0)\rangle$ equals $\langle \hat{n}_i\rangle^2$, which leads to

$$\frac{1}{Z}\sum_{a} e^{-\beta E_a}|\langle\psi_a|\hat{n}_i|\psi_a\rangle|^2 = \left[\frac{1}{Z}\sum_{a} e^{-\beta E_a}\langle\psi_a|\hat{n}_i|\psi_a\rangle\right]^2 \ . \tag{6.21}$$

Defining

$$\mathcal{P}_\beta[n_i] = \frac{1}{Z}\sum_{a} e^{-\beta E_a}\delta[\langle\psi_a|\hat{n}_i|\psi_a\rangle - n_i] \tag{6.22}$$

as the probability distribution of n_i^a over eigenstates sampled at temperature $1/\beta$, Eq. (6.21) can hold if and only if

$$\mathcal{P}_\beta[n_i] \underset{N\to\infty}{\to} \delta\left[n_i - \langle\hat{n}_i\rangle\right] \ . \tag{6.23}$$

Since the sum is dominated by eigenvectors that have energy E_a of the order of the average energy at temperature β, the equation above states that the quantity $n_i^a = \langle\psi_a|\hat{n}_i|\psi_a\rangle$ *does not fluctuate* from eigenvalue to eigenvalue in this range of energy. Indeed, even if up to now we chose the canonical ensemble, this requirement is unessential and one could have equivalently stated this concentration

property of local observables also at the level of microcanonical averages. This assumption is known as a weak form of the *eigenstate thermalization hypothesis* [130, 131, 32, 132, 33], see [133] for a more detailed discussion.

We now repeat the same discussion in the glass phase. To this aim, we need to make an important assumption on the spectrum of the Hamiltonian in the 1RSB phase. Indeed, as we previously discussed, the cavity method allows us to establish that the imaginary-time path Gibbs measure constructed via the Suzuki-Trotter formalism undergoes a clustering transition as in the classical case. Yet, imaginary time paths are abstract objects, and the consequences of this clustering transition on the spectrum of the Hamiltonian are not clear, since a priori clustering might depend on the particular basis that is chosen and on other details of the Suzuki-Trotter decomposition. In the following, we *assume* that in the clustered phase, the relevant eigenstates of the Hamiltonian (those which dominate the canonical sum) are also arranged in disconnected *clusters* corresponding to the thermodynamic states [134, 23]. Other states of the Hilbert space do not belong to any cluster, but their energies are extensively different from the thermodynamic energy and therefore they are exponentially suppressed in the canonical sum. We can then decompose the canonical sum as a sum over the clusters and a sum over the eigenstates belonging to the same cluster. A reasonable hypothesis that holds in the classical case and that we believe to hold also here, is that the dynamical behavior of the states inside each cluster is *thermal* (or *ergodic*). In other words, we assume that the reasoning we made for the liquid can be applied within any cluster α, leading to

$$\frac{1}{\mathcal{Z}_\alpha} \sum_{a \in \alpha} e^{-\beta E_a} |\langle \psi_a | \hat{n}_i | \psi_a \rangle|^2 \underset{N \to \infty}{\to} \langle \hat{n}_i \rangle_\alpha^2 = \left[\frac{1}{\mathcal{Z}_\alpha} \sum_{a \in c} e^{-\beta E_a} \langle \psi_a | \hat{n}_i | \psi_a \rangle \right]^2 \qquad (6.24)$$

and

$$\mathcal{P}_\beta^\alpha[n_i] = \frac{1}{\mathcal{Z}_\alpha} \sum_{a \in \alpha} e^{-\beta E_a} \delta(n_i - \langle \psi_a | \hat{n}_i | \psi_a \rangle) \underset{N \to \infty}{\to} \delta[n_i - \langle \hat{n}_i \rangle_\alpha] \ . \qquad (6.25)$$

On the other hand, we expect $\langle \hat{n}_i \rangle_\alpha$ to fluctuate from cluster to cluster, therefore eigenstate thermalization can be assumed to hold at most inside each cluster, signaling, globally, a breakdown of ergodicity. Substituting (6.24) in (6.19) one obtains:

$$\langle \hat{n}_i(\tau) \hat{n}_i(0) \rangle \to \frac{1}{Z} \sum_a e^{-\beta E_a} |\langle \psi_a | \hat{n}_i | \psi_a \rangle|^2 =$$

$$= \frac{1}{Z} \sum_\alpha \mathcal{Z}_\alpha \left[\frac{1}{\mathcal{Z}_\alpha} \sum_{a \in \alpha} e^{-\beta E_a} |\langle \psi_a | \hat{n}_i | \psi_a \rangle|^2 \right] \underset{N \to \infty}{\to} \frac{1}{Z} \sum_\alpha \mathcal{Z}_\alpha \langle \hat{n}_i \rangle_\alpha^2 \ . \quad (6.26)$$

This reduces to the average of the square local density over the amorphous states. Averaging over different sites and subtracting the connected term one recovers the definition of Eq. (6.11), since $W_\alpha = \mathcal{Z}_\alpha / Z$:

$$\langle \hat{n}_i(\tau) \hat{n}_i(0) \rangle - \langle \hat{n}_i \rangle^2 \underset{\beta J \gg \tau J \gg 1}{\longrightarrow} \frac{1}{Z} \sum_\alpha \mathcal{Z}_\alpha \langle \hat{n}_i \rangle_\alpha^2 - \left[\frac{1}{Z} \sum_\alpha \mathcal{Z}_\alpha \langle \hat{n}_i \rangle_\alpha \right]^2 = q_{EA} \ . \qquad (6.27)$$

When the quantity in (6.27) goes to zero, it means that (6.23) holds in the whole Hilbert space and thus the system is ergodic. We note that a consequence of this discussion is that in the quantum case, the RS solution can give informations about clustering. Remarkably, in fact, the quantum cavity method contains information about the imaginary time dynamics and, at the RS level the slow decay of $\langle \hat{n}_i(\tau) \hat{n}_i(0) \rangle$ signals the proximity of the glass transition.

In Fig. 6.8 we have plotted the time dependent density-density correlation for the same parameters used for the Green functions, namely $\beta = 30$, $J = 0.1$ and two different densities such that the system is in the superfluid and in the liquid phase close to the glass transition. The plot shows that the function within the glass does not relax at large times. It remains at a high plateau, higher than q_{EA}. The discrepancy might be due to the fact that βJ is not sufficiently high to allow the complete relaxation of the correlations. This is seen also in the superfluid phase where the correlation remains always above zero.

6.3 Discussion

The novelties of the system that we studied are the following: (i) it presents a glass transition at zero temperature as a function of density, and (ii) it presents a large degeneracy of glassy states with different entropies. Investigating the thermodynamics of the model we find a complex phase diagram displaying superfluid, normal liquid, and glass phases, separated by different phase transitions. We showed that at low enough temperature the glass transition line is re-entrant as a function of quantum fluctuations, implying that one can form a glass by increasing quantum fluctuations at fixed density. This result is the same that we found in Section 3.7 when discussing the condensation transition of the random subcubes model. Similar results have been also obtained in [116] by an extension of mode-coupling theory to quantum hard spheres, and analytically with replica techniques in [117]. Additionally, we showed that the standard RFOT glass transition is replaced by a first order superfluid-glass transition at zero temperature, accompanied by phase coexistence between the two phases, while at the same time the glass transition completely disappears. This shows that for a model with such a complex phase space in the classical limit, introducing quantum fluctuations has a dramatically singular effect, changing completely the nature of the transition between the liquid and the glass phases. Moreover, the first order superfluid-glass transition is accompanied by a jump in density, implying that there exists an interval of densities where the two phases would coexist in a finite dimensional version of the model. One would therefore obtain a simultaneous presence of superfluid and glassy ordering, which however would not give rise to a true superglass phase since they would be phase separated. At variance to what happens in models displaying a second-order spin glass transition [24, 26], we did not find any pure "superglass" phase in the quantum Biroli-Mézard model: in more technical terms this means that, for the range of parameters considered here, we have not found a solution of the quantum 1RSB equations within the broken phase $\langle \hat{a} \rangle \neq 0$.

7

Investigation of superfluidity in amorphous solids

In this Chapter we aim to investigate in more details the interplay between superfluidity and glassiness. As we mentioned in Section 5.1 the experiments on solid Helium suggest that highly disordered samples show a larger NCRI, but it is unclear why disorder should help superfluidity. In Chapter 6 we found that for a lattice model the glass phase is insulating. Here instead we will see what happens in the continuum. We present a study devoted to the understanding of the constraints on the superfluid fraction of an amorphous solid following from a variational upper bound derived by Leggett [20]. In his work on supersolidity, Leggett showed how to derive an upper bound for the fraction of superfluid density of a generic many-body system in which translational invariance is broken, by means of a variational computation [20]. The output of Leggett's computation is a formula that needs as only input the average density profile of the solid. This formula has been applied to Helium crystals, and the aim of this work is to use it to study the amorphous solid. At present, there is not yet any reliable first principle computation or experimental measurements of the density profile of amorphous Helium 4. We endeavor to generate robust estimates of it using a number of different techniques, in particular by investigating a model of zero-point Gaussian fluctuations around classical configurations, and Path Integral Monte Carlo (PIMC) simulations without exchange (which should be closer to the classical dynamics).

The Chapter is organized as follows. In Section 7.1, we discuss how to adapt Leggett's bound to an amorphous solid. In Section 7.2 we compute the bound for a profile made of Gaussian fluctuations around a classical configuration, and compare the results for an amorphous and an ordered solid. Then, we discuss previous numerical computations [25]. In Section 7.3 we try to obtain more precise information by comparing a classical simulation of a glass-forming system with a PIMC numerical simulation of Helium. In Section 7.4, we show that under some approximations one can obtain a formula for the bound that can – at least in principle – be computed from neutron or X-ray scattering data.

7.1 Non-classical rotational inertia and Leggett's bound

In his work Leggett [20] studied the NCRI of a solid confined in a rotating annulus at $T = 0$. Inspired by the case of liquid Helium he argued that the change in the energy of the system in the rest frame

as a consequence of the rotation, for small ω, should be of the form:

$$E(\omega) = E_0 + \frac{1}{2}I_0\omega^2 + \Delta E(\omega) \ , \tag{7.1}$$

where E_0 is the energy for $\omega = 0$ and I_0 is the classical moment of inertia. He assumed that the departure from the classical energy should be of the form

$$\Delta E(\omega) = -\frac{1}{2}\frac{\rho_s}{\rho}I_0\omega^2 \ , \tag{7.2}$$

allowing for a definition of the superfluid fraction ρ_s/ρ. For a system of N bosonic particles E_0 is the expectation value over the ground state wavefunction of the generic interacting Hamiltonian describing the particles in the annulus:

$$\hat{H} = -\frac{\hbar^2}{2m}\sum_{i=1}^{N}\nabla_i^2 + \frac{1}{2}\sum_{i,j=1}^{N}U(|\vec{r}_i - \vec{r}_j|) + \sum_{i=1}^{N}V(\vec{r}_i) \ , \tag{7.3}$$

where V is the potential induced by the enclosing walls, which is time-independent when the system is at rest. The ground state wavefunction of the system at rest, in order to be single valued, must satisfy in cylindrical coordinates the boundary condition:

$$\psi(r_1, z_1, \theta_1; \ldots; r_j, z_j, \theta_j + 2\pi; \ldots; r_N, z_N, \theta_N) = \psi(r_1, z_1, \theta_1; \ldots; r_j, z_j, \theta_j; \ldots; r_N, z_N, \theta_N) \ , \tag{7.4}$$

for all j. Leggett showed that the wavefunction of the ground state inside the rotating cylindrical container can be obtained by considering the ground state of the non-rotating system but with new boundary conditions. He argued, in fact, that, for a rotating cylinder the condition for a single-valued wave function should be substituted by:

$$\psi(r_1, z_1, \theta_1; \ldots; r_j, z_j, \theta_j + 2\pi; \ldots; r_N, z_N, \theta_N) = e^{-2\pi i m R^2 \omega/\hbar} \psi(r_1, z_1, \theta_1; \ldots; r_j, z_j, \theta_j; \ldots; r_N, z_N, \theta_N) \ , \tag{7.5}$$

where R is the radius of the annulus, m is the particle mass and ω is the frequency of rotation. In Eq. (7.5) we assumed that the thickness of the cylinder is much smaller than the radius R. From the difference in energy $\Delta E(\omega) = E(\omega) - E_0$ between the expectation value of the Hamiltonian (7.3) defined for the system in the annulus over a ground state wave function satisfying (7.4) or (7.5) one could define the superfluid fraction for the (solid) system, through:

$$\frac{\rho_s}{\rho} = \lim_{\omega \to 0}\frac{1}{I_0}\frac{\partial^2 E_{min}(\omega)}{\partial \omega^2} \tag{7.6}$$

where ρ is the particle density and $I_0 = NmR^2$ the classical moment of inertia. From this expression it is clear that upper bounds on the superfluid density can be obtained by using variational wavefunctions that in the $\omega \to 0$ limit tend to the wavefunction for a non-rotating container. Leggett used a variational wavefunction of the form $\Psi(\vec{r}_1, \cdots, \vec{r}_N) = \Psi_0(\vec{r}_1, \cdots, \vec{r}_N)\exp[i\sum_i \varphi(\vec{r}_i)]$, where Ψ_0 is the ground state wavefunction for the non-rotating case and $\phi = \sum_i \varphi(\vec{r}_i)$ a sum of phases satisfying the condition $\varphi(\theta) = \varphi(\theta + 2\pi) - 2\pi m R^2 \omega/\hbar$ [20, 135]. Note that in the following, we will denote the fraction of superfluid density by "superfluid fraction" and we always refer to Leggett's upper bound obtained with this variational ansatz to this quantity, unless otherwise specified. Defining

$$\rho(\vec{r}) = \int d\vec{r}_1 \cdots d\vec{r}_N |\Psi_0(\vec{r}_1, \cdots, \vec{r}_N)|^2 \sum_i \delta(\vec{r} - \vec{r}_i), \tag{7.7}$$

which is the density profile in the ground state, one finds that the variational estimation of $E_{min}(\omega)$ reads:

$$E_{min}(\omega) = E_0 + \frac{\hbar^2}{2m} \int d\vec{r} [\nabla \varphi(\vec{r})]^2 \rho(\vec{r}), \tag{7.8}$$

where E_0 is the ground state energy in the non-rotating case.

Because of the assumption that the thickness of the cylinder is much smaller than the radius, one can simplify the problem even further by "unrolling" the annulus and consider the system inside a parallelepiped of length $L = 2\pi R$ in the x direction. In this geometry the phase φ has to satisfy the boundary condition $\varphi(0, y, z) = \varphi(L, y, z) - v_0 L$ where $v_0 = mR\omega/\hbar$. The minimization of (7.8) with respect to φ leads to the equation for $\varphi(\vec{r})$:

$$\vec{\nabla} \cdot [\rho(\vec{r}) \nabla \varphi(\vec{r})] = 0 \tag{7.9}$$

and results in an upper bound on the superfluid density:

$$\rho_s = \frac{1}{V v_0^2} \int_V d\vec{r} \rho(\vec{r}) |\nabla \varphi(\vec{r})|^2 . \tag{7.10}$$

Note that if $\varphi_{v_0}(\vec{r})$ is a solution of (7.9) with boundary conditions $\varphi(0, y, z) = \varphi(L, y, z) - v_0 L$, then $\varphi_{v_0'} = (v_0'/v_0)\varphi_{v_0}$ is a solution with boundary conditions corresponding to v_0'. Hence, Eq. (7.10) does not depend on v_0 and we can choose $v_0 = 1$ without loss of generality. Furthermore, while in the geometry described above the wavefunction should satisfy hard wall conditions at the boundary of the box in the y and z directions, we will simplify the problem by considering periodic boundary conditions in the y and z directions.

In order to find a solution of Eq. (7.9) satisfying the correct boundary condition it is useful to rewrite φ as

$$\varphi(\vec{r}) = \vec{v}_0 \cdot \vec{r} + \delta\varphi(\vec{r}), \tag{7.11}$$

where $\delta\varphi(\vec{r})$ is defined inside the volume V and satisfies periodic boundary conditions, and $\vec{v}_0$ is a unit vector. In the original problem $\vec{v}_0 = \hat{x}$, but since we reformulated the problem in a periodic cubic box, the direction of $\vec{v}_0$ can be varied without affecting the result, in the limit $V \to \infty$. Since $\delta\varphi(\vec{r})$ is periodic, we can write the equations in Fourier space (see Appendix B for details):

$$\vec{q} \cdot \vec{v}_0 \rho_{\vec{q}} = \sum_{\vec{p} \neq \vec{0}} (\vec{q} \cdot \vec{p}) \rho_{\vec{q}-\vec{p}} i\delta\varphi_{\vec{p}} , \tag{7.12}$$

and from the solution for $i\delta\varphi_{\vec{q}}$ one can obtain the Leggett bound [135], that reads in Fourier space:

$$\frac{\rho_s}{\rho} = 1 - \frac{1}{\rho v_0^2} \sum_{\vec{q} \neq \vec{0}} (\vec{v}_0 \cdot \vec{q}) i\delta\varphi_{\vec{q}} \rho_{-\vec{q}} . \tag{7.13}$$

Given the density profile, the linear equation (7.12) for $i\delta\varphi_{\vec{q}}$ can be solved by truncating the sum over momenta at a given cutoff, $|\vec{q}| < q_{max}$, so that the problem reduces to solving a finite set of linear equations, which can be done by matrix inversion.

An important remark is that the truncation preserves the variational nature of the computation. Indeed, it can be seen as setting $\delta\varphi_{\vec{q}} = 0$ for $|\vec{q}| \geq q_{max}$, which amounts to a particular choice of the variational function $\delta\varphi(\vec{r})$ and hence still gives an upper bound on the true superfluid fraction.

Another important remark is that the bound derived above applies only, strictly speaking, to the true ground state of the system. In the following however, we are interested in applying it to the glass state, which is at best a long-lived metastable state, the crystal being always the true ground state. Still, it is clear from the derivation that if the life time τ of the state is very long, such that for any experimentally accessible frequency one has $\omega\tau \gg 1$, then the system does not have time to escape from the metastable state during the experiment and the bound should apply without modification.
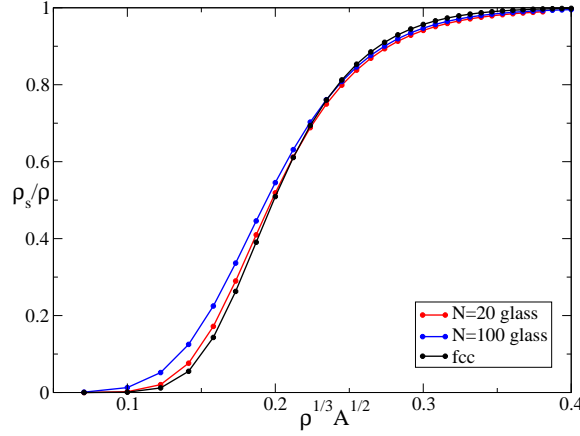
Figure 7.1: Leggett upper bound for ρ_s/ρ, for a Gaussian profile of width $A^{1/2}$ around an amorphous jammed configuration and in a FCC lattice, as a function of the adimensional parameter $\ell = \rho^{1/3} A^{1/2}$ (the Lindemann ratio).

7.2   Superfluid fraction of amorphous solids

7.2.1   Hard sphere systems

In order to understand whether disorder in the density profile can lead to an increase of the superfluid density, we shall compare the result of the bound for an amorphous glassy profile and the corresponding crystal. The only input for our study are the density profiles of the amorphous and crystal state. Unfortunately, the former is not available for He^4 in realistic conditions. As a consequence, we decided for a first study to focus on a more simple and academic case that can still provide insights on the role of disorder. We consider the amorphous and crystalline density profiles that one obtains for classical hard spheres. Although this certainly is not a realistic model of density profiles for He^4, it allows us to address the role of disorder on ρ_s. Furthermore, a mapping from quantum systems at zero temperature and classical Brownian systems allows one to find quantum many particle models whose ground state wave-function can be mapped exactly on (the square of) the probability distribution of classical hard spheres systems [23]. Thus, the results of this section apply directly to those models.

Classical hard spheres are known to be characterized by a high density crystal FCC phase. However, if compressed fast enough, or due to a small polydispersity, the hard spheres freeze in an amorphous glassy state. A typical density profile of a very quickly compressed glassy state can be obtained by the Lubachevski-Stillinger compression algorithm [136] (we used the implementation of [137]), which is know to be very efficient in producing amorphous jammed configurations. The output of the algorithm are the positions $\mathcal{R} = \{R_1, \cdots, R_N\}$ of the particles in a random close packed state (at infinite pressure). The algorithm is deterministic, but different final configurations are obtained by starting the compression from random initial configurations of points. The compression runs were performed at very fast rates (we fixed the parameter $\gamma = 0.1$, see [137, 112] for details) in order to avoid crystallization.

Furthermore, we will assume that the density profile of a typical glassy configuration at finite pressure is the sum of Gaussians centered around the amorphous sites, which are the output of the previous algorithm. For classical systems, this assumption has been tested numerically for FCC crystals [138], and has been often used in density functional computations of both ordered [139] and amorphous

ρ (Å^{-3})	ℓ	HCP, Leggett's bound Ref.[142] ρ_s/ρ	Glass, Leggett's bound (this work) ρ_s/ρ	Glass, QMC (Ref. [25]) ρ_s/ρ
0.029	0.167	0.22	0.282	0.6
0.0353	0.143	0.06	0.127	0.07

Table 7.1: Leggett's bound for ^{4}He in the HCP crystal state [142] and glassy state. Quantum Monte Carlo results for the glass are also reported [25].

structures [112], giving accurate results. For quantum systems, the Gaussian model has been shown to be accurate enough, at least for the purpose of computing the Leggett's upper bound [140, 141, 142].

For a given configuration $\mathcal{R}$, the density profile we use is defined as

$$\rho(\vec{r}|\mathcal{R}) = \sum_i \gamma_A(|\vec{r} - \vec{R}_i|) = \int_V d\vec{s}\, \gamma_A(|\vec{r} - \vec{s}|) \sum_i \delta(\vec{s} - \vec{R}_i) \ , \qquad (7.14)$$

where $\gamma_A(\vec{x}) = \exp(-|\vec{x}|^2/(2A))/(2\pi A)^{3/2}$ is a normalized Gaussian of width A, and $|\vec{r} - \vec{R}_i|$ is the distance on the periodic box, i.e. it is the distance between $\vec{r}$ and its closest image of $\vec{R}_i$. The corresponding Fourier transform reads (neglecting terms of order $\exp(-L^2/A)$):

$$\rho_{\vec{q}}(\mathcal{R}) = e^{-Aq^2/2} \frac{1}{V} \sum_i e^{i\vec{q}\cdot\vec{R}_i} \ . \qquad (7.15)$$

In solving Eqs. (7.12) and (7.13) we considered amorphous configurations of $N = 20$ and $N = 100$ particles. We solved numerically Eq. (7.13) via a LU decomposition [143]. All the calculations were done with the cut-off set at $q_{max} = 20\pi/L$. We checked that the result does not depend on the specific amorphous configuration used by considering different amorphous configurations $\mathcal{R}^\alpha$, $\alpha = 1, \cdots, \mathcal{N}$, as it is expected since the superfluid density is a macroscopic quantity. The reported results are therefore averaged over 10 independent configurations. More details on the numerics can be found in Appendix B.

The results are plotted in Figure 7.1. One can notice that, apart from the smallest values of the dimensionless parameter, the two curves corresponding to 20 and 100 particle configurations perfectly agree. The discrepancy in the region of small $\ell = \rho^{1/3}A^{1/2}$ is due to the approximation brought by the introduction of a cut-off, and vanishes in the limit $q_{max} \gg 1/\sqrt{A}$.

In order to understand to what extent the disorder influences the value of the superfluid density, we compare the superfluid fraction found in the amorphous system to the values obtained through the same calculations in the case of a crystal [135, 140, 141, 142]. Figure 7.1 reports the results for the average superfluid fraction of the amorphous solid just described and those corresponding to the FCC lattice (which is the thermodynamically stable one for hard spheres) for the $\vec{R}_i$, according to the same Gaussian model (in the latter case our results are consistent with previous ones [135, 140, 141, 142]). The difference between the two is very small, suggesting two conclusions.

1. Disorder does not influence much the superfluid behavior of the system for comparable values of $\rho^{1/3}A^{1/2}$, at least at the level of this variational calculation.

2. The dependence of ρ_s on the density profile is mainly through the Lindemann ratio $\ell = \rho^{1/3}A^{1/2}$. This conjecture allows us to obtain an estimate of the Leggett upper bound for ρ_s in more realistic cases as we will do in the next section.

To conclude this section, we observe that the above results allow to obtain a quantitative upper bound for the superfluid fraction of a system whose wavefunction is exactly the Jastrow wavefunction corresponding to classical hard spheres. The quantum glassy phase of this system has been discussed in [23]. In both the crystal and glassy phases, the values of $A^{1/2}$ for classical hard spheres do not exceed 0.1 (in units of the sphere diameter) [138, 139, 112], and the same is true for ℓ, since the density is very close to 1 (in the same units) in both solid phases. Using the results of Fig. 7.1, we obtain an upper bound $\rho_s/\rho \lesssim 0.1\%$, which is consistent with the extremely small values of the condensate fraction found in [23].

7.2.2   Superfluid fraction of amorphous solid Helium 4

In the following, we attempt an application of our results to the more interesting case of disordered solid He^4, based on the observation above, that an estimate of the Lindemann ratio $\ell = \rho^{1/3}A^{1/2}$, together with the results of Fig. 7.1, should provide a reasonable estimate of Leggett's bound.

At the end of Ref. [142] it is stated that, by fitting the Path Integral Monte Carlo density profile of HCP solid He^4, one obtains a value $\sqrt{A} = 0.1274\,d$ at $\rho = 0.0353$ Å^{-3} and $\sqrt{A} = 0.1486\,d$ at $\rho = 0.029$ Å^{-3}. Here d is the nearest-neighbor distance for the HCP lattice. The number density of the HCP lattice satisfies the relation $\rho d^3 = \sqrt{2}$, hence $d = 2^{1/6}/\rho^{1/3}$ and $\ell = \sqrt{A}\rho^{1/3} = 2^{1/6}\sqrt{A}/d$. In the same reference it is also stated that the upper bound computed by using the fitted Gaussian density profile coincides with the one obtained by using the true PIMC density profile, and corresponds respectively to $\rho_s/\rho = 0.06$ and 0.22. These values are reported in table 7.1.

We now make the following assumptions:

1. *At least for the purpose of computing Leggett's upper bound*, the true density profile can be fitted to a Gaussian profile. This is true for the crystal [142] and we assume that it remains true for an amorphous solid.

2. The parameter ℓ for the amorphous solid is smaller than that of the crystal at the same density. This can be understood by observing that crystalline configurations are better packed than amorphous configurations, therefore leaving more room ("free volume") for fluctuations. It is true for Jastrow wavefunctions [23] (i.e. classical system) and we do not find any reason why quantum fluctuations should dramatically affect this property.

Based on these assumptions, the true Leggett's bound for the amorphous system should be smaller than the same bound for the crystal at the same density. This can be estimated using the values of ℓ reported in [142] and reading the corresponding superfluid fraction from Fig. 7.1 or using the results obtained in [142] for the HCP crystal. These values are reported in table 7.1 and are similar.

We compare the upper bound obtained in this way with the values of ρ_s obtained numerically by Boninsegni et al. via PIMC [25]. Interestingly, we find that the bound is very close to the PIMC numerical result, and in particular at the smallest density the bound is violated by the PIMC result. This can be due either to the very rough approximations involved in our computation, or to the fact that the glass is not a really long-lived metastable state at this very low density. The latter possibility, i.e. that the system is rapidly evolving out of equilibrium, would invalidate the derivation of Leggett's bound but it would also raise problematic questions regarding the measurement of ρ_s using the Ceperley formula [144], which is strictly valid if thermodynamic equilibrium is achieved and in the limit of small frequency.

7.3 Comparing dynamics: from a classical glass to Helium 4

In order to study the stability of the glass phase in Helium 4, we performed Path Integral Monte Carlo simulations, that we discuss in this section. Before discussing the more complex quantum simulation, we present some classical simulations in order to deal with a well controlled situation, where the presence of a glass transition has been firmly established.
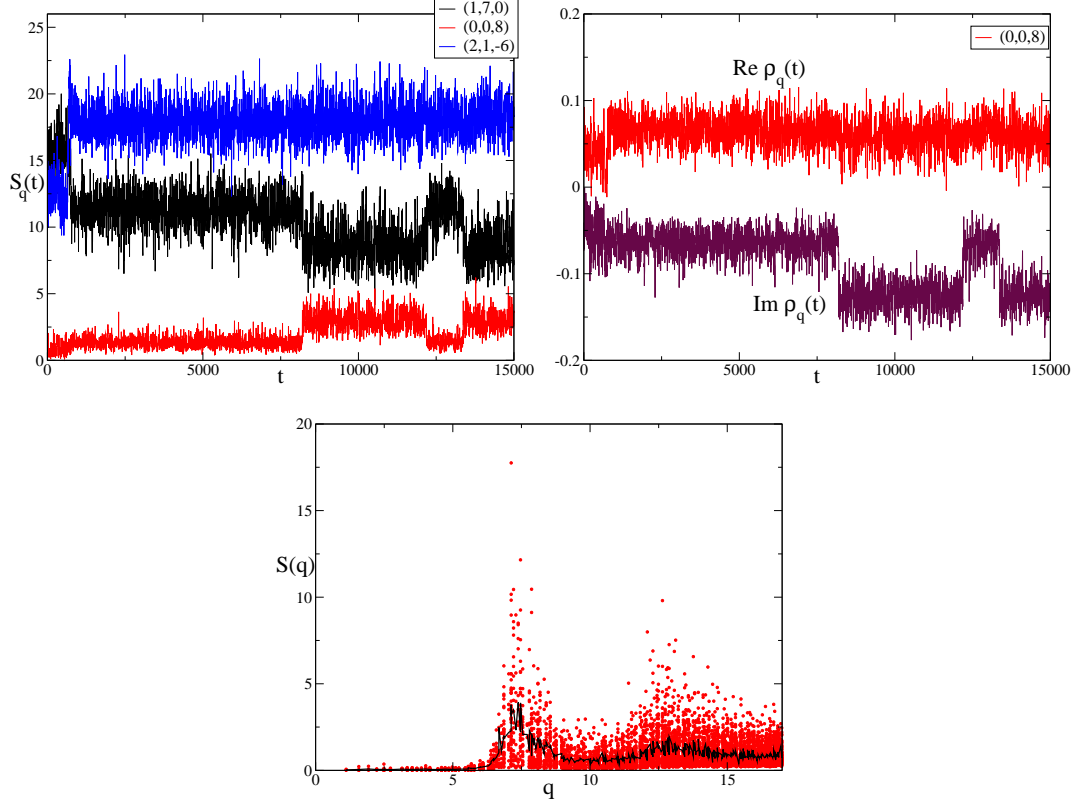
Figure 7.2: Evolution of the density profile after a quench from high to low temperature for a classical glass forming system, using Molecular Dynamics. *Top left*: instantaneous value of $S_{\vec{q}}(t)$ for three representative values of $\vec{q}$ (the corresponding (n_x, n_y, n_z) are indicated in the caption). *Top right*: instantaneous values of $\rho_{\vec{q}}(t)$ for a representative value of $\vec{q}$. *Bottom*: the time average of $S_{\vec{q}}(t)$ over the whole simulation, as a function of q (in reduced LJ units). Scatter points are values for a given $\vec{q}$, the full black line is the angular average over all vectors with the same modulus.

Dynamics in glass-forming systems: a classical simulation

We performed standard Molecular Dynamics (MD) simulations of the Kob-Andersen binary mixture [120], which is known to be a good glass former and does not show any sign of crystallization even after very long MD runs at low temperature. The latter is a mixture of two types of particles (A and B) with the same mass m, interacting through different Lennard-Jones potentials:

$$V_{\alpha\beta}(r) = 4\varepsilon_{\alpha\beta}\left(\left(\frac{\sigma_{\alpha\beta}}{r}\right)^{12} - \left(\frac{\sigma_{\alpha\beta}}{r}\right)^{6}\right) \tag{7.16}$$

with $\alpha, \beta \in \{A, B\}$ and parameters $\varepsilon_{AA} = 1, \sigma_{AA} = 1, \varepsilon_{BB} = 0.5, \sigma_{BB} = 0.88, \varepsilon_{AB} = 1.5, \sigma_{AB} = 0.8$, as specified in [120]. In the rest of this section we use reduced Lennard-Jones units, namely we use

σ_{AA} and ε_{AA} as units of length and energy, and m as unit of mass. Consequently, $\sqrt{m\sigma_{AA}^2/\varepsilon_{AA}}$ is the unit of time (the latter convention is slightly different from the one of [120]). Note that to compare with Helium one should keep in mind that for that system $\sigma \sim 2.56\,\text{Å}$ and $\varepsilon \sim 10.2$ K.

We quenched a dense ($\rho = 1.2$) system of $N = 216$ particles from very high temperature ($T = 2$) to very low temperature ($T = 0.05$) deep in the glass phase (the glass transition temperature being around $T = 0.435$ at this density [120]). We run the simulation for a total time $\tau = 15000$ and we printed configurations every $\Delta t = 5$ which is of the order of the decorrelation time in the glass (estimated from the decay of the self scattering functions). From each configuration we deduced

$$\rho_{\vec{q}}(t) = \frac{1}{V}\sum_j e^{i\vec{q}\cdot\vec{r}_j(t)} \ , \tag{7.17}$$

where $\vec{r}_j(t)$ is the position of particle j at time t, and the corresponding instantaneous value of the static structure factor $S_{\vec{q}}(t) = V|\rho_{\vec{q}}(t)|^2/\rho$.

In Fig. 7.2 we plotted $\rho_{\vec{q}}(t)$ and the structure factor $S_{\vec{q}}(t)$ as a function of MD time after the quench. The vectors $\vec{q} = 2\pi/L(n_x, n_y, n_z)$ and the corresponding integers are given in the caption. We see that after a short transient, the density profiles fluctuate around a non-zero value which is quite stable, except for some rare "crack" events where the density changes abruptly. These are probably due to groups of particles that switch back and forth between two different locally stable configurations. This system is indeed extremely dense and at very low T, therefore its dynamics is basically that of harmonic vibrations around local minima of the potential (except for the rare cracks). The largest instantaneous value of $S_{\vec{q}}(t)$ corresponds to the $(2, 1, -6)$ curve in Fig. 7.2 for all $t > 1000$; therefore, all values are smaller than 20 at all times, showing that there are no Bragg peaks. This is what we expect to see in a glass. In this case, we can easily deduce the average values of $\rho_{\vec{q}}$ for a given glassy configurations by taking the average of $\rho_{\vec{q}}(t)$ over a time interval where there are no crack events. From these, we could compute the Leggett bound as previously discussed.

Absence of a stable glass phase from a Path Integral Monte Carlo simulation

Motivated by results of [25] we tried to compute the superfluid fraction based directly on Path Integral Monte Carlo data. Unfortunately, PIMC does not give access to the real time dynamics of the system, but following [25] we studied the Monte Carlo dynamics, in the hope that this is a reasonable proxy for the real time dynamics.

The representation of quantum systems in PIMC involves certain important extensions beyond the classical representation of point particles. To begin with, particles are represented by paths (or polymers) in space. These paths manifest the zero point motion inherent in the quantum mechanical system. For distinguishable particles, this is the only difference. For particles with statistics (bosons), these paths then can permute onto each other forming larger paths or cycles.

We initially focus on studying a quenched quantum system of Helium particles but require that they act like distinguishable particles. There are a number of potential advantages of this approach. To begin with, one may hope that distinguishable particles are more likely to retain the relationship between real dynamics and the Monte Carlo dynamics. Secondly, the simulation of distinguishable particles is faster and able to be parallelized over many processors allowing for longer simulations.

We used the Aziz potential as a model for Helium [145], and in this section we always use Angstroms as units of length and Kelvins as units of temperature. The pair product action is used as the approximation for the high temperature density matrix and an imaginary time step of $\delta\tau = 0.025$ K is used. We equilibrated a system of $N = 216$ particles in the liquid phase at a density of 0.029 Å^{-1}
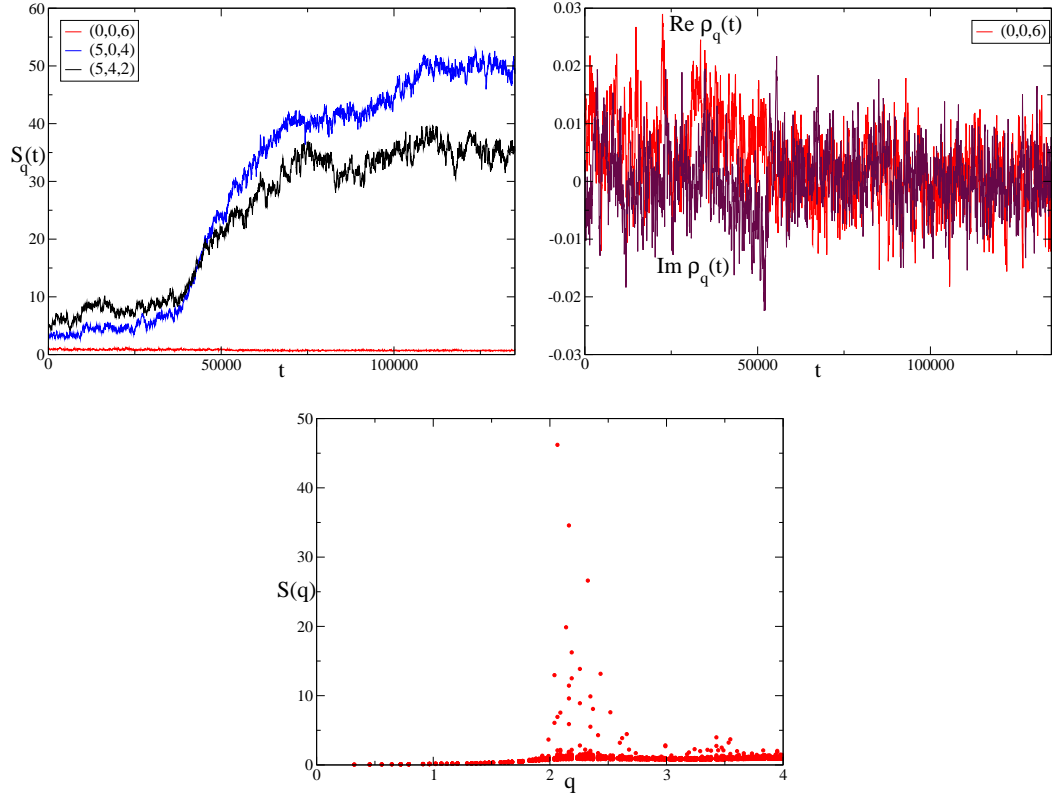
Figure 7.3: Evolution of the density profile after a quench from high to low temperature for a quantum Helium 4 system, using Path Integral Monte Carlo. Time here represents the number of Monte Carlo sweeps (see text). The panels are the same as in Fig. 7.2, except that the average of $S_{\vec{q}}(t)$ in the lower panel has been taken for $t > 75000$, and the angular average is not reported because of the strong anisotropy of the result. All quantities are plotted using Å as units of length.

and a temperature of $T = 2$ K. The system is then instantaneously quenched to $T = 0.166$ K. This is accomplished by taking a snapshot of the paths from $T = 2$ K and then, for each time slice of the old path, placing 12 time slices for the new lower temperature path, similarly to what was done by Boninsegni et al. [25]. We then run the PIMC from this quenched configuration. These paths are obviously highly artificial because the distances between many adjacent time slices are zero. Over a very short period at the beginning of the quenched run, though, this artificial aspect of the path quickly relaxes leaving the paths in a configuration that mirrors the higher temperature formation.

In the following we refer to t as the PIMC "time" (number of PIMC sweeps, a sweep being defined as N particle moves), while τ is the imaginary time. At each "time" t, the PIMC code returns a configuration $\vec{r}_j^{\tau}(t)$, the latter being the imaginary time trajectory of particle j as function of the imaginary time τ. We can define the instantaneous density as

$$\rho_{\vec{q}}(t) = \frac{1}{\beta V} \sum_j \int_0^{\beta} d\tau \, e^{i\vec{q} \cdot \vec{r}_j^{\tau}(t)} \ , \tag{7.18}$$

and the instantaneous structure factor

$$S_{\vec{q}}(t) = \frac{1}{\beta N} \sum_{j,k} \int_0^{\beta} d\tau \, e^{i\vec{q} \cdot [\vec{r}_j^{\tau}(t) - \vec{r}_k^{\tau}(t)]} \ . \tag{7.19}$$

Note that in the quantum case, at variance with the classical case, these two quantities are not directly related. At each PIMC sweep we recorded the values of the above quantities, which we then averaged over 50 PIMC sweeps in order to eliminate part of the fluctuations.

The results for a representative run of the above procedure are reported in Fig. 7.3. Unfortunately, the dynamics of this system looks quite different from the formation of a glass from a quenched liquid. First of all, the structure factor becomes quite large for some values of $\vec{q}$, therefore suggesting the presence of large crystallites in the sample. Indeed, the largest value of the structure factor corresponds to the $(5, 0, 4)$ curve in Fig. 7.3 at large times and to the $(5, 4, 2)$ curve in Fig. 7.3 at short times. We see that while at short times the values of $S_{\vec{q}}(t)$ are smaller than 10, at larger times they grow up to 50, which clearly indicates the presence of large crystallites in the sample (note in addition that these values have been averaged over 50 PIMC sweeps and also over imaginary time). Moreover, the $\rho_{\vec{q}}(t)$ (reported for a representative value of $\vec{q}$ in the middle panel of Fig. 7.3) are not fluctuating around some stable value; they display a sluggish evolution that does not allow to identify a region of times where the system is close to some metastable density profile that does not evolve in time. What we can learn from this is that the quenching from a (exchange-free) liquid to a (exchange-free) low temperature liquid froze to a crystal relatively quickly without showing any intermediate signs of glassiness. Note however that this behavior was not observed in all runs: some runs did not display signs of crystallization for times up to ~ 200000 PIMC sweeps. Still the dynamics was sluggish enough to prevent the identification of a stable glass phase. We also tried turning off some moves (the displace moves) in order to slow down the relaxation to the crystal, but the system still seems to freeze just as quickly.

In conclusions, we were not able to find a long-lived metastable glassy state in our quantum simulations. This is probably due to the fact that monodisperse systems always crystallize quite fast. This is well known in the classical case and seems to also hold true when quantum zero point motion is introduced (at least in this specific example). One possibility is that exchange, that we neglected, may be critically important for exhibiting the glassy behavior of Helium 4: it could be that the path integral at the low temperatures we are focusing on is dominated by exchange paths, whereas the paths that make the glass unstable are mainly without exchange; indeed we find them with our PIMC. In this case, the instability of the glass would be a much rarer process once one takes into account exchange paths. In particular, since crystals have a very low or zero superfluid fraction, we know that their corresponding path integral is dominated by paths without exchange. In consequence, eliminating the exchange could also make crystal nucleation easier since it makes it a less rare process.

An additional possibility is that the glassy behavior is sensitive to the specific details of the simulation (type of Monte Carlo moves, length of the paths, etc.). We leave a more detailed investigation of this point for future study.

7.4   Leggett bound and non-ergodic factor

As we discussed previously, the problem in applying our analysis to realistic system is that the amorphous density profile of He^4 cannot be easily measured experimentally. Below, we endeavor to connect the bound on ρ_s to the so-called non-ergodic factor $\widetilde{g}_q$, which in principle could be measured in experiments, e.g. by neutrons or X-ray scattering. It is defined as

$$\frac{\rho^2}{N}\widetilde{g}_q = \frac{1}{\mathcal{N}}\sum_\alpha \rho_{\vec{q}}^\alpha \rho_{-\vec{q}}^\alpha = \overline{\rho_{\vec{q}}\rho_{-\vec{q}}} \; , \tag{7.20}$$

where the overbar denotes the statistical average over the amorphous states sampled statistically by the system. These are indexed by $\alpha = 1, \cdots, \mathcal{N}$, and under the Gaussian approximation each profile $\rho_{\vec{q}}^{\alpha}$ is obtained from Eq. (7.15) by plugging the reference positions corresponding to each different amorphous configuration $\mathcal{R}^{\alpha}$. The statistical average is performed with the weights α that correspond to the frequency with which they appear in an experiment, or equivalently their Boltzmann weight. First, let us focus on $\overline{\rho}_s$, which is the average of the superfluid density ρ_s^{α} corresponding to each amorphous state. Since the superfluid density is a macroscopic quantity we expect (and we have checked numerically, see Appendix B) a self-averaging behavior, i.e. the fluctuations of ρ_s^{α} are negligible. However, as usual for disordered systems, the computations are easier for $\overline{\rho}_s$. Multiplying Eq. (7.12) by $\rho_{-\vec{q}}^{\alpha}$ and averaging over α we obtain

$$(\vec{q} \cdot \vec{v}_0) \frac{\rho^2}{N} \widetilde{g}_q = \sum_{\vec{p} \neq \vec{0}} (\vec{q} \cdot \vec{p}) F(\vec{q}, \vec{p}) \; , \tag{7.21}$$

where we define, for $\vec{p}, \vec{q} \neq 0$ (that are the only cases involved in the equation above)

$$F(\vec{q}, \vec{p}) = \frac{1}{\mathcal{N}} \sum_{\alpha} \rho_{\vec{q}-\vec{p}}^{\alpha} i\delta\varphi_{\vec{p}}^{\alpha} \rho_{-\vec{q}}^{\alpha} = \overline{\rho_{\vec{q}-\vec{p}} i\delta\varphi_{\vec{p}} \rho_{-\vec{q}}} \; . \tag{7.22}$$

Clearly $i\varphi_{\vec{q}}$ is strongly correlated to $\rho_{\vec{q}}$, being the solution of (7.12). In order to simplify the problem we assume that these variable are Gaussian distributed. Using Wick's theorem, one has

$$F(\vec{q}, \vec{p}) = \overline{\rho_{\vec{q}-\vec{p}}} \; \overline{i\delta\varphi_{\vec{p}}} \; \overline{\rho_{-\vec{q}}} + \overline{\rho_{\vec{q}-\vec{p}}} \; \overline{i\delta\varphi_{\vec{p}}\rho_{-\vec{q}}}$$
$$+ \overline{\rho_{\vec{q}-\vec{p}} i\delta\varphi_{\vec{p}}} \; \overline{\rho_{-\vec{q}}} + \overline{\rho_{\vec{q}-\vec{p}}\rho_{-\vec{q}}} \; \overline{i\delta\varphi_{\vec{p}}} \; . \tag{7.23}$$

Note that, due to translation invariance of the averages over α, one has $\overline{\rho_{\vec{q}}} = \rho\delta_{\vec{q},\vec{0}}$ and $\overline{\rho_{\vec{q}}\rho_{-\vec{p}}} = \frac{\rho^2}{N} \widetilde{g}_q \delta_{\vec{q},\vec{p}}$. Hence, for $\vec{p}, \vec{q} \neq 0$, we get

$$F(\vec{q}, \vec{p}) = \overline{\rho_{\vec{q}-\vec{p}}} \; \overline{i\delta\varphi_{\vec{p}}\rho_{-\vec{q}}} = \rho\delta_{\vec{q},\vec{p}} \overline{i\delta\varphi_{\vec{q}}\rho_{-\vec{q}}} \equiv \rho\delta_{\vec{q},\vec{p}} F(\vec{q}) \; . \tag{7.24}$$

Substituting the last expression in (7.21), we obtain

$$F(\vec{q}) = \frac{\rho(\vec{q} \cdot \vec{v}_0)\widetilde{g}_q}{Nq^2} \; . \tag{7.25}$$

Averaging (7.13) over α, we get

$$\frac{\overline{\rho_s}}{\rho} = 1 - \frac{1}{\rho v_0^2} \sum_{\vec{q} \neq \vec{0}} (\vec{v}_0 \cdot \vec{q}) F(\vec{q}) = 1 - \frac{1}{N} \sum_{\vec{q} \neq \vec{0}} \frac{(\vec{v}_0 \cdot \vec{q})^2}{v_0^2 q^2} \widetilde{g}_q \; . \tag{7.26}$$

In the thermodynamic limit, the sum can be replaced by an integral, and performing the angular integration we obtain:

$$\frac{\overline{\rho_s}}{\rho} = 1 - \frac{2}{3} \int_0^{\infty} \frac{dq \, q^2}{(2\pi)^2 \rho} \widetilde{g}_q \; . \tag{7.27}$$

The same result can be obtained by means of a large A expansion of the system of equations, which however is poorly convergent and cannot be used in a systematic way, see Appendix B.

As before we need to introduce a cut-off in the sum on $\vec{q}$ in (7.15) and calculate numerically the non-ergodic factor $\widetilde{g}_q$ by averaging the density over the same configurations $\mathcal{R}^{\alpha}$ considered above. We set the cutoff according to the spherical constraint $|\vec{q}| \leq q_{max}$. We increased q_{max} until $q_{max} = 20\pi/L$, when the convergence in $\widetilde{g}_q$ was reached. For the purpose of computing the non-ergodic factor and then the approximate bound, as given in Eq. (7.26), we averaged over 100 different configurations.
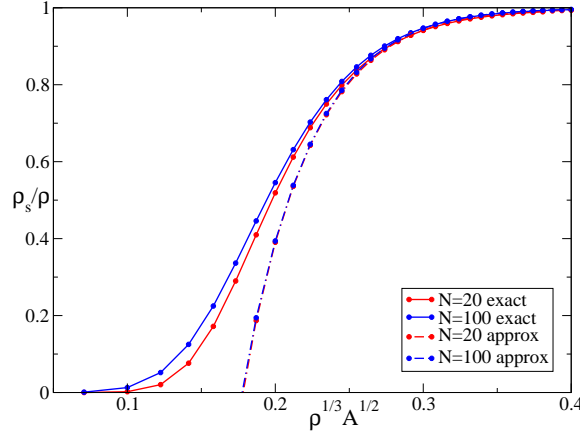
Figure 7.4: Result for ρ_s/ρ as a function of $\ell = \rho^{1/3}A^{1/2}$, where $\vec{R}_i$ are the center of the spheres in an amorphous jammed configuration of N spheres with periodic boundary conditions. We report the exact computation according to Eq. (7.12) and the approximate result Eq. (7.27).

In this case, in fact, one does not face the computational problem of inverting the linear system (7.12) and thus a larger statistics can easily be taken. The results of the computations are shown in Figure 7.4. We plotted the superfluid fraction obtained through the exact procedure (7.13) and the approximated one (7.27), both for the configurations with 20 and 100 particles. The agreement between the approximated curve and the exact one is good for large value of ℓ while they start to differ when the localization parameter decreases, for values of the bound around 0.7. Unfortunately for the interesting values of ℓ the approximated calculation gives wrong results. However, we find it useful, since it allows to estimate the typical scale of ℓ at which the bound starts decreasing fast from 1 to 0 and we hope that it will be possible to improve it in the future, in order to be able to apply it to realistic cases.

7.5   Discussion

In this Chapter we discussed Leggett's upper bound for amorphous quantum solids. We showed that for quantum systems described by a hard sphere Jastrow wavefunction, the superfluid fraction must be smaller that 0.1%, which is consistent with a previous investigation that found extremely small condensate fractions for this system [23]. Moreover, the hard sphere result suggests that crystal and glass phases characterized by the same Lindemann ratio should have similar Leggett's upper bounds for the superfluid fraction.

On this basis, we attempted to apply our results to glassy He^4 [25]. We found that the upper bound for ρ_s is in general very close to the numerical results of Ref. [25], and at density $\rho = 0.029$ Å^{-3} it is below. One possible origin of this discrepancy could be that at such low density the life time of the metastable glassy state is too short, and the system is intrinsically out of equilibrium; in that situation Leggett's bound is inapplicable, since it assumes that the reference wave-function corresponds to a truly metastable state. Indeed we generically found from Path Integral Monte Carlo calculations that (at least if exchange is neglected) the system crystallizes very fast after the quench, which is consistent with a very short lifetime of the metastable glass.

Overall, our findings suggest two possible scenarios (not necessarily antithetic) relative to the region of

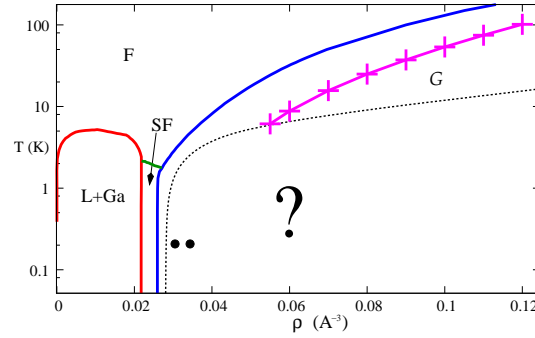Figure 7.5: Phase diagram of ^{4}Helium. Note that here we draw the phase diagram in the plane density ρ and temperature T instead of the more common representation in terms of pressure and temperature. Equilibrium phases: The red line delimits the liquid (L)-gas (Ga) coexistence region. The green line is the λ-line that separates the liquid from the superfluid (SF). The blue line is the melting transition below which the crystal phase is stable, and the disordered phase is metastable. Glass phase: The pink line is the glass (G) transition line obtained in [117] within a first-order semiclassical expansion which neglects the permutation symmetry of particles. The behavior of the amorphous phase, say, within the dashed black line is currently not understood. The two black dots mark the state point investigated numerically in Ref. [25]. Figure from [117].

low densities and temperatures studied in this work. (1) An amorphous stable glass has a superfluid fraction, not only a Leggett's upper bound, very similar to a defect-free crystal with the same Lindemann ratio. Since we know from experiments and simulations that this superfluid fraction is very small, or possibly zero, we are bound to conclude that the glassy supersolid phase found in experiments does not correspond to a truly stable glass: the system is instead rapidly evolving out of equilibrium and, somehow, this enhances superfluidity. (2) Exchange promotes glassiness and a superglass can develop. This could be partially tested by comparing the stability of the glass phase in imaginary time simulations with and without exchange. Finally, based on the experience on classical systems, we remark that it is likely that in more complex systems (such as binary mixtures) crystallization will be avoided and a long-lived quantum glass phase will be stable even without exchange [116]. In this case, it should be very easy to measure the density profile and compute the Leggett bound using the procedure detailed above.

In Fig. 7.5 we present the phase diagram of ^{4}He as a function of density and temperature, with the inclusion of the results of [117] for the high temperature/density amorphous phase and with the indication of the two points studied in [25].

Combining the results of the works [117, 146, 23, 26, 24] and those of Chapters 6 and 7 we speculate about the possible phase diagrams that concern the metastable phases of ^{4}He, as discussed in [117]. The models studied in those works are quite abstract with respect to a 3-dimensional sample of ^{4}He. However as we argued in Chapter 5, at least for classical systems, mean field glassy models still reproduce nicely the property of amorphous solids (or supercooled liquid) interacting via van der Walls-like interactions. For this reason we think that it is instructive to take inspiration from them in considering the phases of ^{4}He. Different scenarios emerge from these works and in particular the way in which the λ-line continues in the metastable phase is not understood. (i) The study of mean-field glassy systems suggests that the transition becomes first order before crossing the glass transition. The model considered in Chapter 6 was studied at finite, but very low, temperature and in
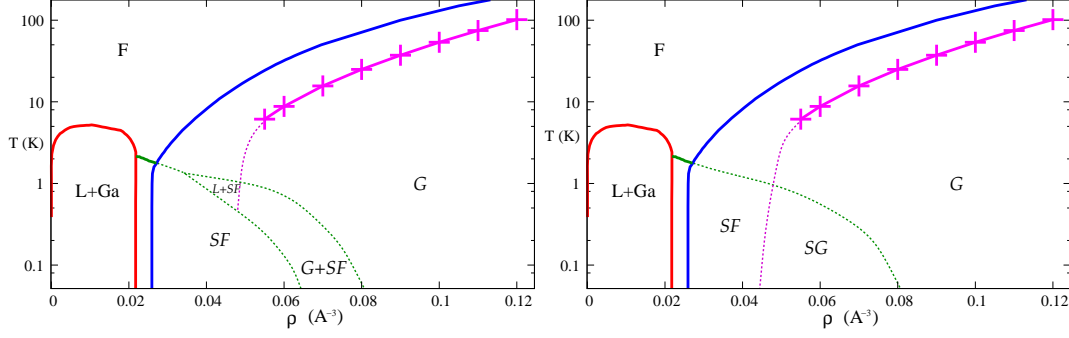
Figure 7.6: *Left panel*: a conjectural phase diagram for amorphous phase of ^{4}Helium as it is suggested by the works [117, 146] and the results in Chapter 6 and 7. The equilibrium parts of the phase diagram are the same as in Fig.7.5. The metastable "supercooled" phases are indicated in italic. The pink line is the glass transition line obtained in [117]. The λ-line becomes, at some point inside the supercooled liquid, a first-order transition line as for the model studied in Chapter 6. One should therefore observe a superfluid (SF)-glass (G) coexistence. Note that we currently do not have any quantitative estimate of the behavior of the λ-line inside the metastable phase, which is drawn at arbitrary position in the figure. *Right panel*: another possible phase diagram for metastable ^{4}Helium, based on the results of [24, 23]. The λ-line always remains a second-order transition. When it crosses the glass transition line, a superglass (SG) phase appears. Figures from [117].

this regime the glass phase was found not superfluid. This implies that superfluid and glassy behavior would coexist in a region of the phase diagram but they would be phase separated. This hypothesis is schematized in Fig. 7.6 (left panel), where the green dotted line represents the continuation of the superfluid transition in the metastable phase while the pink curve represents the the glass transition. (ii) Other studies [23, 24, 26] instead suggest the possibility of a true superglass phase, where the λ-line remains of second order and thus intersects the glass transition in a continuous way. However there are difficulties in drawing a clear explanation from the results of the models considered in [23, 24, 26] since they are quite different among themselves:

- In [23] the model has at $T = 0$ a glass transition which is of RFOT type, i.e. that is the prototype of structural glasses. This is different from the other quantum models with RFOT transitions where at low temperature the transition becomes first order [13, 74, 128]. However the ground state wave function in [23] is obtained from a classical-to-quantum mapping that does not allow for long range correlations between the particles, and this might be a simplification of the description of the system at very low temperature. The superglass phase shows a superfluid fraction which is small but strictly not zero. This small number could be not in contradiction with the results of Chapter 6, that found an insulating *lattice* glass.

- In [24, 26] instead, the transition to the amorphous solid is a spin-glass transition (a full replica symmetry breaking). Contrary to RFOT this transition is characterized by an order parameter which grows continuously and the relaxational dynamics approaching the glass transition would be very different from the one of classical supercooled liquids. In [24, 26] the superglass phase develops a superfluid fraction which is not necessarily small. A scenario compatible with this situation could imply that the pink line that at high temperature has a genuine RFOT transition, becomes of second order, as it happens for instance for the p-spin model in a longitudinal field [147].

Part C

Out-of-equilibrium quantum dynamics

8

Effective temperatures

In this Chapter we introduce the concept of effective temperature which has been developed in different contexts to characterize the out-of-equilibrium dynamics of classical and quantum systems. We start the analysis with the study of the out-of-equilibrium dynamics of classical glasses and we discuss the thermodynamical meaning of the effective temperature defined in that case on the basis of generalized fluctuation-dissipation relations. Then we discuss how the same definition has been applied in the context of dissipative quantum glassy systems. Finally we introduce the problem and the motivations for studying the quantum dynamics in isolated systems driven out of equilibrium, typically by a sudden change of a parameter in the Hamiltonian, i.e. a quantum quench. We discuss how the effective temperature has been defined in this context. In Section 8.1 we introduce the definitions of classical and quantum dynamical correlations and responses, as well as the associated FDRs. In Section 8.2 we outline different out-of-equilibrium situations. In particular we discuss the physical framework from which we borrow the definition of an effective temperature and the context where we aim to apply it, i.e. within quantum quenches.

8.1   Linear response theory in and out-of-equilibrium

8.1.1   Correlations and responses

In this section we provide the basic definitions of the dynamical correlations and responses in classical and quantum systems. Then, we recall the fluctuation-dissipation theorem in the two cases.

Classical systems

The dissipative dynamics of a classical system in contact with an environment is usually described by a Langevin equation. The motion of a particle of mass m coupled to a thermal bath at temperature T, which may be seen as a collection of harmonic oscillators, is characterized by the stochastic law for the position $x(t)$

$$m\ddot{x}(t) + \int_0^t dt\gamma(t - t')\dot{x}(t') = -V'(x(t)) + \xi(t) \tag{8.1}$$

$$\langle \xi(t)\xi(t') \rangle = T\gamma(t - t') \ , \tag{8.2}$$

where $\gamma(t)$ is the retarded friction and $\xi(t)$ is a time-dependent Gaussian random force with zero mean and correlations given by Eq. (8.2). The average in (8.2) is over the probability distribution of the noise and very often the friction is memory-less, $\gamma(t - t') = \gamma_0\delta(t - t')$. Equation (8.1) was

first introduced in order to describe the Brownian motion and later applied to model a variety of phenomena [148]. The equation can be generalized to study more complex situations like many-body interacting systems and/or systems subject to time dependent or non-conservative forces.

The Langevin equation is the starting point to study the dynamics of the system. Its solution $x_\xi^{sol}(t)$ encodes the trajectory of the particle for a particular realization of the noise $\xi(t)$. The macroscopic properties of the system are then recovered by averaging over the dynamical histories, namely over the distribution of the noise. The dynamical average can be recast within the generating functional Martin-Siggia-Rose-Janssen-De Dominicis-Peliti path integral formalism [149, 150]. The correlation function of two observables $A(t)$ and $B(t)$ is defined by

$$C^{AB}(t,t') = \langle A(t)B(t') \rangle \ , \tag{8.3}$$

where the average is over the probability of the possible paths. In general one considers connected correlations so that if $\langle \mathcal{O}(t) \rangle \neq 0$ the observable under consideration is replaced with $\mathcal{O}(t) \to \mathcal{O}(t) - \langle \mathcal{O}(t) \rangle$.

The response function is the average reaction of an observable A to a perturbation that modifies the potential $V \to V - h(t)B$ in Eq. (8.1) at a given instant of time t. At the linear order in the perturbing field h the response reads:

$$R^{AB}(t,t') = \frac{\delta \langle A(t) \rangle}{\delta h(t')} \Big|_{h=0} \ . \tag{8.4}$$

Clearly the instantaneous linear response is also a two-time function. Note that $R(t,t')$ vanishes if $t < t'$ because of the causality principle. Often one is interested more in the integrated dynamical susceptibility $\chi(t,t_w)$ than in the instantaneous response, defined as:

$$\chi^{AB}(t,t_w) = \int_{t_w}^{t} dt' \ R^{AB}(t,t') \ , \tag{8.5}$$

where we used the notation t_w to recall the notion of "waiting time" as it is often referred to in the literature. This quantity represents the response at time t to a step-like perturbation in the interval $t' \in [t_w, t]$. At equilibrium time translational invariance holds and the correlation and response functions are stationary, so $C(t,t') = C(t-t')$ and $R(t,t') = R(t-t')$.

Quantum systems

The dynamics of a quantum system and its bath is dictated by the Shrödinger equation. Langevin-like equations for quantum systems have been considered in several cases but they typically remain strongly model-dependent and there, no general formalism emerges. Differently from the classical case, the noise statistics generated by the quantum thermal bath is usually correlated in time. The real time dynamics of a system coupled to a bath is more conveniently studied, in and out of equilibrium, within the Schwinger-Keldysh formalism. Let us consider the case of a system described by the Hamiltonian $\hat{H}$ and at equilibrium, so that its density matrix is $\hat{\rho}(\beta) = \exp(-\beta\hat{H})/Z(\beta)$, where β is the inverse temperature. Dynamical correlations are usually more easily studied in the Heisenberg representation, which evolves the operator $\hat{A}(t)$ as given by

$$\hat{A}(t) = e^{i\hat{H}t}\hat{A}e^{-i\hat{H}t} \ . \tag{8.6}$$

Two-times correlations in equilibrium are defined by

$$C^{AB}(t,t') = \left\langle \hat{A}(t)\hat{B}(t') \right\rangle = \text{Tr}\left[\hat{\rho}(\beta)\hat{A}(t)\hat{B}(t') \right] \tag{8.7}$$

and clearly for generic $\hat{A}, \hat{B}$ one has $\left\langle \hat{A}(t)\hat{B}(t') \right\rangle \neq \left\langle \hat{B}(t')\hat{A}(t) \right\rangle$. Accordingly, we define the symmetric and antisymmetric correlations as follows:

$$C_{\pm}^{AB}(t,t') = \left\langle \left[\hat{A}(t), \hat{B}(t') \right]_{\pm} \right\rangle \tag{8.8}$$

where $[X,Y]_{\pm} = (XY \pm YX)/2$. Without loss of generality we consider operators with zero mean and we take $\hat{\mathcal{O}}(t) \to \hat{\mathcal{O}}(t) - \left\langle \hat{\mathcal{O}}(t) \right\rangle$ otherwise. The instantaneous linear response function is defined as for classical systems from the variation of the expectation $\left\langle \hat{A}(t) \right\rangle$ due to a perturbation which couples to the operator $\hat{B}$, up to the linear term. In and out of equilibrium it is related to the antisymmetric correlation by the Kubo formula [151]:

$$R^{AB}(t,t') = 2i\theta(t-t')C_{-}^{AB}(t,t') , \tag{8.9}$$

where $\theta(t)$ is the Heaviside function, $\theta(t < 0) = 0$ and $\theta(t > 0) = 1$, which enforces causality. Clearly at equilibrium time-translational invariance holds and correlations and responses are stationary, $C_{\pm}^{AB}(t,t') = C_{\pm}^{AB}(t-t')$. The same definition of the susceptibility (8.5) given for classical systems applies also to the quantum case. In the following we will be concerned with Fourier transforms of these quantities, defined for the stationary case as:

$$\tilde{f}(\omega) = \int_{-\infty}^{\infty} dt \; e^{-i\omega t} f(t) \qquad f(t) = \int_{-\infty}^{\infty} \frac{d\omega}{2\pi} \; e^{i\omega t} \tilde{f}(\omega) \tag{8.10}$$

Generalization to a non-stationary case can also be considered [115].

8.1.2 Fluctuation-Dissipation Theorem

The fluctuation-dissipation theorem (FDT) establishes a relation between the linear response of a given system to an external perturbation and the spontaneous fluctuations of the system in thermal equilibrium. The FDT provides fundamental model and observable-independent equations which the dynamics of the system has to obey. The search for the connection between fluctuations and dissipation started with Einstein who derived a relation between the mobility and the diffusion coefficient of a particle suspended in a fluid in his study on the Brownian motion. The mobility is in fact related to the frictional force generated against the action of a perturbation, while the diffusion constant is determined from the mean-square displacement, and it is defined by the unperturbed fluctuation. Eq. (8.2) is already a fluctuation-dissipation relation which express the equilibrium of the bath.

Classical systems

For classical systems at equilibrium FDT relates correlation and response as follows:

$$R^{AB}(t-t') = -T^{-1}\partial_t C^{AB}(t-t')\theta(t-t') . \tag{8.11}$$

The proof of this relation can be done in several ways, for instance within the generating functional formalism mentioned in the previous section. Integrating Eq. (8.11) FDT becomes:

$$\chi^{AB}(t-t_w) = T^{-1}(C^{AB}(0) - C^{AB}(t-t_w)) , \tag{8.12}$$

i.e. it establishes a linear relation between the susceptibility χ^{AB} and the correlation C^{AB}. A parametric plot of χ^{AB} versus C^{AB} constructed with fixed t_w and for increasing t is therefore a straight

line with slope $-1/T$. This relation, being independent of A and B and of the time scale considered, unambiguously defines the temperature of the system.

The departure from the linear relation between χ^{AB} and C^{AB} is the signal of a non equilibrium behavior. In fact out of equilibrium Eq. (8.12), or equivalently Eq. (8.11), does not hold. Moreover time-translational invariance is not guaranteed and the two-time dependences must be considered separately. One can still introduce the FDT fluctuation-dissipation ratio and define an effective temperature through it:

$$X^{AB}(t,t') \equiv \frac{T R^{AB}(t,t')}{\partial_{t'} C^{AB}(t,t')} \quad ; \quad T_{\text{eff}}^{AB}(t,t') \equiv \frac{T}{X^{AB}(t,t')} \,, \tag{8.13}$$

where we assumed $t > t'$ and T is the temperature of the thermal bath. One can consider for instance the situation in which the system is quenched from a high temperature T' to a low temperature T and it evolves in contact with a thermal bath at temperature T. If the dynamics is slow the system falls out-of-equilibrium because of its large relaxation time scales. The asymptotic value

$$X_{\infty}^{AB} = \lim_{t' \to \infty} \lim_{t \to \infty} X^{AB}(t,t') \text{ and the associated quantity } T_{\infty}^{AB} \equiv \frac{T}{X_{\infty}^{AB}} \,, \tag{8.14}$$

is often considered and it turned out to be particularly useful for critical quenches [152, 153, 154]. Clearly one can always define an effective temperature through a generalized fluctuation-dissipation relation (FDR), as in Eq. (8.14), however its interpretation is not straightforward and the possible thermodynamic significance of T_{eff} is not ensured a priori.

Quantum systems

In the following we reinstate $\hbar$ to make the classical limit $\hbar \to 0$ of the quantum FDT transparent. The quantum FDT is obtained by combining the Kubo formula (8.9) with the Kubo-Martin-Schwinger (KMS) conditions stating that correlation functions at equilibrium must satisfy the relation:

$$C^{AB}(t,t') = C^{BA}(t',t+i\hbar\beta) = C^{BA}(-t-i\hbar\beta,t') \,, \tag{8.15}$$

where analytic continuation to complex times is considered and Eq. (8.15) follows from the cyclic properties of the trace. In the frequency domain the KMS properties take the form:

$$\tilde{C}^{AB}(\omega) = \exp(-\beta\hbar\omega)\tilde{C}^{BA}(-\omega) \,, \tag{8.16}$$

from which the relation between symmetric and antisymmetric correlations are easily derived. As for classical observables, quantum FDT implies a relation between R^{AB} and C_+^{AB} through a function of the temperature [151]. The quantum FDT can be expressed in the time domain as follows:

$$R^{AB}(t) = \frac{i}{\hbar} \int_{-\infty}^{\infty} \frac{d\omega}{\pi} e^{-i\omega t} \tanh\left(\frac{\beta\hbar\omega}{2}\right) \tilde{C}_+^{AB}(\omega) \,, \tag{8.17}$$

and the classical FDT is recovered when $\hbar \to 0$. Eq. (8.17) reveals the double source of fluctuations which may be attributed to thermal (β) or quantum ($\hbar$) effects. Fourier transforming Eq. (8.17) the quantum FDT can be recast in a compact form in the frequency domain:

$$\hbar \, \text{Im}\tilde{R}^{AB}(\omega) = \tanh\left(\frac{\beta\hbar\omega}{2}\right) \tilde{C}_+^{AB}(\omega) \,. \tag{8.18}$$

8.2 Non-equilibrium dynamics

8.2.1 Classical glasses

As we mentioned several times, glasses fall out of equilibrium, because from their very definition, the equilibration time exceeds the experimental time. The hallmark of their out-of-equilibrium dynamics is the aging behavior. Aging means that the older the systems is, the slower its relaxation dynamics becomes, taking longer to forget the past. The age of a system is the time spent in the phase under study. Generally, in equilibrium, one does not specify the reference time at which the system is prepared in the conditions after which it is let evolve, or this time is implicitly taken to be $t^* = -\infty$. On the contrary, out of equilibrium this time is a fundamental reference for the definition of the age of the system. In the context of thermal or quantum sudden quenches, this is the time of the quench and here and thereafter we will assume $t^* = 0$.

The analysis in terms of generalized FDRs in mean-field glasses brought to a deeper understanding of fluctuations in these systems and it made possible a comparison with replica/cavity calculations describing static thermodynamical properties [27, 148]. Fig. 8.1 shows a sketch of the equilibrium ($T \gtrsim T_d$) and of the aging ($T < T_d$) dynamics of a mean-field glassy system, of RFOT type. One can think of the dynamical correlation reported there as a spin-spin correlation for the p-spin model or a density-density correlation for Lennard-Jones-like interacting particles. The left panel presents the stationary correlation as a function of time for different temperatures. Similarly to what we
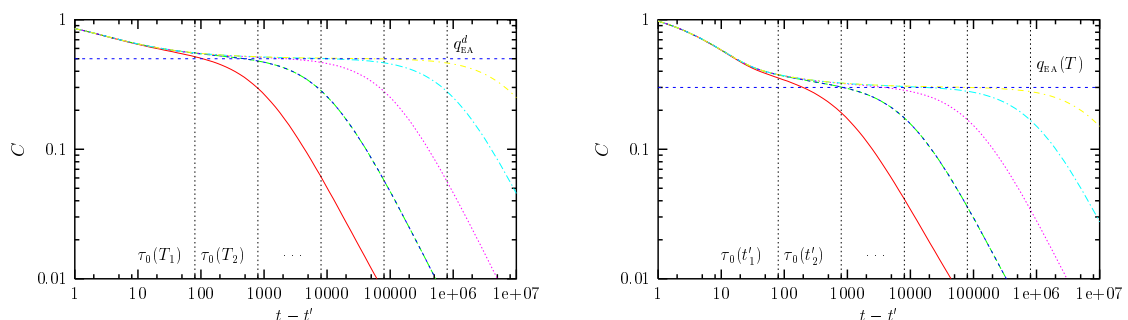
Figure 8.1: *Left panel*: Stationary relaxation of the correlation for $T_1 \gtrsim T_2 \gtrsim \cdots \gtrsim T_d$. *Right panel*: Aging decay of the correlation at fixed $T < T_d$ for several t_w. Picture from [148].

discussed in Section 5.1.4 the decay presents a two-step relaxation and the approach to the plateau is independent of T. Moreover the plateau, as soon as it appears, has a finite height, while its length increases with the inverse temperature β. The right panel of Fig. 8.1 shows the out-of-equilibrium aging regime that we aim to discuss in this context. Observables in the aging phase depend upon two times and Fig. 8.1 reports the correlation with fixed $t' = t_w$ (the age of system) as a function of $t - t'$, for a fixed temperature and for several waiting times t_w. For long t' the correlation displays a separation of time scales. It first reaches in a t'-independent manner a plateau $q_{EA}(T)$ which depends upon temperature. Then the time to relax below the plateau value $q_{EA}(T)$ increases with t'. Finally, for each t' there is a sufficiently large time after which the correlation decays to zero. This phenomenology was referred to as a *weak ergodicity-breaking scenario* suggesting that at fixed t' there exists a crossover in t between two time-scales regimes. This crossover is identified by a characteristic

time $\tau(t')$ which is an increasing function of t' defined by the model under study. In particular for $t > t'$ and $t - t' \ll \tau(t')$ the correlation decays from 1 to $q_{EA}(T)$ in a stationary way. While for larger $t - t'$ it relaxes from $q_{EA}(T)$ to zero in a t'-dependent manner.

Let us discuss this out-of-equilibrium dynamics in terms of generalized FDRs which demonstrated to be very fruitful. Following the equilibrium relation (8.12) one can study the relation between $\chi(t, t_w)$ and $C(t, t_w)$ at different times (t, t_w). Plotting $\chi(t, t_w)$ and $1 - C(t, t_w)$ at fixed t_w as a function of $t - t_w$ one obtains the plots shown in the left panel of Fig. 8.2. The curves go together and also coincide for different t_w, until $t - t_w$ reaches a certain time which is identified as $\tau(t_w)$. Then, in the fastest time scale, $t - t_w < \tau(t_w)$ FDT holds. For larger $t - t_w$ the two curves differ and the behavior depends on t_w. In the slowest time scale FDT does not hold. What turned out to be particularly remarkable is the way in which these non-equilibrium effects can be recast in a modification of FDT. The starting point is suggested by the analytical solution of mean-field models, from which it follows that in the limit $t_w \to \infty$, after that $N \to \infty$, where N is the size of the system, it holds:

$$\lim_{t_w \to \infty, C(t,t_w)=C} \chi(t, t_w) = \chi(C) \; . \tag{8.19}$$

This means that in the limit $t > t_w \to \infty$ the susceptibility as a function of C reaches a limit curve. Motivated by Eq. (8.12) one can define an effective temperature as follows:

$$T_{\text{eff}}(C) = -[\chi'(C)]^{-1} \; , \tag{8.20}$$

that is in general a function of C. Under appropriate circumstances this quantity has the properties of a temperature in the sense that it can be measured by a suitable thermometer [28] and it determines the direction of the heat flow when other systems at different temperatures are put in contact. The graphical interpretation of this relation is easy. One fixes t_w and then plots $\chi(t, t_w)$ vs $C(t, t_w)$ letting t vary from t_w to ∞. Assuming that $C(t_w, t_w) = 1$ and $C(\infty, t_w) = 0$ and defining $\chi(\infty, t_w) = \bar{\chi}$ the curve will join the point $(1, 0)$ and $(0, \bar{\chi})$. The right panel of Fig. 8.2 shows in red and in green this construction for two different t_w. The solid blue line represents the limiting curve obtained in mean field structural glasses (RFOT-like) when $t_w \to \infty$. The very suggesting result concerns the asymptotic curve, made by two straight lines. The slope of the line for larger values of C concides with the "equilibrium" $-1/T$, while the second is identified with an effective temperature which governs the out-of-equilibrium aging regime. The dashed and dot-dashed lines represent, respectively, the results for the out-of-equilibrium dynamics of mean field systems undergoing domain growth and models with full replica-symmetry breaking, like the Sherrington-Kirpatrick model.

Let us conclude by mentioning that many works have been devoted to the study of the out-of-equilibrium dynamics of classical systems driven by external currents [155], and their analysis in terms of FDRs. Note that in the driven case the non-equilibrium is a consequence of an external force, differently from glasses or coarsening systems, where the large time scales of the system do not allow for equilibration.

8.2.2   Open quantum systems

The analysis of the out-of-equilibrium dynamics through generalized FDRs in quantum dissipative systems is a field much less explored and understood than its classical counterpart. However, it is recently receiving growing consideration. Early works focused on quantum mean-field glassy systems, described by Hamiltonians of the form considered in the previous Chapters, i.e. a classical glassy term and a transverse field or a simple non-commuting term (we denote with Γ its strength) [156, 115, 157].
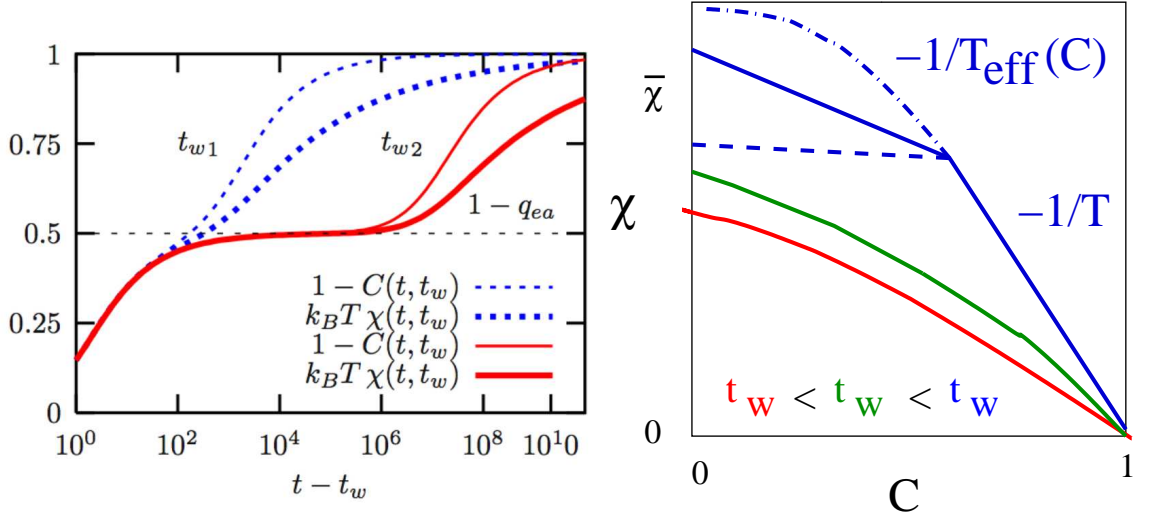
Figure 8.2: *Left panel*: $\chi(t, t_w)$ and $1 - C(t, t_w)$ at t_w fixed as a function of $t - t_w$ for two different t_w. *Right panel*: Parametric plot of $\chi(t, t_w)$ vs $C(t, t_w)$ at fixed t_w in a slowly relaxing out-of-equilibrium system. Different curves represent different values of t_w. The blue curve is the limit $t_w \to \infty$ in three different kinds of models. The solid line represents mean-field structural glasses. Figure from [148].

As in the classical case the out-of-equilibrium behavior is induced by a quench from the disordered to the ordered phase, which may be performed via a sudden change of the temperature or of Γ, the system being in contact with a thermal bath.

Let us summarize the results obtained for the real-time dynamics in mean-field quantum glasses [115, 157], that complement the discussion of the previous Chapters. Like in classical systems the dynamical correlations of mean-field quantum glasses in the ordered phase develop a plateau at intermediate times. The relaxation though, is modulated by quantum oscillations at very short times t (and for any t_w) which later disappear. Also in the quantum case the comparison between responses and correlations in the low-temperature phase is particularly instructive. It turns out that for $t - t_w \ll t_w$ correlation and response functions satisfy the quantum FDT (8.17), with the temperature of the thermal bath. The two quantities then display a (quantum) equilibrium-like behavior, until the correlation reaches the plateau value. In the aging regime, quantum FDT does not hold, similarly to the classical case. However, a parametric plot in which the integrated response is compared to the classical correlation, as explained in the previous sections, shows that they satisfy a *classical* FDR with an effective temperature $T_{\text{eff}} > T$ that depends on T and Γ, the strength of quantum fluctuations (and on the properties of the bath).

As for the classical case, a different and very natural set-up in which the out-of-equilibrium dynamics of quantum systems takes place is when driving currents are induced by unbalanced reservoirs. Also in this context, the study of the non-equilibrium dynamics in terms of generalized FDRs is receiving attention. In particular mesoscopic systems subject to time dependent magnetic/electric fields or currents have been considered [158, 159] but also the competition of driving currents and glassiness have been addressed [157]. In these works it was shown that for gently driven systems a constant effective temperature emerges.

8.2.3   Quantum quenches in isolated systems

Quite important differences compared to the cases discussed in the previous sections emerge when studying isolated systems, whose dynamics occur at constant energy. In the case of quantum quenches, the system is not described by a thermal equilibrium state - it is a generic highly excited state, different from a Gibbs density matrix $\hat{\rho}(\beta)$ - and the dynamics is unitary. The study of this non-equilibrium quantum dynamics and the issue of thermalization in this situation, in the limit of long times and large system sizes, is currently attracting a lot of interest [160, 161, 162, 163, 164, 165, 166, 33, 167, 168, 169, 170, 171]. It is a quite well-established empirical fact that a large enough isolated system reaches equilibrium and is able to act as a thermal bath for a part of itself. In the classical case this is usually justified in terms of a chaotic dynamics, that ensures ergodicity in phase space and thermalization in terms of a microcanonical ensemble [172]. This implies also that a large subpart of a much larger system thermalizes to a canonical ensemble. How this is justified in a quantum setting remains an open and fundamental problem, which was actually posed more that 90 years ago [173, 174]. Indeed, the analogy between classical and quantum systems hides many subtleties and many concepts, as for instance the integrals of motions for the dynamics, deserve a separate consideration.

Without going in the details of the state of the art of the subject, which is very broad, here we aim to recall only few notions that will be important for the study of Chapter 9 and that represent a bridge to the previous discussion. These notions concern the definitions of effective temperatures that have emerged in this context. In quantum quenches the system is prepared at time $t = 0$ at equilibrium in the ground state of $\hat{H}(\Gamma_0)$, that we denote $|0\rangle_{\Gamma_0}$, and afterwards it is let evolve, isolated, with $\hat{H}(\Gamma)$, where $\Gamma \neq \Gamma_0$. The sudden change in the parameter Γ pushes the system out of equilibrium and injects an extensive amount of energy into it. Note that the initial condition $|\psi(t = 0)\rangle = |0\rangle_{\Gamma_0}$ is the most studied but one could consider much more general protocols. Very often quantum quenches have been studied (and we will do it next) in low-dimensional and integrable systems and clearly this context is very different from that of mean-field glasses. However, in both cases, the desire to characterize the out of equilibrium behavior has naturally called for an operative definition of effective temperature T_{eff}, in order to understand if the behavior of the system could be described with an effective equilibrium description at the temperature $T = T_{\text{eff}}$. Instead of taking inspiration from FDRs, in quantum quenches T_{eff} is usually defined through the energy of the system. This choice is the most natural, also compared to that of classical systems, as it reflects a fundamental property of the dynamics which occurs at constant energy. On the contrary, when the system is in contact with a thermal bath, the FDRs are very naturally defined. The dynamics is dissipative, the temperature is fixed and it appears explicitly in the FDT. Note however that FDRs hold also for an isolated dynamics once that the initial condition is an equilibrium thermal (Gibbs) state.

Let us specify the common definition of $T_{\text{eff}} = T_{\text{eff}}^E$ in quantum quenches. Since the system dynamics is unitary the energy is conserved and one can define an implicit equation for T_{eff}^E as follows [163, 164, 166, 33]:

$$\left\langle \hat{H}(\Gamma) \right\rangle_{\mathcal{Q}} = \left\langle \hat{H}(\Gamma) \right\rangle_{T = T_{\text{eff}}^E} \,, \tag{8.21}$$

where the average on the l.h.s. is over the ground state of $\hat{H}(\Gamma_0)$ while on the r.h.s. it is over an equilibrium state of $\hat{H}(\Gamma)$ at temperature $T = T_{\text{eff}}^E$. Note that Eq. (8.21) is time independent because the energy is a constant of motion, but in general one has to deal with time varying quantities $\left\langle \hat{\mathcal{O}}(t) \right\rangle_{\mathcal{Q}}$ and eventually study the stationary limit. In this way it is possible to compare generic stationary averages $\left\langle \hat{\mathcal{O}} \right\rangle_{\mathcal{Q}} = \lim_{t \to \infty} \left\langle \hat{\mathcal{O}}(t) \right\rangle_{\mathcal{Q}}$ after the quench with the thermal ones $\left\langle \hat{\mathcal{O}} \right\rangle_{T = T_{\text{eff}}^E}$ and see whether they are equal or not. Of course, if the two averages coincide this would support an

effective thermal-like behavior of the system, with temperature $T = T_{\text{eff}}^E$, but this is not always the case [163, 164, 166, 33].

It turns out that when the system is integrable the situation is quite subtle [175, 176, 169]. Suppose to be able to write the Hamiltonian in the diagonal form:

$$\hat{H}(\Gamma) = \sum_k \epsilon_k(\Gamma) \, \hat{c}_k^\dagger \hat{c}_k \tag{8.22}$$

where the $\hat{c}_k$'s are creation operators for free bosonic or fermionic particles (here k is just an index to label the degrees of freedom) and let us call $\hat{n}_k = \hat{c}_k^\dagger \hat{c}_k$ their number. Clearly it holds $[\hat{n}_k, \hat{H}] = 0$, implying that the set $\{\hat{n}_k\}$ is a set of constants of motion for the dynamics induced by $\hat{H}(\Gamma)$, regardless of the state of the system. When the quench is performed this enforces a large number of integrals of motions that constraint the dynamics. Similarly to Eq. (8.21) one can then define a set of effective temperatures $\{T_{\text{eff}}^k\}$, one for each k, from the equality $\langle \hat{n}_k \rangle_{\mathcal{Q}} = \langle \hat{n}_k \rangle_{T=T_{\text{eff}}^k}$. These quantities proved to be particular meaningful since they naturally appear in the computation of (stationary and non) expectation values [175, 176, 169]. It was in fact suggested [175] that the stationary behavior of the system after quenches towards Hamiltonians of the form (8.22) is captured by the density matrix $\hat{\rho}_{\text{GGE}}$ that is obtained by maximizing the von Neumann entropy $S = -\text{Tr}[\hat{\rho} \log \hat{\rho}]$ and satisfying the constraints on the expectation values of $\langle \hat{n}_k \rangle$. This density matrix is of the form:

$$\hat{\rho}_{\text{GGE}} = \frac{1}{Z} \exp[-\sum_k \lambda_k \hat{n}_k] \, , \tag{8.23}$$

where $\lambda_k = \epsilon_k / T_{\text{eff}}^k$ are Lagrange multipliers that enforce the values of the integrals of motion. Although $\hat{\rho}_{\text{GGE}}$ is not in a strict sense the state that is evolving, very often the averages in the long time limit after the quench coincide with averages over the density matrix (8.23). The ensemble (8.23) is known as Generalized Gibbs Enseble (GGE). Despite the definition of all the temperatures T_{eff}^k is quite natural and the conjecture that Eq. (8.23) provides the correct long-time averages is very reasonable it remains to be understood whether out of this infinite set of temperatures one could extract few relevant "thermodynamic" quantities and how they stand, together with T_{eff}^E, with respect to the possible definition of effective temperatures derived from FDRs. In the next Chapter we will address this issue for the particular case of the transverse field Ising chain.

9

Critical quenches in the transverse field Ising chain

In this Chapter we study the unitary dynamics of the transverse field Ising chain after a quantum quench, i.e. after a sudden change in the parameter of the Hamiltonian that drives the system out of equilibrium. Focusing on critical quenches, we study several observables. We characterize the time-dependent behavior of correlations and responses, mainly in the stationary regime. We study and compare the different effective temperatures proposed in Chapter 8, with particular emphasis on the analysis of generalized FDRs. In Section 9.1 we introduce the model as well as the procedure to exactly solve the spectrum and compute the dynamics. In Sections 9.2, 9.3 and 9.4 we discuss respectively the dynamics of the transverse magnetization, of the global transverse magnetization and of the order parameter. In Section 9.5 we discuss our results.

9.1 The Ising model and its dynamics after a quantum quench

9.1.1 The model

We consider the transverse field Ising chain of finite lenth L, described by the Hamiltonian:

$$\hat{H}(\Gamma) = -J \sum_{i=1}^{L} \left[\hat{\sigma}_i^x \hat{\sigma}_{i+1}^x + \Gamma \, \hat{\sigma}_i^z \right] , \qquad (9.1)$$

where we assume periodic boundary conditions $\hat{\sigma}_{L+1}^x = \hat{\sigma}_1^x$ and the length L of the chain to be even. Note that the Hamiltonian (9.1) is precisely of the form considered, for instance, for the quantum annealing in Chapter 1, the only difference being that here, in (9.1), we exchanged the role of the z and x-components of the Pauli matrices in order to adopt a standard convention for the model. The reason for this convention, and for which we follow it here, consists in thinking of the transverse field term as the diagonal part of $\hat{H}$ and then to introduce a transformation able to handle the interacting part and to turn the Hamiltonian into a quadratic form. In what follows we set $J, \hbar, k_B = 1$ and we measure time in units of $\hbar/J$ and the temperature T in units of J/k_B. The Hamiltonian can be diagonalized performing three transformations. First we introduce Jordan-Wigner fermionic operators $\hat{c}_j^\dagger, \hat{c}_j$ [177]:

$$\hat{\sigma}_j^+ = \hat{c}_j^\dagger \exp \left[i\pi \sum_{k=1}^{j-1} \hat{c}_k^\dagger \hat{c}_k \right] , \qquad (9.2)$$

where $\hat{\sigma}_j^+ = (\hat{\sigma}_j^x + i\hat{\sigma}_j^y)/2$. Note that in terms of the fermions $\hat{c}_j^\dagger$, $\hat{c}_j$, the operator $\hat{\sigma}_j^z$ reads:

$$\hat{\sigma}_j^z = 2\hat{c}_j^\dagger \hat{c}_j - 1 \ , \tag{9.3}$$

and $\hat{\sigma}_j^x = \hat{\sigma}_j^+ + (\hat{\sigma}_j^+)^\dagger$ follows from Eq. (9.2). After this change of variables the Hamiltonian reads:

$$\hat{H}(\Gamma) = -J \sum_{i=1}^{L-1} \left[\hat{c}_i^\dagger \hat{c}_{i+1} + \hat{c}_i^\dagger \hat{c}_{i+1}^\dagger + h.c. \right] - 2\Gamma \sum_{i=1}^{L} \hat{c}_i^\dagger \hat{c}_i + (-1)^{N_F} \left[\hat{c}_L^\dagger \hat{c}_1 + \hat{c}_L^\dagger \hat{c}_1^\dagger + h.c. \right] \ , \tag{9.4}$$

where $N_F = \sum_{i=1}^{L} \hat{c}_i^\dagger \hat{c}_i$ is the number of fermions. From the last term it follows that when N_F is odd periodic boundary conditions on the fermions must be enforced and antiperiodic otherwise. The Hamiltonian conserves the parity of fermions $N_F\%2$, and we restrict to the even sector which contains the ground state. Note that however the restriction to one of the two sectors is justified only when one considers expectation values of operators defined by an even number of fermions. Eq. (9.4) is the sought-for quadratic Hamiltonian. However in order to diagonalize it the next step is to perform a Fourier transformation

$$\hat{c}_j = \frac{1}{\sqrt{L}} \sum_{k=1}^{L} e^{ikj} \hat{c}_k \qquad k = \pm \frac{\pi(2n+1)}{L} \tag{9.5}$$

with $n = 0, \ldots, L/2 - 1$. In the l.h.s. of Eq. (9.5) we consider the fermions in real space and in the r.h.s. the fermions in Fourier space. Finally the Hamiltonian is diagonalized by a Bogoliubov rotation:

$$\begin{pmatrix} \hat{\gamma}_k^\Gamma \\ \hat{\gamma}_{-k}^{\Gamma\,\dagger} \end{pmatrix} = \begin{pmatrix} \cos\theta_k^\Gamma & -i\sin\theta_k^\Gamma \\ -i\sin\theta_k^\Gamma & \cos\theta_k^\Gamma \end{pmatrix} \begin{pmatrix} \hat{c}_k \\ \hat{c}_{-k}^\dagger \end{pmatrix} = \mathcal{R}(\theta_k^\Gamma) \begin{pmatrix} \hat{c}_k \\ \hat{c}_{-k}^\dagger \end{pmatrix} \tag{9.6}$$

where $\hat{\gamma}_k^\Gamma$ represents fermionic quasi-particles and

$$\tan 2\theta_k^\Gamma = \frac{\sin k}{\Gamma - \cos k} \ . \tag{9.7}$$

In terms of $\hat{\gamma}_k^\Gamma$ the Hamiltonian reads:

$$\hat{H}(\Gamma) = \sum_{k>0} \epsilon_k(\Gamma) \left(\hat{\gamma}_k^{\Gamma\,\dagger} \hat{\gamma}_k^\Gamma + \hat{\gamma}_{-k}^{\Gamma\,\dagger} \hat{\gamma}_{-k}^\Gamma - 1 \right) \ , \tag{9.8}$$

with $\epsilon_k(\Gamma) = 2\sqrt{\Gamma^2 - 2\Gamma\cos k + 1}$ being the dispersion law of the quasiparticles. Fig. 9.1 shows the dispersion relation $\epsilon_k(\Gamma)$ as a function of $k \in [-\pi, \pi]$ for different Γ. At $\Gamma = 1$ the spectrum is gapless. The ground state of the system $|0\rangle_\Gamma$ is the vacuum of quasiparticles, $\hat{\gamma}_k^\Gamma |0\rangle_\Gamma = 0 \ \forall k$ and as a function of the fermions $\hat{c}_k$ takes the form:

$$|0\rangle_\Gamma = \prod_{k>0} \left(\cos\theta_k^\Gamma \, \hat{c}_k^\dagger \hat{c}_{-k}^\dagger + i\sin\theta_k^\Gamma \right) |\tilde{0}\rangle \ , \tag{9.9}$$

where $|\tilde{0}\rangle$ is the vacuum of fermions $\hat{c}_k |\tilde{0}\rangle = 0$. Then, the structure of $|0\rangle_\Gamma$ is that of a superposition of Cooper pairs $\hat{c}_k^\dagger \hat{c}_{-k}^\dagger$. At zero temperature and in the thermodynamical limit, the system is characterized by a quantum phase transition at $\Gamma = 1$ which separates a paramagnetic phase (PM, $\Gamma > 1$) $\langle \hat{\sigma}_i^x \rangle = 0$ from a ferromagnetic phase (FM, $\Gamma < 1$) with spontaneous symmetry breaking $\langle \sigma_i^x \rangle \neq 0$ and long-range order along the x direction. $\langle \sigma_i^z \rangle \neq 0$ for all $\Gamma > 0$.

9.1.2   Equilibrium and non-equilibrium dynamics

Thanks to the transformations (9.2), (9.5) and (9.6) the Hamiltonian (9.1) becomes diagonal, Eq. (9.8), which makes the system and its dynamics exactly solvable. However, the possibility to arrive at
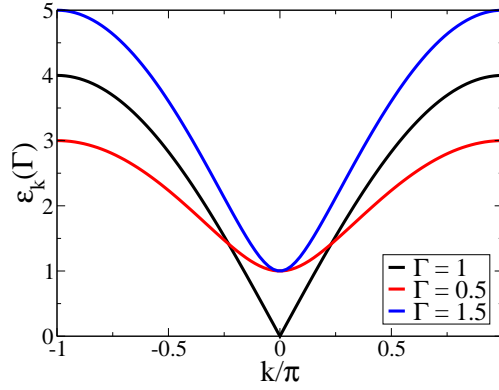
Figure 9.1: Dispersion relation $\epsilon_k(\Gamma)$ as a function of k for different values of the transverse field Γ.

this form is not just a fortunate chance, but has a major effect on the physics of the problem. Clearly the building blocks of the model are the quasiparticle operators $\hat{\gamma}_k^\Gamma$ associated to $\hat{H}(\Gamma)$ and they represent the key to access all (thermo)dynamical properties. These quasi-particles evolve trivially in the Heisenberg picture:

$$\left(\begin{array}{c} \hat{\gamma}_k^\Gamma(t) \\ \hat{\gamma}_{-k}^{\Gamma\,\dagger}(t) \end{array} \right) = \left(\begin{array}{cc} e^{-i\epsilon_k(\Gamma)t} & 0 \\ 0 & e^{i\epsilon_k(\Gamma)t} \end{array} \right) \left(\begin{array}{c} \hat{\gamma}_k^\Gamma \\ \hat{\gamma}_{-k}^{\Gamma\,\dagger} \end{array} \right) = \mathcal{U}(\epsilon_k^\Gamma, t) \left(\begin{array}{c} \hat{\gamma}_k^\Gamma \\ \hat{\gamma}_{-k}^{\Gamma\,\dagger} \end{array} \right) . \qquad (9.10)$$

This property is completely independent of the state of the system under study and, in a similar way, the average number of quasiparticles $\langle \hat{n}_k^\Gamma(t) \rangle = \left\langle \hat{\gamma}_k^{\Gamma\,\dagger}(t)\hat{\gamma}_k^\Gamma(t) \right\rangle = \langle \hat{n}_k^\Gamma \rangle$ is a constant of motion regardless of the measure that determines the expectation value. At equilibrium the dynamics for a given observable $\mathcal{O}(t)$ is then solved by expressing $\mathcal{O}(t)$ in terms of the quasiparticles $\hat{\gamma}_k^\Gamma(t)$ (it is easier through the intermediate transformation into $\hat{c}_k^\Gamma(t)$ fermions) and then calculating the expectation values that are traced back to some function of the integrals of motion $\langle \hat{n}_k^\Gamma \rangle$.

In the quench set-up the system is prepared at $t = 0$ in the ground state $|0\rangle_{\Gamma_0}$ of $\hat{H}(\Gamma_0)$, while it subsequently evolves, isolated, with $\hat{H}(\Gamma)$. The quench from Γ_0 to Γ injects an extensive amount of energy into the system which is henceforth conserved. A convenient way to compute correlations in this situation consists in expressing all the (time-dependent) observables in terms of the operators $\hat{\gamma}_k^{\Gamma_0}(t)$ of the original Hamiltonian, $\hat{H}(\Gamma_0)$. The merit of this procedure is evident when computing the expectation values over $|0\rangle_{\Gamma_0}$, because by definition $|0\rangle_{\Gamma_0}$ is the vacuum of $\hat{\gamma}_k^{\Gamma_0}(t)$ and this simplifies at this stage the calculations. The mapping between the quasiparticles of $\hat{H}(\Gamma)$ and those of $\hat{H}(\Gamma_0)$ consists in a rotation of the suitable Bogoliubov angles. Note that $\mathcal{R}(\theta_k^\Gamma)\mathcal{R}^\dagger(\theta_k^{\Gamma_0}) = \mathcal{R}(\theta_k^\Gamma - \theta_k^{\Gamma_0}) \equiv \mathcal{R}(\delta_k(\Gamma, \Gamma_0))$.

The time evolution of the fermionic operators $\hat{c}_k(t)$ can be finally expressed as follows:

$$\left(\begin{array}{c} \hat{c}_k(t) \\ \hat{c}_{-k}^\dagger(t) \end{array} \right) = \mathcal{R}^\dagger(\theta_k^\Gamma)\mathcal{U}(\epsilon_k^\Gamma, t)\mathcal{R}(\delta_k(\Gamma, \Gamma_0)) \left(\begin{array}{c} \hat{\gamma}_k^{\Gamma_0} \\ \hat{\gamma}_{-k}^{\Gamma_0\,\dagger} \end{array} \right) \equiv \left(\begin{array}{cc} u_k^{\Gamma,\Gamma_0}(t) & -(v_k^{\Gamma,\Gamma_0}(t))^* \\ v_k^{\Gamma,\Gamma_0}(t) & (u_k^{\Gamma,\Gamma_0}(t))^* \end{array} \right) \left(\begin{array}{c} \hat{\gamma}_k^{\Gamma_0} \\ \hat{\gamma}_{-k}^{\Gamma_0\,\dagger} \end{array} \right) .$$
$$(9.11)$$

Thanks to this mapping one can then express all the averages in terms of $u_k^{\Gamma,\Gamma_0}(t)$ and $v_k^{\Gamma,\Gamma_0}(t)$ defined above, where, here and in the following, the expectation values $\langle \bullet \rangle = {}_{\Gamma_0}\langle 0| \bullet |0\rangle_{\Gamma_0}$ are over the initial condition $|0\rangle_{\Gamma_0}$.

In the out-of-equilibrium situation induced by the quench protocol, all the observables but the integrals of motion (and their functions) show a non-stationary behavior. After a transient (studied in Ref. [178,

179] for the chain with free boundaries) the system reaches an asymptotic stationary regime. The time scale of this transient depends on the observable under study and on the initial and the final condition, Γ_0 and Γ.

Recalling the notation of Chapter 8 (see Eq. (8.8)) for two-time quantities, natural choices for A and B are the order parameter $\hat{\sigma}_i^x$ and the transverse magnetization $\hat{\sigma}_i^z$. We will denote by $C_{\pm}^x(t)$ and $C_{\pm}^z(t)$ the respective autocorrelation functions. Moreover, we will also consider the global magnetization $\hat{M}(t) = 1/L \sum_{i=1}^L \hat{\sigma}_i^z$ and thus $C_{\pm}^M(t)$. Let us here introduce an important property that distinguishes these operators [180, 165]: $\hat{\sigma}_i^x$ is non-local with respect to the quasi-particles in the sense that it has non-vanishing matrix elements with most of the states of the Hilbert space. $\hat{\sigma}_i^z$, instead, is local in the same variables, in the sense that it couples only few states. This distinction should appear more transparent if one recalls their expression in terms of the Jordan-Wigner fermions (9.2): $\hat{\sigma}_i^z$ is a quadratic function of the $\hat{c}_k$, and thus also of the excitations $\hat{\gamma}_k^\Gamma$, while $\hat{\sigma}_i^x$ is the product of a string of fermions and therefore it is not local in these operators that define the natural basis of the Hilbert space.

9.1.3   Effective temperatures for the Ising model

Let us recall here the various definitions of effective temperatures given in Chapter 8 and make them specific for this case. As we anticipated in Section 9.1.2, because of the quench and of the unitary dynamics, the energy of the system is conserved. This suggests to compare this energetic excess with an equilibrium thermal average. The effective temperature $T_{\text{eff}}^E(\Gamma, \Gamma_0)$ given by this energetic balance is implicitly defined by

$$\int_0^\pi \frac{\mathrm{d}k}{2\pi} \epsilon_k(\Gamma) \cos \Delta_k(\Gamma, \Gamma_0) = \int_0^\pi \frac{\mathrm{d}k}{2\pi} \epsilon_k(\Gamma) \tanh \frac{\epsilon_k(\Gamma)}{2T_{\text{eff}}^E(\Gamma, \Gamma_0)} \ , \tag{9.12}$$

with $\Delta_k(\Gamma, \Gamma_0) = 2\delta_k(\Gamma, \Gamma_0)$ and

$$\cos \Delta_k(\Gamma, \Gamma_0) = \frac{4 \left[\Gamma\Gamma_0 - (\Gamma + \Gamma_0) \cos k + 1 \right]}{\epsilon_k(\Gamma) \epsilon_k(\Gamma_0)} \ . \tag{9.13}$$

In Eq. (9.12) the l.h.s. represents the average $\left\langle \hat{H}(\Gamma) \right\rangle$ over the state $|0\rangle_{\Gamma_0}$, while the r.h.s. is the average $\left\langle \hat{H}(\Gamma) \right\rangle_{T=T_{\text{eff}}^E}$ over the equilibrium density matrix $\hat{\rho} = \exp[-\hat{H}/T_{\text{eff}}^E]/Z$. The angle $\Delta_k(\Gamma, \Gamma_0)$ is a crucial quantity that encodes the dependence on the initial state and fixes the non-thermal statistics of the excitations created at $t = 0$. Requiring that the integrands of (9.12) equalize, i.e. that $\cos \Delta_k(\Gamma, \Gamma_0) = \tanh \frac{\epsilon_k(\Gamma)}{2T_{\text{eff}}^k(\Gamma, \Gamma_0)}$, defines a mode-dependent effective temperature T_{eff}^k. This is nothing but the temperature that controls the population of the k-th mode and could be derived equivalently by imposing that each mode k is populated according to a Fermi distribution with temperature $T_{\text{eff}}^k(\Gamma, \Gamma_0)$:

$$\left\langle \hat{n}_k^\Gamma \right\rangle = \left\langle \hat{n}_{-k}^\Gamma \right\rangle = \frac{1}{1 + e^{\epsilon_k(\Gamma)/T_{\text{eff}}^k}} \ . \tag{9.14}$$

Note that in the thermodynamic limit $T_{\text{eff}}^k(\Gamma, \Gamma_0)$ is actually a continuous function of k. This means that the diagonal structure of $\hat{H}(\Gamma)$ (i.e. the integrability of the model) naturally introduces an infinity of "microscopic" temperatures, each one associated with a particular integral of motion $\left\langle \hat{n}_k^\Gamma \right\rangle$. The relevance of these temperatures is transparent recalling that all expectations values, in the end, are recovered from functions of $\left\langle \hat{n}_k^\Gamma \right\rangle$. However, for generic observables, these functions are typically complex combinations of multidimensional integrals, determinants, oscillatory factors in times, etc.

The quest for understanding whether, out of this, one could extract a single (or a few) "macroscopic" temperature, and the relation with $T_{\text{eff}}^E(\Gamma, \Gamma_0)$, is definitely an important issue. This led us to consider generalized FDRs, as in Chapter 8, in order to test the physical properties of the system in the framework of the linear response theory. In the following we will focus on the stationary regime after the quench. Because of time-translational invariance we can easily move from the time to the frequency domain. We study correlations and responses enforcing the quantum FDR relation

$$\hbar \, \text{Im} \tilde{R}^{AB}(\omega) = \tanh\left(\frac{\beta_{\text{eff}}^{AB}(\omega)\,\hbar\,\omega}{2}\right) \tilde{C}_+^{AB}(\omega) \, , \tag{9.15}$$

where we assumed stationary $C_+^{AB}(t)$ and $R^{AB}(t)$. Eq. (9.15) allows us to define an observable dependent effective temperature $\beta_{\text{eff}}^{AB}(\omega)$. Note that a priori one must explicitly take into account the frequency dependence because in the non-equilibrium case the temperature varies with the time scale. The study of the ω dependence clearly provides an important piece of information about the dynamical scales of the system with respect to a given observable. As we mentioned we could also consider a time-dependent formulation of the quantum FDT, which takes a slightly more complicated form:

$$R^{AB}(t) = \frac{i}{\hbar} \int_{-\infty}^{\infty} \frac{\mathrm{d}\omega}{\pi} \mathrm{e}^{-i\omega t} \tanh\left(\frac{\beta_{\text{eff}}^*\,\hbar\,\omega}{2}\right) \tilde{C}_+^{AB}(\omega) \, , \tag{9.16}$$

where we enforced a single effective temperature β_{eff}^* (we removed the AB superscript to simplify the notation but the dependence on the observable remains). Note that Eqs. (9.15) and (9.16) are equivalent only if the frequency dependence of β_{eff} is allowed. This is because in the definition of the ω-dependent $\beta_{\text{eff}}^{AB}(\omega)$ there are no assumptions and it represents just a way of writing $\tilde{R}^{AB}(\omega)$ in terms of $\tilde{C}_+^{AB}(\omega)$. In this respect then, with the ω-dependent value, Eqs. (9.15) and (9.16) express the same condition over the symmetric and the antisymmetric correlations.

In the following we will be interested in understanding if it is possible to make contact between the effective description that emerges considering the FDRs in the frequency and in the time, at least for some regimes (small frequencies and long times). In particular we aim to compare $\beta_{\text{eff}}^{AB}(\omega \to 0^+)$ with the value β_{eff}^* obtained taking the long time limit in Eq. (9.16). Clearly in equilibrium β does not depend on time and this is possible. In order to take the long-time limit in Eq. (9.16) - which may not be evident for the non-equilibrium case despite the knowledge of $C_+^{AB}(t)$ and $R^{AB}(t)$ - one can expand in power series the hyperbolic tangent in Eq. (9.16) and observe that this returns a sum over the odd time derivatives of $C_+^{AB}(t)$. At this point one can compare, order by order in the long time decay, the l.h.s. and the r.h.s. of Eq. (9.16). This will turn in an equation for β_{eff}^* that hopefully at the leading order does not depend on time. The result of this procedure is what we take as a good definition of the effective temperature in the long time limit. Since one could expect the quantum behavior being more relevant for the short time scales, we will also consider, in the same long time limit, the effective temperature extrapolated from the classical FDT:

$$T_{\text{eff}}^{\text{cl}} = -\lim_{t \to \infty} \frac{\partial_t C_+^{AB}(t)}{R^{AB}(t)} \, . \tag{9.17}$$

9.1.4 Critical quenches. Motivations

Even though all the considerations up to now are very general, in what follows we will focus on the case $\Gamma = 1$, i.e. on critical quenches. Since this choice may appear rather arbitrary let us argue about the reasons behind it. The model presents three regimes: two phases PM ($\Gamma > 1$) and FM ($\Gamma < 1$) and the critical point ($\Gamma = 1$). Clearly, in the quench problem, the possibilities are much more because one has to consider these three regimes in the initial and in the final Hamiltonian and to treat them

separately. Pragmatically, since a detailed study leaves room for several analysis, we preferred to fix the value of the final field and do not constraint the initial condition. From this perspective, there are many reasons to choose the critical point.

1. There are evidences that the expectation values of some operators in the long time limit after the quench to $\Gamma = 1$ are thermal with the temperature $T_{\text{eff}}^E(\Gamma, \Gamma_0)$, while the same does not hold in the gapped phases. We will recall some of these results in the next Section. Then, it is natural to investigate up to which extent the "thermalization" found for one-time quantities at $\Gamma = 1$, carries over to two-time observables in the same stationary limit. The generalized FDRs precisely provide the tools to accomplish this goal.

2. Among the motivations of the study of thermalization in quantum quenches there is the idea that the correlations within the entire, infinite, system could work as a thermal bath mechanism for a small subpart of the system itself, once the remaining degrees of freedom are traced out. From this point of view, one can heuristically argue that the thermal bath mechanism may be favored in the presence of a gapless spectrum, in the sense that energy exchanges at any scale are facilitated by the absence of gaps.

3. Finally, since our study will be strongly based on a frequency analysis and eventually in its $\omega \to 0$ limit, it is reasonable to start the investigation in the absence of an energy gap, where we expect it to be well posed. Depending on the observable considered, the presence of the gap may in fact introduce different frequency scales and more heterogeneous patterns within the corresponding regimes. This issue definitely merits attention but it requires a dedicated study which is the natural continuation of the investigation presented here for $\Gamma = 1$.

9.1.5 Review of the results in the literature

As we mentioned in Section 8.2.3, the study of the unitary non-equilibrium dynamics in the long time limit following a quantum quench is receiving increasing attention. Basic questions as to whether a stationary state is reached and how this can be characterized naturally arise. These questions have been addressed in a number of simple models, including the one-dimensional systems reviewed in Refs. [181, 165]. Early studies led to the following picture: non-integrable systems should eventually reach a thermal stationary state characterized by a Gibbs distribution with a single temperature. Integrable systems, instead, are not expected to thermalize but their asymptotic stationary state should nonetheless be described by the so-called generalized Gibbs ensemble (GGE) with one effective temperature for each conserved quantity [175, 176, 169, 182] (see Section 8.2.3).

Interestingly enough, depending on the specific quantity and the system's parameters a Gibbs ensemble turns out to capture anyhow some relevant features of the non-equilibrium dynamics of integrable systems [163]. Very interestingly it was observed in [163, 180], based on the study of the transverse field Ising chain, that observables that are non-local in the quasi-particles, $\hat{\sigma}^x$, display numerically the same relaxation scales as in equilibrium with the temperature $T \simeq T_{\text{eff}}^E$, at least for small quenches [163, 182]. Local quantities such as $\hat{\sigma}^z$, instead do not, with possible exceptions for quenches at criticality where the stationary expectation value after the quench $\langle \hat{\sigma}^z \rangle_Q$ is found equal to the thermal equilibrium value $\langle \hat{\sigma}^z \rangle_{T=T_{\text{eff}}^E}$.

Before presenting our results let us summarize with more details what is known, for the transverse Ising chain, about $C_\pm^{z,x}$ for quenches towards the critical point $\Gamma = 1$. In equilibrium ($\Gamma_0 = \Gamma$) $\langle \hat{\sigma}_i^z(t + t_0)\hat{\sigma}_i^z(t_0) \rangle$ decays algebraically as $|t|^{-3/2}$ at $T = 0$ and as $|t|^{-1}$ at finite temperature [163]. Out

of equilibrium the stationary decay of C_+^z is $|t|^{-2}$ [178]. For the special case of a fully polarized initial condition ($\Gamma_0 = \infty$) C_-^z follows the same $|t|^{-2}$ decay, as can be inferred from the results in Ref. [181]. In the long time limit the expectation value $\langle \hat{\sigma}^x \rangle_\mathcal{Q}$ decays to zero, for all $\Gamma \neq \Gamma_0$, consistently with the thermal behavior for $T > 0$. A generic exponential relaxation of $\langle \hat{\sigma}_i^x(t_0) \hat{\sigma}_j^x(t_0) \rangle$ was argued in [162] using semi-classical methods and later shown to hold exactly [182]. Moreover, as anticipated above, an exponential decay of $|\langle \hat{\sigma}_i^x(t + t_0) \hat{\sigma}_i^x(t_0) \rangle|$ with numerically the same relaxation scales as in equilibrium with the temperature $T \simeq T_{\text{eff}}^E$, at least for small quenches, was found in [163, 180]. This is in contrast to the power-law decay of the $T = 0$ equilibrium order-parameter spatio-temporal correlations. As far as we know, instead, C_-^x has not been analyzed so far. In the following we complete this picture by calculating $C_\pm^x$ and $C_\pm^z$ for generic Γ_0. We also study $C_\pm^M$, where $\hat{A}, \hat{B} = \hat{M} = \sum_{i=1}^L \hat{\sigma}_i^z / L$.

9.2 Transverse magnetization

We start the analysis considering first the stationary expectation value of $\langle \hat{\sigma}^z(t) \rangle$ after the quench:

$$\langle \hat{\sigma}^z \rangle_\mathcal{Q} = \lim_{t \to \infty} \langle \hat{\sigma}^z(t) \rangle_\mathcal{Q} = -\int_0^\pi \frac{dk}{\pi} \, \cos(2\theta_k^\Gamma) \cos \Delta_k(\Gamma, \Gamma_0) \, , \qquad (9.18)$$

where here and in the following we took the thermodynamic limit $1/L \sum_k \to 1/2\pi \int_{-\pi}^\pi dk$ [180]. As it was shown in [180] this value is in general different from the thermal one, at temperature $T = T_{\text{eff}}^E$. However at the critical point it turns out that:

$$\langle \hat{\sigma}^z \rangle_\mathcal{Q} = \langle \hat{\sigma}^z \rangle_{T=T_{\text{eff}}^E} \, . \qquad (9.19)$$

This is due to the fact that for critical quenches in the stationary regime, as well as at thermal
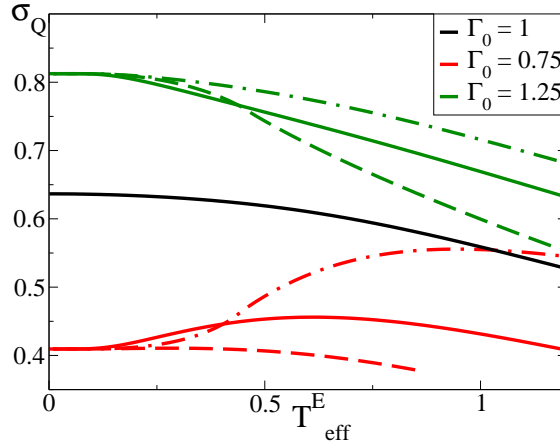
Figure 9.2: Comparison between the stationary expectation value $\langle \hat{\sigma}^z \rangle_\mathcal{Q}$ after the quench and the thermal equilibrium value as a function of T_{eff}^E, for different quenches. Solid lines correspond to the equilibrium thermal value of $\langle \hat{\sigma}^z \rangle$ at temperature $T = T_{\text{eff}}^E$, for different values of Γ. Red, black and green curves represent respectively $\Gamma = 0.75, 1$ and 1.25. Dashed ($\Gamma_0 < \Gamma$) and dotted-dashed ($\Gamma_0 > \Gamma$) lines show the asymptotic value of $\langle \hat{\sigma}^z \rangle_\mathcal{Q}$ after the quench as a function of $T_{\text{eff}}^E(\Gamma, \Gamma_0)$ for different quenches, $\Gamma = 0.75, 1$ and 1.25. The convention for the colors is the same as before. For critical quenches $\Gamma = 1$, the thermal value and the value after the quenched coincide.

equilibrium and $\Gamma = 1$, $\langle \hat{\sigma}^z \rangle = \langle \hat{H} \rangle /2$. Thus the equality $\langle \hat{\sigma}^z \rangle_\mathcal{Q} = \langle \hat{\sigma}^z \rangle_{T=T_{\text{eff}}^E}$ follows from Eq. (9.12)

by definition. In Fig. 9.2 we show the value of $\langle \hat{\sigma}^z \rangle_{\mathcal{Q}}$ for different quenches as a function of T_{eff}^E compared to the equilibrium thermal expectation values at $T = T_{\text{eff}}^E$, similarly to what was presented in [180]. As we anticipated in the previous Section, this result motivates a further investigation in order to understand up to which extent thermalization occurs at the critical point for $\hat{\sigma}^z$. The two-time symmetric connected correlation and response for generic Γ and Γ_0 are given by the following expressions:

$$C_+^z(t + t_0, t_0) = \frac{4}{\pi^2} \int_0^\pi dk \int_0^\pi dl \, \text{Re}\Big[v_k(t + t_0) \, v_k^*(t_0) \, u_l(t + t_0) \, u_l^*(t_0) \Big] \tag{9.20}$$

$$R^z(t + t_0, t_0) = -\frac{8}{\pi^2} \int_0^\pi dk \int_0^\pi dl \, \text{Im}\Big[v_k(t + t_0) \, v_k^*(t_0) \, u_l(t + t_0) \, u_l^*(t_0) \Big] . \tag{9.21}$$

In Eqs. (9.20), (9.21), and in the following, $v_k(t) = v_k^{\Gamma, \Gamma_0}(t)$ and $u_k(t) = u_k^{\Gamma, \Gamma_0}(t)$ are the matrix elements defined in Eq. (9.11). For critical quenches the stationary correlation and response obtained in the limit $t_0 \to \infty$ read:

$$C_+^z(t) = \Big[\frac{1}{\pi} \int_0^\pi dk \cos(\epsilon_k t) \Big]^2 - \Big[\frac{1}{\pi} \int_0^\pi dk \cos(\epsilon_k t) \cos \Delta_k \sin k/2 \Big]^2$$
$$+ \Big[\frac{1}{\pi} \int_0^\pi dk \sin(\epsilon_k t) \sin k/2 \Big]^2 - \Big[\frac{1}{\pi} \int_0^\pi dk \sin(\epsilon_k t) \cos \Delta_k \Big]^2 , \tag{9.22}$$

$$R^z(t) = \frac{4}{\pi^2} \Big[\int_0^\pi dk \sin(\epsilon_k t) \cos \Delta_k \int_0^\pi dl \cos(\epsilon_l t) - \int_0^\pi dk \sin(\epsilon_k t) \sin \frac{k}{2} \int_0^\pi dl \cos(\epsilon_l t)(\sin \frac{l}{2} \cos \Delta_l) \Big] , \tag{9.23}$$

with $\epsilon_k = 4 \sin k/2$. If $\Gamma_0 = 0$ or $\Gamma_0 = \infty$ the expressions simplify to:

$$C_+^z(t) = (J_0(4t))^2 - \frac{1}{4}(J_0(4t) - J_2(4t))^2 \tag{9.24}$$

$$R^z(t) = 2J_1(4t)(J_0(4t) + J_2(4t)) , \tag{9.25}$$

where $J_\alpha(x)$ are Bessel functions of order α. These results are consistent with those found in [181, 178]. The long time dynamics for generic Γ_0 is

$$C_+^z(t) = -\frac{1}{8\pi t^2} \cos 8t + \mathcal{O}(t^{-3}) , \tag{9.26}$$

$$R^z(t) = \frac{1}{4\pi t^2} \big[\Upsilon^{-1} - \sin 8t \big] + \mathcal{O}(t^{-3}) , \tag{9.27}$$

where $\Upsilon = [(1 + \Gamma_0)/(1 - \Gamma_0)]^2$. Note that Υ, as well as all the stationary expectation values at the critical point are invariant under the mapping $\Gamma_0 \mapsto \Gamma_0^{-1}$ (at least for all the observables that we considered). This is because $\cos \Delta_k(1, \Gamma_0) = \cos \Delta_k(1, \Gamma_0^{-1})$ is the sole quantity bringing about the dependence on Γ_0 in the stationary limit $t_0 \to \infty$ of $C_\pm^z$. Note in fact that for $\Gamma = 1$ one has:

$$\cos \Delta_k(\Gamma = 1, \Gamma_0) = \frac{(1 + \Gamma_0) |\sin k/2|}{\sqrt{\Gamma_0^2 - 2\Gamma_0 \cos k + 1}} = \frac{\sqrt{\Upsilon} |\sin k/2|}{\sqrt{1 + (\Upsilon - 1)(\sin k/2)^2}} . \tag{9.28}$$

The non-stationary transient, however, does not respect this symmetry. This is because $\Delta_k(\Gamma = 1, \Gamma_0) = -\Delta_k(\Gamma = 1, \Gamma_0^{-1})$ and in the non-stationary correlations it also appears $\sin \Delta_k$. Let us consider the frequency domain. From Eq. (9.22) and (9.23) it is clear that the Fourier transform will concern real values of frequencies ω which coincide either with the sum $\epsilon_k + \epsilon_l$ or with the difference $\epsilon_k - \epsilon_l$ of the energy of two quasiparticles, depending on the range of ω. This is due to the quadratic form of $\hat{\sigma}^z$ with respect to the fermionic excitations and will induce a finite cut-off
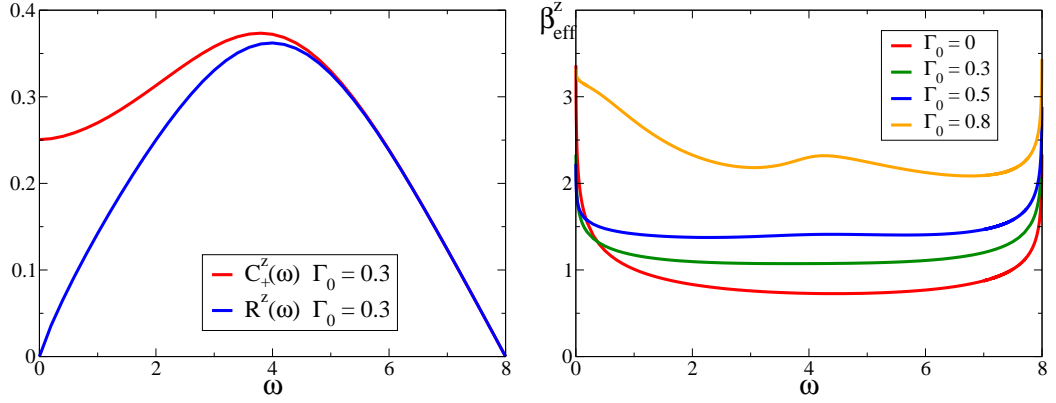
Figure 9.3: *Left panel*: Correlation and response of $\hat{\sigma}^z$ as a function of the frequency ω for $\Gamma_0 = 0.3$ and $\Gamma = 1$. $\tilde{C}_+^z(\omega)$ and $\tilde{R}^z(\omega)$ are shown respectively with a red and a blue line. *Right panel*: Effective inverse temperatures $\beta_{\text{eff}}^z(\omega)$ found for $\Gamma = 1$ and different initial conditions Γ_0. The red, green, blue and yellow curves correspond, respectively, to $\Gamma_0 = 0, 0.3, 0.5, 0.8$.

frequency $\omega_{\max} = 2\epsilon_{k=\pi}$ because of the upper bound to the dispersion relation $\epsilon_k(\Gamma)$. In Fig. 9.3 (left panel) we present the result for $\tilde{C}_+^z(\omega)$ and $\tilde{R}^z(\omega)$ for $\Gamma_0 = 0.3$. Note that thanks to the symmetry properties of $\tilde{C}_+^{AB}(\omega) = \tilde{C}_+^{AB}(-\omega)$ and $\tilde{R}^{AB}(\omega) = -\tilde{R}^{AB}(-\omega)$ with respect to the mapping $\omega \to -\omega$ we discuss only the results for $\omega > 0$. The complementary analysis in the frequency domain allows us to define a frequency-dependent effective temperature $T_{\text{eff}}^z(\omega)$, or $\beta_{\text{eff}}^z(\omega)$, via the FDR in Eq. (9.15). The function $T_{\text{eff}}^z(\omega)$ is shown in Fig. 9.4 for $\Gamma_0 = 0.3$ as a (red) solid line and it has to be compared with the constant value obtained from Eq. (9.12), as in Ref. [180], and shown with a black dashed line. The asymptotic regime corresponds to the limit $\omega \to 0$, zoomed in the inset, in which

$$\beta_{\text{eff}}^z(\omega \to 0) \to -1/2(1 - 1/\Upsilon)/[1 + (\Upsilon - 2)\arctan(\sqrt{\Upsilon - 1})/\sqrt{\Upsilon - 1}] \ln \omega \tag{9.29}$$

diverges logarithmically (green dashed line). We conclude that, although $\langle \hat{\sigma}_i^z \rangle_{\mathcal{Q}}$ takes a thermal value [180], the dynamics of $\hat{\sigma}_i^z$ is not compatible with an equilibrium thermal behavior that would require all these temperatures to be equal within a Gibbs description. For different values of Γ_0, T_{eff}^z still vanishes at $\omega = 0$ and $\omega = \omega_{\max} \equiv 8$ but it takes a slightly more complex shape, not concave for $\Gamma_0 \gtrsim 0.35$. For increasingly narrower quenches with $\Gamma_0 \to 1$, $\beta_{\text{eff}}^z \to \infty$ uniformly over all frequencies, as expected to recover the equilibrium value $T = 0$ for $\Gamma_0 \to \Gamma = 1$. In Fig. 9.3 (right panel) we show the values of β_{eff}^z for different Γ_0.

9.3 Global transverse magnetization

We consider here the global transverse magnetization $\hat{M} = 1/L \sum_{i=1}^L \hat{\sigma}_i^z$. The general expressions for two-time connected correlation and response involving $\hat{M}(t)$ are the following:

$$C_+^M(t + t_0, t_0) = \frac{8}{\pi} \int_0^\pi dk \, \text{Re}\Big[v_k^*(t_0)v_k(t + t_0)u_k^*(t_0)u_k(t + t_0)\Big] \tag{9.30}$$

$$R^M(t + t_0, t_0) = -\frac{16}{\pi} \int_0^\pi dk \, \text{Im}\Big[v_k^*(t_0)v_k(t + t_0)u_k^*(t_0)u_k(t + t_0)\Big] , \tag{9.31}$$

where we have rescaled the fluctuations of $\hat{M}$ by a factor L before taking the thermodynamic limit, as it is required for global observables whose fluctuations are otherwise suppressed. For critical quenches
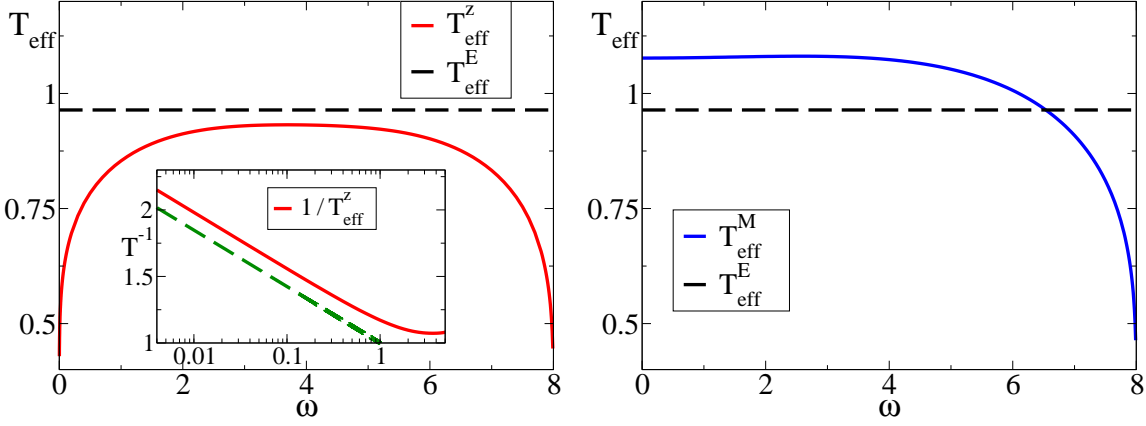
Figure 9.4: Comparison between the effective temperature T_{eff} defined via the frequency-domain FDR (see Eq. (9.15)) and the effective temperature T_{eff}^E defined through conservation of energy (see Eq. (9.12)). All the curves refer to the case $\Gamma_0 = 0.3$. $T_{\text{eff}}^z(\omega)$ for $\hat{\sigma}_i^z$ is shown in the left panel with a solid red line. The inset highlights the logarithmic divergence of $1/T_{\text{eff}}^z(\omega)$ for $\omega \to 0$. $T_{\text{eff}}^M(\omega)$ for $\hat{M}$ is shown in the right panel with a solid blue line. In both panels the black dashed horizontal line represents the effective temperature defined from the energy.

the stationary correlation and the response read:

$$C_+^M(t) = \frac{2}{\pi} \int_0^\pi \mathrm{d}k \Big[(1 - \cos \Delta_k^2)\frac{1}{2}(1 - \cos k) + \frac{1}{2}(1 + \cos k)\frac{1}{2}(\cos \Delta_k^2 + 1)\cos(2\epsilon_k^\Gamma t)\Big] , \qquad (9.32)$$

$$R^M(t) = \frac{4}{\pi} \int_0^\pi \mathrm{d}k \frac{1}{2}(1 + \cos k)\sin(2\epsilon_k^\Gamma t)\cos \Delta_k , \qquad (9.33)$$

with $\epsilon_k = 4\sin k/2$. If $\Gamma_0 = 0$ or $\Gamma_0 = \infty$ the expressions symplify:

$$C_+^M(t) = \frac{1}{4} + \frac{1}{8}\Big(5J_0(8t) + 4J_2(8t) - J_4(8t)\Big) \qquad (9.34)$$

$$R^M(t) = J_1(8t) + J_3(8t) . \qquad (9.35)$$

The long-time stationary decay of the global magnetization correlations are even slower than the one of $C_\pm^z(t)$:

$$C_+^M(t) = \frac{1}{8\sqrt{\pi}t^{3/2}} \sin(8t - \pi/4) + \mathcal{O}(t^{-5/2}), \qquad (9.36)$$

$$R^M(t) = -\frac{1}{4\sqrt{\pi}t^{3/2}} \cos(8t - \pi/4) + \mathcal{O}(t^{-5/2}). \qquad (9.37)$$

Note that in Eq. (9.36) we neglected the constant term $\frac{2}{\pi}\int_0^\pi \mathrm{d}k\Big[(1 - \cos \Delta_k^2)\frac{1}{2}(1 - \cos k)\Big]$ which is not important for the study of FDRs. The leading-order decay $t^{-3/2}$ is the same as in equilibrium at finite T. However, while the prefactor depends upon T in equilibrium [183], out of equilibrium the dependence on Γ_0 appears only at the next-to-leading order, i.e., the long-t limit of $C_\pm^M(t)$ does not retain memory of the initial condition. Let us focus on these observables in the frequency domain. After Fourier transforming Eq. (9.32) and Eq. (9.33) each frequency ω selects a mode k such that $\omega = 2\epsilon_k$. Moreover, it turns out that $T_{\text{eff}}^M(\omega)$ defined here from the FDR (9.15) coincides with the temperature T_{eff}^k of the GGE (9.14). This can be seen quite straightforwardly identifying $\cos \Delta_k =$
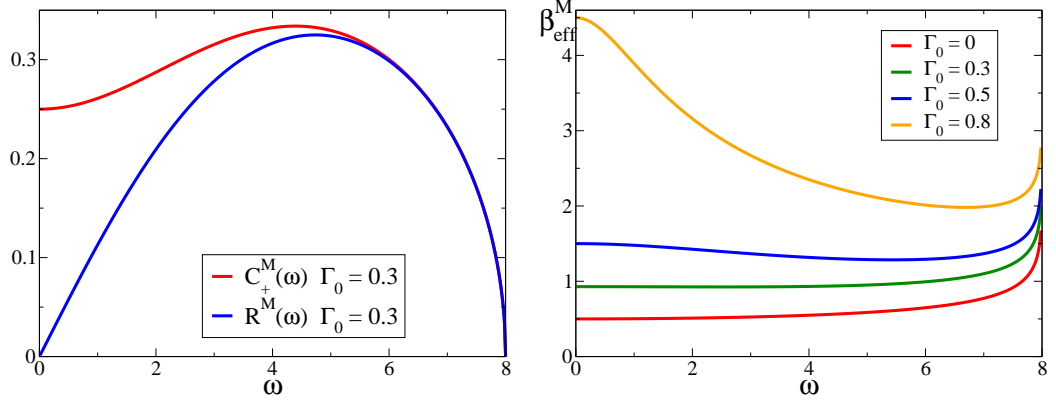
Figure 9.5: *Left panel*: Correlation and response of $\hat{M}$ as a function of the frequency for $\Gamma_0 = 0.3$ and $\Gamma = 1$. $\tilde{C}_+^M(\omega)$ and $\tilde{R}^M(\omega)$ are shown respectively as a red and a blue line. *Right panel*: Effective inverse temperatures $\beta_{\text{eff}}^M(\omega)$ found for $\Gamma = 1$ and different initial conditions Γ_0. The red, green, blue and yellow curves correspond respectively to $\Gamma_0 = 0, 0.3, 0.5, 0.8$.

$\tanh \frac{\epsilon_k(\Gamma)}{2T_{\text{eff}}^k}$ in Eq. (9.32) and Eq. (9.33) and applying a Fourier transform. In this way one ends up with the ratio:

$$\frac{\tilde{R}^M(\omega)}{\tilde{C}_+^M(\omega)} = \tanh\left(\frac{\omega}{2T_{\text{eff}}^k}\right) , \tag{9.38}$$

where k corresponds to the one selected by the frequency, $\omega = 2\epsilon_k$. The Fourier Transform of Eq. (9.32) and Eq. (9.33) can be calculated analytically. They yield:

$$\tilde{C}_+^M(\omega) = \frac{1}{(\sqrt{\Upsilon}+1)^2}\delta(\omega) + \frac{1}{4}\sqrt{1-\left(\frac{\omega}{8}\right)^2}\frac{1+(2\Upsilon-1)\left(\frac{\omega}{8}\right)^2}{1+(\Upsilon-1)\left(\frac{\omega}{8}\right)^2} \tag{9.39}$$

$$\tilde{R}^M(\omega) = \frac{\omega}{16}\sqrt{1-\left(\frac{\omega}{8}\right)^2}\sqrt{\Upsilon}\left[1+(\Upsilon-1)\left(\frac{\omega}{8}\right)^2\right]^{-1/2} . \tag{9.40}$$

The blue line in the right panel of Fig. 9.4 is $T_{\text{eff}}^M(\omega)$ as obtained from the FDR (9.15), applied to $\tilde{C}_\pm^M$. Analogously to what we did for $T_{\text{eff}}^z(\omega)$ we can study the value of $T_{\text{eff}}^M(\omega)$ for small ω:

$$T_{\text{eff}}^M = \lim_{\omega \to 0} T_{\text{eff}}^M(\omega) = \frac{2}{\sqrt{\Upsilon}} . \tag{9.41}$$

Then, differently from before, T_{eff}^M approaches a finite value at low frequencies, while it vanishes for $\omega = \omega_{\max}$. The resulting $T_{\text{eff}}^M(\omega)$ is shown for various values of Γ_0 in Fig. 9.5 (right panel). Quite naturally, one may expect to recover the value T_{eff}^M by treating the time-domain FDR in the long-t limit as we said in Section 9.1.3. Replacing β by a constant effective value β_{eff}^* on the r.h.s. of Eq. (9.16), the integral can be written as series of odd time derivatives of $C_+^M(t)$. Inserting Eqs. (9.36) and (9.37) in the r.h.s. and l.h.s. of this expression, respectively, yields $1 = \tanh(4\beta_{\text{eff}}^*)$ at the leading order in $t \to \infty$ and therefore $T_{\text{eff}}^* = 0$. The fact that $T_{\text{eff}}^M(\omega \to 0) \neq T_{\text{eff}}^*$ indicates that $\beta_{\text{eff}}^M(\omega)$ cannot be approximated by an average constant in the integral. Indeed, since only the derivatives of the oscillating factor in (9.36) contribute to the leading order of Eq. (9.16), T_{eff}^* can be interpreted as a temperature associated to the oscillatory frequency $\omega = 8$. Note that this oscillation occur at the threshold value $\omega = \omega_{\max}$ and, for $\omega \to \omega_{\max}$, β_{eff}^M diverges as $\beta_{\text{eff}}^M(\omega) \simeq -\ln(\omega_{\max}-\omega)/4$. The independence from Γ_0 in this divergence is consistent with the fact that the leading order of the long

time limit of $C_+^M(t)$ and $R^M(t)$ is also independent of Γ_0 and it is sensitive to the largest frequencies (that, in turn, are associated to the largest energies). Such threshold $\omega_{\max}$ results from the maximum of the dispersion relation and the quadratic dependence of $\hat{M}$ on the fermionic excitations, as noted for $\hat{\sigma}^z$. It is therefore unclear how the same value as $T_{\mathrm{eff}}^M(\omega \to 0)$ can be recovered from the FDR in the time domain.

9.4   Order parameter

As we anticipated a careful observation of the *stationary* correlations and responses presented in Section 9.2 and 9.3 reveals that all these quantities are invariant under $\Gamma_0 \mapsto \Gamma_0^{-1}$. We argued that this is because $\cos \Delta_k(1, \Gamma_0) = \cos \Delta_k(1, \Gamma_0^{-1})$ (see Eq. (9.28)) is the sole quantity bringing about the dependence on Γ_0 in the stationary limit $t_0 \to \infty$ of $C_\pm^{M,z}$. In the stationary regime and for $\Gamma = 1$ we find numerically that this invariance also holds for $C_\pm^x$.

9.4.1   Computation of the correlation functions

As it was already pointed out in [163, 162, 182] the stationary expectation value of $\langle \hat{\sigma}^x(t) \rangle$ decays to zero for any $\Gamma \neq \Gamma_0$. This is consistent with the equilibrium thermal scenario in which there is no long-range order along the x-component, as soon as $T > 0$. Then we looked for the two-time correlations $C_\pm^x$ that we computed with the methods employed in Refs. [163] that generalize the equilibrium case discussed in [177]. For periodic boundary conditions the computation of $C_\pm^x$ is not trivial because the operator $\hat{\sigma}_i^x(t_0 + t)\,\hat{\sigma}_i^x(t_0)$ has non-zero matrix elements between states with different $\hat{c}$-fermionic parity. For this computation, the assumption mentioned in Section 9.1.1 about the restriction to the even sector is not justified. On the other hand, we do not have the tools to compute matrix elements between the two sectors because they are diagonalized by imposing different rule of quantization over momenta k. Then, following [180, 177] we consider a four-spin correlation function on a chain of length L:

$$C^{xx}(t, t_0; L) = \left\langle \hat{\sigma}_{L+1}^x(t_0 + t)\, \hat{\sigma}_1^x(t_0)\, \hat{\sigma}_{\frac{L}{2}+1}^x(t_0 + t)\, \hat{\sigma}_{\frac{L}{2}+1}^x(t_0) \right\rangle . \tag{9.42}$$

The spin $\hat{\sigma}_{L+1}^x$ is identified with the spin $\hat{\sigma}_1^x$ after that the full string of Jordan-Wigner fermions, from 1 to L, has been inserted. By using the cluster property and taking the thermodynamic limit in fact, from this quantity one can recover $C_\pm^x(t + t_0, t_0)$:

$$\left[C^x(t + t_0, t_0)\right]^2 = \lim_{L \to \infty} C^{xx}(t, t_0; L) , \tag{9.43}$$

with $C^x(t_1, t_2) = C_+^x(t_1, t_2) + i\, C_-^x(t_1, t_2)$. The advantage of this strategy is that the four-point correlation function in Eq. (9.42) conserves the parity of the number of $\hat{c}$-fermions, and can therefore be evaluated in the (antiperiodic) even sector [180, 177]. Following [180] we introduce the operators $\hat{A}_j(t) \equiv \hat{c}_j^\dagger(t) + \hat{c}_j(t)$ and $\hat{B}_j(t) \equiv \hat{c}_j^\dagger(t) - \hat{c}_j(t)$ in terms of Jordan-Wigner fermions. Note that $(1 - 2\hat{c}_j^\dagger \hat{c}_j) = \hat{A}_j \hat{B}_j = -\hat{B}_j \hat{A}_j$ and $\{\hat{A}_j, \hat{B}_l\} = 0 \;\; \forall j, l$. Then, recalling the transformation in Eq. (9.2) we get:

$$C^{xx}(t, t_0; L) = \left\langle [\hat{B}_{\frac{L}{2}+1}(t_0 + t) \cdots \hat{B}_L(t_0 + t)][\hat{A}_{\frac{L}{2}+2}(t_0 + t) \cdots \hat{A}_{L+1}(t_0 + t)] \right. $$
$$\left. \times [\hat{B}_1(t_0) \cdots \hat{B}_{\frac{L}{2}}(t_0)][\hat{A}_2(t_0) \cdots \hat{A}_{\frac{L}{2}+1}(t_0)] \right\rangle . \tag{9.44}$$

The next and final step is to write the Pfaffian Eq. (9.44) in terms of the determinant of a $(2L - 4r) \times (2L - 4r)$ matrix [177, 180]:

$$
\left[C^{xx}(t, t_0; L) \right]^2 =
\begin{vmatrix}
\langle BB \rangle_{j_1,l_1}^{t_0+t,t_0+t} & \langle BA \rangle_{j_1,l_2}^{t_0+t,t_0+t} & \langle BB \rangle_{j_1,l_3}^{t_0+t,t_0} & \langle BA \rangle_{j_1,l_4}^{t_0+t,t_0} \\
-\langle BA \rangle_{l_1,j_2}^{t_0+t,t_0+t} & \langle AA \rangle_{j_2,l_2}^{t_0+t,t_0+t} & \langle AB \rangle_{j_2,l_3}^{t_0+t,t_0} & \langle AA \rangle_{j_2,l_4}^{t_0+t,t_0} \\
-\langle BB \rangle_{l_1,j_3}^{t_0+t,t_0} & -\langle AB \rangle_{l_2,j_3}^{t_0+t,t_0} & \langle BB \rangle_{j_3,l_3}^{t_0,t_0} & \langle BA \rangle_{j_3,l_4}^{t_0,t_0} \\
-\langle BA \rangle_{l_1,j_4}^{t_0+t,t_0} & -\langle AA \rangle_{l_2,j_4}^{t_0+t,t_0} & -\langle BA \rangle_{l_3,j_4}^{t_0,t_0} & \langle AA \rangle_{j_4,l_4}^{t_0,t_0}
\end{vmatrix}
\tag{9.45}
$$

with $\langle \phi\phi \rangle_{i,j}^{t_1,t_2} = \left\langle \hat{\phi}_{[i]}(t_1) \hat{\phi}_{[j]}(t_2) \right\rangle$ and $\phi \in \{A, B\}$. In Eq. (9.45) the two indexes j, l have subscripts which indicate their range: an index with label $_1$ runs from $\frac{L}{2} + 1$ to L, with $_2$ runs from $\frac{L}{2} + 2$ to $L + 1$, with $_3$ runs from 1 to $\frac{L}{2}$, with $_4$ runs from 2 to $\frac{L}{2} + 1$. All the diagonal entries of the matrix in (9.45) are zero, since they do not enter the contractions. The matrix elements take the form:

$$
\begin{cases}
\left\langle \hat{A}_j(t_1) \hat{A}_l(t_2) \right\rangle = \dfrac{1}{L} \sum_k e^{ik(j-l)} \big(u_k(t_1) + v_k(t_1)\big) \big(u_k^*(t_2) + v_k^*(t_2)\big) \\[2mm]
\left\langle \hat{A}_j(t_1) \hat{B}_l(t_2) \right\rangle = \dfrac{1}{L} \sum_k e^{ik(j-l)} \big(u_k(t_1) + v_k(t_1)\big) \big(u_k^*(t_2) - v_k^*(t_2)\big) \\[2mm]
\left\langle \hat{B}_j(t_1) \hat{A}_l(t_2) \right\rangle = \dfrac{1}{L} \sum_k e^{ik(j-l)} \big(v_k(t_1) - u_k(t_1)\big) \big(u_k^*(t_2) + v_k^*(t_2)\big) \\[2mm]
\left\langle \hat{B}_j(t_1) \hat{B}_l(t_2) \right\rangle = \dfrac{1}{L} \sum_k e^{ik(j-l)} \big(u_k(t_1) - v_k(t_1)\big) \big(v_k^*(t_2) - u_k^*(t_2)\big) \,.
\end{cases}
\tag{9.46}
$$

and the k-sums are taken for fermion antiperiodic boundary conditions. Some care is in order when one wants to extract the real and the imaginary part of $C^x(t)$ numerically from the value of $\left[C^{xx}(t, t_0; L) \right]^2$.

9.4.2 Numerical results for the dynamics

Here we computed $C_\pm^x$ for a chain with $L = 10^3$ and we set $t_0 = 10$. We estimated these values to be large enough for accessing the thermodynamic and the stationary limit. We also checked for some values of Γ_0 that we obtain the same results as in the bulk of an open chain with free boundary conditions [184, 179]. At fixed parameters in fact, $C_\pm^x$ computed in the two cases perfectly overlap, at least up to times much shorter than the length of chain, after which finite-size effects are expected to appear. Note that in the open chain the distinction between the even and the odd sectors as well as translational invariance are absent. Therefore, the treatment of these two cases is quite different. With this comparison we found confidence that, despite these differences, also out of equilibrium the choice of the boundary conditions does not affect the bulk properties of the system, which is actually expected. When the times become of the order of the length of the chain the correlations manifest finite-size effects. This is because the excitations created by $\hat{\gamma}_k^\Gamma$ travel at finite speed $\mathcal{V}_k = \partial_k \epsilon_k(\Gamma)$. Thus, after long enough times they scatter against the boundary of the open chain and go back, or against particles that are moving coherently with them but in the opposite direction on the closed chain. Moreover at the critical point all the low energy particles move with the same speed $|\mathcal{V}_k| = 1$ approximately, as it is clear from Fig. 9.1 and this makes the dynamics particularly coherent. These finite size effects have been thoroughly studied in [184, 179]. In Fig. 9.6 we show the qualitative behavior displayed by $C_+^x(t)$ (left panel) and $R^x(t)$ (right panel) for different initial conditions. Note that here and in the following we focus only on quenches originated in the ferromagnet region $\Gamma_0 < 1$ because of the symmetry under the change $\Gamma_0 \to \Gamma_0^{-1}$. Our numerical results are fitted very accurately,
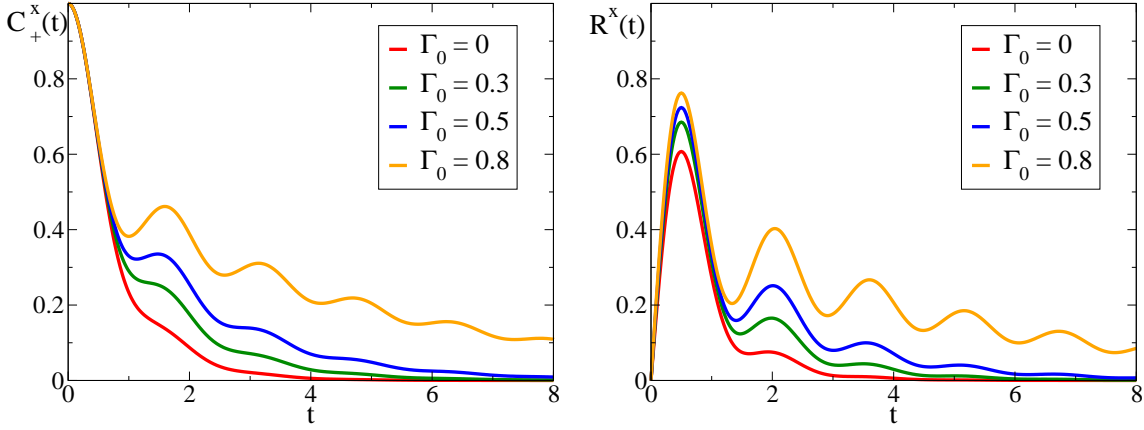
Figure 9.6: $C_+^x(t)$ (*left panel*) and $R^x(t)$ (*right panel*) for different initial conditions. Red, green, blue and yellow lines correspond respectively to $\Gamma_0 = 0, 0.3, 0.5, 0.8$.

for $t \gtrsim 10$, by

$$C_+^x(t) \simeq e^{-\frac{t}{\tau}} A_C \Big[1 + \frac{a_C}{t^{1/2}} \, \sin(4t + \phi) \Big], \tag{9.47}$$

$$R^x(t) \simeq e^{-\frac{t}{\tau}} A_R \Big[1 - \frac{a_R}{t^{1/2}} \, \cos(4t + \phi) \Big], \tag{9.48}$$

with (numerically) the rate τ^{-1} given by

$$\tau^{-1} = - \int_0^\pi \frac{dk}{\pi} \, \frac{d\epsilon_k(\Gamma)}{dk} \, \ln \cos \Delta_k(1, \Gamma_0) = \frac{4 \arctan(\sqrt{\Upsilon - 1})}{\pi \sqrt{\Upsilon - 1}} \tag{9.49}$$

analytically proved [182] to characterize the exponential long-time decay of $\langle \hat{\sigma}_i^x(t) \rangle$ and similarly the one of the equal time correlation $\langle \hat{\sigma}_i^x(t) \hat{\sigma}_j^x(t) \rangle$. The expression for τ finds further support from the fact that with the substitution $\cos \Delta_k = \tanh(\beta_{\text{eff}}^k \epsilon_k / 2) \to \tanh(\beta \epsilon_k / 2)$ one recovers the equilibrium characteristic time τ_{eq} [185]. This substitution in fact allows one to turn all the statistical averages considered up to now into the corresponding ones at thermal equilibrium with temperature β^{-1}. The substitution amounts to a GGE description of the stationary regime for the quantity under study, where the dependence on the initial condition survives only at the level of the population of the k-modes.

The non-equilibrium coherence time τ decreases upon increasing $|1 - \Gamma_0|$, i.e. , the energy injected into the system and $\tau \sim |1 - \Gamma_0|^{-1}$ for $\Gamma_0 \to 1$. In Fig. 9.7 we compare $C_+^x(t)$ and $R^x(t)$ for a particular choice of $\Gamma_0 = 0.3$. In the upper inset we show with a zoom the long-time decay together with its comparison with the leading exponential decay. The lower inset confirms the high quality of the fit of the correction terms to the forms given in Eqs. (9.47) and (9.48) which are actually indistinguishable from the data. Although several fitting parameters are involved in Eqs. (9.47) and (9.48), we tested these expressions for several values of $\Gamma_0 \in \{0, 0.1, 0.2, \ldots, 0.9\}$ and they turned out to be always remarkably accurate. The exponential decay sets in very soon, usually already after the first oscillation of $C_\pm^x$. The next-to leading order oscillatory correction involving a power law decay is more complex, but still we found a remarkable agreement quite soon. While the parameters $A_{R,C}$ depend on Γ_0, their ratio $A_C / A_R = 1.210(5)$ does not within our numerical accuracy. In the left panel of Fig. 9.8 we show the exponential decay of $C_+^x(t)$ for several initial conditions Γ_0 and its comparison with the rate in Eq. (9.49). The decay of $R^x(t)$ is precisely the same. In the right panel we show the
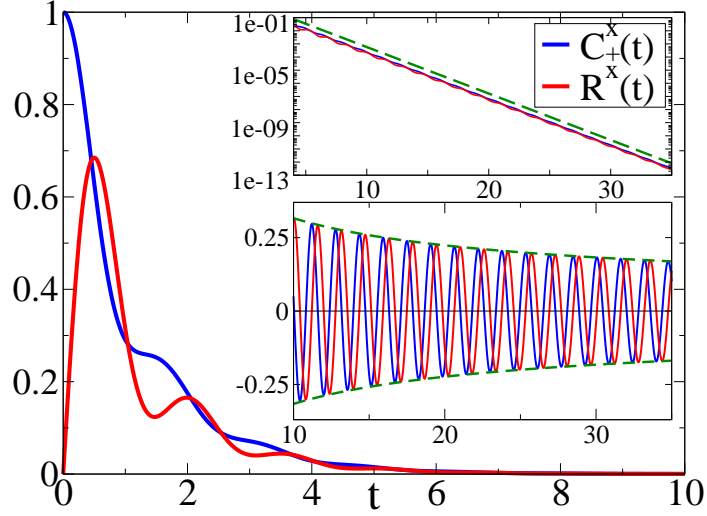
Figure 9.7: Decay of the order-parameter correlation C_+^x (blue line) and the linear response R^x (red line) as a function of t for $\Gamma_0 = 0.3$. Upper inset: zoom into the long-t decay that demonstrates the exponential relaxation with the characteristic time τ defined in Eq. (9.49) (dashed green line). Lower inset: $(e^{t/\tau}C_+^x/A_C - 1)/a_C$ and $(e^{t/\tau}R^x/A_R - 1)/a_r$ vs. t; the green dashed line is the $t^{-1/2}$ envelope of the damped oscillations, in agreement with Eqs. (9.47) and (9.48).

damped oscillations displayed by $C_+^x(t)\, e^{\frac{t}{\tau}}/A_C$ and with a dashed line the envelop $\propto t^{-1/2}$. In the inset of the same figure we took a zoom in time that shows the phase shift ϕ between the different curves. Note that the curves almost overlap, despite little differences remain, as for instance in the phase shift. We do not know whether these differences are a finite-size effects or they survive in the thermodynamic and stationary limit. Of course, since the numerical computations are done for a finite chain, there is also an upper bound in the long time limit to the expressions in (9.48). However a detailed discussion of finite-size effects is beyond the scope of our study.

We conclude our numerical investigation with some selected results regarding two-time and two-point functions:

$$C_\pm^x(r, t_0 + t, t_0) = \frac{1}{2}\left\langle \left[\hat{\sigma}_{i+r}^x(t_0 + t), \hat{\sigma}_i^x(t_0)\right]_\pm \right\rangle , \tag{9.50}$$

which provide, from Kubo formula, $R^x(r, t_0 + t, t_0) = 2iC_-^x(r, t_0 + t, t_0)$. The computation for this quantity is still based on the same determinant equation (9.45) where an index with label $_1$ runs from $\frac{L}{2} + 1$ to $L - r$, with $_2$ runs from $\frac{L}{2} + 2$ to $L - r + 1$, with $_3$ runs from 1 to $\frac{L}{2} - r$, with $_4$ runs from 2 to $\frac{L}{2} - r + 1$. We fixed the length of the chain $L = 1000$ and the waiting time $t_0 = 10$ and we studied the initial conditions with $\Gamma_0 \in \{0, 0.1, 0.2, \ldots, 0.9\}$ exactly as before. Differently from the case $r = 0$ shown in Fig. 9.7, correlations with $r \neq 0$ display a light-cone effect due to the finite speed of the quasi-particles [162, 182, 179, 184]. In Fig. 9.9 and Fig. 9.10 the light-cone effect and the finite speed of the quasiparticles is apparent, as both correlations and responses remain almost constant up to times $t \simeq r/2$. This is evident in Fig. 9.9 where we show the qualitative behavior of $C_+^x(r, t)$ (left panel) and $R^x(r, t)$ (right panel) at fixed $r = 10$ and for different Γ_0. In Fig. 9.10 we show the exponential decay of $C_+^x(r, t)$ (left panel) and $R^x(r, t)$ (right panel) at fixed $\Gamma_0 = 0.3$ and for different $r = 5, 10, 20$ together with the rate in Eq. (9.49). The spatial de-correlation decay for $t = 0$, i.e. for $\langle \hat{\sigma}_{i+r}^x(t_0)\hat{\sigma}_i^x(t_0)\rangle$, was determined in [182].
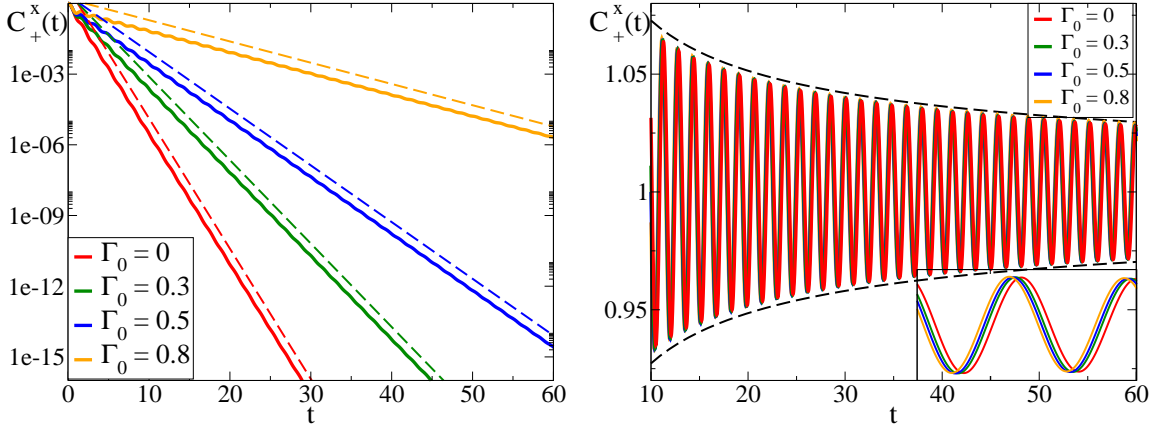
Figure 9.8: *Left panel*: Solid lines show the exponential time decay of the correlation function $C_+^x(t)$ for several initial conditions. Dashed lines show the corresponding rate decay obtained from Eq. (9.49). *Right panel*: Oscillatory correction to the leading order of the correlation $C_+^x(t)$. With solid lines we show $C_+^x(t)e^{t/\tau}/A_C$ (see Eq. (9.47)). The dashed line is the envelope $1 \pm 0.23/\sqrt{t}$ that show the damped amplitude of the oscillations. The inset is a zoom in the time interval $t \in [24, 27]$ that shows the slight phase shift among the different curves. In both panels red, green, blue and yellow lines correspond respectively to $\Gamma_0 = 0, 0.3, 0.5, 0.8$. For the sake of simplicity we do not show here $R^x(t)$, but we found the same characteristic time and an analogous oscillatory behavior.

9.4.3 Effective temperatures

In the following we present the study of the effective temperatures defined for $\hat{\sigma}^x$ in time and in the frequency domain in the limit of $\omega \to 0$. Let us start the discussion from the frequency analysis. Due to the numerical calculation in time of $C_\pm^x(t)$ it is very hard to access the full frequency dependence of $\tilde{C}_\pm^x(\omega)$. We are forced to consider finite time intervals and this makes the computation of large frequencies unreliable. We studied the small frequency regime in a time interval $t \in [0, t_{\max}]$ for different values of $t_{\max}$ and we found that it stabilizes rapidly with increasing $t_{\max}$, $t_{\max}$ being an increasing function of τ. Small frequencies capture the exponential decay and they are less sensitive to other details. For these reasons, their extrapolation in a sufficiently large, but finite, time interval is expected to provide reliable results. Luckily, the region of small ω is the one that interest us the most because we aim to compare $\beta_{\text{eff}}^x(\omega \to 0)$ with a long time determination of the β_{eff}^* obtained from Eq. (9.16). The zero frequency limit of Eq. (9.15) yields:

$$\beta_{\text{eff}}^x(\omega \to 0) = \frac{\int_0^\infty \mathrm{d}t\, t R^x(t)}{\int_0^\infty \mathrm{d}t\, C_+^x(t)} \ , \tag{9.51}$$

that we take as our working definition for $\beta_{\text{eff}}^x(\omega \to 0)$. Alternatively as discussed above, we can enforce a constant value β_{eff}^* in the (generalized) FDT (9.16) in the time domain. This operation allows to interpret the r.h.s. of the equation into a series of time derivatives of $C_+^x(t)$ which yields

$$\hbar A_R/(2A_C) = \tan(\hbar \beta_{\text{eff}}^x/2\tau) \tag{9.52}$$

for $t \to \infty$, i.e. when one neglects the oscillatory corrections in Eqs. (9.47) and (9.48). In this case we found that the effective temperatures determined in frequency and time domain are equivalent. For $\hbar \beta_{\text{eff}}^x/2\tau \ll 1$ in Eq. (9.52) one recovers the classical limit (9.17) $\beta_{\text{eff}}^x \simeq -R^x(t)/[\mathrm{d}C^x(t)/\mathrm{d}t] \simeq$
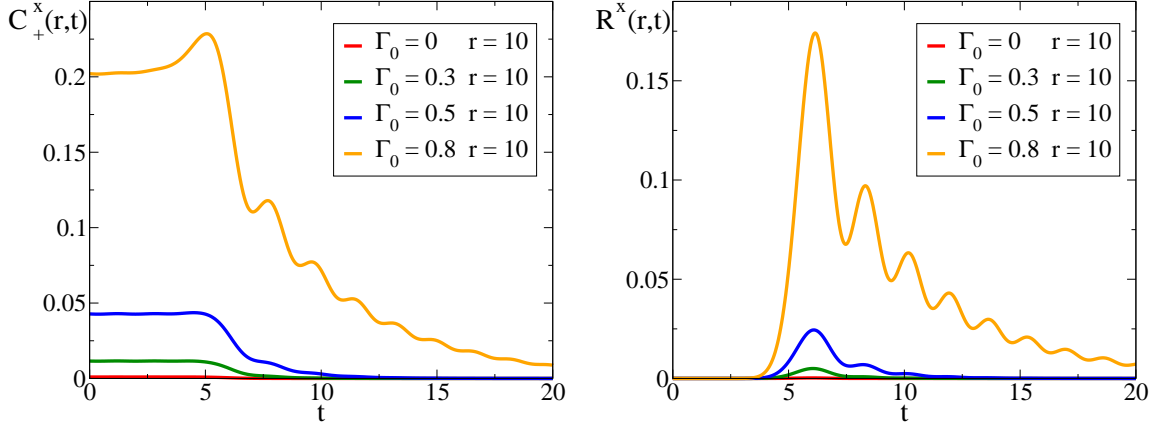
Figure 9.9: $C_+^x(r = 10, t)$ (*left panel*) and $R^x(r = 10, t)$ (*right panel*) for different initial conditions. Red, green, blue and yellow lines correspond, respectively, to $\Gamma_0 = 0, 0.3, 0.5, 0.8$.
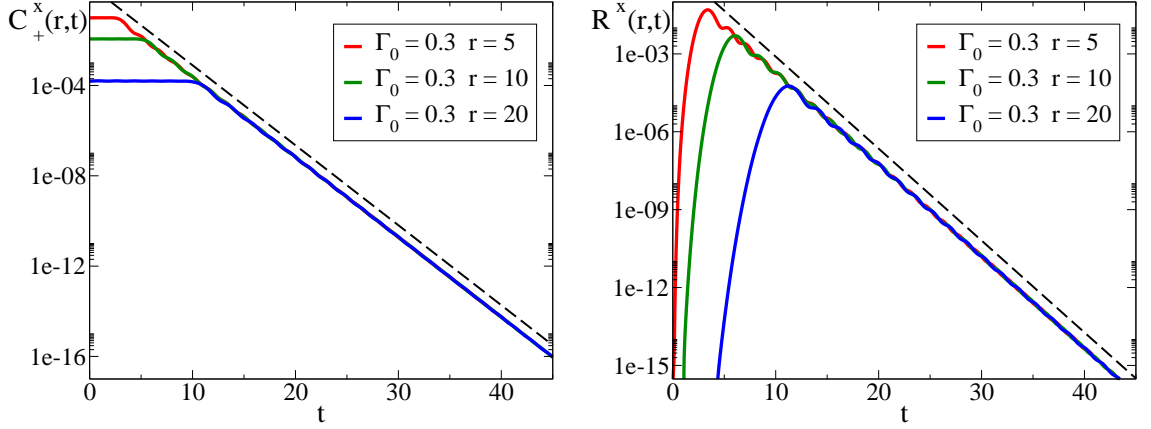
Figure 9.10: $C_+^x(r, t)$ (*left panel*) and $R^x(r, t)$ (*right panel*) for $\Gamma_0 = 0.3$ and different values of r. Red, green, blue lines correspond, respectively, to $r = 5, 10, 20$. The dashed lines are the exponential decay with rate given by Eq. (9.49).

$\tau A_R / A_C$. All three determinations of T_{eff}^x are shown in Fig. 9.11 as functions of Γ_0 and they are compared to T_{eff}^E (dashed line) from Eq. (9.12) [163]. In the same Figure we also show as a function of Γ_0 the zero-frequency effective temperature obtained from Eq. (9.51) applied to the two-point functions $C_+^x(r, t)$ and $R^x(r, t)$ with $r = 10$.

9.5 Discussion

Let us summarize the results that we have obtained. As a first observation let us note that independently of the functional form of the correlations involved, the FDRs allow us to define various effective temperatures. This is a great advantage which allows the investigation also of power-law decays, for instance. Indeed, other strategies that base the comparison between the quench (out of equilibrium) and the thermal (equilibrium) dynamics on the analysis of characteristic times or lengths are limited to exponential decays. Moreover, the investigation of the equilibrium properties of the system in
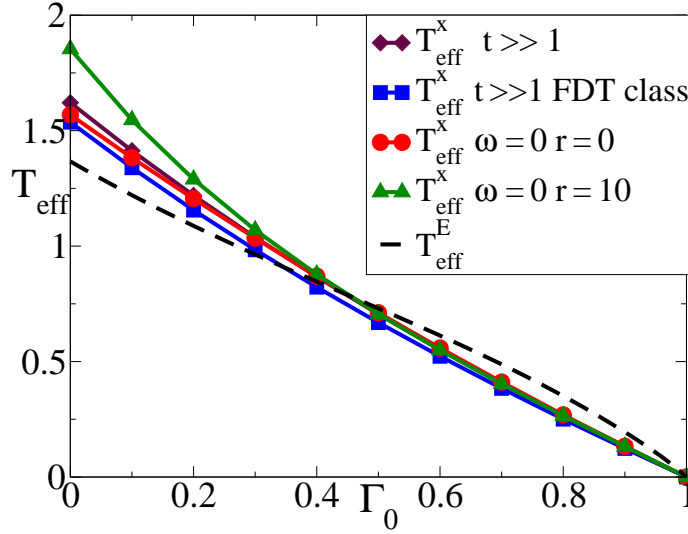
Figure 9.11: Γ_0 dependence of the order parameter effective temperature $T^x_{\rm eff}$ compared to $T^E_{\rm eff}$ defined from the energy [see Eq. (9.12)] (dashed line). The solid lines, from bottom to top, indicate the values determined on the basis of the classical limit of the FDR in the time domain, of the limit $\omega \to 0$ of the frequency-domain FDR, of Eq. (9.52), and of the limit $\omega \to 0$ of the frequency-domain FDR but for spins separated by a distance $r = 10$. The dependence on Γ_0 can be read from the one of τ and from Eq. (9.52).

terms of FDRs provides the possibility to analyze the behavior of the system in different time (or frequency) regimes, separately. It might be, in fact, that the characterization of the non-equilibrium dynamics requires a separate treatment over different time scales. This is, for instance, the case of slowly evolving systems such as glasses or coarsening systems. Here, we calculated the (self) FDR for three observables that are local ($\hat{\sigma}^{x,z}_i$) or non-local ($\hat{M}$) in space and local ($\hat{\sigma}^z_i$, $\hat{M}$) or non-local ($\hat{\sigma}^x_i$) in the quasi-particles. By detecting a violation of the FDT we conclude that the dynamics of $\hat{\sigma}^z_i$ is not compatible with Gibbs thermal equilibrium at any effective temperature, in spite of the fact that thermal-like behavior is observed for the stationary expectation value $\langle \hat{\sigma}^z \rangle_{\mathcal{Q}} = \langle \hat{\sigma}^z \rangle_{T=T^E_{\rm eff}}$. The frequency-domain FDR for $\hat{M}$ yields a finite $T^M_{\rm eff}(\Gamma_0)$ in the limit $\omega \to 0$ however we did not find the way to recover this value in the time domain in the limit of long times. The dynamics of the operator $\hat{\sigma}^x_i$ shows instead a very different behavior. Both $C^x_+(t)$ and $R^x(t)$ decay exponentially with a characteristic time given by Eq. (9.49) that decreases upon increasing the energy injected in the system. Moreover, the determination of the effective temperature $T^x_{\rm eff}(\Gamma_0)$ in the frequency and the time-domain, leads to the same value. $T^M_{\rm eff}$ and $T^x_{\rm eff}$ have the same qualitative dependence on Γ_0 but they differ (and they also differ from $T^E_{\rm eff}$). This excludes a single temperature effective Gibbs description (as the one discussed in Ref. [186]) of the full stationary dynamics of this model but the question remains as to whether some of the temperatures which emerge can be attributed a thermodynamic meaning.

We conclude with a remark about the different structure of correlations and responses displayed by the quantities that we studied and their consequences on the effective temperatures found in time and frequency space. We recall the fact that the effective temperature $T^*_{\rm eff}$ of the long-time dynamics of $C^M_\pm(t)$ (and derivatives) is somehow controlled by the behavior at high frequencies, as discussed in Section 9.3. This is, to us, very surprising and unexpected. However it is a natural consequence

of the presence of oscillating terms at the leading order in $C_\pm^M(t)$ with a frequency equal to $\omega_{\max}$. This structure highlights that not only the slow power-law decay of $C_\pm^{M,z}(t)$ is important, but also the oscillations are a constitutive ingredient. This structure, as well as the presence of the maximum frequency $\omega_{\max}$, can not be resolved in a mere lattice effect. As we noted for $\hat{\sigma}^z$ in fact, it is the combination of a lattice cut-off that bounds the dispersion relation, but also of the particular quadratic form of the observable with respect to the elementary excitations of the model. In other words, it may be interpreted as a consequence of the locality of the operator in Hilbert space. Indeed as we saw in Section 9.4 the order parameter $\hat{\sigma}^x$, which has a much more complex structure in terms of the quasi-quarticles, does not display oscillations at the leading order of $C_\pm^x(t)$ but only a pure exponential decay. This supports the intuition that for this observable oscillations are not so fundamental for the dynamics, i.e., a simpler lattice effect, and the long time limit of the corresponding T_{eff}^* could be regularly recovered from a small frequency expansion, as it is actually the case (see Fig. 9.11). The difference between $C_\pm^x(t)$ and $C_\pm^z(t)$ (or $C_\pm^M(t)$), though, that is manifested not only in the different character of the long time the decay - power-law vs exponential - but also in the oscillatory "correction", resides not in the lattice but in the properties of the operators $\hat{\sigma}^{x,z}$.

In conclusion, going back to the issue of thermalization in quantum quenches that motivated our study, we stress that a *bona fide* thermal behavior should be accompanied by the validity of suitable FDRs also in this context.

10

Conclusions and perspectives

We started this work with the aim of investigating the properties of quantum glasses. Along the way we realized that it is very difficult to provide a unique definition of what a *quantum glass* is. This turned out to be a source of continuous discovery and new questions, as quantum glasses may be found in very different contexts and can be addressed from very different perspectives. We hope that our results (summarized in Section I.4 of the Introduction) although limited to the study of some particular models could contribute to the insight of the subject.

Below we outline relevant research directions which deserve further investigation. Following the structure of the thesis we divide them into three topics.

Quantum optimization problems

- In Chapters 1, 3 and 4 we argued that we do not expect that quantum adiabatic computation will be able to *solve* hard optimization problems in general, because of their complex spectrum. However we are confident that quantum computation in general, and thus also the quantum annealing as an algorithm, if physically realizable, has very powerful tools at its disposal, i.e. the possibility to operate simultaneously over superpositions of the classical computational basis. For this reason, in our opinion it is important to continue the study of quantum random optimization problems. However, we believe that the most effective approach consists in understanding in more details the spectral properties and the thermodynamical behavior of these models in order to design strategies that focus, for instance, on the possibility to get approximate solutions in a well-controlled manner [67, 68]. Moreover, as we stressed several times, the understanding of the properties of quantum random optimization problems is strictly connected to that of glassy systems. At the moment, the most important study of quantum random optimization problems that has not been considered yet, is the quantum k-SAT problem or the quantum q-coloring problem, paradigmatic models of CSPs. Compared to the studies already presented in the literature, these models have the peculiar feature that the ground state is extremely degenerate and organized in a complex manner. On the one hand this makes their study particularly hard, but on the other hand this aspect is very important to complete the picture of the physics of quantum CSPs.

- Since quantum computers are not available, the study of quantum systems for the moment is limited to the use of classical tools. In this direction much progress can be made. The development of powerful algorithms or general techniques able to investigate the average properties of

quantum systems is a broad and open problem. This is of practical and theoretical importance also for the understanding of mean-field disordered/glassy systems. In particular, the combination of the knowledge and the techniques developed in the context of classical glasses (such as BP, SP or the cavity method) could be combined with the experience and the algorithms developed for many-body quantum systems, such as the density matrix renormalization group, or similar approaches. The research in this direction already started and many techniques are by now available. Indeed, the quantum cavity method has already been applied to several problems (see the works [82, 83, 35, 24, 128], some of them discussed in Chapters 4 and 6). A different, approximate but faster, version of the method has been proposed in [85, 86, 87]. Other techniques, called "quantum belief propagation" [187, 188] have been developed on the basis of similar ideas. It would be extremely interesting to find a common theoretical understanding of all these methods and to develop strategies to improve their efficiency.

Quantum glasses

- The studies carried out on quantum mean-field glasses highlight important differences between models that classically are believed to describe structural glasses and those that are spin-glasses [13, 128, 24, 26]. Technically the former are described by the 1-RSB solution, while the latter by the full-RSB solution of the cavity or replica method. The main difference consists in the appearance of first-order vs. second-order quantum phase transitions, shown respectively, by structural glasses and spin-glasses. Whether this result is "universal" is not obvious, since, for instance, in [23] a model with a 1-RSB transition was shown to have a second order phase transition to a superglass phase. Moreover a related problem is the study of the effect of the statistics of the particles in the works [116, 117], where the results concerning the glass phase are derived neglecting the exchange of the particles. We think that this point is particularly important to get a consistent description of quantum glassy systems, at least at the mean-field level and it is desirable to understand the properties of disordered systems at low temperature.

- On the basis of the results outlined in Chapter 6 we think it would be interesting to investigate the Biroli-Mézard model in finite dimensions, by quantum Monte Carlo. This could help in understanding the properties of the quantum system beyond the mean-field approximation that we considered. It is important to determine the robustness of the first-order phase transition against fluctuations. Moreover, to complete the analysis it would be very interesting to study the real-time quantum dynamics of the system and to compare it with the results obtained for the classical model.

Out-of-equilibrium quantum dynamics

- We aim to complete our results on the non-equilibrium dynamics following a quantum quench of the transverse field Ising chain with a study of quenches towards the gapped phases, a topic which was not discussed in Chapter 9. We expect that the gap could induce different frequency or time scales, depending on the observable, which would enrich the dynamical behavior. Moreover we would like to investigate the role of the initial condition and, consequently, the degree of universality which can be recognized in the asymptotic behavior of such non-equilibrium dynamics, depending on the initial state.

- Beyond the model considered in Chapter 9 the most important development of the work, in our

view, concerns the study of generalized FDRs in non-integrable systems. Very often in fact, it has been found that non-integrable systems, in the long-time limit after a quantum quench, show, at least at the level of some observables, a thermal behavior [165]. This seems reasonable as most of the physical systems are not integrable and we expect that, under opportune conditions, thermalization takes place. The study of FDRs in this context can thus provide insight into the investigation of a thermal behavior for these models. Moreover it would be interesting to understand how this is connected to the spectral properties of the system.

Appendix A

Quantum cavity method for the Biroli-Mézard model

In this Appendix we derive the cavity method for the Biroli-Mézard model that we used to derive the properties of the model discussed in Chapter 6. We derive the self-consistent equations and we explain how we solve them. This procedure is based on the results obtained in [83].

Derivation of the cavity equations

Rewriting the partition function as a simple factor graph

We use in this section the same notation as in [83] for the imaginary time copies of the occupation variables. We consider a discrete number of Suzuki-Trotter slices labeled by $\alpha = 1, \cdots, N_s$. We denote by n_i^α the occupancy of site i at Suzuki-Trotter time α, by $\boldsymbol{n}_i = (n_i^1, \cdots, n_i^{N_s})$ the imaginary time trajectory of site i, by $\underline{n}^\alpha = (n_1^\alpha, \cdots, n_N^\alpha)$ the configuration at time α, by $\underline{\boldsymbol{n}} = (\underline{n}^1, \cdots, \underline{n}^{N_s})$ the imaginary time trajectory of the full system.

We write the partition function

$$Z = \text{Tr}\left[e^{-\beta \hat{H}}\right] = \lim_{N_s \to \infty} \sum_{\underline{n}^1, \cdots, \underline{n}^{N_s}} \exp\left[-\frac{\beta}{N_s}\sum_{\alpha=1}^{N_s}\sum_{i=1}^{N} v(n_i^\alpha, \{n_{j\in\partial i}^\alpha\})\right] \prod_{\alpha=1}^{N_s} \langle \underline{n}^\alpha | e^{\frac{\beta}{N_s}\sum_{\langle i,j\rangle} J(\hat{a}_i^\dagger \hat{a}_j + \hat{a}_j^\dagger \hat{a}_i)} |\underline{n}^{\alpha+1}\rangle \tag{A.1}$$

where

$$v(n_i^\alpha, \{n_{j\in\partial i}^\alpha\}) = V \; n_i^\alpha \; q_i^\alpha \; \theta(q_i^\alpha) - \mu n_i^\alpha$$
$$q_i^\alpha = \sum_{j\in\partial i} n_j^\alpha - \ell \tag{A.2}$$

and we write here and in the following $\theta(x) = \mathbb{1}(x \geq 0)$ and $\mathbb{1}(A) = 1$ if the condition A is fulfilled, 0 otherwise (A.1). It is simple to show that [83]:

$$\langle \underline{n}^\alpha | e^{\frac{\beta}{N_s}\sum_{\langle i,j\rangle} J(\hat{a}_i^\dagger \hat{a}_j + \hat{a}_j^\dagger \hat{a}_i)} |\underline{n}^{\alpha+1}\rangle = \sum_{\underline{\boldsymbol{y}}} \prod_{\langle i,j\rangle} \left(\frac{\beta J\sqrt{n_j^{\alpha+1} n_i^\alpha}}{N_s}\right)^{y_{i\to j}^\alpha} \left(\frac{\beta J\sqrt{n_i^{\alpha+1} n_j^\alpha}}{N_s}\right)^{y_{j\to i}^\alpha}$$
$$\prod_{i=1}^{N} \mathbb{1}\left(n_i^{\alpha+1} = n_i^\alpha + \sum_{j\in\partial i}[y_{j\to i}^\alpha - y_{i\to j}^\alpha]\right) + O\left(\frac{1}{N_s^2}\right). \tag{A.3}$$

where we introduced variables y with the following notations: we denote by $y^\alpha_{i\to j} \in \{0,1\}$ the variable that indicates an hopping event from site i to j at time α; by $y^\alpha_{\langle i,j\rangle} = \{y^\alpha_{i\to j}, y^\alpha_{j\to i}\}$ the two hopping variables on link $\langle i,j\rangle$; and as for occupation variables, we use bold notation to indicate the imaginary time trajectory of a variable and an underline to indicate the full configuration of the y's. Finally, we take by convention $x^{y=0} = 1$ for any value of x (including zero).

Eq. (A.3) can be checked by inspecting the behavior of its left and right-hand-side order by order in $1/N_s$. The leading term corresponds to $\underline{n}^\alpha = \underline{n}^{\alpha+1}$, and indeed all y's must vanish at this order. We note that the partition function has the following form:

$$Z = \lim_{N_s \to \infty} \sum_{\underline{n},\underline{y}} \prod_{\langle i,j\rangle} w_h(\boldsymbol{y}_{\langle i,j\rangle}) \prod_{i=1}^{N} w_s(\boldsymbol{n}_i, \{\boldsymbol{n}_j\}_{j\in\partial i}, \{\boldsymbol{y}_{\langle i,j\rangle}\}_{j\in\partial i}) \tag{A.4}$$

with

$$w_h(\boldsymbol{y}_{\langle i,j\rangle}) = \prod_{\alpha=1}^{N_s} \left(\frac{\beta J}{N_s}\right)^{y^\alpha_{i\to j}+y^\alpha_{j\to i}} , \tag{A.5}$$

and

$$w_s(\boldsymbol{n}_i, \{\boldsymbol{n}_j\}_{j\in\partial i}, \{\boldsymbol{y}_{\langle i,j\rangle}\}_{j\in\partial i}) = \exp\left[-\frac{\beta}{N_s}\sum_{\alpha=1}^{N_s} v(n^\alpha_i, \{n^\alpha_{j\in\partial i}\})\right]$$

$$\prod_{\alpha=1}^{N_s} \left\{ \mathbb{1}\left(n^{\alpha+1}_i = n^\alpha_i + \sum_{j\in\partial i}[y^\alpha_{j\to i} - y^\alpha_{i\to j}]\right) \left(\sqrt{n^{\alpha+1}_i}\right)^{\sum_{j\in\partial i} y^\alpha_{j\to i}} \left(\sqrt{n^\alpha_i}\right)^{\sum_{j\in\partial i} y^\alpha_{i\to j}} \right\}$$

$$= \exp\left[-\frac{\beta}{N_s}\sum_{\alpha=1}^{N_s} v(n^\alpha_i, \{n^\alpha_{j\in\partial i}\})\right] \widetilde{w}_s(\boldsymbol{n}_i, \{\boldsymbol{y}_{\langle i,j\rangle}\}_{j\in\partial i}) .$$

One can easily recognize that the graph of the interactions in the above representation has small loops, so, at first glance, it may appear not suited for cavity calculations. In order to avoid these loops and thus to set down an appropriate cavity treatment of the problem we adopt a trick which consists in copying on each site the variables of the neighboring sites and the jumps across the edges connected to the site. Let us introduce then:

$$\nu^\alpha_i = \{n^\alpha_i, \{n^{i\alpha}_j\}_{j\in\partial i}\} \tag{A.6}$$

where $\{n^{i\alpha}_j\}_{j\in\partial i}$ are the copies on site i of the occupation numbers of its neighbors at time α. In addition, we copy each variable $y^\alpha_{i\to j}$ on the two sites i,j, introducing $y^{i\alpha}_{j\to i} = y^{j\alpha}_{j\to i} = y^\alpha_{j\to i}$, and on each site we store these variables in a variable Υ^α_i:

$$\Upsilon^\alpha_i = \{y^{i\alpha}_{\langle i,j\rangle}\}_{j\in\partial i} = \{y^{i\alpha}_{i\to j}, y^{i\alpha}_{j\to i}\}_{j\in\partial i} . \tag{A.7}$$

Then we impose the consistency among neighboring sites' jumps and occupation numbers through a constraint

$$\widetilde{w}_l(\boldsymbol{\nu}_i, \boldsymbol{\Upsilon}_i; \boldsymbol{\nu}_j, \boldsymbol{\Upsilon}_j) = \prod_{\alpha=1}^{N_s} \delta_{n^\alpha_i, n^{j\alpha}_i} \delta_{n^\alpha_j, n^{i\alpha}_j} \delta_{y^{i\alpha}_{i\to j}, y^{j\alpha}_{i\to j}} \delta_{y^{i\alpha}_{j\to i}, y^{j\alpha}_{j\to i}} \tag{A.8}$$

Putting together this constraint and the hopping weight $w_h(\boldsymbol{y}_{\langle i,j\rangle})$ (properly expressed in terms of the new variables Υ) we obtain a total weight on each link:

$$w_l(\boldsymbol{\nu}_i, \boldsymbol{\Upsilon}_i; \boldsymbol{\nu}_j, \boldsymbol{\Upsilon}_j) = w_h(\boldsymbol{\Upsilon}_i, \boldsymbol{\Upsilon}_j)\widetilde{w}_l(\boldsymbol{\nu}_i, \boldsymbol{\Upsilon}_i; \boldsymbol{\nu}_j, \boldsymbol{\Upsilon}_j) \tag{A.9}$$

The partition function now becomes:

$$Z = \lim_{N_s \to \infty} \sum_{\underline{\boldsymbol{\nu}},\underline{\boldsymbol{\Upsilon}}} \prod_{\langle i,j\rangle} w_l(\boldsymbol{\nu}_i, \boldsymbol{\Upsilon}_i; \boldsymbol{\nu}_j, \boldsymbol{\Upsilon}_j) \prod_{i=1}^{N} w_s(\boldsymbol{\nu}_i, \boldsymbol{\Upsilon}_i) . \tag{A.10}$$

where we have defined $\underline{\boldsymbol{\Upsilon}} = \{\boldsymbol{\Upsilon}_i\}$ and the argument of w_s has been expressed in terms of the copied variables $\{\boldsymbol{\nu}_i, \boldsymbol{\Upsilon}_i\}$, living on site i.

The last form of Z is a standard form with local weights and link weights only, which is therefore defined on the original graph and hence without short loops; it is therefore suitable for a cavity treatment and the cavity equations as well as the Bethe free energy can be written straightforwardly. Introducing $\tilde{\eta}_{i \to j}(\boldsymbol{\nu}_i, \boldsymbol{\Upsilon}_i) = Z_{i \to j}(\boldsymbol{\nu}_i, \boldsymbol{\Upsilon}_i)/z_{i \to j}$, which represents the marginal probability of the variables $\boldsymbol{\nu}_i$ and $\boldsymbol{\Upsilon}_i$ defined on site i, in absence of site j, the cavity equations read [78]:

$$\tilde{\eta}_{i \to j}(\boldsymbol{\nu}_i, \boldsymbol{\Upsilon}_i) = \frac{1}{z_{i \to j}} w_s(\boldsymbol{\nu}_i, \boldsymbol{\Upsilon}_i) \prod_{k \in \partial i \setminus j} \sum_{\boldsymbol{\nu}_k, \boldsymbol{\Upsilon}_k} \tilde{\eta}_{k \to i}(\boldsymbol{\nu}_k, \boldsymbol{\Upsilon}_k) w_l(\boldsymbol{\nu}_k, \boldsymbol{\Upsilon}_k; \boldsymbol{\nu}_i, \boldsymbol{\Upsilon}_i) \; . \tag{A.11}$$

The Bethe free energy associated to the partition function, expressed in terms of the copied variables as in Eq. (A.10), is:

$$F = -\frac{1}{\beta} \ln Z = \quad - \quad \frac{1}{\beta} \sum_{i=1}^{N} \ln \left(\sum_{\boldsymbol{\nu}_i, \boldsymbol{\Upsilon}_i} w_s(\boldsymbol{\nu}_i, \boldsymbol{\Upsilon}_i) \prod_{j \in \partial i} \sum_{\boldsymbol{\nu}_j, \boldsymbol{\Upsilon}_j} \tilde{\eta}_{j \to i}(\boldsymbol{\nu}_j, \boldsymbol{\Upsilon}_j) w_l(\boldsymbol{\nu}_i, \boldsymbol{\Upsilon}_i; \boldsymbol{\nu}_j, \boldsymbol{\Upsilon}_j) \right)$$

$$+ \quad \frac{1}{\beta} \sum_{\langle i,j \rangle} \ln \left(\sum_{\substack{\boldsymbol{\nu}_i, \boldsymbol{\Upsilon}_i \\ \boldsymbol{\nu}_j, \boldsymbol{\Upsilon}_j}} w_l(\boldsymbol{\nu}_i, \boldsymbol{\Upsilon}_i; \boldsymbol{\nu}_j, \boldsymbol{\Upsilon}_j) \tilde{\eta}_{i \to j}(\boldsymbol{\nu}_i, \boldsymbol{\Upsilon}_i) \tilde{\eta}_{j \to i}(\boldsymbol{\nu}_j, \boldsymbol{\Upsilon}_j) \right) \; . \tag{A.12}$$

This expression is exact whenever the underlying graph is a tree while it corresponds to the Bethe approximation for a general graph.

Simplification of the cavity equation

The cavity equations written above are not very practical to handle, since there is a lot of redundancy in the copied variables. We can eliminate much of this redundancy by using the delta functions in the weights w_l.

First we make explicit the dependence of the cavity field on the original variables in the following form:

$$\tilde{\eta}_{i \to j}(\boldsymbol{\nu}_i, \boldsymbol{\Upsilon}_i) = \tilde{\eta}_{i \to j}(\boldsymbol{n}_i, \boldsymbol{n}_j^i, \{\boldsymbol{n}_k^i\}_{k \in \partial i \setminus j}, \boldsymbol{y}_{\langle i,j \rangle}^i, \{\boldsymbol{y}_{\langle i,k \rangle}^i\}_{k \in \partial i \setminus j}) \; . \tag{A.13}$$

Next we introduce a new cavity field:

$$\eta_{k \to i}(\boldsymbol{n}_k, \boldsymbol{n}_i^k, \{\boldsymbol{n}_l^k\}_{l \in \partial k \setminus i}, \boldsymbol{y}_{\langle i,k \rangle}^k) = w_h(\boldsymbol{y}_{\langle i,k \rangle}^k) \sum_{\{\boldsymbol{y}_{\langle k,l \rangle}^k\}_{l \in \partial k \setminus i}} \tilde{\eta}_{k \to i}(\boldsymbol{n}_k, \boldsymbol{n}_i^k, \{\boldsymbol{n}_l^k\}_{l \in \partial k \setminus i}, \boldsymbol{y}_{\langle i,k \rangle}^k, \{\boldsymbol{y}_{\langle l,k \rangle}^k\}_{l \in \partial k \setminus i}) \; , \tag{A.14}$$

and we note that using the delta functions:

$$\sum_{\boldsymbol{\nu}_k, \boldsymbol{\Upsilon}_k} \tilde{\eta}_{k \to i}(\boldsymbol{\nu}_k, \boldsymbol{\Upsilon}_k) w_l(\boldsymbol{\nu}_k, \boldsymbol{\Upsilon}_k; \boldsymbol{\nu}_i, \boldsymbol{\Upsilon}_i) = \sum_{\{\boldsymbol{n}_l^k\}_{l \in \partial k \setminus i}} \eta_{k \to i}(\boldsymbol{n}_k^i, \boldsymbol{n}_i, \{\boldsymbol{n}_l^k\}_{l \in \partial k \setminus i}, \boldsymbol{y}_{\langle i,k \rangle}^i) \; . \tag{A.15}$$

This allows to write closed equations for the new cavity fields as follows:

$$\eta_{i \to j}(\boldsymbol{n}_i, \boldsymbol{n}_j^i, \{\boldsymbol{n}_k^i\}_{k \in \partial i \setminus j}, \boldsymbol{y}_{\langle i,j \rangle}^i) = \frac{1}{z_{i \to j}} w_h(\boldsymbol{y}_{\langle i,j \rangle}^i) \sum_{\{\boldsymbol{y}_{\langle i,k \rangle}^i\}_{k \in \partial i \setminus j}} w_s(\boldsymbol{n}_i, \boldsymbol{n}_j^i, \{\boldsymbol{n}_k^i\}_{k \in \partial i \setminus j}, \boldsymbol{y}_{\langle i,j \rangle}^i, \{\boldsymbol{y}_{\langle i,k \rangle}^i\}_{k \in \partial i \setminus j})$$

$$\prod_{k \in \partial i \setminus j} \sum_{\{\boldsymbol{n}_l^k\}_{l \in \partial k \setminus i}} \eta_{k \to i}(\boldsymbol{n}_k^i, \boldsymbol{n}_i, \{\boldsymbol{n}_l^k\}_{l \in \partial k \setminus i}, \boldsymbol{y}_{\langle i,k \rangle}^i) \; . \tag{A.16}$$

We notice at this point that the upper indices of the variables in the equation above are redundant: they can all be eliminated by renaming the variables. We obtain the following equation:

$$\eta_{i\to j}(\boldsymbol{n}_i, \boldsymbol{n}_j, \{\boldsymbol{n}_k\}_{k\in\partial i\backslash j}, \boldsymbol{y}_{\langle i,j\rangle}) = \frac{1}{z_{i\to j}} w_h(\boldsymbol{y}_{\langle i,j\rangle}) \sum_{\{\boldsymbol{y}_{\langle i,k\rangle}\}_{k\in\partial i\backslash j}} w_s(\boldsymbol{n}_i, \boldsymbol{n}_j, \{\boldsymbol{n}_k\}_{k\in\partial i\backslash j}, \boldsymbol{y}_{\langle i,j\rangle}, \{\boldsymbol{y}_{\langle i,k\rangle}\}_{k\in\partial i\backslash j})$$

$$\prod_{k\in\partial i\backslash j} \sum_{\{\boldsymbol{n}_l\}_{l\in\partial k\backslash i}} \eta_{k\to i}(\boldsymbol{n}_k, \boldsymbol{n}_i, \{\boldsymbol{n}_l\}_{l\in\partial k\backslash i}, \boldsymbol{y}_{\langle i,k\rangle}) . \quad \text{(A.17)}$$

To further simplify the equations, we introduce a variable $s_{i\to j}^\alpha$ which indicates if a site i at time α is saturated by all its neighbors but j:

$$q_{i\to j}^\alpha = \sum_{k\in\partial i\backslash j} n_k^\alpha - \ell , \qquad s_{i\to j}^\alpha = \theta(q_{i\to j}^\alpha) , \quad \text{(A.18)}$$

where we recall that we assume $\theta(0) = 1$, then we consider:

$$\eta_{i\to j}(\boldsymbol{n}_i, \boldsymbol{n}_j, \boldsymbol{\sigma}_{i\to j}, \boldsymbol{y}_{\langle i,j\rangle}) = \sum_{\{\boldsymbol{n}_k\}_{k\in\partial i\backslash j}} \eta_{i\to j}(\boldsymbol{n}_i, \boldsymbol{n}_j, \{\boldsymbol{n}_k\}_{k\in\partial i\backslash j}, \boldsymbol{y}_{\langle i,j\rangle}) \, \delta_{\boldsymbol{\sigma}_{i\to j}, \theta(\boldsymbol{q}_{i\to j})} \quad \text{(A.19)}$$

with $\delta_{\boldsymbol{\sigma}_{i\to j}, \theta(\boldsymbol{q}_{i\to j})} = \prod_{\alpha=1}^{N_s} \delta_{s_{i\to j}^\alpha, \theta(q_{i\to j}^\alpha)}$. Using the relation

$$q_i\theta(q_i) = (q_{i\to j} + n_j)\theta(q_{i\to j} + n_j) = (q_{i\to j} + n_j)\theta(q_{i\to j}) = (q_{i\to j} + n_j)s_{i\to j} , \quad \text{(A.20)}$$

which can be checked by inspection of the cases $q_{i\to j} \lessgtr -1$, Eq.(A.17) becomes:

$$\eta_{i\to j}(\boldsymbol{n}_i, \boldsymbol{n}_j, \boldsymbol{\sigma}_{i\to j}, \boldsymbol{y}_{\langle i,j\rangle}) = \frac{1}{z_{i\to j}} w_h(\boldsymbol{y}_{\langle i,j\rangle}) \sum_{\{\boldsymbol{y}_{\langle i,k\rangle}\}_{k\in\partial i\backslash j}} \tilde{w}_s(\boldsymbol{n}_i, \boldsymbol{y}_{\langle i,j\rangle}, \{\boldsymbol{y}_{\langle i,k\rangle}\}_{k\in\partial i\backslash j})$$

$$\sum_{\{\boldsymbol{n}_k\}_{k\in\partial i\backslash j}} e^{-\frac{\beta}{N_s}\sum_{\alpha=1}^{N_s} n_i^\alpha \left(V s_{i\to j}^\alpha (n_j^\alpha + q_{i\to j}^\alpha) - \mu\right)} \delta_{\boldsymbol{\sigma}_{i\to j}, \theta(\boldsymbol{q}_{i\to j})} \prod_{k\in\partial i\backslash j} \sum_{\{\boldsymbol{\sigma}_{k\to i}\}} \eta_{k\to i}(\boldsymbol{n}_k, \boldsymbol{n}_i, \boldsymbol{\sigma}_{k\to i}, \boldsymbol{y}_{\langle i,k\rangle}) .$$

$$\text{(A.21)}$$

Now we note that the function $\eta_{i\to j}(\boldsymbol{n}_i, \boldsymbol{n}_j, \boldsymbol{\sigma}_{i\to j}, \boldsymbol{y}_{\langle i,j\rangle})$ has a dependence on the variable n_j of the form $\eta_{i\to j}(\boldsymbol{n}_i, \boldsymbol{n}_j, \boldsymbol{\sigma}_{i\to j}, \boldsymbol{y}_{\langle i,j\rangle}) = e^{-\frac{\beta}{N_s}\sum_{\alpha=1}^{N_s} V n_i^\alpha s_{i\to j}^\alpha n_j^\alpha} \hat{\eta}_{i\to j}(\boldsymbol{n}_i, \boldsymbol{\sigma}_{i\to j}, \boldsymbol{y}_{\langle i,j\rangle})$, so, in terms of the marginal $\hat{\eta}_{i\to j}(\boldsymbol{n}_i, \boldsymbol{\sigma}_{i\to j}, \boldsymbol{y}_{\langle i,j\rangle})$ we finally obtain:

$$\hat{\eta}_{i\to j}(\boldsymbol{n}_i, \boldsymbol{\sigma}_{i\to j}, \boldsymbol{y}_{\langle i,j\rangle}) = \frac{w_h(\boldsymbol{y}_{\langle i,j\rangle})}{z_{i\to j}}$$

$$\sum_{\substack{\{\boldsymbol{n}_k\}_{k\in\partial i\backslash j} \\ \{\boldsymbol{\sigma}_{k\to i}\}_{k\in\partial i\backslash j} \\ \{\boldsymbol{y}_{\langle i,k\rangle}\}_{k\in\partial i\backslash j}}} w_{\text{iter}}(\boldsymbol{n}_i, \boldsymbol{\sigma}_{i\to j}, \boldsymbol{y}_{\langle i,j\rangle}, \{\boldsymbol{n}_k, \boldsymbol{\sigma}_{k\to i}, \boldsymbol{y}_{\langle i,k\rangle}\}_{k\in\partial i\backslash j}) \prod_{k\in\partial i\backslash j} \hat{\eta}_{k\to i}(\boldsymbol{n}_k, \boldsymbol{\sigma}_{k\to i}, \boldsymbol{y}_{\langle i,k\rangle}) \quad \text{(A.22)}$$

where

$$w_{\text{iter}}(\boldsymbol{n}_i, \boldsymbol{\sigma}_{i\to j}, \boldsymbol{y}_{\langle i,j\rangle}, \{\boldsymbol{n}_k, \boldsymbol{\sigma}_{k\to i}, \boldsymbol{y}_{\langle i,k\rangle}\}_{k\in\partial i\backslash j}) = \tilde{w}_s(\boldsymbol{n}_i, \boldsymbol{y}_{\langle i,j\rangle}, \{\boldsymbol{y}_{\langle i,k\rangle}\}_{k\in\partial i\backslash j}) \, \delta_{\boldsymbol{\sigma}_{i\to j}, \theta(\boldsymbol{q}_{i\to j})}$$

$$e^{-\frac{\beta}{N_s}\sum_{\alpha=1}^{N_s} n_i^\alpha \left(V q_{i\to j}^\alpha s_{i\to j}^\alpha - \mu\right)} \prod_{k\in\partial i\backslash j} e^{-\frac{\beta}{N_s}\sum_{\alpha=1}^{N_s} V n_i^\alpha n_k^\alpha s_{k\to i}^\alpha} \quad \text{(A.23)}$$

From Eq. (A.22) we see that $s_{i\to j}^\alpha$ enters in the equation only through its product with n_i^α. This means that in order to characterize the state of each site one has actually to consider the variables

$\{n_i^\alpha, n_i^\alpha s_{i\to j}^\alpha\}$ and sum over $s_{i\to j}^\alpha$ in case the site is empty. Roughly speaking, defining $e = \{0,0\}$, $u = \{1,0\}$ and $s = \{1,1\}$ we can interpret $\hat{\eta}_{i\to j}(\boldsymbol{n}_i, \boldsymbol{\sigma}_{i\to j}, \boldsymbol{y}_{\langle i,j\rangle})$ as the marginal probability over trajectories of the kind $[0,\beta] \to \{e, u, s\}$ which describe the state of each "cavity site". Finally one can note that the variable $\boldsymbol{\sigma}_{i\to j}$ is completely determined by the neighbors' occupation numbers. This ensures that, even if locally in order to write the cavity recursions one needs three possible states to describe each site, globally the Hilbert space has size 2^N.

In terms of the cavity marginal probabilities $\hat{\eta}_{i\to j}(\boldsymbol{n}_i, \boldsymbol{\sigma}_{i\to j}, \boldsymbol{y}_{\langle i,j\rangle})$ the occupation site trajectory on site i is then expressed as:

$$\eta(\boldsymbol{n}_i) = \frac{1}{z_i} \sum_{\substack{\{\boldsymbol{n}_j\}_{j\in\partial i} \\ \{\boldsymbol{y}_{\langle i,j\rangle}\}_{j\in\partial i}}} w_s(\boldsymbol{n}_i, \{\boldsymbol{n}_j\}_{j\in\partial i}, \{\boldsymbol{y}_{\langle i,j\rangle}\}) \prod_{j\in\partial i} \sum_{\boldsymbol{\sigma}_{j\to i}} \hat{\eta}_{j\to i}(\boldsymbol{n}_j, \boldsymbol{\sigma}_{j\to i}, \boldsymbol{y}_{\langle i,j\rangle}) e^{-\frac{\beta}{N_s} \sum_{\alpha=1}^{N_s} V n_i^\alpha n_j^\alpha s_{j\to i}^\alpha} ,$$

(A.24)

which allows to compute all the local observables. From (A.12) we can recover the free energy as a function of the last defined messages:

$$F = -\frac{1}{\beta}\ln Z = -\frac{1}{\beta}\sum_{i=1}^N \ln\Big(\sum_{\substack{\boldsymbol{n}_i, \{\boldsymbol{n}_j\}_{j\in\partial i} \\ \{\boldsymbol{y}_{\langle i,j\rangle}\}_{j\in\partial i}}} w_s(\boldsymbol{n}_i, \{\boldsymbol{n}_j\}, \{\boldsymbol{y}_{\langle i,j\rangle}\})$$

$$\prod_{j\in\partial i} \sum_{\boldsymbol{\sigma}_{j\to i}} \hat{\eta}_{j\to i}(\boldsymbol{n}_j, \boldsymbol{\sigma}_{j\to i}, \boldsymbol{y}_{\langle i,j\rangle}) e^{-\frac{\beta V}{N_s}\sum_{\alpha=1}^{N_s} n_i^\alpha n_j^\alpha s_{j\to i}^\alpha}\Big)$$

$$+ \frac{1}{\beta}\sum_{\langle i,j\rangle} \ln\left(\sum_{\substack{\boldsymbol{n}_i, \boldsymbol{\sigma}_{i\to j} \\ \boldsymbol{n}_j, \boldsymbol{\sigma}_{j\to i} \\ \boldsymbol{y}_{\langle i,j\rangle}}} \frac{e^{-\frac{\beta V}{N_s}\sum_{\alpha=1}^{N_s} n_i^\alpha n_j^\alpha (s_{i\to j}^\alpha + s_{j\to i}^\alpha)}}{w_h(\boldsymbol{y}_{\langle i,j\rangle})} \hat{\eta}_{i\to j}(\boldsymbol{n}_i, \boldsymbol{\sigma}_{i\to j}, \boldsymbol{y}_{\langle i,j\rangle}) \hat{\eta}_{j\to i}(\boldsymbol{n}_j, \boldsymbol{\sigma}_{j\to i}, \boldsymbol{y}_{\langle i,j\rangle}) \right) .$$

In the case of a regular Bethe lattice where all sites have degree c, denoting η_{cav} the common value of the distributions $\hat{\eta}_{i\to j}$ on all edges, we obtain for the RS free energy density:

$$f = -\frac{1}{\beta N}\ln Z = -\frac{1}{\beta}\ln\Big(\sum_{\substack{\boldsymbol{n}_0 \\ \{\boldsymbol{n}_j, \boldsymbol{y}_{0j}\}_{j\in\{1,\dots,c\}}}} w_s(\boldsymbol{n}_0, \{\boldsymbol{n}_j, \boldsymbol{y}_{0j}\})$$

$$\prod_{j\in\{1,\dots,c\}} \sum_{\boldsymbol{\sigma}_{j\to 0}} \eta_{\text{cav}}(\boldsymbol{n}_j, \boldsymbol{\sigma}_{j\to 0}, \boldsymbol{y}_{0j}) e^{-\frac{\beta V}{N_s}\sum_{\alpha=1}^{N_s} n_0^\alpha n_j^\alpha s_{j\to 0}^\alpha}\Big)$$

$$+ \frac{c}{2\beta}\ln\left(\sum_{\substack{\boldsymbol{n}_0, \boldsymbol{\sigma}_{0\to 1} \\ \boldsymbol{n}_1, \boldsymbol{\sigma}_{1\to 0} \\ \boldsymbol{y}}} \frac{e^{-\frac{\beta V}{N_s}\sum_{\alpha=1}^{N_s} n_0^\alpha n_1^\alpha (s_{0\to 1}^\alpha + s_{1\to 0}^\alpha)}}{w_h(\boldsymbol{y})} \eta_{\text{cav}}(\boldsymbol{n}_0, \boldsymbol{\sigma}_{0\to 1}, \boldsymbol{y}) \eta_{\text{cav}}(\boldsymbol{n}_1, \boldsymbol{\sigma}_{1\to 0}, \boldsymbol{y}) \right) .$$

Resolution of the cavity equation for the random regular graph

In this section we explain the idea and the method used to solve the quantum cavity equation for a random regular graph. This task is rather demanding since already at the RS level it consists in a functional self-consistent equation. However, as it was shown in [82, 83], there is a representation of the equation which allows for its numerical resolution.

Let us define $\boldsymbol{h}_i = \{\boldsymbol{n}_i, \boldsymbol{\sigma}_{i\to j}, \boldsymbol{y}_{\langle i,j\rangle}\}$ the whole set of variables argument of the cavity marginals in Eq. (A.22), which determine the "field" on the i site when j is absent. In the following we deal with a random regular graph, so for simplicity, we will label with 0 the root site which is added in the cavity

iteration when we merge $k = c - 1$ neighboring sites and their associated fields $\{\boldsymbol{h}_i\}_{i \in \{1,\dots,k\}}$. Finally, we label with an index $k + 1$ the new site which is missing "downwards" with respect to the root. The calculation is based on the observation [82, 83] that for a random regular graph Eq. (A.22) has the form

$$\eta_{\mathrm{cav}}^0(\boldsymbol{h}_0) = \frac{1}{z_{\mathrm{cav}}} \sum_{\boldsymbol{h}_1 \cdots \boldsymbol{h}_k} \mathcal{Z}(\boldsymbol{h}_1, \dots, \boldsymbol{h}_k) P(\boldsymbol{h}_0 | \boldsymbol{h}_1 \cdots \boldsymbol{h}_k) \eta_{cav}^1(\boldsymbol{h}_1) \cdots \eta_{\mathrm{cav}}^k(\boldsymbol{h}_k) \ , \qquad (A.25)$$

where P is a conditional probability, positive for all arguments and normalized and

$$\mathcal{Z}(\boldsymbol{h}_1, \dots, \boldsymbol{h}_k) = \sum_{\boldsymbol{h}_0 = \{\boldsymbol{n}_0, \boldsymbol{\sigma}_{0 \to k+1}, \boldsymbol{y}_{\langle 0, k+1 \rangle}\}} w_h(\boldsymbol{y}_{\langle 0, k+1 \rangle}) w_{\mathrm{iter}}(\boldsymbol{n}_0, \boldsymbol{\sigma}_{0 \to k+1}, \boldsymbol{y}_{\langle 0, k+1 \rangle}, \{\boldsymbol{h}_j\}_{j \in \{1,\dots,k\}}) \ .$$
$$(A.26)$$

We note that at the RS level we look for the homogeneous solution so all $\eta_{\mathrm{cav}}^i = \eta_{\mathrm{cav}}$ are equivalent, however in equation (A.25) we keep the general form to allow the generalization to the 1RSB case. As detailed in [82, 83], a strategy of resolution is based on the representation of $\eta(\boldsymbol{h})$ as a weighted sample of trajectories:

$$\eta_{\mathrm{cav}}(\boldsymbol{h}) = \sum_{i=1}^{\mathcal{N}_{\mathrm{traj}}} g_i \, \delta(\boldsymbol{h} - \boldsymbol{h}_i) \ , \qquad (A.27)$$

where the $\mathcal{N}_{\mathrm{traj}}$ weights of the trajectories are normalized according to

$$\sum_{i=1}^{\mathcal{N}_{\mathrm{traj}}} g_i = 1 \ . \qquad (A.28)$$

One should not confuse this population of quantum trajectories (that represents the RS solution of the quantum problem) with the population of cavity fields that we introduced in the classical case in Eq. (2.17) to describe the 1RSB solution. The form (A.27) provides an approximate representation of η_{cav} which becomes more and more accurate as $\mathcal{N}_{\mathrm{traj}}$ grows. Starting from an initial weighted sample of η_{cav} in the form of (A.27) the procedure amounts to iterate the following three steps:

1. extract k trajectories $\boldsymbol{h}_i = \{\boldsymbol{n}_i, \boldsymbol{\sigma}_{i \to j}, \boldsymbol{y}_{\langle i, j \rangle}\}$ in $[1, \dots, \mathcal{N}_{\mathrm{traj}}]$ from (A.27) according to their weight g_i

2. draw the new trajectory from $P(\boldsymbol{h}_0 | \boldsymbol{h}_1 \cdots \boldsymbol{h}_k)$

3. set $\boldsymbol{h}_i' = \boldsymbol{h}_0$ and $g_i' = \mathcal{Z}(\boldsymbol{h}_1, \dots, \boldsymbol{h}_k)$

where the second point amounts to a single site problem that will be further explained in the next section. Once a new representation of η_{cav} in terms of $\boldsymbol{h}_i'$ is available it can be substituted in the r.h.s. of Eq. (A.25) and the procedure is iterated until the convergence, in the sense of the observable expectation values, is reached.

Before entering into the description of the generation of the new trajectory given the k neighbors, we anticipate that, as in the classical case, also the quantum model is characterized by a glass phase at high enough densities, where the RS equations are no more correct (they have the same pathologies as in the classical case, yielding for instance negative entropies). The 1RSB treatment is needed also for the quantum problem and within this framework we have derived all the results concerning the glass phase, presented in the following.

At this level however, the generalization of the classical 1RSB equation (6.6) is straightforward. The only difference is that now the fields $h = \{\psi^e, \psi^u, \psi^s\}$ of Eq. (6.6) are probability distributions over paths, namely the "cavity fields" η_{cav} of the RS equations (A.25) and Z_{iter} is the normalization

constant z_{cav} that appears in the same Eq.(A.25). Then, the 1-RSB cavity equation for the random regular graph reads:

$$P[\eta_{\text{cav}}] \propto \int dP[\eta_{\text{cav}}^1] \dots dP[\eta_{\text{cav}}^k] \delta \left(\eta_{\text{cav}} - f(\eta_{\text{cav}}^1, \dots, \eta_{\text{cav}}^k) \right) z_{\text{cav}}^m \ , \tag{A.29}$$

where $f(\eta_{\text{cav}}^1, \dots, \eta_{\text{cav}}^k)$ is the r.h.s. of Eq. (A.25), and a normalization constant has been hidden in the notation $\propto$. The numerical resolution of the equation (A.29) necessarily goes through the representation of $P[\eta_{\text{cav}}]$ as a population of "fields" η_{cav}

$$P[\eta_{\text{cav}}] = \sum_{i=1}^{\mathcal{N}} w_i \, \delta(\eta_{\text{cav}} - \eta_i) \ , \tag{A.30}$$

where the weights derive from the cavity iteration $w \propto z_{\text{cav}}^m$ (analogously as in the classical case) and each η_{cav} is itself a population of trajectories. This procedure is of course accompanied by a demanding computational cost which is however still attainable and controllable.

Generation of a trajectory

In this section we will focus on the problem of the generation of trajectories for the thermodynamic limit of a random regular graph of connectivity c. As we said before the strategy of resolution is based on the representation of $\eta(\boldsymbol{h})$ as a weighted sample of trajectories. Then one will pick k trajectories $\boldsymbol{h}_1 \cdots \boldsymbol{h}_k$ from the corresponding distributions, and use $P(\boldsymbol{h}_0 | \boldsymbol{h}_1 \cdots \boldsymbol{h}_k)$ to draw a new trajectory $\boldsymbol{h}_0$, to which a weight $\mathcal{Z}(\boldsymbol{h}_1, \dots, \boldsymbol{h}_k)$ is assigned.

In order to calculate $\mathcal{Z}$ and to generate a new path we need to take into account all events encoded in the neighboring trajectories. In particular we can distinguish between three of them:

- a particle jump from or towards the neighboring sites, which is encoded in $\{\boldsymbol{n}_i\}_{i \in \{1,\dots,k\}}$

- a change in the $\{\boldsymbol{\sigma}_{i \to 0}\}_{i \in \{1,\dots,k\}}$ variables

- a jump from or towards the neighboring sites along the edge connecting the site under consideration, described by $\{\boldsymbol{y}_{\langle i,0 \rangle}\}_{i \in \{1,\dots,k\}}$ variables.

The last class of events is a subset of the first one, but it is important to take it into account separately because it induces constraints on the new occupation number trajectory. All the other events, instead, will enter as shifts of the effective chemical potential induced on the added site. Moreover we stress that in the continuous time limit ($N_{\text{s}} \to \infty$) the hopping trajectories $\boldsymbol{h}$ typically contain only a finite number (with respect to N_{s}) of events. We can thus assume that they occur at different values of the discrete time for the different trajectories. We call p the total number of hopping events occuring in $(\boldsymbol{h}_1, \dots, \boldsymbol{h}_k)$. We also denote $\alpha_1 < \dots < \alpha_p$ their discrete time of occurence.

We consider the Hilbert space of a single site, with a and $a^\dagger$ the annihilation/creation operators. We introduce the operator $b_j = a$ (resp. $b_j = a^\dagger$) if at time α_j there is a jump towards (resp. outside) the site under consideration, while $b_j = \mathbb{1}$ when there is an event which does not involve the new vertex, but only the neighboring trajectories. The former case corresponds to the occurrence of an event of the third kind, while the latter corresponds to an event of the first or second kind. Finally we introduce $c_\alpha = b_j$ when $\alpha = \alpha_j$, $c_\alpha = \mathbb{1}$ (the identity operator) otherwise. In terms of these operators

we get the following expression for $\mathcal{Z}$:

$$\mathcal{Z}(\boldsymbol{h}_1,\ldots,\boldsymbol{h}_k) = \sum_{\boldsymbol{h}_0} w_h(\boldsymbol{h}_0) w_{\text{iter}}(\boldsymbol{h}_0,\{\boldsymbol{h}_i\}_{i\in\{1,\ldots,k\}})$$

$$= \sum_{\boldsymbol{n}_0} \prod_{\alpha=1}^{N_{\text{s}}} \langle n_0^\alpha | e^{\frac{\beta}{N_{\text{s}}}(\mu^\alpha(\{n_i^\alpha, s_{i\to 0}^\alpha\}_{i\in\{1,\ldots,k\}})a^\dagger a + J(a+a^\dagger))} c_\alpha | n_0^{\alpha+1} \rangle \tag{A.31}$$

up to corrections of order N_{s}^{-2}, where we have introduced an effective chemical potential, which depends on the state of the neighboring sites and is defined as follows:

$$\mu^\alpha(\{n_i^\alpha, s_{i\backslash 0}^\alpha\}_{i\in\{1,\ldots,k\}}) = -V\left(q_{0\to k+1}^\alpha \theta(q_{0\to k+1}^\alpha) + \sum_{i=1}^k n_i^\alpha s_{i\to 0}^\alpha\right) + \mu . \tag{A.32}$$

To take the continuous time limit it is convenient to define $\tau_j = \frac{\beta}{N_{\text{s}}}\alpha_j$, which are the continuous times of the hopping events in $(\boldsymbol{h}_1,\ldots,\boldsymbol{h}_k)$, and to denote μ_i the common value of the μ_α for $\alpha \in [\alpha_{i-1},\alpha_i]$. We also introduce $\widehat{W}_i(\lambda) = e^{\lambda(\mu_i a^\dagger a + J(a+a^\dagger))}$, the propagator of an imaginary time evolution on an interval of length λ for a single site Hamiltonian $H_i = -\mu_i a^\dagger a - J(a+a^\dagger)$. This propagator is a two by two matrix and it easily allows to compute $\mathcal{Z}$ in the continuous limit according to the relation:

$$\mathcal{Z}(\boldsymbol{h}_1,\ldots,\boldsymbol{h}_k) = \text{Tr}\left(\widehat{W}_1(\tau_1)b_1\widehat{W}_2(\tau_2-\tau_1)b_2\ldots\widehat{W}_p(\tau_p-\tau_{p-1})b_p\widehat{W}_{p+1}(\beta-\tau_p)\right) . \tag{A.33}$$

We can now look at the process of the generation of a new trajectory $\boldsymbol{h}_0$ given the ones of the $c-1$ other neighbors, which respects the following probability law

$$P(\boldsymbol{h}_0|\boldsymbol{h}_1,\ldots,\boldsymbol{h}_k) = \frac{w_h(\boldsymbol{h}_0)w_{\text{iter}}(\boldsymbol{h}_0,\{\boldsymbol{h}_i\}_{i\in\{1,\ldots,k\}})}{\mathcal{Z}(\boldsymbol{h}_1,\ldots,\boldsymbol{h}_k)} . \tag{A.34}$$

The general scheme to determine $\boldsymbol{h}_0 = \{\boldsymbol{n}_0, \boldsymbol{\sigma}_0, \boldsymbol{y}_{\langle 0,k+1\rangle}\}$ consists in first drawing the occupation number trajectory $\boldsymbol{n}_0$ and then deduce $\boldsymbol{y}_{\langle 0,k+1\rangle}$ from its jumps not associated to the events in $(\boldsymbol{y}_{\langle 0,1\rangle},\ldots,\boldsymbol{y}_{\langle 0,k\rangle})$. Finally the trajectory of $\boldsymbol{\sigma}_0$ is completely determined by the neighboring ones $(\boldsymbol{n}_1,\ldots,\boldsymbol{n}_k)$ and does not have to be generated. We keep the notation $\tau_1 < \cdots < \tau_p$ and $b_1,\ldots,b_p$ for the continuous time of the events in $(\boldsymbol{h}_1,\ldots,\boldsymbol{h}_k)$. Let us call $n_0 = n(\tau=0)$, n_i (resp. n_i') the value of $n(\tau)$ at a time just after τ_i (resp. just before τ_{i+1}), with the conventions $n_p' = n_0$. The joint probability law of these occupation numbers which arises from the expressions of w_h and w_{iter} given in Eqs. (A.5) and (A.23) reads in the continuous time limit

$$P(n_0, n_0', n_1, n_1', \ldots, n_p|\boldsymbol{h}_1,\ldots,\boldsymbol{h}_k) = \frac{1}{\mathcal{Z}(\boldsymbol{h}_1,\ldots,\boldsymbol{h}_k)}\langle n_0|\widehat{W}_i(\tau_1)|n_0'\rangle \times$$

$$\times \prod_{i=1}^p \left\{ \langle n_{i-1}'|b_i|n_i\rangle\langle n_i|\widehat{W}_{i+1}(\tau_{i+1}-\tau_i)|n_i'\rangle \right\} , \tag{A.35}$$

with $\tau_{p+1} = \beta$. This probability law is well normalized according to the above expression of $\mathcal{Z}(\boldsymbol{h}_1,\ldots,\boldsymbol{h}_k)$. It follows immediately from the above equation that whenever the operator b_i is non trivial, i.e. when there is a jump along the edge connecting the neighbors to the new site, the state of the site is uniquely defined by the direction of the jump. This is a trivial consequence of the fact that we are dealing with hard-core bosons. Then, we have to generate only those values in the sequence $(n_0, n_0', n_1, n_1', \ldots, n_p)$ which are not already fixed. This is a task that can be done sequentially, starting from n_0, quite easily. Once all the intermediate occupation numbers are fixed, the generation of the rest of the path will proceed independently for every interval $\{\tau_{i+1} - \tau_i\}$. Inside each of them, in fact, one has to generate a

trajectory with fixed boundary conditions according to the path integral representation of an effective Hamiltonian which depends on time interval $\hat{H}_i = -\mu_i \hat{a}^\dagger \hat{a} - J(\hat{a} + \hat{a}^\dagger)$. From this point the procedure is exactly equivalent to the one used for the Bose-Hubbard model, explained in [83]. At this level, in fact, the task is completely equivalent to that of the Bose-Hubbard model, despite the different interaction between neighboring sites, which is here hidden in effective single site Hamiltonians. For the same reason it is also very similar to the procedure outlined in Section 2.2 for a spin system in a transverse field. Thus, we remand to Chapter 2 and to [83] for further details.

The computation of the observables

Here we explain how one can compute the expectation value of generic observables, how we deal with the symmetry breaking associated to $\langle \hat{a} \rangle$ and the computation of the imaginary time correlations. Below we report only the main steps, following [83], and for more details we remand to [83].

Let us focus first on the thermal average $\left\langle q(\hat{a}_i^\dagger \hat{a}_i) \right\rangle = \langle q(\hat{n}_i) \rangle$ of an arbitrary single-site operator function of the occupation number $\hat{n}$. The expectation value can be read from the knowledge of $\eta_{\mathrm{cav}}(\boldsymbol{h})$ and the expression:

$$\left\langle q(\hat{a}_i^\dagger \hat{a}_i) \right\rangle = \frac{1}{z_{\mathrm{site}}} \sum_{\boldsymbol{h}_1,\ldots,\boldsymbol{h}_c} \eta_{\mathrm{cav}}(\boldsymbol{h}_1)\ldots\eta_{\mathrm{cav}}(\boldsymbol{h}_c)\mathrm{Tr}\left(q(\hat{a}^\dagger \hat{a})\widehat{W}_1'(\tau_1)b_1\widehat{W}_2'(\tau_2 - \tau_1)b_2\ldots b_p\widehat{W}_{p+1}'(\beta - \tau_p)\right) ,$$

(A.36)

where here we defined $\widehat{W}_i'(\lambda) = e^{-\lambda\mu_i(\hat{a}^\dagger \hat{a})}$, the single-site propagator without its hopping term. In fact, in this computation all the possible hopping events involving the considered site are fixed by the c neighboring trajectories $\boldsymbol{h}_1,\ldots,\boldsymbol{h}_c$. Eq. (A.36) allows to compute at the RS level the density of particles or the onsite potential.

Similarly, the order parameter $\langle \hat{a}_i \rangle$ is obtained by the insertion of an annihilation operator in the effective single-site problem,

$$\langle \hat{a}_i \rangle = \frac{1}{z_{\mathrm{site}}} \sum_{\boldsymbol{h}_1,\ldots,\boldsymbol{h}_c} \eta_{\mathrm{cav}}(\boldsymbol{h}_1)\ldots\eta_{\mathrm{cav}}(\boldsymbol{h}_c)\mathrm{Tr}\left(\hat{a}\widehat{W}_1'(\tau_1)b_1\widehat{W}_2'(\tau_2 - \tau_1)b_2\ldots b_p\widehat{W}_{p+1}'(\beta - \tau_p)\right) . \quad \text{(A.37)}$$

The other sites, different from i, are in fact unmodified, and hence, one can integrate over them and obtain the same equation for η_{cav}. At this point the importance of a suitable initial condition on the population, mentioned in Section 6.2, becomes more transparent. The problem is connected to the symmetry associated to the conservation of the total number of particles. Indeed, Eq. (A.37) strictly vanishes whenever all hopping trajectories in the support of η_{cav} have the same number of jumps in the two directions of their edge. Moreover this symmetry is conserved by the iterative equation (A.22). Then, in order to investigate possible phases with $\langle \hat{a} \rangle \neq 0$ we have to allow for the breaking of the corresponding symmetry. The strategy that we used is to initialize the population dynamics algorithm including asymmetric hopping trajectories. In the "insulating" phase these trajectories disappear during the iterations, while in the "superfluid" a finite fraction of them keeps the asymmetry, and thus one finally obtains a non zero value of $\langle \hat{a} \rangle$.

Also for the computation of the Green function we follow [83]. Again, from the definition $G_>^i(\tau) = \mathrm{Tr}[e^{-(\beta-\tau)\hat{H}}\hat{a}_i e^{-\tau\hat{H}}\hat{a}_i^\dagger]/Z$, one is back to a single site problem, once that η_{cav} is known. The insertion of two creation/annihilation operators occurs on the same site but at different times. Similarly to

Eq. (A.36), one obtains:

$$
G_>(\tau) = \frac{1}{z_{\text{site}}} \sum_{\boldsymbol{h}_1,\ldots,\boldsymbol{h}_c} \eta_{\text{cav}}(\boldsymbol{h}_1)\ldots\eta_{\text{cav}}(\boldsymbol{h}_c)\times
$$
$$
\times \text{Tr}\left(\hat{a}\widehat{W}'_i(\tau_1)b_1\widehat{W}'_2(\tau_2-\tau_1)b_2\ldots b_i\widehat{W}'_i(\tau-\tau_i)\hat{a}^\dagger\widehat{W}'_{i+1}(\tau_{i+1}-\tau)b_{i+1}\cdots b_p\widehat{W}'_{p+1}(\beta-\tau_p)\right) ,
$$
$$
\text{(A.38)}
$$

where the index i is such that $\tau_i < \tau < \tau_{i+1}$.

Appendix B

Numerical computation of Leggett's bound

In this Appendix we provide some details on the numerical procedure used to compute the Leggett's upper bound on the superfluid fraction of an amorphous solid, discussed in Chapter 7.

Leggett's bound and its numerical solution

We define the Fourier transforms in the cubic box of side L and volume $V = L^3$ as follows:

$$\rho_{\vec{q}} = \frac{1}{V} \int_V d\vec{r} \rho(\vec{r}) e^{i\vec{q}\cdot\vec{r}} , \qquad \rho(\vec{r}) = \sum_{\vec{q}} \rho_{\vec{q}} e^{-i\vec{q}\cdot\vec{r}} , \tag{B.1}$$

where $\vec{q} = \frac{2\pi}{L}(n_x, n_y, n_z)$, and each of the integers $n_i \in Z$, and similarly

$$\delta\varphi_{\vec{q}} = \frac{1}{V} \int_V d\vec{r} \delta\varphi(\vec{r}) e^{i\vec{q}\cdot\vec{r}} . \tag{B.2}$$

Note that $\delta\varphi_{\vec{0}}$ is an irrelevant constant phase in the variational wavefunction so we set it to zero. Finally,

$$\vec{v}_{\vec{q}} = \begin{cases} \vec{v}_0 & \vec{q} = \vec{0} , \\ -i\vec{q}\varphi_{\vec{q}} & \vec{q} \neq \vec{0} . \end{cases} \tag{B.3}$$

which leads immediately to Eq. (7.12).

We performed the calculations for different values of the Lindemann parameter $\ell = \rho^{1/3} A^{1/2}$, increasing the number of vectors $\vec{q}$ according to the spherical constraint $|\vec{q}| \leq q_{max}$, until a reasonable convergence in the value of the bound (7.13) was achieved, at least for large values of A. From Eq. (7.15) one sees that for large $|\vec{q}|$ the corresponding component $\rho_{\vec{q}}$ is suppressed through the factor $e^{-Aq^2/2}$. Thus, one needs to truncate the sum over $\vec{q}$ at $q_{max} \sim 1/\sqrt{A}$, as higher terms will not contribute. Unfortunately, for small A, this cut-off is too heavy in terms of computational time and we should use a lower one. Still, considering small configurations and sufficiently large values of A, which nevertheless span the physical region of interest, we could reach a good convergence or keep the error under control. Note additionally that by increasing the number of vectors $\vec{q}$ in (7.15), the value found for the superfluid fraction monotonically decreases, as expected because of the variational property already discussed. This permits to preserve the nature of upper bound for Eq. (7.13), despite the cut-off approximation. Overall, we found that the better compromise was to set $q_{max} = 20\pi/L$.
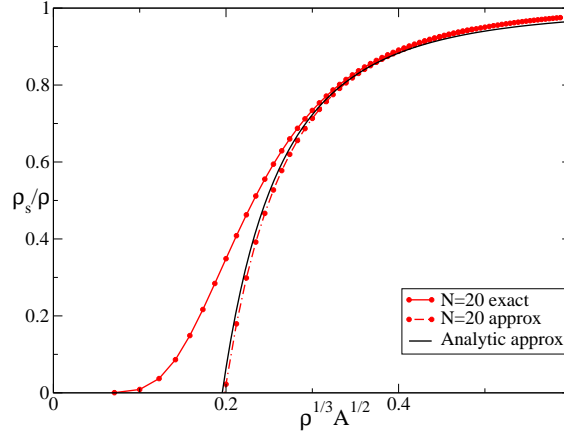
Figure B.1: Result for $\overline{\rho_s/\rho}$ as a function of the localization parameter $\rho^{1/3}A^{1/2}$, where $\vec{R}_i$ are N random points in $[0, L]^3$ with periodic boundary conditions.

In order to check the independence of the bound on the flow direction, we also compared the results obtained with the velocity v_0 along the $(1, 0, 0)$ direction to those along $(1, 1, 1)$ and we observed a negligible difference which is expected to vanish in the thermodynamic limit, because amorphous solids are statistically homogeneous on large scales.

We have also checked that the bound for the superfluid density almost does not fluctuate by considering different amorphous configurations $\mathcal{R}^\alpha$, $\alpha = 1, \cdots, \mathcal{N}$, as it is expected since the superfluid density is a macroscopic quantity. We computed the corresponding superfluid fraction ρ_s^α and the average $\overline{\rho}_s = \sum_\alpha \rho_s^\alpha/\mathcal{N}$ for 10 different configurations. The variance of ρ_s is very small. In this paper we presented results averaged over 10 realizations of $\mathcal{R}^\alpha$, a larger statistics do not lead to appreciable differences.

Finally, as a check of our codes, we repeated all the calculations on configurations of 20 particles occupying uncorrelated uniformly random positions in the box, i.e. where $\vec{R}_i$ are uniform and independent random variables in $[0, L]^3$. In this case it is easy to show that $\widetilde{g}_q = \exp(-Aq^2)$. Hence Eq. (7.27) becomes

$$\frac{\overline{\rho_s}}{\rho} = 1 - \frac{2}{3(2\pi)^2\rho} \int_0^\infty dq \, q^2 \, e^{-Aq^2} = 1 - \frac{1}{24\pi^{3/2} \, \rho A^{3/2}} \ . \tag{B.4}$$

In this case the values of the bound were more sensitive to the particular realization, so we took averages over 30 configurations. For every value of the localization parameter, the superfluid fractions that we found were on average smaller, as reported in Figure B.1.

Large A expansion

For large A, we expect that the density becomes uniform. Hence, $\rho_{\vec{0}} \to \rho$, and $\rho_{\vec{q}} \to 0$ for $\vec{q} \neq \vec{0}$. We can use this to expand $i\delta\varphi_{\vec{q}}$ systematically in powers of $\rho_{\vec{q}}$. We rewrite Eq. (7.12) as

$$\vec{q} \cdot \vec{v}_0 \rho_{\vec{q}} = q^2 \rho i\delta\varphi_{\vec{q}} + \sum_{\vec{p} \neq \vec{0}, \vec{q}} (\vec{q} \cdot \vec{p})\rho_{\vec{q}-\vec{p}} \, i\delta\varphi_{\vec{p}} \ . \tag{B.5}$$

We write $\delta\varphi_{\vec{q}} = \delta\varphi_{\vec{q}}^{(1)} + \delta\varphi_{\vec{q}}^{(2)} + \cdots$ where the different terms are of order $(\rho_{\vec{q}})^k$. At first order

$$i\delta\varphi_{\vec{q}}^{(1)} = \frac{\vec{q} \cdot \vec{v}_0}{q^2\rho}\rho_{\vec{q}} \ , \tag{B.6}$$

at second order

$$
\begin{aligned}
i\delta\varphi_{\vec{q}}^{(2)} &= -\frac{1}{q^2\rho} \sum_{\vec{p}\neq\vec{0},\vec{q}} (\vec{q}\cdot\vec{p})\rho_{\vec{q}-\vec{p}} \, i\delta\varphi_{\vec{p}}^{(1)} \\
&= -\sum_{\vec{p}\neq\vec{0},\vec{q}} \frac{(\vec{q}\cdot\vec{p})(\vec{p}\cdot\vec{v}_0)}{p^2 q^2 \rho^2} \rho_{\vec{q}-\vec{p}}\rho_{\vec{p}} \,,
\end{aligned}
\tag{B.7}
$$

at third order

$$
\begin{aligned}
i\varphi_{\vec{q}}^{(3)} &= -\frac{1}{\vec{q}^2\rho} \sum_{\vec{p}\neq\vec{0},\vec{q}} (\vec{q}\cdot\vec{p})\rho_{\vec{q}-\vec{p}} \, i\varphi_{\vec{p}}^{(2)} \\
&= \sum_{\vec{p}\neq\vec{0},\vec{q}} \sum_{\vec{p}'\neq\vec{0},\vec{p}} \frac{(\vec{q}\cdot\vec{p})(\vec{p}\cdot\vec{p}')(\vec{p}'\cdot\vec{v}_0)}{q^2 p^2 p'^2 \rho^3} \rho_{\vec{q}-\vec{p}}\rho_{\vec{p}-\vec{p}'}\rho_{\vec{p}'}
\end{aligned}
\tag{B.8}
$$

from which we can guess the order k:

$$
i\varphi_{\vec{q}}^{(k)} = (-1)^{k-1} \sum_{\vec{p}_1\neq\vec{0},\vec{q};\ \vec{p}_2\neq\vec{0},\vec{p}_1;\ \cdots\ \vec{p}_{k-1}\neq\vec{0},\vec{p}_{k-2}} \frac{(\vec{q}\cdot\vec{p}_1)(\vec{p}_1\cdot\vec{p}_2)\cdots(\vec{p}_{k-1}\cdot\vec{v}_0)}{q^2 p_1^2\cdots p_{k-1}^2 \rho^k} \rho_{\vec{q}-\vec{p}_1}\rho_{\vec{p}_1-\vec{p}_2}\cdots\rho_{\vec{p}_{k-2}-\vec{p}_{k-1}}\rho_{\vec{p}_{k-1}}
\tag{B.9}
$$

and so on. Plugging this in Eq. (7.13) we get

$$
\begin{aligned}
\frac{\rho_s}{\rho} =\, &1 - \sum_{\vec{q}\neq\vec{0}} \frac{(\vec{v}_0\cdot\vec{q})^2}{\rho^2 v_0^2 q^2} \rho_{\vec{q}}\rho_{-\vec{q}} + \sum_{\vec{q}\neq\vec{0}} \sum_{\vec{p}\neq\vec{0},\vec{q}} \frac{(\vec{v}_0\cdot\vec{q})(\vec{q}\cdot\vec{p})(\vec{p}\cdot\vec{v}_0)}{q^2 p^2 v_0^2 \rho^3} \rho_{\vec{q}-\vec{p}}\rho_{\vec{p}}\rho_{-\vec{q}} \\
&- \sum_{\vec{q}\neq\vec{0}} \sum_{\vec{p}\neq\vec{0},\vec{q}} \sum_{\vec{p}'\neq\vec{0},\vec{p}} \frac{(\vec{v}_0\cdot\vec{q})(\vec{q}\cdot\vec{p})(\vec{p}\cdot\vec{p}')(\vec{p}'\cdot\vec{v}_0)}{q^2 p^2 p'^2 v_0^2 \rho^4} \rho_{\vec{q}-\vec{p}}\rho_{\vec{p}-\vec{p}'}\rho_{\vec{p}'}\rho_{-\vec{q}} + \cdots \,.
\end{aligned}
\tag{B.10}
$$

While this expansion seems a simple strategy of solution of Eq. (7.12), it is very poorly convergent and in practice it is not very helpful.

Bibliography

[1] L. Berthier, G. Biroli. *Rev. Mod. Phys.*, **83**, 587 (2011).

[2] L. Berthier, G. Biroli, J. Bouchaud, L. Cipelletti, W. Van Saarloos. *Dynamical heterogeneities in glasses, colloids, and granular media*. Oxford University Press (2011).

[3] S. Kirkpatrick, C. Gelatt, M. Vecchi. *Science*, **220**, 671 (1983).

[4] M. Mézard, G. Parisi, R. Zecchina. *Science*, **297**, 812 (2002).

[5] G. Biroli, R. Monasson, M. Weigt. *Eur. Phys. J. B*, **14**, 551 (2000).

[6] F. Krzakala, A. Montanari, F. Ricci-Tersenghi, G. Semerjian, L. Zdeborova. *Proceedings of the National Academy of Sciences*, **104**, 10318 (2007).

[7] T. Kadowaki, H. Nishimori. *Phys. Rev. E*, **58**, 5355 (1998).

[8] E. Farhi, J. Goldstone, S. Gutmann, J. Lapan, A. Lundgren, D. Preda. *Science*, **292**, 472 (2001).

[9] J. Zinn-Justin. *Intégrale de chemin en mécanique quantique: Introduction*. L'Editeur: EDP Sciences (2003).

[10] R. Moessner. *Canadian journal of physics*, **79**, 1283 (2001).

[11] Y. Y. Goldschmidt. *Phys. Rev. B*, **41**, 4858 (1990).

[12] T. Nieuwenhuizen, F. Ritort. *Physica A*, **250**, 8 (1998).

[13] L. F. Cugliandolo, D. R. Grempel, C. A. Da Silva Santos. *Phys. Rev. B*, **64**, 014403 (2001).

[14] W. Wu, D. Bitko, T. Rosenbaum, G. Aeppli. *Physical review letters*, **71**, 1919 (1993).

[15] M. Ben-Chorin, Z. Ovadyahu, M. Pollak. *Phys. Rev. B*, **48**, 15025 (1993).

[16] S. Ludwig, D. Osheroff. *Phys. Rev. Lett.*, **91**, 105501 (2003).

[17] C. Panagopoulos, V. Dobrosavljević. *Phys. Rev. B*, **72**, 014536 (2005).

[18] E. Kim, M. Chan. *Nature*, **427**, 225 (2004).

[19] S. Balibar, F. Caupin. *Journal of Physics: Condensed Matter*, **20**, 173201 (2008).

[20] A. Leggett. *Phys. Rev. Lett.*, **25**, 1543 (1970).

[21] B. Hunt, E. Pratt, V. Gadagkar, M. Yamashita, A. V. Balatsky, J. C. Davis. *Science*, **324**, 632 (2009).

[22] A. Rittner, J. Reppy. *Phys. Rev. Lett.*, **97**, 165301 (2006).

[23] G. Biroli, C. Chamon, F. Zamponi. *Phys. Rev. B*, **78**, 224306 (2008).

[24] G. Carleo, M. Tarzia, F. Zamponi. *Phys. Rev. Lett.*, **103**, 215302 (2009).

[25] M. Boninsegni, N. Prokof'ev, B. Svistunov. *Phys. Rev. Lett.*, **96**, 105301 (2006).

[26] K.-M. Tam, S. Geraedts, S. Inglis, M. J. P. Gingras, R. G. Melko. *Phys. Rev. Lett.*, **104**, 215301 (2010).

[27] L. Cugliandolo, J. Kurchan. *Phys. Rev. Lett.*, **71**, 173 (1993).

[28] L. Cugliandolo, J. Kurchan, L. Peliti. *Phys. Rev. E*, **55**, 3898 (1997).

[29] I. Bloch, J. Dalibard, W. Zwerger. *Rev. Mod. Phys.*, **80**, 885 (2008).

[30] P. W. Anderson. *Phys. Rev.*, **109**, 1492 (1958).

[31] D. Basko, I. Aleiner, B. Altshuler. *Annals of physics*, **321**, 1126 (2006).

[32] A. Pal, D. Huse. *Phys. Rev. B*, **82**, 174411 (2010).

[33] E. Canovi, D. Rossini, R. Fazio, G. Santoro, A. Silva. *Phys. Rev. B*, **83**, 094431 (2011).

[34] T. Mora, L. Zdeborová. *Journal of Statistical Physics*, **131**, 1121–1138 (2008).

[35] T. Jörg, F. Krzakala, G. Semerjian, F. Zamponi. *Phys. Rev. Lett.*, **104**, 207206 (2010).

[36] G. Biroli, M. Mézard. *Phys. Rev. Lett.*, **88**, 25501 (2001).

[37] C. Papadimitriou, K. Steiglitz. *Combinatorial Optimization: Algorithms and Complexity*. Dover, New York (1998).

[38] G. Semerjian. *J. Stat. Phys.*, **130**, 251 (2008).

[39] M. Mézard, T. Mora, R. Zecchina. *Phys. Rev. Lett.*, **94**, 197205 (2005).

[40] F. Altarelli, R. Monasson, G. Semerjian, F. Zamponi. In A. Biere, M. Heule, H. v Maaren, T. Walsh, editors, *Handbook of Satisfiability, Frontiers in Artificial Intelligence and Applications*. IOS Press (2009).

[41] E. Friedgut. *Journal of the American Mathematical Society*, **12**, 1017 (1999).

[42] D. Achlioptas, Y. Peres. *Journal of the American Mathematical Society*, **17**, 947 (2004).

[43] S. Cocco, O. Dubois, J. Mandler, R. Monasson. *Phys. Rev. Lett.*, **90**, 047205 (2003).

[44] M. Mézard, F. Ricci-Tersenghi, R. Zecchina. *J. Stat. Phys.*, **111**, 505 (2003).

[45] M. Ibrahimi, Y. Kanoria, M. Kraning, A. Montanari. `arXiv:1107.5377` (2011).

[46] D. Achlioptas, M. Molloy. `arXiv:1107.5550` (2011).

[47] D. Achlioptas, F. Ricci-Tersenghi. `arXiv:cs.CC/0611052`. *Proceedings of the thirty-eighth annual ACM symposium on Theory of computing* (2006).

[48] C. Papadimitriou. In *Proceedings of the 32th Annual Symposium on Foundations of Computer Science*, page 163 (1991).

[49] S. Cocco, R. Monasson. *Ann. Math. Artif. Intell.*, **43**, 153 (2005).

[50] R. Monasson. *Lecture Notes in Computer Science*, **3624**, 402 (2005).

[51] M. Mézard, R. Zecchina. *Phys. Rev. E*, **66**, 056126 (2002).

[52] M. Mézard, A. Montanari. *Information, Physics and Computation.* Oxford University Press (2009).

[53] A. Amraoui, A. Montanari, T. Richardson, R. Urbanke. `arXiv:cs.IT/0406050` (2004).

[54] P. Shor. In *Foundations of Computer Science, 1994 Proceedings., 35th Annual Symposium on*, page 124. IEEE (1994).

[55] L. Grover. *Phys. Rev. Lett.*, **79**, 325 (1997).

[56] D. Deutsch. *Proceedings of the Royal Society of London. A. Mathematical and Physical Sciences*, **400**, 97 (1985).

[57] A. Messiah. *Quantum mechanics vol. 2.* North-Holland, Amsterdam (1962).

[58] L. D. Landau, E. M. Lifshitz. *Quantum Mechanics, vol. 3.* Pergamon Press, Oxford (1977).

[59] T. Jörg, F. Krzakala, J. Kurchan, A. C. Maggs. *Phys. Rev. Lett.*, **101**, 147204 (2008).

[60] M. H. S. Amin, V. Choi. *Phys. Rev. A*, **80**, 062326 (2009).

[61] A. P. Young, S. Knysh, V. N. Smelyanskiy. *Phys. Rev. Lett.*, **104**, 020502 (2010).

[62] B. Altshuler, H. Krovi, J. Roland. *Proceedings of the National Academy of Sciences*, **107**, 12446 (2010).

[63] S. Knysh, V. Smelyanskiy. `arXiv:1005.3011` (2010).

[64] E. Farhi, J. Goldstone, D. Gosset, S. Gutmann, H. B. Meyer, P. Shor. `arXiv:0909.4766` (2009).

[65] N. Dickson, M. Amin. `arXiv:1108.3303` (2011).

[66] N. G. Dickson. *New Journal of Physics*, **13**, 073011 (2011).

[67] V. Vazirani. *Approximation algorithms.* Springer Verlag (2001).

[68] V. Bapst, G. Semerjian. in preparation (2011).

[69] G. Santoro, R. Martoňák, E. Tosatti, R. Car. *Science*, **295**, 2427 (2002).

[70] J. Roland, N. J. Cerf. *Phys. Rev. A*, **65**, 042308 (2002).

[71] T. Caneva, M. Murphy, T. Calarco, R. Fazio, S. Montangero, V. Giovannetti, G. Santoro. *Phys. Rev. Lett.*, **103**, 240501 (2009).

[72] S. Sachdev. *Quantum phase transitions.* Cambridge University Press (2001).

[73] D. S. Fisher. *Phys. Rev. B*, **51**, 6411 (1995).

[74] G. Biroli, L. F. Cugliandolo. *Phys. Rev. B*, **64**, 014206 (2001).

[75] B. Derrida. *Phys. Rev. B*, **24**, 2613 (1981).

[76] D. Gosset. PhD Thesis, Case Studies in Quantum Adiabatic Optimization (2011).

[77] J. S. Yedidia, W. T. Freeman, Y. Weiss. *Exploring artificial intelligence in the new millennium*, **8**, 236 (2003).

[78] M. Mézard, G. Parisi. *Eur. Phys. J. B*, **20**, 217 (2001).

[79] R. Monasson. *Phys. Rev. Lett.*, **75**, 2847 (1995).

[80] A. Montanari, G. Semerjian. *J. Stat. Phys.*, **124**, 103 (2006).

[81] M. Mézard, G. Parisi. *J. Stat. Phys.*, **111**, 1 (2003).

[82] F. Krzakala, A. Rosso, G. Semerjian, F. Zamponi. *Phys. Rev. B*, **78**, 134428 (2008).

[83] G. Semerjian, M. Tarzia, F. Zamponi. *Phys. Rev. B*, **80**, 014524 (2009).

[84] C. Laumann, A. Scardicchio, S. L. Sondhi. *Phys. Rev. B*, **78**, 134424 (2008).

[85] L. B. Ioffe, M. Mézard. *Phys. Rev. Lett.*, **105**, 037001 (2010).

[86] M. V. Feigel'man, L. B. Ioffe, M. Mézard. *Phys. Rev. B*, **82**, 184534 (2010).

[87] O. Dimitrova, M. Mézard. *J. Stat. Mech.*, **2011**, P01020 (2011).

[88] R. C. Thompson. *Linear Algebra and its Applications*, **13**, 69 (1976).

[89] A. J. Bray, M. A. Moore. *Phys. Rev. Lett.*, **58**, 57 (1987).

[90] F. Krzakala, O. Martin. *Eur. Phys. J. B*, **28**, 199 (2002).

[91] F. Buccheri, A. De Luca, A. Scardicchio. *Phys. Rev. B*, **84**, 094203 (2011).

[92] L. Zdeborová, M. Mézard. *Phys. Rev. Lett.*, **101**, 078702 (2008).

[93] S. Franz, M. Leone, F. Ricci-Tersenghi, R. Zecchina. *Phys. Rev. Lett.*, **87**, 127209 (2001).

[94] S. Franz, M. Mézard, F. Ricci-Tersenghi, M. Weigt, R. Zecchina. *Europhys. Lett.*, **55**, 465 (2001).

[95] `http://code.google.com/p/relsat` (2011).

[96] E. Farhi, J. Goldstone, D. Gosset, S. Gutmann, P. Shor. `arXiv:1010.0009` (2010).

[97] `http://www.laria.u-picardie.fr/∼cli/maxsatz2009.c` (2009).

[98] E. Farhi, D. Gosset. private communication (2011).

[99] C. Angell. *Science*, **267**, 1924 (1995).

[100] F. Sausset, G. Biroli, J. Kurchan. *J. Stat. Phys.*, **140**, 718 (2010).

[101] A. Cavagna. *Physics Reports*, **476**, 51 (2009).

[102] R. Richert, C. Angell. *J.. Chem. Phys.*, **108**, 9016 (1998).

[103] A. Montanari, G. Semerjian. *J. Stat. Phys.*, **125**, 23 (2006).

[104] E. Kim, M. Chan. *Science*, **305**, 1941 (2004).

[105] S. Balibar. *Nature*, **464**, 176 (2010).

[106] A. Rittner, J. Reppy. *Phys. Rev. Lett.*, **98**, 175302 (2007).

[107] T. Kirkpatrick, D. Thirumalai, P. Wolynes. *Phys. Rev. A*, **40**, 1045 (1989).

[108] G. Adam, J. Gibbs. *J.. Chem. Phys.*, **43**, 139 (1965).

[109] W. Götze. *Complex dynamics of glass-forming liquids: A mode-coupling theory.* Oxford University Press, USA (2009).

[110] M. Mézard, G. Parisi, M. Virasoro. *Spin glass theory and beyond.* World scientific Singapore (1987).

[111] M. Mézard, G. Parisi. *J.. Chem. Phys.*, **111**, 1076 (1999).

[112] G. Parisi, F. Zamponi. *Rev. Mod. Phys.*, **82**, 789 (2010).

[113] H. Jacquin, L. Berthier, F. Zamponi. *Phys. Rev. Lett.*, **106**, 135702 (2011).

[114] H. Westfahl, J. Schmalian, P. G. Wolynes. *Phys. Rev. B*, **68**, 134203 (2003).

[115] L. Cugliandolo, G. Lozano. *Phys. Rev. Lett.*, **80**, 4979 (1998).

[116] T. E. Markland, J. A. Morrone, B. J. Berne, K. Miyazaki, E. Rabani, D. R. Reichman. *Nature Physics*, **7**, 134 (2010).

[117] G. Biroli, F. Zamponi. `arXiv:1107.2758` (2011).

[118] M. Boninsegni, A. Kuklov, L. Pollet, N. Prokof'ev, B. Svistunov, M. Troyer. *Phys. Rev. Lett.*, **97**, 80401 (2006).

[119] M. Rossi, E. Vitali, D. Galli, L. Reatto. *Journal of Low Temperature Physics*, **153**, 250 (2008).

[120] W. Kob, H. Andersen. *Phys. Rev. E*, **51**, 4626 (1995).

[121] O. Rivoire, G. Biroli, O. Martin, M. Mézard. *Eur. Phys. J. B*, **37**, 55 (2003).

[122] K. Dawson, A. Lawlor, P. d Gregorio, G. McCullagh, E. Zaccarelli, P. Tartaglia. *Physica A*, **316**, 115 (2002).

[123] R. Darst, D. Reichman, G. Biroli. *J.. Chem. Phys.*, **132**, 044510 (2010).

[124] L. Berthier, A. Moreno, G. Szamel. *Phys. Rev. E*, **82**, 060501 (2010).

[125] F. Krzakala, M. Tarzia, L. Zdeborová. *Phys. Rev. Lett.*, **101**, 165702 (2008).

[126] T. Castellani, A. Cavagna. *J. Stat. Mech.*, **2005**, P05012 (2005).

[127] O. Penrose, L. Onsager. *Phys. Rev.*, **104**, 576 (1956).

[128] L. Foini, G. Semerjian, F. Zamponi. *Phys. Rev. B*, **83**, 094513 (2011).

[129] W. Kob, H. Andersen. *Phys. Rev. E*, **52**, 4134 (1995).

[130] J. M. Deutsch. *Phys. Rev. A*, **43**, 2046 (1991).

[131] M. Srednicki. *Phys. Rev. E*, **50**, 888 (1994).

[132] T. Berkelbach, D. Reichman. *Phys. Rev. B*, **81**, 224429 (2010).

[133] G. Biroli, C. Kollath, A. Läuchli. *Phys. Rev. Lett.*, **105**, 250401 (2010).

[134] B. Gaveau, L. S. Schulman. *Journal of Mathematical Physics*, **39**, 1517 (1998).

[135] W. Saslow. *Phys. Rev. Lett.*, **36**, 1151 (1976).

[136] B. Lubachevsky, F. Stillinger. *J. Stat. Phys.*, **60**, 561 (1990).

[137] A. Donev, S. Torquato, F. Stillinger. *Journal of Computational Physics*, **202**, 737 (2005).

[138] D. A. Young, B. J. Adler. *J. Chem. Phys.*, **60**, 1254 (1974).

[139] A. Denton, N. Ashcroft, W. Curtin. *Phys. Rev. E*, **51**, 65 (1995).

[140] J. Fernandez, M. Puma. *J. Low Temp. Phys.*, **17**, 131 (1974).

[141] W. Saslow, S. Jolad. *Phys. Rev. B*, **73**, 092505 (2006).

[142] D. Galli, L. Reatto, W. Saslow. *Phys. Rev. B*, **76**, 052503 (2007).

[143] *Numerical recipes: the art of scientific computing.* Cambridge University Press (2007).

[144] E. Pollock, D. Ceperley. *Phys. Rev. B*, **36**, 8343 (1987).

[145] D. M. Ceperley. *Rev. Mod. Phys.*, **67**, 279 (1995).

[146] F. Zamponi. *Nature Physics*, **7**, 99 (2011).

[147] A. Cavagna, J. Garrahan, I. Giardina. *Journal of Physics A: Mathematical and General*, **32**, 711 (1999).

[148] L. F. Cugliandolo. Lecture notes, Les Houches, `arXiv:cond-mat/0210312v2` (2002).

[149] P. Martin, E. Siggia, H. Rose. *Phys. Rev. A*, **8**, 423 (1973).

[150] H. Janssen. *Z. Phys. B Cond. Matt.*, **42**, 151 (1981).

[151] R. Kubo, M. Toda, N. Hashitsume. *Statistical physics.* Springer Berlin (1991).

[152] C. Godreche, J. Luck. *Journal of Physics A: Mathematical and General*, **33**, 1151 (2000).

[153] P. Calabrese, A. Gambassi. *J. Stat. Mech.*, **2004**, P07013 (2004).

[154] P. Calabrese, A. Gambassi. *Journal of Physics A: Mathematical and General*, **38**, R133 (2005).

[155] L. Berthier, J. Barrat, J. Kurchan. *Phys. Rev. E*, **61**, 5464 (2000).

[156] L. F. Cugliandolo, D. R. Grempel, G. Lozano, H. Lozza, C. A. Da Silva Santos. *Phys. Rev. B*, **66**, 014444 (2002).

[157] C. Aron, G. Biroli, L. Cugliandolo. *Phys. Rev. Lett.*, **102**, 50404 (2009).

[158] A. Caso, L. Arrachea, G. Lozano. `arXiv:1102.4491` (2011).

[159] L. Arrachea, L. Cugliandolo. *Europhys. Lett.*, **70**, 642 (2005).

[160] M. Srednicki. *Phys. Rev. E*, **50**, 888 (1994).

[161] J. Deutsch. *Phys. Rev. A*, **43**, 2046 (1991).

[162] P. Calabrese, J. Cardy. *Phys. Rev. Lett.*, **96**, 136801 (2006).

[163] D. Rossini, A. Silva, G. Mussardo, G. Santoro. *Phys. Rev. Lett.*, **102**, 127204 (2009).

[164] M. Eckstein, M. Kollar, P. Werner. *Phys. Rev. Lett.*, **103**, 56403 (2009).

[165] A. Polkovnikov, K. Sengupta, A. Silva, M. Vengalattore. *Rev. Mod. Phys.*, **83**, 863 (2010).

[166] G. Carleo, F. Becca, M. Schiró, M. Fabrizio. `arXiv:1109:2516` (2011).

[167] A. Gambassi, P. Calabrese. *Europhys. Lett.*, **95**, 66007 (2011).

[168] B. Sciolla, G. Biroli. *Phys. Rev. Lett.*, **105**, 220401 (2010).

[169] D. Fioretto, G. Mussardo. *New Journal of Physics*, **12**, 055015 (2010).

[170] G. Biroli, C. Kollath, A. Läuchli. *Phys. Rev. Lett.*, **105**, 250401 (2010).

[171] B. Sciolla, G. Biroli. `Arxiv preprint arXiv:1108.5068` (2011).

[172] G. Gallavotti. *Statistical mechanics: A short treatise.* Springer Verlag (1999).

[173] J. Neumann. *Zeitschrift für Physik A Hadrons and Nuclei*, **57**, 30 (1929).

[174] S. Goldstein, J. Lebowitz, R. Tumulka, N. Zanghi. *Eur. Phys. J. H*, **35**, 173 (2010).

[175] M. Rigol, V. Dunjko, V. Yurovsky, M. Olshanii. *Phys. Rev. Lett.*, **98**, 50405 (2007).

[176] A. Iucci, M. Cazalilla. *Phys. Rev. A*, **80**, 063619 (2009).

[177] B. M. McCoy, E. Barouch, D. B. Abraham. *Phys. Rev. A*, **4**, 2331 (1971).

[178] F. Iglói, H. Rieger. *Phys. Rev. Lett.*, **85**, 3233 (2000).

[179] F. Iglói, H. Rieger. *Phys. Rev. Lett.*, **106**, 35701 (2011).

[180] D. Rossini, S. Suzuki, G. Mussardo, G. Santoro, A. Silva. *Phys. Rev. B*, **82**, 144302 (2010).

[181] D. Karevski. `arXiv:cond-mat/0611327` (2006).

[182] P. Calabrese, F. Essler, M. Fagotti. *Phys. Rev. Lett.*, **106**, 227203 (2011).

[183] T. Niemeijer. *Physica*, **36**, 377 (1967).

[184] H. Rieger, F. Iglói. *Phys. Rev. B*, **84**, 165117 (2011).

[185] P. Deift, X. Zhou. *NATO ASI Series B Physics*, **320**, 183 (1994).

[186] A. Mitra, T. Giamarchi. *Phys. Rev. Lett.*, **107**, 150602 (2011).

[187] M. Hastings. *Phys. Rev. B*, **76**, 201102 (2007).

[188] D. Poulin, E. Bilgin. *Phys. Rev. A*, **77**, 052318 (2008).